Imperial College London

Department of Mechanical Engineering
Rolls-Royce Vibration University Technology Centre

Experimental and Numerical Investigation of Turbomachinery Blade Vibration

By
Daniel Heller

A thesis submitted to Imperial College London for the degree of
Doctor of Philosophy

May 2020

For my darling wife, Layla
and my adorable daughter, Amira

Statement of Originality

I declare that the content of this dissertation is my own work and that all else is appropriately referenced.

Copyright Declaration

The copyright of this thesis rests with the author. Unless otherwise indicated, its contents are licensed under a Creative Commons Attribution-Non Commercial-No Derivatives 4.0 International Licence (CC BY-NC-ND).

Under this licence, you may copy and redistribute the material in any medium or format on the condition that: you credit the author, do not use it for commercial purposes and do not distribute modified versions of the work.

When reusing or sharing this work, ensure you make the licence terms clear to others by naming the licence and linking to the licence text.

Please seek permission from the copyright holder for uses of this work that are not included in this licence or permitted under UK Copyright Law.

Acknowledgements

First of all, I would like to express my deep gratitude to both Dr. Christoph Schwingshackl and Dr. Ibrahim Sever for giving me the opportunity to pursue a PhD at Imperial College London, their support and advice during my research. Rolls-Royce plc is to be thanked for providing funding and for their trust in me to conduct this interesting and challenging industrial project. The same is conveyed to Rolls-Royce Deutschland Ltd & Co KG, especially to Thomas Giersch who supplied additional experimental data.

A keen sense of indebtedness is owed to all my colleagues who made my time in London merrier and with whom I was able to eagerly engage in discussions about my research and experimental test rig. Their useful and friendly advice and assistance will be ever appreciated. To be particularly mentioned are Alessandra Vizzaccaro, Alex Haslam, Alfredo Fantetti, Ali Tatar, Giuliano Tuzzi, Leroy Grey, Loïc Salles, Luke Muscutt, Mertol Tüfekci, Michał Szydłowski, Prathiban Sureshkumar, Sam Mitchell, Tom Mace, Václav Ondra, Valentina Ruffini, Venkatesh Suriyanarayanan, and Xing Wang, not forgetting Peter Higgs who was not only a great help in acquiring equipment for my project and organising my conference journeys but also in sorting out any administrative issues that appeared throughout my PhD.

Without my precious wife Layla, my wonderful daughter Amira, my family and friends, I would have never become the person who I am today. You are my towers of strength. Your enormous encouragement and your patience with me have been unwavering. I will always love you!

Abstract

Despite constant research on Blade Tip-Timing (BTT) for decades, the major limitation of this turbomachinery blade vibration measurement technique in terms of insufficient data sampling is still not overcome. Complex vibrations cannot reliably be analysed and, to tackle this issue, an innovative data analysis approach to increasing the amount of useful data was developed. Instead of only being used for determining vibration parameters on the basis of times of blade arrival at a sensor, complete waveforms produced by stationary casing-mounted sensors are processed. Such waveforms usually hold multiple data points of the blade vibration trajectory, yet these data points are hidden and not directly accessible when eyeing the sensor output. Their analysis thus provides new opportunities in respect of the following: characterising multi-mode vibrations occurring within the same instant of time; detecting non-linear vibration responses arising from excitation of engine components with non-linear behaviour; ascertaining axial, radial, and tangential blade positions during operation.

After an introduction to state-of-the-art BTT, the novel concept of investigating blade vibration in turbomachinery is presented on the principle of Blade Tip-Timing (BTT) and clearance sensor waveform analysis (BLASMA), which was filed for patent protection by Rolls-Royce. It is shown that the modulation of the sensor output by blade vibration can offer additional information compared with under-sampled time-of-arrival (TOA) data from traditional BTT applications. The sensor data can help to not only dispel doubts on the validity of statements on blade vibration but also lessen the dependence on contact-based strain gauges measurements for producing reference data. A numerical and experimental study was conducted to evaluate the merit of sensor waveform analysis for describing multi-harmonic blade vibration. Results are carefully discussed in this work and future strategies for proceeding with BLASMA are proposed.

Contents

List of Figures **17**

List of Tables **27**

Nomenclature **29**

1 Introduction **39**

1.1 Problem definition 39

1.2 Project description 42

2 Literature review **45**

2.1 Blade vibration in turbomachinery 45

2.1.1 Sources of vibration 45

2.1.2 Synchronous vibration 47

2.1.3 Asynchronous vibration 48

2.1.3.1 Vortex shedding 49

2.1.3.2 Rotating stall and surge 49

2.1.3.3 Flutter 50

2.1.4 Response characteristics 50

2.2 Classical Blade Tip-Timing 54
2.2.1 Working principle 54
2.2.2 Sensor technology 57
2.2.2.1 Optical sensors 58
2.2.2.2 Capacitive sensors 60
2.2.2.3 Eddy current sensors 62
2.2.2.4 Magnetoresistive sensors 64
2.2.2.5 Microwave sensors 65
2.2.2.6 Summary 66
2.2.3 Data analysis 67
2.2.3.1 Methods 67
2.2.3.2 Practical considerations 72
2.2.4 Discussion 74

3 Fundamentals of sensor waveform analysis for characterising blade vibration 77

3.1 Related art 78
3.1.1 Group from MIT 78
3.1.2 Group from Swansea University 79
3.1.3 Group from Samara University 80
3.2 Methodology 82

4 Modelling of a bladed disk and sensor **87**

4.1 Model assumptions 88

4.2 Bladed disk model 89

4.2.1 Dynamics of a bladed disk 91

4.2.2 Blade trajectory 94

4.2.3 Blade width 96

4.3 Sensor model 97

4.3.1 Waveform equation 98

4.3.2 Sensor position 101

4.3.3 Sampling waveforms 102

4.3.4 Angular instantaneous and apparent width of the sensor field 103

4.3.5 Number of complete vibration cycles in a trajectory snapshot 105

5 BLASMA-SCP **107**

5.1 Model parameterisation 110

5.2 Simulation results 114

5.3 Post-processing of the data 115

5.3.1 Integral of the waveform 115

5.3.2 Slopes of the waveform 121

5.4 Conclusion 127

6 BLASMA-IWE **129**

6.1 Model parameterisation 130

6.2 Simulation results 134

6.3 Conclusion 142

7 BLASMA-OPT **145**

7.1 Model parameterisation 147

7.2 Simulation results 154

7.2.1 Asynchronous single-harmonic excitation of the blades 155

7.2.1.1 Determination of the processable part of a waveform 156

7.2.1.2 Alternatives in the event of poor results . . . 157

7.2.1.3 Parameterisation of the optimiser 158

7.2.1.4 Convergence study 160

7.2.1.5 Comparison with traditional BTT 161

7.2.1.6 Summary 163

7.2.2 Synchronous single-harmonic excitation of the blades . 163

7.2.2.1 Sensitivity analysis of BLASMA-OPT 164

7.2.2.2 Summary 169

7.2.3 Asynchronous multi-harmonic excitation of the blades . 170

7.2.3.1 Parameterisation of the optimiser 171

7.2.3.2 Convergence study 174

7.2.3.3 Summary 177

7.2.4 Synchronous multi-harmonic excitation of the blades . 178

7.3 Conclusion 179

8 Experimental validation of sensor waveform analysis 183

8.1 Test rig 184

8.1.1 Blisk 185

8.1.2 Actuators and sensors 189

8.1.2.1 Capacitive sensor for evaluating BLASMA . . 189

8.1.2.2 Encoder and tachometer for speed measurements 190

8.1.2.3 Piezoelectric patches for exciting blades . . . 190

8.1.2.4 Strain gauges and LDV for reference measurements 191

8.1.3 Mistuning analysis 192

8.1.4 Calibration 197

8.1.4.1 Phase lag 198

8.1.4.2 Parameter curves 200

8.2 Experimental results 208

8.2.1 Synchronous single-harmonic excitation of the blades . 212

8.2.2 Asynchronous and synchronous multi-harmonic excitation of the blades 217

8.3 Conclusion 220

9 Contributions and outlook **223**

Bibliography **227**

List of Figures

2.1 Typical mode shapes of a cantilever 52

(a) 2^{nd} edge-wise bending mode 52

(b) 2^{nd} flap-wise bending mode 52

(c) 2^{nd} torsional mode 52

2.2 1^{st} flap-wise bending mode of a bladed disk with two nodal diameters 53

2.3 Working principle of BTT 55

3.1 Principle of BLASMA 82

3.2 Waveform from a blade passage 83

(a) Blade is approaching the sensor 83

(b) Blade is beneath the sensor 83

(c) Blade is leaving the sensor 83

4.1 Top view of an unrolled simplified rotor stage on the left, front view of this rotor stage on the right 90

4.2 Bladed disk model 93

4.3 Meshing of a blade 97

4.4 Width of the sensor field at the location of the sensor 104

5.1 Some waveforms characteristics 108

5.2 Case studies for assessing BLASMA-SCP where a vibrating blade (red (■)) is compared with a fictitiously rigid reference blade (blue (■)) in different situations 109

5.3 Vibration characteristics 112

(a) Deflection trajectory of the vibrating blades at resonance – with a zoomed-in view in grey ( ) 112

(b) FRF – Magnitude 112

5.4 Replication of a capacitive sensor waveform reported in the literature 113

5.5 Case (i) 115

(a) Sensor waveforms 115

(b) Trajectory of vibration deflection and velocity during the passage 115

5.6 Case (ii) 116

(a) Sensor waveforms 116

(b) Trajectory of vibration deflection and velocity during the passage 116

5.7 Case (iii) 117

(a) Sensor waveforms 117

(b) Trajectory of vibration deflection and velocity during the passage 117

5.8 Differences between the waveforms from the passages of a vibrating blade and a rigid blade for each case 120

(a) Case (i) 120

(b) Case (ii) 120

(c) Case (iii) 120

5.9 Errors in vibration velocities computed using the slopes of the waveforms at the signal rise (SR) and signal fall (SF) from the passages of a vibrating blade in each of the three case studies . 124

6.1 Analysis of the waveform fit 133

(a) Replication of an eddy current sensor waveform reported in the literature 133

(b) Fit error 133

6.2 Vibration characteristics 134

(a) Deflection trajectory of the vibrating blades at resonance – with a zoomed-in view in grey ( ) 134

(b) FRF – Magnitude 134

6.3 Sensor output with waveforms from passages of blade 1 on the left and a zoomed-in view of a waveform on the right 135

6.4 Blade deflection (a) causes the modulation of waveform (b) . . 136

(a) Blade deflection 136

(b) Waveform 136

6.5 Errors in vibration properties 137

(a) Vibration deflection amplitudes 137

(b) Vibration frequencies 137

6.6 Fractions of the vibration hypersurface 139

(a) First harmonic 139

(b) Second harmonic 139

6.7 Comparison of the actual vibration deflection signal with the signal computed using the vibration parameters found by applying BLASMA-IWE and with the signal computed using the BLASMA-IWE amplitudes, BLASMA-IWE frequencies, and FFT phases (IWE-FFT-Phases) 141

7.1 FRF – Magnitude 149

7.2 Experimental waveforms from a BTT and clearance measurement system applied to Rolls-Royce Rig750 at TU Darmstadt in Germany 150

7.3 Replication of an experimentally measured waveform 151

7.4 Deflection trajectory of the vibrating blades at resonance in the case of **asynchronous** and **synchronous** single-harmonic excitation – with a zoomed-in view in grey ( ) 154

7.5 Sensor output with waveforms from passages of blade 1 on the left and a zoomed-in view of a waveform on the right 155

7.6 Blade deflection (a) causes the modulation of waveform (b) . . 156

(a) Blade deflection 156

(b) Waveform 156

7.7 Results from the convergence study in the case of **asynchronous** single-harmonic vibration 160

(a) Vibration deflection amplitude X^1 160

(b) Vibration frequency ω^1 160

7.8 Results from the convergence study in the case of **synchronous** single-harmonic vibration 164

(a) Vibration deflection amplitude X^1 164

(b) Vibration frequency ω^1 164

7.9 Results from the sensitivity study in the case of **synchronous** single-harmonic vibration 165

(a) Dependence on the position in the vibration cycle . . . 165

(b) Amplitude sensitivity 165

(c) Speed sensitivity 165

(d) Campbell diagram 165

7.10 Identification of a travelling wave of **synchronous** single-harmonic blade vibration 169

(a) Inter-blade phase angles and nodal diameters 169

(b) Determination of inter-blade phase angles 169

7.11 Deflection trajectory of the vibrating blades at resonance in the case of multi-harmonic excitation – with a zoomed-in view in grey ( ) 171

(a) Asynchronous vibration 171

(b) Synchronous vibration 171

7.12 Results from the convergence study in the case of **asynchronous** multi-harmonic vibration 173

(a) Vibration deflection amplitude X_1^1 173

(b) Vibration frequency ω_1^1 173

(c) Vibration deflection amplitude X_3^1 173

(d) Vibration frequency ω_3^1 173

7.13 Comparison of the actual vibration deflection signal with the signal computed using the vibration parameters from optimisation (OPT), with the signal computed using the optimum amplitudes, optimum frequencies and FRF steady-state phases (OPT-SS-Phases), and with the signal computed using the optimum amplitudes, optimum frequencies and FFT phases (OPT-FFT-Phases) 175

7.14 Results from the convergence study in the case of **synchronous** multi-harmonic vibration 179

(a) Vibration deflection amplitude X_1^1 179

(b) Vibration frequency ω_1^1 179

(c) Vibration deflection amplitude X_2^1 179

(d) Vibration frequency ω_2^1 179

8.1 View of the test rig 184

8.2 Equipment at the front of the test rig 185

8.3 Equipment at the rear of the test rig 186

8.4 Equipment at the top of the test rig 187

8.5 Cold bending of a blade 193

(a) Warped blade 193

(b) Corrected blade 193

8.6 Modal analysis of the blisk 195

(a) Hardware configuration 195

(b) FRF - Average Magnitude 195

8.7 Lag with respect to the LDV integrated velocity signal 199

(a) Capacitive sensor 199

(b) Piezoelectric patch 199

(c) Strain gauge 199

8.8 Calibration curves belonging to the first bending mode family 201

8.9 Model of a beam with clamped-free boundary conditions . . . 202

8.10 Measurements of global parameters 211

(a) Rotational speed 211

(b) Tachometer 211

(c) Shaft position 211

(d) Capacitive sensor 211

8.11 Excitation and response signals from the synchronous single-harmonic excitation study 213

(a) Piezoelectric patch signal – with a zoomed-in view in grey ( ) 213

(b) Strain gauge signal – with a zoomed-in view in grey ( ) 213

(c) Waveform 213

(d) Section of the strain gauge signal corresponding to the waveform in (c) 213

8.12 Results from the study of single-harmonic excitation 215

(a) Vibration deflection amplitude X_1^1 215

(b) Vibration frequency ω_1^1 215

(c) Vibration deflection amplitude X_2^1 215

(d) Vibration frequency ω_2^1 215

8.13 Errors in vibration properties in the case of single-harmonic excitation 216

(a) Vibration deflection amplitudes 216

(b) Vibration frequencies 216

8.14 Excitation and response signals from the asynchronous and synchronous multi-harmonic excitation study 218

(a) Piezoelectric patch signal – with a zoomed-in view in grey ( ) 218

(b) Strain gauge signal – with a zoomed-in view in grey ( ) 218

(c) Waveform 218

(d) Section of the strain gauge signal corresponding to the waveform in (c) 218

8.15 Results from the study of multi-harmonic excitation 219

(a) Vibration deflection amplitude X_1^1 219

(b) Vibration frequency ω_1^1 219

(c) Vibration deflection amplitude X_2^1 219

(d) Vibration frequency ω_2^1 219

8.16 Errors in vibration properties in the case of multi-harmonic excitation 220

(a) Vibration deflection amplitudes 220

(b) Vibration frequencies 220

List of Tables

2.1 Major advantages and disadvantages of optical sensors for BTT applications 59

2.2 Major advantages and disadvantages of capacitive sensors for BTT applications 61

2.3 Major advantages and disadvantages of eddy current sensors for BTT applications 63

2.4 Major advantages and disadvantages of magnetoresistive sensors for BTT applications 65

2.5 Major advantages and disadvantages of microwave sensors for BTT applications 66

2.6 Data analysis methods for BTT applications 71

3.1 Some important variables of the model 84

5.1 Parameters for the sensor model 110

5.2 Parameters for the bladed disk model 111

5.3 Numerical integrals of the waveforms 118

5.4 Numerical slopes of the waveform edges 122

5.5 Estimated velocities of a blade at the time of the rise and fall of a waveform 123

5.6 Average vibration velocities of a blade and average times of waveform occurrences 125

6.1 Parameters for the sensor model 130

6.2 Parameters for the bladed disk model 131

6.3 Parameters for the least-squares fitting 138

7.1 Parameters for the bladed disk model 148

7.2 Parameters for the sensor model 153

7.3 Parameters for the optimisation problem in the case of **asynchronous** and **synchronous** single-harmonic vibration 159

7.4 Vibration parameters computed on the basis of the traditional TOA 162

7.5 Parameters for the optimisation problem in the case of **asynchronous** multi-harmonic vibration 172

7.6 Parameters for the optimisation problem in the case of **synchronous** multi-harmonic vibration 178

8.1 Material and geometrical properties of the blisk 188

Nomenclature

List of global abbreviations

BLASMA-IWE	Inverse waveform equation method
BLASMA-OPT	Optimisation method
BLASMA-SCP	Signal characteristics processing method
BLASMA	Blade Tip-Timing (BTT) and clearance sensor waveform analysis
BTT	Blade Tip-Timing
CPU	Central processing unit (within a computer)
DFT	Discrete Fourier Transform
FE	Finite element
FFT	Fast Fourier transform
FRF	Frequency response function
LDV	Laser Doppler vibrometer
NSMS	Non-Intrusive Stress Measurement System
NUDFT	Non-uniform discrete Fourier Transform
OPR	Once-per-revolution
PID	Proportional–integral–derivative (controller)
RPM	Revolutions per minute
TOA	Time of arrival

List of symbols

α	Blade stagger angle
$\bar{z}$	Variable of integration for the z-dimension
$\ddot{\boldsymbol{x}}(t)$	Vibration acceleration vector
$\dot{\boldsymbol{x}}(t)$	Vibration velocity vector
$\boldsymbol{\Gamma}_{\mathrm{B}}(t)$	Total blade deflection trajectory
$\boldsymbol{\varphi}_{\mathrm{B}}^{0}$	Vector containing the angular starting position of each blade (t=0 s)
$\boldsymbol{\varphi}_{\mathrm{S}}^{0}$	Vector containing the initial angular position of each sensor
$\boldsymbol{\varphi}_{\mathrm{B}}^{\mathrm{E}}$	Sampled trajectory sections of the edge-wise deflection
$\boldsymbol{a}_{\mathrm{B}}$	Sampled trajectory sections of the axial deflection
$\boldsymbol{f}(t)$	Force vector specifying excitation frequency and amplitude
$\boldsymbol{u}$	Vector containing the sampled points of a waveform
$\boldsymbol{u}_{\mathrm{m}}$	Vector containing the sampled points of a measured waveform
$\boldsymbol{x}(t)$	Displacement vector
$\Delta(t)$	Term that comprises a signal offset $\Delta_{\mathrm{O}}(t)$ and possible noise $\Delta_{\mathrm{N}}(t)$
$\Delta\theta_{\mathrm{M,CS\text{-}LDV}}$	Phase lag between the capacitive sensor and LDV
$\Delta\theta_{\mathrm{M,PEP\text{-}LDV}}$	Phase lag between the piezoelectric patch and LDV
$\Delta\theta_{\mathrm{M,SG\text{-}LDV}}$	Phase lag between the strain gauge and LDV

$\Delta\theta_{\mathrm{M}}$	Phase lag owed to the mechanics of the system
$\Delta\varphi_{\mathrm{S}}^{0}$	Angular distance between two sensors
$\Delta\Omega$	Change in the rotational speed
$\Delta d_{\mathrm{B\text{-}B}}^{\max}$	Maximum measured deviation of the linear distance between two facing blade edges at the tip from the theoretical value
$\Delta L_{\mathrm{CF}}(t)$	Elongation of the blade due to centrifugal loading
Δt	Additional time delay
δt	Time step
Δt_{BTT}	BTT time difference
Δt_{BT}	Blade travelling time along the sensor
δt_{C}	Time step of the smallest clearance between the blade and the sensor
δt_{d}	Time step of blade departure from the sensor field
δt_{e}	Time step of blade entry into the sensor field
δt_{peak}	Time step of reaching the waveform peak
$\Delta x_{\mathrm{offset}}$	Static blade offset position
ϵ	Radius of the ϵ-neighbourhood
$\epsilon_{\%}$	Percentage that defines the radius of the ϵ-neighbourhood
ϵ_{BTT}	BTT error
$\epsilon_{\mathrm{SG}}(t, z)$	Strain in the contact area between the blade and strain gauge
κ	Coefficient
λ	Speed calibration parameter

λ_e	Experimental speed calibration parameter
Λ_und	Undamped eigenvalue matrix
$\mathcal{A}_\mathrm{B}$	Blade cross-sectional area
$\mathcal{I}_\mathrm{A,y}$	Area moment of inertia about the y-axis (uncoupled blade)
$\mathcal{I}_\mathrm{BD}$	Mass moment of inertia of the blisk
$\mathcal{I}_\mathrm{BO}$	Mass moment of inertia of the bores
$\mathcal{I}_\mathrm{B}$	Mass moment of inertia of a blade
$\mathcal{I}_\mathrm{D}$	Mass moment of inertia of the disk
$\mathfrak{T}$	Complex amplitude
$\mathfrak{t}(t)$	Temporal solution
$\mathfrak{x}(z)$	Spatial solution
μ_u	Average of waveforms
ν	Complex eigenvalue
Ω	Rotational frequency of the shaft
ω	Vibration frequency
$\omega_\mathrm{d}^\mathrm{C}$	Damped natural frequency of a cantilever
$\omega_\mathrm{und}^\mathrm{C}$	Undamped natural frequency of a cantilever
ω^p	Vibration frequency at a peak of the FRF magnitude
ω_BTT	BTT vibration frequency
ω_r	Peak frequency of either mode family in the rotating frame of reference

ω_{Start}	Starting point of the vibration frequency for BLASMA-OPT
ω_{s}	Peak frequency of either mode family in the inertial frame of reference
ω_k	Frequency of the k-th harmonic
$\overline{t}$	Average time
$\overline{t}_{\mathrm{case(i)}}$	Average time in BLASMA-SCP case(i)
$\overline{t}_{\mathrm{case(ii)}}$	Average time in BLASMA-SCP case(ii)
$\overline{t}_{\mathrm{case(iii)}}$	Average time in BLASMA-SCP case(iii)
$\overline{t}_{\mathrm{SF}}$	Average time at the falling edge of a waveform
$\overline{t}_{\mathrm{SR}}$	Average time at the rising edge of a waveform
$\overline{v}^{\mathrm{v}}_{\mathrm{B,case(i)}}$	Average vibration velocity in BLASMA-SCP case(i)
$\overline{v}^{\mathrm{v}}_{\mathrm{B,case(ii)}}$	Average vibration velocity in BLASMA-SCP case(ii)
$\overline{v}^{\mathrm{v}}_{\mathrm{B,case(iii)}}$	Average vibration velocity in BLASMA-SCP case(iii)
ϕ	Angular dimension in or against the direction of rotation
Ψ_{und}	Undamped eigenvector matrix
ρ_{S304}	Density of SAE 304 stainless steel
$\sigma_{\mathrm{SG}}(t,z)$	Bending stress in the contact area between the blade and strain gauge
σ_{u}	Standard deviation of waveforms
τ	Nominal motor torque
θ_{BTT}	BTT phase
θ_k	Phase of the k-th harmonic

φ_{S}^{0}	Initial angular position of the sensor
φ_{B}^{0}	Angular starting position of a blade
$\varphi_{\mathrm{B}}^{\mathrm{E}}(t)$	Vibration in the angular edge-wise direction
$\varphi_{\mathrm{B}}^{\mathrm{F}}(t)$	Vibration in the angular flap-wise direction
$\varphi_{\mathrm{B}}^{\mathrm{r}}(t)$	Rigid angular position of a blade
$\varphi_{\mathrm{B}}^{\mathrm{T}}(t)$	Vibration in the angular torsional direction
$\varphi_{\mathrm{B}}^{\mathrm{v}}(t)$	Function of blade vibration
φ_{S}	Angular position of the sensor
$\varphi_{\mathrm{B}}(t)$	Total angular blade position along the ϕ-axis
$\widetilde{\Lambda}_{\mathrm{und}}$	New eigenvalues after transformation
$\widetilde{K}$	New stiffness matrix after transformation
$\widetilde{z}$	Variable of integration for the z-dimension
$\xi_{\mathrm{S304}}\left(\omega_{\mathrm{d}}^{\mathrm{C}}\right)$	Damping ratio of SAE 304 stainless steel at frequency $\omega_{\mathrm{d}}^{\mathrm{C}}$
ζ	Coefficient
a	Axial dimension
$A_{\mathrm{B,P}}^{0}$	Initial axial position of the measurement location at the blade tip
A_{B}^{0}	Initial axial position of the blade tip
$a_{\mathrm{B}}(t)$	Vibration in the translational axial direction
b	Metric width of a blade tip
C	Damping matrix

c_{B}^{0}	Initial clearance between the blade and the casing at engine standstill
$C_{\mathrm{BO,l}}$	Distance from the large bore centroid to the rotation axis
$C_{\mathrm{BO,s}}$	Distance from the small bore centroid to the rotation axis
C_{B}	Distance from the blade centroid to the rotation axis
$c_{\mathrm{B}}(t)$	Clearance between the blade and the casing
$c_{\mathrm{B}}\left(\omega_{\mathrm{d}}^{\mathrm{C}}\right)$	Damping coefficient at frequency $\omega_{\mathrm{d}}^{\mathrm{C}}$
$d_{\mathrm{B\text{-}B}}$	Theoretical linear distance between two facing blade edges at the tip
D_{BD}	Blisk depth
E_{S304}	Young's modulus of SAE 304 stainless steel
F_{PEP}	Force amplitude of the piezoelectric patch
$f_{\mathrm{PEP}}(t, z)$	Force function of the piezoelectric patch
f_{S}	Sampling frequency of the data acquisition system
i	Index variable
K	Stiffness matrix
k	Index variable
k_{F}	Force-to-voltage ratio
$L_{\mathrm{S,P}}^{0}$	Distance between the longitudinal axis of the blade and the measurement location P at the blade tip along the chord line at the beginning of the measurement when there is no torsion

L_{B}	Blade length
L_{S1}	Distance between the longitudinal axis of the blade and the measurement location of sensor 1 at the blade tip along the chord line
L_{S2}	Distance between the longitudinal axis of the blade and the measurement location of sensor 2 at the blade tip along the chord line
M	Mass matrix
m_{B}	Blade mass
$M_{\mathrm{y}}(t, z)$	Internal bending moment about the y-axis
N	Number of harmonics in the vibration signal
N_{B}	Number of blades
n_{C}	Number of complete vibration cycles in a waveform snapshot
$n_{\mathrm{R}}(t)$	Number of revolutions
$n_{\mathrm{S}}(t)$	Number of samples of a waveform
N_{W}	Number of processed waveforms
$q_{\mathrm{PEP}}(t, z)$	Distributed load due to the external force $f_{\mathrm{PEP}}(t, z)$ with amplitude F_{PEP}
r	Radial dimension
R_{B}^{0}	Initial radial distance between the blade tip and the centre of the rotor
$R_{\mathrm{BO,l}}$	Large bore radius
$R_{\mathrm{BO,s}}$	Small bore radius
$r_{\mathrm{B}}(t)$	Vibration in the translational radial direction

R_{D}	Disk radius
r_{F}	Percentage discrepancy between force amplitudes
T	Torsional dimension
t	Time
$t^{\star}$	Time of evaluation
$t^{\mathrm{r}}_{\mathrm{BTT}}$	Reference time
$t^{\mathrm{v}}_{\mathrm{BTT}}$	Time of arrival
t_0	Measurement starting time
t_{BTT}	Time of waveform occurrence
t_{d}	Time of blade departure from the sensor field
t_{e}	Time of blade entry into the sensor field
t_{M}	Measurement time determining the amount of sensor data
t_C	Time of the smallest clearance between the blade and the sensor
U	Nominal amplitude of a waveform in $u(t)$
$u(t)$	Sensor function
u^{r}	Sensor function in the case of rigid blades
u^{v}	Sensor function in the case of vibrating blades
$v^{\mathrm{r}}_{\mathrm{B}}$	Constant rotational speed of the blade
$v^{\mathrm{v}}_{\mathrm{B,s}}$	Averaged solution of the instantaneous vibration velocity of the blade
$v^{\mathrm{v}}_{\mathrm{B}}(t)$	Instantaneous vibration velocity of the blade

$v_{\mathrm{B}}(t)$	Instantaneous total velocity of the vibrating blade
$W_{\mathrm{B}}^{\mathrm{C}}$	Chord length of an undeformed blade
W_{B}	Blade width
w_{B}	Angular width of a blade tip
$w_{\mathrm{S}}(t)$	Angular instantaneous and apparent width of the sensor medium
x	x-coordinate
$x(t, z)$	Displacement of the cantilever at time t and location z
$x_{\mathrm{B}}^{\mathrm{F}}(t)$	Vibration in the flap-wise direction
X_{BTT}	BTT deflection amplitude
$x_{\mathrm{B}}(t)$	Periodic steady-state blade vibration
X_{LDV}	Amplitude of the LDV integrated velocity
$x_{\mathrm{LDV}}(t, z)$	LDV integrated velocity function
x_{SG}	Location of the strain gauge on the x-axis
$x_{\mathrm{ss}}(t, z)$	Real-valued steady-state solution
X_{Start}	Starting point of the amplitude for BLASMA-OPT
X_k	Amplitude of the k-th harmonic
y	y-coordinate
z	z-coordinate
z_{PEP}	Location of the piezoelectric patch along the blade
z_{SG}	Location of the strain gauge along the blade

Chapter 1

Introduction

1.1 Problem definition

Vibration in turbomachinery continuously stresses the material and deteriorates performance. Consequently, fatigue damage may occur - particularly in form of high-cycle fatigue. This might lead to a complete failure of the engine and has to be avoided under any circumstances. Because of their geometry and arrangement, rotor blades are prone to fatigue damage. Much research has been conducted in this regard to develop measurement methods for understanding and analysing blade vibration [1].

Contact measurement methods, such as well-established strain gauges, are often utilised to detect and analyse blade vibration. Strain gauges are traditionally mounted on the surface of the blade for measuring vibratory strain. The major disadvantages of this technique are the need for direct access to the blades, the limited number of blades that can be instrumented, high equipment costs, great effort of installation, the short operating lifetime in harsh environments, the perturbation of the fluid flow, and mistuning. These drawbacks prevent the continuous application of strain gauges in turbomachinery during normal operation [2–6].

The frequency modulated grid is another measurement method for detecting blade vibration. A wire is installed around the casing, and a magnet is mounted on the tip of a blade. The magnet generates an alternating current in the wire, which is modulated by blade vibration. The downsides of applying this method are the exorbitant cost of installation, disruptions to the fluid

flow, the considerable preparation time, and the inability of monitoring all blades simultaneously [7–9].

Laser Doppler vibrometer (LDV) and laser Doppler distance sensors can be used to determine the vibration displacement and vibration velocity of blades by taking advantage of the modulation of a laser beam when struck and reflected by a moving blade (Doppler effect). The sensor is normally operated either in tracking mode or scanning mode. In the first, a laser beam emitted by the instrument follows a particular blade whilst it rotates. The scanning mode, by contrast, enables measurements on a stationary bladed disk where different points of the bladed disk are measured in quick succession by redirecting the laser beam along a particular predefined path, which can be a circle or line. Regardless of the chosen mode, the blade that is targeted by the sensor at a certain point in time reflects a distorted laser beam back to the sensor, whereupon a comparison with the emitted beam is made for determining the vibratory quantities. The read-outs are afterwards accessible to the operator. Unfortunately, only blade motion in the direction of the reflected laser beam can be determined without further effort, which is why the sensors require direct sight of the bladed disk. On top of that, laser Doppler sensors are infamous for being bulky and relatively heavy, which are not desired features of aeroengine measurement equipment [10–21].

Digital image processing techniques have become more popular with the development and improvement of high-speed cameras. Such a camera is mounted on a rack for taking pictures of rotating and vibrating blades that are analysed in a subsequent step. If the number and quality of the images are sufficiently high to extract vibration data, it is possible to visualise the blade dynamics that can be found in an engine. The disadvantages of this measurement technique are the necessity of acquiring and installing expensive and sensitive high-speed cameras and the requirement of having the appropriate computer infrastructure to store and process a large amount of data [22, 23].

Less conventional measurement devices that help to determine blade vibration are casing-mounted accelerometers [24, 25] and pressure sensors [26–29]. The problem with these methods is, however, that they do not measure quantities that directly describe or relate to the motion of a blade. Therefore, measurement results obtained in such a way can merely function as a vague indicator of blade vibration.

In addressing these issues, the turbomachinery industry and research institutes have been working since the 1960s on an alternative non-contact measurement technique that is today widely known as Blade Tip-Timing (BTT) or Non-Intrusive Stress Measurement System (NSMS). Sensors are mounted around the circumference of the casing to determine the times when blades pass by. These values are then compared with the passing times of simulated fictitiously rigid blades. On the basis of these comparisons, it is possible to detect vibration at a certain measurement location on the tip of a blade. The vibration of the entire blade is then obtained by extrapolation [30–36].

Blades can show complicated forms of multi-harmonic and non-linear vibration, which cannot be measured with BTT at the present time according to Rolls-Royce [37]. The main reason is that most natural frequencies of the blades are not less than half the frequency at which the blade trajectory is sampled, leading to under-sampled BTT data. Unfortunately, this sampling frequency, which is not be confused with the sampling frequency of the data acquisition system, is fairly static because it is essentially a function of the number of sensors employed and the rotational speed, which are themselves limited for financial, operational, and safety reasons. Besides, BTT suffers as any other measurement method from the general effects of measurement uncertainty that causes data scattering. The interpretation of such data is difficult, requiring new methods that can cope with these conditions to find a reliable replacement for strain gauges in the future [38].

1.2 Project description

Current BTT technology seems to have reached its limits, and a novel approach to blade vibration monitoring is required. The major target of this work was to introduce an application and analysis methodology that had not previously been pursued by research bodies and industry. Enhancing existing approaches to computing vibration quantities from BTT blade passing times by fitting experimental data to a model had been done countless times in the field and was thus not part of this work. With this in mind, work was directed towards overcoming the principal drawback of BTT: under-sampling of vibration data. The amount of passing time data generated per blade is primarily bound to the number of sensors which is limited by technical and economic restrictions, such as the necessity to guarantee engine integrity and data processability and to observe target costs. Traditional BTT has to be accompanied or substituted by a more convincing data source to estimate the vibration behaviour of a blade as accurately as possible.

Therefore, effort was devoted to identifying a path forward that led to the development of Blade Tip-Timing (BTT) and clearance sensor waveform analysis (BLASMA), which was filed for patent protection by Rolls-Royce. Signal waveforms are generated by a sensor in the moment of a blade passage and are used in traditional BTT applications to determine the time of a blade arrival, requiring only a single point on the waveform. It is demonstrated in this work that signal waveforms are modulated as a whole by blade vibration and that these modulated waveforms contain more information on blade vibration than standard blade passing times. By using BLASMA together with suitable mathematical and signal processing methods, it is possible to determine important parameters of complex blade vibration that could not previously be examined with standard BTT.

First and foremost, it was necessary to become familiar with blade vibration and BTT at the beginning of the project. A thorough literature review served to identify not only the most recent but also historical research and industry

efforts to upgrade BTT. Concurrently, a computer model of a bladed disk and sensor was developed. A measurement procedure was programmed to simulate signal waveforms from the passages of blades along sensors. With the help of these waveforms, vibration quantities were deduced.

Model improvement and the development of methods for determining vibration parameters came next in the project schedule. The central aim was to implement advanced procedures for detecting vibration phenomena with the focus being on multi-harmonic vibration responses hidden in simulated waveform data. Additionally, it was required to develop algorithms that separated the desired information from the vast amount of recorded data. For later experiments, it was helpful to have routines in place that were capable of processing large data sets.

Afterwards, an experimental study was organised and carried out to confirm the potential of BLASMA for the useful exploration of real vibration problems. An already existing yet dismantled test rig, which only consisted of a bearing, casing, and shaft without any measurement equipment, was rebuilt and modified. The first measures include the selection and installation of the drive system and the design and installation of a blisk (integral bladed disk), which was instrumented with piezoelectric patches for exciting the structure and with strain gauges for reference measurements. As regards the latter purpose, the test rig was also equipped with an LDV. Lastly, a capacitive sensor was mounted on the casing of the test rig to produce waveforms from the passing of blades. The fresh methodology was then applied to two test cases of multi-harmonic blade vibration, whose parameters were determined by processing experimental data that was obtained. The outcome of an ensuing error analysis displayed the inherent qualities of BLASMA and served to optimise and verify the computer models.

Chapter 2

Literature review

BTT systems are applied to axial and centrifugal compressors, fans, and turbines to measure blade vibration [39, 40]. Ramifications include the almost inevitable under-sampling of vibration data, which imposes a serious limitation on the applicability of the method. It was for this particular reason why this PhD project was started. The first objective was to identify uncharted areas of improvement, starting from classical BTT. On this account, a thorough literature review was conducted on the basis of nearly 1600 international publications, patents, and theses from six decades of dedicated BTT research. The literature was grouped as regards hardware and software using a reference management program. A more than 500-page long summary was created, whose most fundamental content is found in this chapter and partly in [41, 42]. In the following literature review, relevant aspects of the theory of blade vibration are presented, accompanied by an assessment of state-of-the-art BTT. The shortcomings of the measurement method are discussed to mark the beginning of the actual research work of this PhD project.

2.1 Blade vibration in turbomachinery

2.1.1 Sources of vibration

It is well understood that vibratory stress, if sustained long enough, leads in any material to fatigue and, if not treated appropriately, to failure of that material [43]. This process is accelerated when the material is excited at

resonance, which raises the vibratory stress experienced by the material. Rotor blades in turbomachines are especially vulnerable to vibration because of their often long and slender shapes and the harsh environment they operate in [44]. Even though there are ways to increase the mechanical damping of the blades, e.g., through shrouds and under-platform dampers, the available amount of aerodynamic and mechanical (material and structural) damping is inadequate to avert vibrations entirely [45, 46]. Knowing at which operating conditions resonances are to be anticipated is hence of utmost relevance for damage prevention, which is why aero-engine manufacturers spend a significant amount of resources on the design of bladed disks with maintenance costs above $400M per year for merely dealing with the consequences of vibration [47].

In the design process, already identified excitation sources are taken into account so as to create blades with natural frequencies of which only the least possible number should ever coincide with any of the excitation frequencies for the shortest time during operation. Unfortunately, not all coincidences can be bypassed despite the thorough adaptation of the blades to the rest of the engine and the operating conditions. It needs to be checked if the remaining resonances are damaging and the quality of the blades can be deemed satisfactory. Moreover, determining the natural frequencies of a stationary bladed disk assembly with a finite element (FE) software and validating them through benchtop hammer testing are often not accurate enough since they only cover the dependence of natural frequencies on geometrical and material properties. This is due to the fact that the natural frequencies of the blades reversibly change during normal operation mainly as a function of the rotational speed but with varying magnitude amongst mode families. Responsible for this are various phenomena that only occur in the rotating frame of reference. Worthy of mention are centrifugal stiffening and spin softening, which are caused by the fictitious centrifugal force, and gyroscopic effects, which are attributed to the likewise fictitious Coriolis force. As regards blades, centrifugal stiffening is the most powerful of the three that induces an increase in the values of the natural frequencies, which should consequently be determined along the desired operating line of the turbomachine [48–52].

Blade vibration is traditionally grouped into forced vibration and self-excited vibration (flutter) [53]. The first is frequently attributed to unsteady flow or aerodynamic phenomena, which disturb the exchange of energy between the fluid and the blades and appear in various forms, for instance, flow separation, rotating stall, surge, tip leakage flow, vortex shedding, or wakes [54–56]. Apart from purely flow-induced vibration, the vibration of other engine components, such as shafts or bearings, can also be the root of a forced response of the blades through the transmission of vibrational energy between structural components, although this regularly plays a minor role [57, 58]. On the other hand, flutter is an aeroelastic problem involving the interaction between inertial, elastic, and aerodynamic forces [59].

All these vibration phenomena can additionally be amplified by the bladed disk not being cyclic-symmetric or tuned, which leads to a non-uniform distribution of natural frequencies between blades [60, 61]. Mistuning is unavoidable and mainly caused through the manufacturing and assembly process, geometric tolerances, material inhomogeneities, and mechanical failure modes during operation, such as fatigue, fracture, and wear [61–63]. Sometimes a special mistuning pattern is superposed on the bladed disk design with the intention of reducing vibration levels by inter-blade load counterbalancing [64–67].

In order to conform with the classification of traditional BTT data analysis methods, blade vibration is in this work categorised into synchronous vibration and asynchronous vibration [68]. Each type of vibration has its own idiosyncrasies that are highlighted in the following section with a focus on flow-related vibration.

2.1.2 Synchronous vibration

Synchronous vibration, also known as engine-order vibration, occurs at frequencies which are an integer multiple of the rotational frequency. Large deflection amplitudes can be observed when the blades are passed by a non-uniform but periodic flow field that prompts resonance as a result of the

matching of excitation frequency and natural frequency. Synchronous vibration stems from steady blade row interaction mechanisms or non-uniform inflow conditions. Possible sources of steady blade row interaction are wakes from upstream stator vane rows or potential fields from downstream stator vane rows [69]. Synchronous vibration can, in principle, be caused by any obstructing structural component in the path of the fluid flow, such as diaphragms or moisture separators [70]. The Campbell diagram is a common tool to assess synchronous vibration where the resonance frequencies of the blades are plotted against the rotational speed of the shaft. So-called engine-order lines that represent multiples of the rotational speed are drawn. This enables the operator to identify the critical speeds of the engine that lead to resonance [71, 72].

2.1.3 Asynchronous vibration

Asynchronous or non-engine-order vibration takes place at non-integer multiples of the rotational frequency of the shaft. This type of vibration is more troublesome to predict since there is no analogue of the Campbell diagram that shows the estimated loci of asynchronous resonances [73, 74]. It is, however, common practice to enter asynchronous resonances in the Campbell diagram once they are confirmed by simulation or experiments. The causes of asynchronous vibration are manifold, starting from random excitation to unsteady flow conditions [75]. Over decades of intensive research, it has been found that the most worrying causes are vortex shedding, aerodynamic instabilities (such as rotating stall and surge), and self-excited vibration (flutter), which are explained below [69, 76, 77]. The susceptibility of the blades to vibration from these unwanted phenomena depends largely, but not exclusively, on their weight and geometry as both determine their natural frequencies. Thin blades with large aspect ratios are more likely affected in the presence of high loading. This applies equally to compressor and turbine blades [78, 79].

2.1.3.1 Vortex shedding

Vortex shedding is the circular movement of fluid from a blade. It arises from ill-designed or overloaded profiles, struts, or cavities. The shedding of vortices happens at a certain frequency, which can cause resonance when the shedding frequency reaches a natural frequency of the blade. Off-design operating conditions encourage vortex shedding to appear [80–82].

2.1.3.2 Rotating stall and surge

A flow or aerodynamic instability develops when the turbomachine exceeds its stability limit, for instance, through pressure fluctuation, flow separation at the inlet, or other types of flow distortion. The instabilities, which are most dangerous to the engine and therefore frequently investigated, are rotating stall and surge [83–88]. The first is a steady and local phenomenon and observable when the angle of incidence between the blade and the fluid becomes too large. The fluid is then separated from the suction side of the blade leading to a non-uniform flow. Hence, turbulent flow appears in the blade passage. The region of stalled flow (stall cell) moves circumferentially from one blade to another in the same direction as the rotor typically at 40 to 70 % of the rotor speed [89, 90]. Rotating stall can be a precursor to surge, which is an axisymmetric oscillation of the flow. Surge causes the complete breakdown of steady flow through the compressor and occurs when stalling takes place on all blades at the same time. Depending on the degree of severity, a flow reversal may even be observed during surge. To recover from rotating stall and surge, the engine often requires a change of the operating conditions or a shutdown in the worst case. It is also important to consider that aerodynamic instabilities are able to seed self-excited vibrations if one of the aerodynamic modes locks on to an eigenmode of the blades [91–93].

2.1.3.3 Flutter

Flutter is 'a sustained [or self-excited] oscillation due to the interaction between aerodynamic forces, elastic response, and inertia forces', which can occur in various forms at different points in the operating map of the turbomachine and, thus, makes its study particularly difficult [94–100]. General agreement seems to exists with respect to the mechanics behind the onset of flutter. In contrast to forced-response vibration, flutter is not initiated by an unsteady aerodynamic load. In fact, it develops from stable limit-cycle forced-response vibration in one of the natural modes towards unstable vibration as the rotor approaches the operating conditions at which flutter can be observed [48]. Flutter is a result of the coupling of structural vibration and unsteady aerodynamics, which leads to the cancellation of the positive mechanical damping and negative aerodynamic damping with the typically growing amplitude being controlled by non-linear effects [101]. When the aerodynamic forces become unfavourably large, the initial natural mode of vibration may couple with other modes to appear under a new shape and frequency (mode coalescence). Unfortunately, unstable vibration can usually only be stopped by turning off the engine, component failure, or conversion into stable limit-cycle vibration through non-linear effects [102].

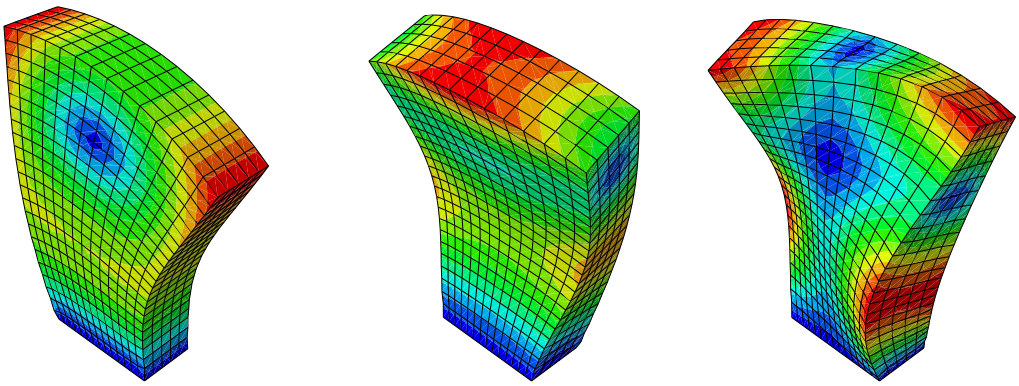
2.1.4 Response characteristics

If the overall excitation is synchronous with the rotational frequency, the blades exhibit a synchronous response in the linear regime, and similarly, asynchronous excitation causes an asynchronous response [103]. When excited, blades initially respond with a transient oscillation that normally quickly decays through damping. The structure afterwards vibrates at a frequency ideally equal to the excitation frequency (steady state) [104]. Depending on the inter-blade phase shift, this vibration can also be expressed as waves that move along the circumference of the rotor either in form of standing waves or (backward or forward) travelling waves, which can be viewed by an

observer in the inertial frame of reference. The latter wave type requires that the blades are, at least partly, out of phase with each other. Each natural vibration mode of the bladed disk has its own set of inter-blade phase angles. It is worth pointing out that neither standing waves nor travelling waves need to be synchronous with the rotor [105, 106].

The response pattern can be viewed as a superposition of the fundamental mode shapes of the bladed disk to which a resonance frequency is attributed each. At this point, it is important to acknowledge that there is a distinction in the theory of vibration between the terms 'resonance frequency' (root of the first derivative of the frequency response function (FRF)), 'damped natural frequency', and 'undamped natural frequency'. From an experimental point of view however, these terms are regularly considered interchangeable because of the often relatively small impact of damping on the frequency values. Thus, the frequencies are collectively called either 'resonance frequencies' or 'natural frequencies', cf. [104]. The experimental nomenclature is chosen for this work.

The resonance frequencies of the bladed disk, which are a function of the (undamped) natural frequencies and mechanical damping, can be identified using the FRF. The receptance as one particular form of the FRF associates excitation frequencies, which are supposed to be in the response spectrum, with the ratios of displacement amplitudes to given force amplitudes. A peak in the FRF normally indicates a resonance at which the modal properties of the system (mode shapes and natural frequencies) can be determined using measurements from either one response location and multiple excitation locations or vice versa. The locations should be chosen wisely so as to cover most of the characteristic points of the mode shapes (inflection, maximum, and nodal points). The modal parameters of the structure are controlled through the underlying design and mistuning. A particular mode shape becomes dominant in the response of the bladed disk when the direction of the excitation force coincides with the direction of the mode shape vector and the synchronous or asynchronous excitation frequency matches the corresponding resonance frequency, thereby significantly amplifying the response amplitude. Mode shapes are generally dimensionless quantities, which show the displacement



(a) 2nd edge-wise bending mode

(b) 2nd flap-wise bending mode

(c) 2nd torsional mode

Figure 2.1: Typical mode shapes of a cantilever

relative to a reference point on the structure [57]. Aeroengine manufacturers are especially concerned about blade bending and torsion. To understand this vibration behaviour better, blades are sometimes modelled as beams. Some common natural modes of a cantilever are displayed in Figures 2.1(a)–2.1(c). Real blade modes can look more complicated and may even couple with each other to occur at several frequencies, making measurements more difficult to analyse [107–110]. Apart from these vibration modes, large forces (such as centrifugal and aerodynamic forces) can give rise to blade elongation and untwist or push the blade axially or tangentially into a new static offset position during operation [111–115]. Radial blade motion is the subject of clearance measurements and investigations of the blade tip rubbing against the casing, e.g., in [116–131]. The clearance between the blade and the casing impacts on the performance of the engine: typically, the smaller the gap, the smaller the leakage flows and the higher the efficiency. Some clearance values can be as large as a few millimetres, cf. [128, 132]. The hardware for studying blade clearance and vibration is similar, enabling both to be measured simultaneously.

In the hypothetical absence of mistuning, all blades would, when regarded individually, have the same natural frequencies, making the bladed disk cyclic-symmetric. The vibration of such a bladed disk would take place in

well-defined single modes (all blades have the same amplitude whilst either being in phase or out of phase by 180° with one another) or double modes (two mode shapes with the same natural frequency but separated circumferentially by a 90° phase shift). Modes with non-zero inter-blade phase angles (i.e., double modes and the out-of-phase single mode) show a sinusoidal variation in the deflection amplitude along the perimeter of the bladed disk. It is noteworthy that these modes are distinguished by their number of nodal diameters, i.e., lines of zero displacement. An example of nodal diameters can be found in Figure 2.2 in which the 1st flap-wise bending mode of a bladed disk with two nodal diameters (1F-2) is depicted. The area of zero to

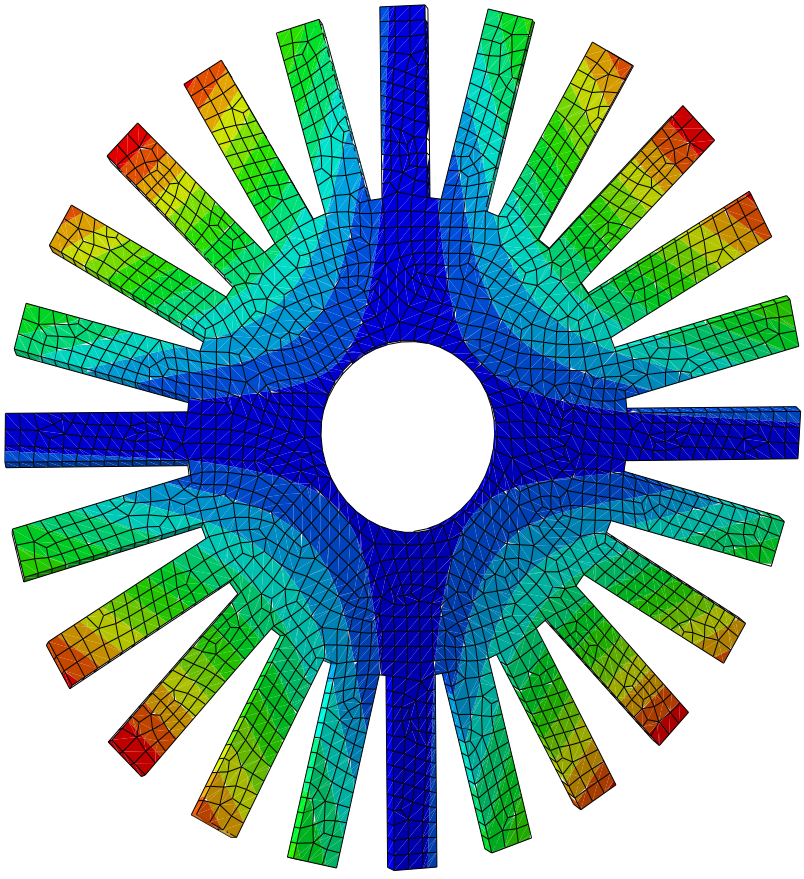


Figure 2.2: 1st flap-wise bending mode of a bladed disk with two nodal diameters

very small displacement is painted dark blue (■) and indicates the positions of the nodal diameters, which can theoretically lie anywhere on the bladed disk and are a sign of travelling wave vibration. The maximum number of nodal diameters of a particular mode depends on the number of blades N_B and is limited to $\frac{N_B}{2}$ if N_B is even or else to $\frac{N_B-1}{2}$. It is also possible to encounter quite isolated points of zero displacement (nodal points) and nodal circles [11, 133–136].

2.2 Classical Blade Tip-Timing

The different types of vibration, which can be observed in an engine, were discussed in the previous section. The working principle, sensor technology, and data analysis techniques of BTT to investigate these vibrations are introduced next. It is explained that the post-processing methods are specifically designed for the investigation of a particular form of vibration to appropriately deal with its concomitant peculiarities [137, 138].

2.2.1 Working principle

The only technique that effectively permits the monitoring of blade vibration during normal operation is BTT, a non-intrusive and non-contact measurement method [139]. The basic mechanics of BTT are depicted in Figure 2.3. Measurements are taken by means of sensors, which are mounted around the casing at a particular rotor stage of the turbomachine [140].

The blades rotate at frequency Ω and may vibrate at one or more unknown frequencies (ω_k), which results in a superposition of rotational and vibrational motion and causes the blades to arrive periodically slightly earlier or later at a sensor [141, 142]. Each time a vibrating blade passes a sensor once per revolution, its time of arrival (TOA) $t^{\mathrm{v}}_{\mathrm{BTT}}$ (also known simply as arrival or passing time) is recorded. Theoretically, any location on the blade tip

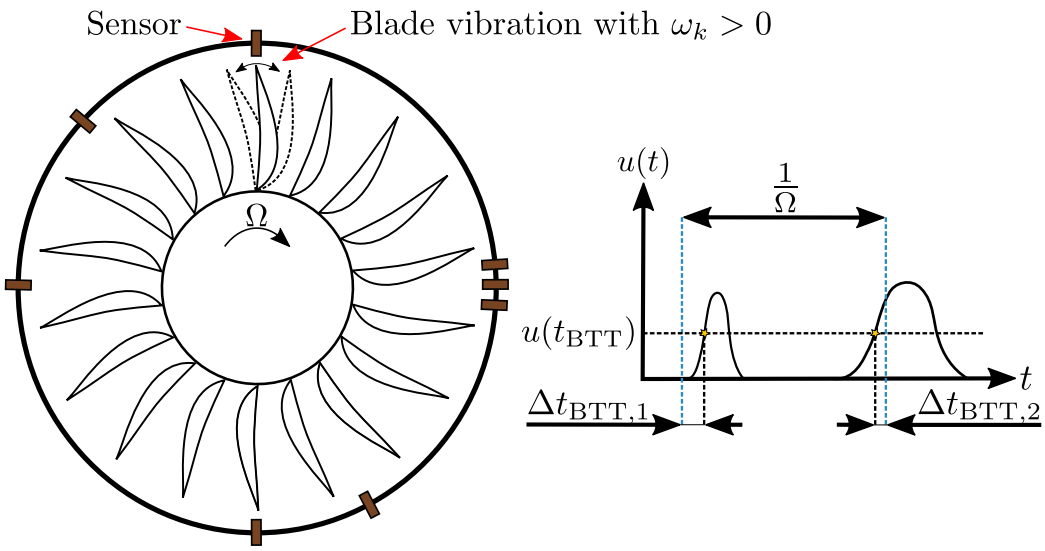


Figure 2.3: Working principle of BTT

can serve to determine the arrival of a blade; common are the leading edge, midchord, and trailing edge [143]. However, selecting the measurement location demands good judgement since it obviously influences which part of the vibration trajectory of the blade tip is sampled [144, 145]. Nodal points, whose existence and number depend on the vibration mode, should be avoided.

Unlike many other measurement techniques, BTT does not measure the kinematic properties of the blades directly [146]. Instead, vibration parameters (amplitudes, frequencies, and phases) are determined on the basis of finite time differences Δt_{BTT} between the TOA data $t^{\mathrm{v}}_{\mathrm{BTT}}$ of vibrating blades and $t^{\mathrm{r}}_{\mathrm{BTT}}$ of fictitiously rigid (non-vibrating) blades, whose TOA effectively depends only on the rotational speed under ideal conditions [147, 148]. The rotational speed is commonly either measured with a tachometer or derived from the shaft position trajectory gauged by an encoder. The model of rigid blades is physically not meaningful for real engine applications, not even when the blades do not resonate. This is due to the constant interaction of the blades with their environment (fluid and other structural components), which inevitably causes a continuous exchange of at least some vibration energy

during operation. The reference values $t^{\mathrm{r}}_{\mathrm{BTT}}$ can, in principle, be determined at any points on the shaft or disk, provided that the vibration there can be considered negligibly small. There are several ways to compute reference values [148–166]; mostly employed is the method with which readings from one or more once-per-revolution (OPR) sensors are processed [167]. Despite the abundance of different techniques, reference times can easily be corrupted, e.g., by general noise, sensor latency, limited signal quantisation, and shaft bending or torsion, cf. [168, 169].

The time differences are converted into single deflection or velocity points of the blade tip as a function of the rotational frequency and the blade tip radius measured from the centre of the rotor [170, 171]. The radius is often assumed to be constant over the course of measurements, and geometrical details, such as the curvature of the circumference of the bladed disk, are frequently neglected. The data points serve to find the vibration parameters using a suitable data analysis method of Table 2.6 or a derivative thereof, which needs to conform with the type of vibration present during the measurements [172]. When time differences appear to be the same, caution should be exercised because their meaning can be ambiguous. They can either hint at the presence of synchronous vibration or no vibration at all.

The recording of blade arrivals and reference points is routinely triggered when a parameterised signal strength level in the sensor output is reached [173]. Several methods have been proposed in the literature to set the trigger level as accurately as possible and to reduce uncertainty arising from sensor positioning and the measurement process [148, 168, 174]. Under normal conditions, triggering takes place somewhere on the rising or falling edge of the sensor waveform produced by the blade passage, or when the sensor output reaches an extremum or a root [175, 176]. The steadiness of the trigger point during the measurements is essential for the quality of the results.

2.2.2 Sensor technology

For more than 60 years [177], BTT has continuously been enhanced and upgraded for health and vibration monitoring of blades [178–182]. One crucial component of this method is the non-contact and non-intrusive sensor for capturing the arrival of blades with the highest accuracy possible. Different sensor types have been developed and suggested for this intention [183–187]. Amongst them are optical, capacitive, eddy current, magnetoresistive, and microwave sensors, which emerged as the most promising ones [188–193]. The choice of a particular sensor should be based on future operating conditions and possible maintenance questions, such as sensor accessibility [194]. Acquiring a signal may be a relatively straightforward task, yet interpreting this data and understanding the limitation imposed by the sensor are much more complicated [195, 196]. Calibration and, if appropriate, adjustments to the measurement conditions are therefore vital to the success of any measurement campaign [197].

Actual measurements are always preceded by the axial and tangential arrangement of sensors on the engine casing [198]. The latter should be carefully executed since slight changes in the sensor position or spacing may lead to the measurement of the response of a different part of the blade tip, possibly a nodal point, or, in the worst case, to the complete missing of a vibration mode [199, 200]. In [194], it was concluded for a particular example that a deviation of 0.3 mm from the ideal axial sensor position for a particular vibration mode may cause an error of 40 % in the response amplitude. Depending on the size of the blade tip part measured or the field of view of the sensor, this can become worse because of the averaging of the response over the measurement area. Similar problems can arise from a decrease in the number of sensors or faulty triggering of the TOA recording [175, 201]. When pondering the positions and number of sensors, potential risks, for example, damage to sensors from blade tip rub should be assessed [121].

The next sections provide an overview of the basic characteristics and working principles of the most established (i.e., optical, capacitive, and eddy current) sensors. Moreover, a short review is attached of magnetoresistive and microwave sensors, which have recently become more popular for producing useful BTT measurements [192, 202].

2.2.2.1 Optical sensors

Compared with all other BTT sensors, optical sensors are the most widely applied ones for detecting the presence of blades at a particular angular position [148, 203, 204]. Small impulses or waveforms are created in the output as the blades pass the sensor, and the corresponding TOA can be recorded at once. In contrast to field sensors, optical proximity sensors do not necessarily require that they are in the immediate vicinity of the blade tip section to be measured. This is because their working medium is light (waves of an electromagnetic field) that is able to propagate through the gap between the blade tips and the casing; thus, they offer greater flexibility in their positioning. Measured is the intensity of reflected light from the blades, which is modulated by the distance that it needs to travel back to the sensor [205].

In the simplest case, an optical sensor unit with a bifurcated cable is employed where a light source (laser) and receiver are connected to the split ends [108]. Laser light is transmitted through one optical fibre and directed onto the blade tip wherefrom it is reflected. The reflected light is collected at the common end of the fibre bundle and transmitted through the second fibre all the way back to the receiver where the light intensity is transformed into an electrical signal by a photodetector. Subsequently, the signal is sampled with a data acquisition system in order to make it processable with a computer for calculating the TOA data [206–208]. It has been found that the sensing precision and accuracy can be improved, for example, by installing more sophisticated cable bundles with a higher degree of furcation and larger number of fibres [195, 198, 209–214].

The major advantages and disadvantages of utilising optical sensors for BTT applications can be found in Table 2.1.

Advantages	Disadvantages
High accuracy and precision due to relatively low measurement uncertainty; high resolution ($\pm$ a few μm and below under laboratory conditions) [215–217]	Influence of light source intensity variations and optical losses on the quality of the measurements [209, 218]
Not affected by electromagnetic noise [219]	Require regular maintenance so as to clean the lenses from fouling caused, for instance, by dirt, dust, oil, and water [146, 203, 220]
Theoretically permit clearance measurements, though sensor alignment and calibration are challenging [221–223]	Require cooling and cleaning devices, which add weight to the engine [174, 224]
Withstand high temperatures and vibratory stress [217, 219, 225, 226]	Reflected light beam is affected by the condition of the blade tip surface (roughness and wear) [175,227]
High bandwidth but risk of high frequency noise [228]	Measurement location and angle of incidence of the laser beam may change through blade deformation and variations in the sensor position, influencing TOA data [229]
Prime response characteristics, thus having a fast signal rise and fall [216, 230]	

Table 2.1: Major advantages and disadvantages of optical sensors for BTT applications

2.2.2.2 Capacitive sensors

Capacitive sensors are field sensors that have to be positioned at the axial location of the blade tip segment to be investigated [181, 189]. An important component of the sensor is the central electrode from which an electric field originates [231]. To attenuate interference from other conductive engine parts near the sensor, the spreading of this electric field is limited to the gap between the sensor and blade by a guard (separate conductor to which the same voltage is applied) [232]. When a blade of conductive material approaches the electrode, a detectable voltage difference is applied between the two, which is accompanied by a change in capacitance [233]. The latter is in the realm of BTT predominantly a function of the distance between the sensor and blade. The electronics of the sensor are specifically designed to produce a certain voltage signal according to the corresponding change in capacitance. The capacitance between the electrode and the blade tip varies dynamically during the blade passage, which is conspicuous in the related sensor output. Beyond a certain distance, the blade is outside the sensing range, and the voltage signal ideally attains its former level until the next blade arrives [234–236].

The geometry and dimensions of the electrode and blade tip influence the shapes of sensor waveforms. The larger the angular size of either of these components is, the wider waveforms may become [175, 223]. Normally after the waveforms are generated, the TOA data is determined by means of a trigger algorithm [237].

The major advantages and disadvantages of utilising capacitive sensors for BTT applications can be found in Table 2.2.

Advantages	Disadvantages
In addition to TOA measurements, sensors produce valuable data for clearance and radial vibration analysis since the waveform amplitude is proportional to the gap between the sensor and the blade [238, 239]	Slower signal rise than optical sensors which can be a problem at very high rotational speeds with respect to the triggering of the TOA recording; it may be arduous to determine the TOA when small blades with a high deflection gradient are to be measured [175, 194]
Durable and inexpensive; simple design; largely unaffected by humidity; less sensitive to changes in the blade material; respond to all conductors [12, 203, 213, 240–242]	Require a high-voltage power supply; have a high output impedance; are susceptible to electromagnetic interference [181, 224]
Multiple sensors can be closely spaced [223]	Bladed disk must be grounded and have at least some electrical conductivity; highly resistive materials can be sensed under certain circumstances [223]
Resistant to very high temperatures and pressures [173, 243–245]	Measurements are impacted by changes in the dielectric properties of the fluid and by material variations and contaminants within the gap between the sensor and blade [181, 224]
Have a greater field of view than optical sensors [194]	
Latest capacitive sensors have a resolution similar to optical sensors [12, 175, 181, 194, 203, 241, 246]	

Table 2.2: Major advantages and disadvantages of capacitive sensors for BTT applications

2.2.2.3 Eddy current sensors

Eddy current sensors and capacitive sensors have some features in common. They are field sensors with similar working principles, which require proximity to the blades [190]. Instead of using an electric field for sensing the arrival of a blade, eddy current sensors are inductive and, therefore, apply a magnetic field that penetrates the blade tip [247].

There are several types of eddy current sensors of which the so-called active eddy current sensor is taken to explain the way they operate. A magnetic field is generated by the flow of alternating current through the coil at the end of the sensor [248, 249]. When a conductive blade tip moves through this magnetic field, an electric current (eddy current) is induced in it [250]. As a consequence, this eddy current produces its own magnetic field which opposes the primary magnetic field of the sensor [251]. The interaction between the two fields causes a change in the impedance of the sensor coil, which can be detected by the sensor electronics. The closer the sensor and blade tip are to each other, the stronger is this interaction and the larger is the change in the corresponding voltage signal in the sensor output [148, 252].

The major advantages and disadvantages of utilising eddy current sensors for BTT applications can be found in Table 2.3.

Advantages	Disadvantages
In addition to TOA measurements, sensors produce valuable data for clearance and radial vibration analysis since the waveform amplitude is proportional to the gap between the sensor and the blade [225, 253–255]	Blade tip must be conductive [227, 252, 256]

Advantages	Disadvantages
Not affected by the matter (fluid, contaminants) within the blade tip gap, thus adapted to hostile environments where oil, coolants, and other substances may appear [121, 122, 220, 257, 258]	Sensitive to the type of blade material used; each material requires different sensor calibration [257]
Durable, inexpensive, light, and small structure [224, 259]	Choosing appropriate coil dimensions is crucial to the measurement outcome [257]
Sensing 'through the casing' is feasible without drilling holes in the casing and direct view of the blades, provided that the casing consists of non-ferromagnetic material and that the casing thickness is sufficiently small [12, 248, 253, 260–263]	A certain minimum blade thickness is necessary to enable eddy currents to be induced in the blade tip [257]
Can be made almost RPM[1]-insensitive when the sensor is driven at a high frequency with respect to the blade speed [252]	
Resistant to very high temperatures and pressures; no cooling is required [121, 252, 255, 259]	
Comparable with capacitive sensors in terms of accuracy [12, 255]	
Variants are available to measure either displacement or velocity of the blade tip [249]	

Table 2.3: Major advantages and disadvantages of eddy current sensors for BTT applications

[1]RPM means 'revolutions per minute' and is also a non-SI unit of the rotational speed.

2.2.2.4 Magnetoresistive sensors

Magnetoresistive sensors are classed as magnetic proximity sensors, whose baseline version often consists of a magnetoresistive sensing element (e.g., permalloy film) beside a permanent magnet [264–267]. The sensing element experiences a change in its electrical resistance when the surrounding magnetic field (i.e., magnetic flux density or magnetic field strength) is altered as a result of the passage of a magnetic blade [216, 268, 269]. When the sensing element is connected to a Wheatstone bridge, it is possible to observe the variation in electrical resistance and to output the corresponding voltage signal [115, 270–272].

The major advantages and disadvantages of utilising magnetoresistive sensors for BTT applications can be found in Table 2.4.

Advantages	Disadvantages
High accuracy, sensitivity, and bandwidth; good noise reduction; quick response allows the detection of two-dimensional blade vibration at a speed of up to 700 $\frac{\mathrm{m}}{\mathrm{s}}$, which corresponds to a rotational frequency of roughly 6685 RPM when the blade tip radius is 1 m [114,115, 152, 256]	Blades must be made of magnetic material [266, 273]
Durable, inexpensive, and small structure; resistant to debris and erosion by water drops under high-humidity conditions [266, 274]	Require a stable magnetic field, which can be difficult to reach because of the persistent interaction between internal and external magnetic fields [275, 276]
Steady and dynamic components of the blade position are measurable [115, 277]	Measurement range depends on the limited maximum of magnetic field strength [275]

Advantages	Disadvantages
Possibility of simultaneous temperature measurements [275]	Application may become troublesome at high temperatures [256, 274]
Useful for clearance measurements [274, 278]	
Quality of measurement results is in line with that of conventional (optical, capacitive, eddy current) sensors [274]	
Output signal can be made independent of the blade velocity, which enables sensor calibration and adjustments under quasi-static engine conditions [115, 256]	

Table 2.4: Major advantages and disadvantages of magnetoresistive sensors for BTT applications

2.2.2.5 Microwave sensors

The principles of operation of microwave and optical sensors are quite comparable. The former emit a continuous beam of microwaves, which are electromagnetic radiation like (visible) light, in order to detect the presence of a blade [192,279–282]. A moving blade that is struck by this beam of microwaves reflects it but not without causing wave modulation. Sensor electronics capture the reflected beam and thereupon determine differences between the emitted and received signals, such as the phase shift that directly relates to the distance between the sensor and blade. A voltage signal equivalent to the wave modulation is subsequently output by the sensor [111, 283, 284].

The major advantages and disadvantages of utilising microwave sensors for BTT applications can be found in Table 2.5.

Advantages	Disadvantages
High accuracy and bandwidth with a spatial resolution superior to conventional (optical, capacitive, eddy current) sensors [173, 285–287]	More research has yet to be conducted on microwave sensors to fully establish their suitability for BTT applications [173, 283]
Useful for clearance measurements [173, 283, 288, 289]	To perform BTT and clearance measurements simultaneously, an additional reference channel, a higher frequency and/or dielectric filling may be needed [173]
Resistant to very high temperatures and pressures [213, 283, 289]	Operating temperature of the sensor can be very high [173]
Can be employed in harsh environments; unaffected by contaminants [173, 213, 283, 285, 288]	

Table 2.5: Major advantages and disadvantages of microwave sensors for BTT applications

2.2.2.6 Summary

Several types of sensors for determining the TOA of blades were presented. Every single one has its own characteristic behaviour and requires individual calibration and adjustments that have to be taken into account when the data is further processed. With TOA data only, it is not possible to make satisfactory statements on blade vibration. Methods for transforming this data into more meaningful parameters of vibration are described in the following section.

2.2.3 Data analysis

2.2.3.1 Methods

The second crucial element of BTT is the data analysis method [290]. It was explained in Section 2.2.1 that blade vibration can be investigated using sensors mounted around the casing. The TOA data, which is determined with the help of trigger algorithms applied to sensor waveforms, is converted into a vibration signal defined by amplitudes, frequencies, and phases [142, 291, 292]. The signal of blade tip displacement is usually calculated first by subtracting the reference TOA data of a fictitiously rigid blade from the TOA data of the corresponding vibrating blade. The time differences obtained are standardly multiplied by the product of the rotational frequency and initial blade tip radius ($\Omega R_{\mathrm{B}}^{0}$), which yields deflection points [168, 293]. The blade tip velocity and acceleration may later be determined by numerical differentiation [149]. The actual deflection signal can be estimated on the basis of these points using one or more data analysis methods of which the most established and some unconventional ones are briefly presented in Table 2.6 and assigned to the type of vibration (synchronous vibration (SV) or asynchronous vibration (ASV)) for whose analysis they have been designed. Methods that received favourable reviews in the literature are surrounded by a red rounded rectangle (▭).

Method and description	**SV**	**ASV**
All-blade spectrum method [141, 149, 172, 175, 294, 295] With this method, the bladed disk is assumed to vibrate in nodal diameter modes. Measurements are taken in blade arrival order at a certain location on the casing to create a single frequency spectrum for all blades.	☐	☑

Method and description	SV	ASV
Autoregressive methods [70, 154, 296–303] It is assumed that each resonance can be modelled on the basis of single-degree-of-freedom systems. In its basic form, the method processes data from four sensors that capture the TOA of a single blade during one revolution. The solution is derived using a Taylor expansion.	☑	☑
Bayesian linear regression method [70] This is an approach to determining the amplitude and phase using Bayesian linear regression whilst estimating the response frequency with optimisation tools.	☑	☐
Determinant method [296] Instead of using a Taylor expansion like autoregressive methods, this method works with the determinant of the solution matrix that contains the vibration parameters.	☑	☐
Fourier frequency spectrum analysis methods [23, 139, 143, 149, 172, 174, 181, 304–316] The discrete Fourier transform (DFT) converts a sequence – usually a discrete deflection signal – of the time domain into samples of the corresponding frequency domain. There are different algorithms for computing the DFT, amongst which the fast Fourier transform (FFT) is considered efficient. The frequency spectrum displays the distribution of amplitudes across the frequency components of the time-domain signal. Large amplitudes may indicate the presence of active vibration modes during the measurements. Some variants of the basic DFT have been proposed, such as the non-uniform discrete Fourier transform (NUDFT) and the non-harmonic Fourier analysis technique, to deal with unevenly spaced samples and more complex signals, e.g., signals under the influence of blade damage and mistuning.	☑	☑

Method and description	SV	ASV
Least-squares complex frequency-domain modal parameter estimator [317] This method is employed to identify modal parameters of mistuned bladed disks. The FRF computed from vibration measurements is modelled using a matrix-fraction description. The coefficients of the denominator polynomial are determined by minimising the difference between the experimental and the modelled FRF. Frequency and damping information is obtained from the roots of the denominator. It was found that this method is helpful in separating closely spaced modes.	☑	☑
Lomb-Scargle periodogram [149] This spectral estimator is based on least-squares fitting. The aim is to detect frequency components with low amplitudes in noisy data whilst overcoming the problem of non-uniformly spaced data.	☑	☑
Minimum variance spectral estimator [172, 318–321] The minimum variance spectral estimator is based on the minimisation of the variance of a time-domain signal of aliased, non-uniform, and irregular data. This method has also been tested on deflection data in combination with other methods, such as the multi-sampling analysis technique, amplitude and phase estimator, Capon algorithm, random filtering, and random sampling. Interesting results encouraged the development of further advanced spectral estimators, such as those proposed in [322, 323].	☑	☑
Multi-degree-of-freedom system identification technique [324] Firstly, the FRF of the bladed disk in the proximity to a resonance is determined using a wavelet transform of measured response data. Secondly, the modal parameters of the system are estimated using a mixed stochastic-deterministic subspace algorithm formulated in the frequency domain.	☑	☑

Method and description	SV	ASV
Multi-parameter sinusoidal fitting method, also known as circumferential fourier fit or least-squares method [70, 141, 149, 154, 172, 174, 199, 203, 306, 311, 325–334] This is the de-facto standard method for determining the vibration parameters. In the simplest case, this is done by fitting a system of single-degree-of-freedom oscillators to the measured TOA data of blades that are assumed to vibrate at a single dominant frequency, e.g., a resonance frequency. A sensor is installed at a predefined position on the casing for each vibration parameter to be computed. In order for the system of equations to be independent, the measurements have to be taken within one vibration period.	☑	☑
Multi-sampling analysis technique [142] The multi-sampling analysis technique is based on using different sets of regularly spaced sensors that simultaneously record the TOA at different sampling frequencies. When frequency spectra are combined, it is hoped that genuine response frequencies and aliases can be identified and separated more easily.	☑	☑
Overall response amplitude method [141, 174, 178, 335, 336] The peak-to-peak amplitude is computed from the measurements of the asynchronous response of a single blade tip over a finite period. This amplitude is assumed to be an approximation of the actual peak-to-peak response amplitude. The method is not intended to calculate the vibration frequency.	☐	☑

Method and description	SV	ASV
Quasi-cross spectrum estimator [172] A recently proposed method is the quasi-cross spectrum estimator. Firstly, the multi-sampling analysis technique is employed to compute differently sampled data sets. Subsequently, a spectrum for each data set is calculated using, e.g., the NUDFT or minimum variance spectral estimator. Finally, these spectra are compared pairwise by computing the power density cross-spectrum each.	☑	☑
Single-blade spectrum method [141, 149, 175, 292, 295, 333, 337] Individual blade-specific frequency spectra are calculated from respective TOA data of consecutive revolutions.	☐	☑
Single tip response parameter technique [141, 153, 199, 301, 326, 331, 338–346] The method is based on calculating a single blade tip response parameter, such as displacement. To determine this quantity, the bladed disk is excited by varying the rotational speed in such a way that the engine has to traverse the resonance of interest.	☑	☐
Subspace method [308, 317, 347–350] Vibration parameters are calculated by employing a state space model which is obtained by transforming the equation of motion into a state equation and an observation equation.	☑	☐
Two-parameter plot technique [141, 153, 297, 301, 331, 342, 351–353] The amplitude, resonance frequency, and engine order of a vibration mode is determined using measurements from two sensors. Displacement-versus-speed plots are created to show the change in the vibration amplitude whilst the engine traverses a resonance.	☑	☐

Table 2.6: Data analysis methods for BTT applications

2.2.3.2 Practical considerations

The most difficult aspect to analyse is the impact of under-sampling of TOA data on the vibration parameters to be computed [172]. The sampling of TOA data should not be confused with the sampling of the sensor signal as part of the digitisation by the data acquisition system. The frequency of the sampling of blade arrivals (i.e., one TOA point per blade, sensor, and revolution) is regularly lower than most, if not all, of the natural frequencies of the blades, which causes frequency aliasing. It is controlled by the rotational speed and the number of sensors installed [354]. Unfortunately, neither the rotational speed nor the number of sensors can arbitrarily be increased. The former depends on the operating limits of the engine, whereas the latter is usually constrained by the manufacturer to no more than 8 sensors per stage in order to guarantee casing integrity outside the laboratory in a high-temperature and high-pressure environment [37, 321, 355]. Furthermore, the continuity of the fluid flow in the tip region, which can be disturbed by the sensors and their mounting holes in the casing, must be ensured [141, 248, 266, 274, 356].

To get an impression of the severity of the under-sampling problem, suppose that the rotor of an axial compressor spins at 16,600 RPM and the largest present vibration frequency is 3.5 kHz. In this case, there would have to be at least 26 sensor equally distributed around the casing in order to prevent the spectrum from being distorted [291]. With the recommended maximum of 8 sensors, though, the theory of signal processing states that the maximum vibration frequency may not be larger than 1.107 kHz to avoid under-sampling [304]. According to Rolls-Royce, most bladed disk modes of interest, however, have a natural frequency of a few kilohertz and more [357]. Consequently, aliasing is almost inevitable and vibration frequencies above half of the sampling frequency appear as smaller frequencies in the spectrum [106]. Expert knowledge is required so as to process and interpret such data. Some techniques for reconstructing the under-sampled TOA signal have been proposed in the literature. Technically, they are based on estimation, interpolation, and a variation in the number and positions of sensors, yet there

is no published evidence of their practicability [172,308,348–350,358–377]. Another way of mitigating the issue with under-sampling is to compare frequency spectra or vibration parameters obtained from TOA data with those from contact-based strain gauge measurements or simulations. This cumbersome and potentially expensive procedure demonstrates the dependence of BTT on reference data, which may not always be available [70, 109, 133, 141, 378–382].

Researchers discovered in the early days of BTT a strong correlation between the sensor position, the type of excitation, and the meaningfulness of TOA data [320]. For instance, equal spacing of sensors around the circumference of the casing produces indistinguishable sets of TOA points when the blades undergo synchronous resonance, which is an obstacle to finding the actual vibration parameters [297, 301, 302, 358, 383]. One way of minimising this inconvenience is to avoid the uniform arrangement of sensors, but this cannot be done without causing another problem [142, 354]. Unfortunately, the standard DFT is not suited for computing the frequency spectrum based on samples that are unevenly spaced in time. More advanced methods would have to be applied, such as re-sampling techniques and the non-uniform discrete Fourier transform (NUDFT) [23, 174, 305]. Different problems exist when asynchronous vibration is present. There is no equivalent of the Campbell diagram that helps to pinpoint critical rotational speeds that bring about asynchronous resonance [321]. Separating the true (asynchronous) vibration frequencies from their aliases in a falsified spectrum is a rather strenuous task because the degree of aliasing is *a priori* difficult to estimate, especially in case of obscure excitation sources [362]. In practice, asynchronous vibration is investigated by making prior assumptions about the anticipated blade response, e.g., in [384]. In the same way as for synchronous vibration, the NUDFT and its variants should be used if the sensors are distributed irregularly [172]. For these reasons, BTT methods have traditionally been tailored to a particular type of vibration [297, 319]. Since asynchronous and synchronous excitation can inseparably appear together in real engines, there has been an endeavour in recent years to develop BTT methods that are capable of coping with both vibration forms without the need for initial assumptions [385]. Additionally,

these methods should be useful for quantifying the extent of (unintentional) mistuning of the bladed disk [107, 327, 348, 386–391].

2.2.4 Discussion

Aero-engine manufacturers are bound to assess blade vibration to avert potentially harmful damage. BTT is currently the only method that can be applied to the monitoring of real engines. It has the advantage of requiring no physical contact between the blade and the sensor, which drastically reduces disruptions to the fluid flow and spares the bladed disk assembly both extra mass loading and greater mistuning. The sensor and the appropriate data analysis method are the two major components, which affect the quality of the results and whose selection should therefore lie at the heart of any measurement planning. Each of these components has its own limitations that demand consideration.

Although BTT has continuously been enhanced, there has been no published evidence yet that the problems with under-sampling have finally been solved. Promising methods, such as the multi-sampling analysis technique or the minimum variance spectral estimator, for attenuating aliasing in the spectrum are hardly beneficial to real vibration monitoring because they require pre-selection and pre-processing of already existing vibration data, which is not necessarily available, and/or a variation in the sensor positions and sensor number.

The situation with regard to under-sampling cannot be resolved by increasing the resolution of the data acquisition system or by developing new sensors. This, admittedly, may improve the quality of TOA data, but eventually, the amount of data matters. Having slightly more accurate results does not contribute to mitigating the consequences of under-sampling as no additional TOA data is produced. Furthermore, vibration in real engines is more difficult to manage than in laboratories because excitation is harder to control, if at all, and may even be unknown irrespective of the shape of the response. The

vibration response can be complex in both scenarios where multiple frequency components and random noise are to be expected. To understand them, merely analysing and processing TOA data from a few sensors is proven to be insufficient to characterise blade vibration. It is, however, not desirable to return to traditional contact-based measurement methods or to abandon BTT completely as there are enough positive aspects of BTT, particularly its compatibility with various well-developed sensor technologies of which two are exploited within the scope of this work.

Additional information about vibration present in an engine is required so as to reliably state the engine condition during operation. A modification of traditional BTT is sought in order to overcome some of its inherent problems. In the following chapter, a new methodology for analysing blade vibration is propounded.

Chapter 3

Fundamentals of sensor waveform analysis for characterising blade vibration

A novel concept of investigating blade vibration in turbomachinery was developed on the basis of Blade Tip-Timing (BTT) and clearance sensor waveform analysis (BLASMA)[1], which was filed for patent protection by Rolls-Royce [392]. The principle of this approach and its distinctness from related art are presented in this chapter. Based on the methodology suggested below, the four subsequent chapters are concerned not only with modelling but also with the numerical evaluation of BLASMA. To simulate reliable data, a model of a bladed disk and sensor was created that can be used for different types of vibrations, e.g., multi-harmonic and multi-directional vibration. The simulations were, however, brought in tune with the later experiments as regards the capabilities of the test rig and the project requirements, which called attention to flap-wise vibration. Amongst the methods developed throughout the doctoral research phase, three methods were selected for vibration analysis, whose outcome is presented in this thesis:

- BLASMA-SCP uses signal attributes or, more precisely, the integral and slopes of a waveform
- BLASMA-IWE pivots on the inverse of the waveform equation
- BLASMA-OPT employs an optimisation routine.

[1]The term is also used to collectively refer to the set of methods applied.

The goal was to determine the parameters, i.e., amplitudes, frequencies, and phases of single-harmonic and multi-harmonic blade vibration. Each method was studied separately, and its capabilities and limitations were ascertained. The method best suited to accomplishing the task underwent a comprehensive examination containing asynchronous and synchronous single-harmonic and multi-harmonic vibration test cases. Only a single sensor was employed in all investigations in order to identify the minimum amount of useful vibration data, which can be obtained, and to provide a solution for situations where a strict curb on the number of sensors is imposed. Some parts of the following content either are currently being reviewed or have already been made public in [41, 42, 393, 394].

3.1 Related art

Blades in real engines can vibrate in a multi-harmonic fashion, which makes the interpretation of BTT data challenging without additional reference data. The situation becomes worse by the often unavoidable under-sampling of vibration trajectories with resonance frequencies of the blades being typically greater than the sampling frequency of the BTT data acquisition system. The analysis of such data is complicated and requires special skill, leading to a desire for new measurement and signal processing methods to surmount these obstacles [31–36, 38]. Sensor waveforms can serve as an additional information source for vibration analysis that enriches traditional TOA data. There have only been three research groups that studied BTT sensor waveforms.

3.1.1 Group from MIT

In [259, 395–397], a model of an eddy current sensor that is based on an exponential expression is put forward. First, waveforms were computed for the case when a non-vibrating blade passes the eddy current sensor.

At a certain operating point during an experiment where vibration was to be observed, the computed signal belonging to the non-vibrating blade was modified using a few measured blade parameters (tip clearance, TOA, velocity, acceleration). This modified analytic signal was then compared with actual measured waveforms, which were modulated by blade vibration, in order to detect vibration effects on waveforms. The presented model was actually not a sufficient fit to the measured data because the sensor model was not adequately adjusted to a vibrating blade in the derivation process. It should be mentioned that strain gauge data was required so as to make their method work and be able to interpret the waveforms. This, however, contradicts the objective of eliminating the need for contact-based intrusive vibration measurement techniques.

3.1.2 Group from Swansea University

In [249, 253, 398–400], purely numerical work is presented on eddy current sensor waveforms. A dynamic FE model of an eddy current sensor and a blisk was created. The behaviour of the eddy current sensor was defined by a differential equation of an electromagnetic field. The blisk was capable of rotating but not of vibrating. The intention behind this approach was to identify the influence of tip clearance, blade and disk geometries, and rotational frequency on the waveforms produced by the virtual sensor. The difference between using active and passive eddy current sensors with respect to changes in the appearance of waveforms is shown. It becomes apparent that the amplitude of a waveform is inversely proportional to tip clearance whereas proportional to the blade length and width, disk radius, and rotational frequency. Depending on the type of eddy current sensor used, the rotational frequency may also affect the timing of the occurrence of the peak amplitude. Another outcome of this study is that two-dimensional sensor models can approximate three-dimensional ones well, which is invaluable information for sensor modelling and ensures computational efficiency.

The authors present the results of an experimental validation of their FE models of active and passive eddy current sensors in [401–404]. The effects of clearance and rotational speed on eddy current sensor waveforms was again investigated. Conventional TOA data of rotating and vibrating blades was further used to compute inter-blade distances for health monitoring purposes. Although the vibration study was based on the traditional BTT measurement methodology, typical blade vibration parameters were not examined. This was followed by an assessment of the damage state of exculsively rotating blades by processing waveforms from an optical sensor and active and passive eddy current sensors, which can be found in [405]. Waveforms were classified with regard to the location of damage on the blades by means of the wavelet transform. Damage was simulated by adding different mass magnets onto the surface of the blades, which essentially introduced a mistuning pattern that had previously been investigated by the same group in a very similar approach in [406].

3.1.3 Group from Samara University

In [407–416], various hardware and software are evaluated for investigating vibration of rotating systems. For the purpose of determining blade vibration parameters, two methods that involve the processing of sensor waveforms are proposed. The first is based on approximating sensor signals [412,416], whereas the second demands solving a system of equations [415]. The latter method refers to n discrete waveform points in order to solve n equations. The problem of this approach is that the entire shape of the waveform and the effect of noise and outliers on the accuracy of the method are neglected. It has to be borne in mind that the processing of the entire waveform has a smoothing and averaging effect on the vibration data to be extracted. Contrarily, processing only a few discrete points as suggested by the research group is prone to statistical variation for which no compensation is practically achievable. This becomes particularly critical when the discretisation step size of the analog-to-digital converter is larger than those small important changes in the sensor signal that

are attributed to blade vibration. Furthermore, the presented work does not include treatment of low-frequency noise and measurement uncertainty. One of the main contributions to measurement uncertainty results from the general inability to determine the sensor position immaculately. Even tiny changes in the sensor position can entail the observation of a different part of the blade vibration trajectory considering that the blade is still vibrating when it is beneath a sensor. The higher the blade vibration frequency, the severer the issue becomes. Unfortunately, measurement uncertainty is further increased by omitting the effects of deviations of initial and static blade positions from nominal values, where the latter can be caused by an axial shift, lean, or untwist of the blades. The disregard for these effects limits the application of the presented models to analysing asynchronous and synchronous blade vibration. Because of the increased measurement uncertainty, distinguishing between different sets of vibration data, which are computed using waveforms of a particular sensor from different revolutions, becomes difficult. Blade position, frequency, and sensor position must therefore be related.

Despite presenting the concepts of the two methods, the group did not attach any useful results, which would help to identify the practicability of the methods with regard to the characterisation of blade vibration. It is also unclear how reference sensor waveforms of fictitiously rigid blades can be calculated. Such waveforms would enable both: comparisons with real sensor waveforms to identify the degree of waveform modulation by blade vibration and the determination of vibration-independent sensor waveform parameters necessary to model and calibrate any sensor. Ultimately, the group focussed merely on single-harmonic flap-wise blade vibration without providing a resolution to crucial multi-harmonic blade vibration problems. To the best knowledge of the author of the present work, there have been no further articles on this matter to this day. Notwithstanding its findings, it is considered appropriate to propose a more sophisticated method for investigating blade vibration on the basis of sensor waveforms.

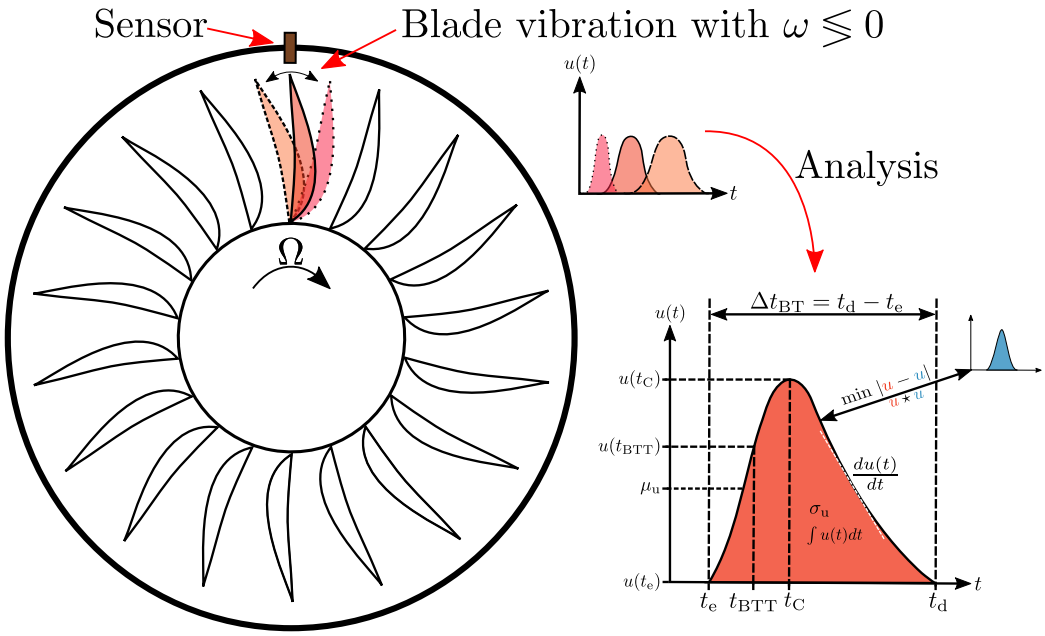
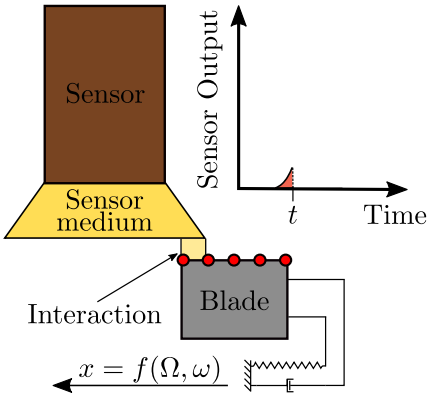


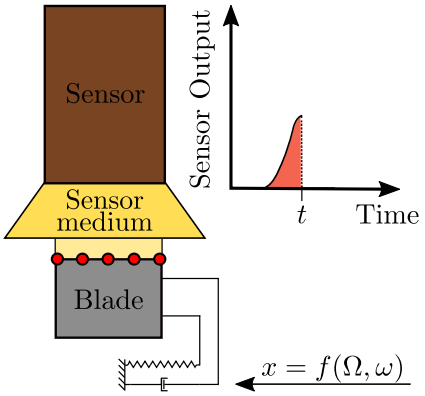
Figure 3.1: Principle of BLASMA

3.2 Methodology

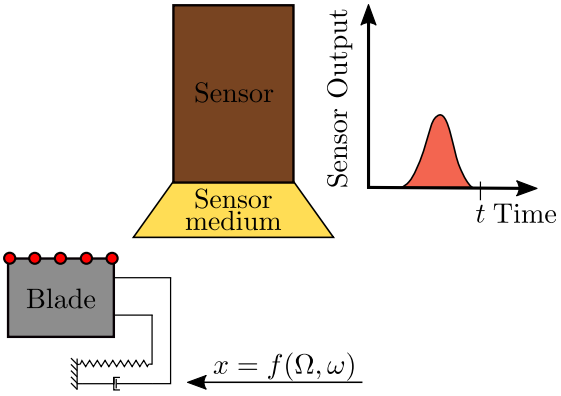
BLASMA is a methodology for extracting blade vibration parameters from sensor waveforms. The principle of BLASMA is depicted in Figure 3.1 where possible waveforms are plotted on top of each other to illustrate how different waveforms can develop as a function of blade vibration. At first, waveforms are generated when rotating and vibrating blades pass beneath a sensor that is mounted on the casing. The dynamic pattern of vibratory blade motion leads to a type of waveform modulation that is different from the imaginary and constant waveform modulation due to purely rotating rigid blades. With traditional BTT, the TOA of a blade would be recorded, normally using a point on the waveform of either the leading or falling signal edge. Afterwards, this waveform would usually be discarded to free storage drives [417]. It should be remembered that only the time information of a single point per waveform is processed into vibration data, contributing to the already well-discussed under-sampling problem. In stark contrast to BTT is BLASMA.



(a) Blade is approaching the sensor



(b) Blade is beneath the sensor



(c) Blade is leaving the sensor

Figure 3.2: Waveform from a blade passage

A waveform associated with a single blade passage along the sensor is saved and can immediately or later serve to analyse vibration with the help of the methods presented in Chapters 5–7. An obvious advantage of BLASMA is the possibility of applying BTT and BLASMA alongside each other for benchmarking without the need to rely on different hardware.

In Figures 3.2(a)–3.2(c), the process of waveform creation is divided into three steps with respect to the position of the blade relative to the sensor:

1. the blade is approaching the sensor
2. blade is beneath the sensor
3. the blade is leaving the sensor.

Parameter	Description
R_{B}^{0}	Initial radial distance between the blade tip and the centre of the rotor
b, w_{B}	Metric and angular width of a blade tip influencing the size of the portion of the blade tip seen by the sensor
M	Mass matrix describing the mass distribution across the bladed disk
C	Damping matrix highlighting areas on the bladed disk of significant damping
K	Stiffness matrix characterising the compliance of the bladed disk subjected to an external force
$\boldsymbol{\varphi}_{\mathrm{B}}^{0}$	Vector containing the angular starting position of each blade (t=0 s)
$u(t)$	Sensor function
w_{S}	Angular instantaneous and apparent width of the sensor medium
$\boldsymbol{\varphi}_{\mathrm{S}}^{0}$	Vector containing the initial angular position of each sensor
f_{S}	Sampling frequency of the data acquisition system
t_{M}	Measurement time determining the amount of sensor data
Ω	Rotational frequency of the shaft
$\boldsymbol{f}(t)$	Force vector specifying excitation frequency and amplitude

Table 3.1: Some important variables of the model

The shape and timing of a waveform depends on several variables, which describe aspects of the bladed rotor (■), the sensor (■) and the operating conditions (■); some important variables are listed in Table 3.1 with a short description. Further details of the modelling are provided in Chapter 4.

When blades are away from the sensor, the sensor output is at a certain basic level that normally depends in real engines to a great extent on the calibration settings, the operating conditions, and general noise. At a specific time t, a blade approaches a sensor and is about to begin to interact with the sensor medium (see Figure 3.2(a)). The sensor medium may be a field or a beam of a physical medium. Interaction in this context means that the blade changes the properties of the sensor medium in a certain way whilst crossing it. The stronger the interaction between the blade and the sensor is,

the more significant is the change in the sensor output, usually in form of an increase in the signal amplitude.

The interaction is strongest when a blade is completely beneath the sensor and completely surrounded by or in contact with the sensor medium (see Figure 3.2(b)). In other words, if the blade with a certain width is thought of as a body of connected discrete mass points, all of these mass points or nodes of a blade (●) are in contact with the sensor medium. This conception also visualises the sampling process for creating a waveform as the result of changes in the properties of the sensor medium that are detected by the sensor. The frequency of detecting these changes has a natural limit that is a feature of the data acquisition system, thereby separating data points in the temporal dimension. This is equivalent to scanning the blade non-continuously. Blade vibration causes an additional distortion of the sensor medium that can sometimes directly be recognised in the sensor output. Often however, this modulation is of such small magnitude that makes further data processing inevitable. In spite of this, waveforms develop their unique shapes which contain vital information on the vibration of a blade.

As soon as a blade leaves the sensor medium, the waveform is ready to be processed and vibration data can be extracted (see Figure 3.2(c)). The time at which waveforms appear is also crucial to vibration analysis because it helps to define the sign of the vibration deflection. A deflection against the direction of rotation causes the blade to arrive slightly later at the sensor in comparison with a fictitiously rigid blade. The opposite applies to a reverse deflection.

Chapter 4

Modelling of a bladed disk and sensor

A novel approach based on the processing of complete waveforms is suggested, where vibration parameters are found through BLASMA. Accessibility to the modulation of a waveform provides means of computing the amplitudes, frequencies, and phases of each harmonic constituent of a blade vibration signal. The method requires the modelling of the blade dynamics and sensor waveform equation to be compatible with the parameters of the operating condition, the sensors used, and the vibration spectrum of interest. BLASMA can, in principle, work with any type of sensor, provided that the sensor waveform equation is known. A key parameter of the sensor and electronics of the data acquisition hardware, which determines the shapes of waveforms (output), is the rise time or response time. It describes how fast the signal output changes as a result of new events detected by the sensor (input). Larger rise times lead to more bell-curve-like waveforms, which are typical of field sensors. In contrast, optical sensors operate with a very small rise time that leads to impulse-like waveforms whose exact modelling is more demanding. The shape of a waveform is also strongly affected by the measurement location, the sensor position, and the time during which the blade presence is sensed. One straightforward way of modelling the waveform equation is to measure waveforms experimentally under the operating conditions of interest. The waveforms are afterwards replicated with a computer using appropriate fitting techniques. It is important that waveforms are produced at a rotational speed, which is close to the intended speed range, in order to obtain representative waveform parameters. This is because waveforms depend heavily on the

operating conditions and changes in the blade geometry caused, for instance, by the centrifugal force and damage. For the purpose of recognising the effect of vibration on waveforms, one may record waveforms near a critical speed at which resonance occurs and compare them with waveforms recorded during resonance. Other more advanced sensor modelling approaches are based on physical principles or, if available, the sensor waveform equation designed by the manufacturer of the sensor.

4.1 Model assumptions

The model of the bladed disk and sensor rests on the following exemplary assumptions:

- the bladed disk is modelled as a linear lumped parameter system
- the blade stagger angle α is 0°, and therefore
  - flap-wise deflection only contributes to blade displacement in or against the direction of rotation
  - no contribution of edge-wise deflection in the direction of rotation
- torsional deflection is reasonably small so that it lays in the rotational plane together with the flap-wise deflection
- measurements are taken only at the leading or falling edge of the blade or both so that it is assumed that flap-wise and torsional vibration are superposed
- flap-wise, radial, and torsional vibration can be detected with a single sensor, whereas a second sensor is needed to detect axial and edge-wise vibration
- different types of vibrations can be differentiated using the frequency spectrum and modal analysis data of the bladed disk model

- a two-dimensional sensor is assumed to produce a bell-curve-like waveform, which is intrinsic to common field sensors
- the sensors are axially positioned at the leading and trailing edges and at arbitrarily selectable circumferential angles, which is in line with Figure 4.1.

The choice of the mathematical function of a sensor medium is to be made by the vibration specialist, who should base his or her decision on the type of study to be conducted. This is because waveform studies are affected by the individual working principle of the specific sensor type employed. The model is technically applicable to all sensor types, which makes BLASMA independent of a particular sensing principle. For a realistic sensor model however, the resemblance to experimentally measured waveforms should be ensured. Various examples thereof can be found in [111, 115, 173, 176, 194, 195, 213, 216, 252, 418]. The above assumptions lead to a specific bladed disk and sensor model. Different operating conditions, hardware, and software compel an adjustment of the model that best suits the present situation.

4.2 Bladed disk model

Multi-directional blade vibration is present when the blade is excited in different directions, which could be the translational axial (a_B), angular edge-wise ($\varphi_\mathrm{B}^\mathrm{E}$), angular flap-wise ($\varphi_\mathrm{B}^\mathrm{F}$), translational radial (r_B), and/or angular torsional direction ($\varphi_\mathrm{B}^\mathrm{T}$) (see Figure 4.1). The coordinate system helps to resolve external forces into their components and to determine the correct signs thereof, where a is the axial dimension, ϕ is the angular dimension in or against the direction of rotation, r is the radial dimension, and T is the torsional dimension. The arrows of the different vibration terms point in the direction of a positive deflection. Similarly to traditional BTT, BLASMA is used to determine vibration at the tip of the blade at an axial position which usually coincides with the axial position of the sensor on the casing. The

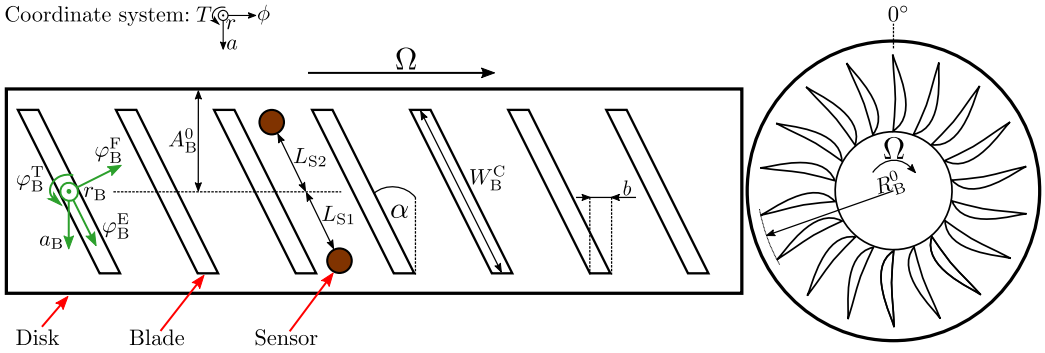


Figure 4.1: Top view of an unrolled simplified rotor stage on the left, front view of this rotor stage on the right

distribution of vibrational energy along the whole blades is afterwards inferred from the vibration at the blade tip. The justification for this approach is based on mainly two conditions:

1. the vibration frequencies can be assumed to be the same for every part of the blade when localisation effects can be disregarded
2. the deflection at the blade tip can be considered the largest because it is the most flexible and furthest point from the disk-blade clamp and any non-tip-located blade-to-blade couplings, such as shrouds.

Tip deflection data is therefore most crucial for blade health and vibration monitoring. In the case of tip-located blade-to-blade couplings, the sensor placement and the measurement location on the blade surface need to be revised (cf. [419] for traditional BTT). For simplification, the term 'blade vibration' implies 'blade tip vibration' in the rest of the document, unless otherwise stated.

4.2.1 Dynamics of a bladed disk

Generally, periodic steady-state blade vibration in any given direction $x_{\mathrm{B}}(t)$ can be described by a sum of harmonic functions, such as:

$$x_{\mathrm{B}}(t) = \Delta x_{\mathrm{offset}} + \sum_{k=1}^{N} X_k \sin(\omega_k t + \theta_k) \tag{4.1}$$

where $\Delta x_{\mathrm{offset}}$ is a static blade offset position, N is the number of harmonics in the vibration signal, X_k is the amplitude, ω_k the frequency, and θ_k the phase of the k-th harmonic. Transient and aperiodic blade vibrations require a time-dependent spectrum analysis so as to detect those vibration parameters that are relevant to a particular time window. It is worth mentioning that the static blade offset position $\Delta x_{\mathrm{offset}}$ can be used to determine the steady-state blade deflection from axial shifts, leans, or untwists. It is important to be able to determine the position of the blade exactly during operation in order to account for new fluid flow conditions. Multi-harmonic is a response when more than one vibration frequency occurs ($N > 1$), where a response is called synchronous or integral when the corresponding vibration frequency is an integer multiple of the rotational frequency. Given the necessary limitation placed on the number of sensors that can realistically be used, BTT alone may not be enough to assess multi-harmonic responses unambiguously because of the well-known under-sampling issue.

There are in practice two options available to model a bladed disk, namely an FE model or a lumped parameter model. FE models are detailed, exhaustive, and costly in terms of computation resources and development effort. They are based on analysing the vibration of the whole structure with a real geometry that has to be known in advance [420]. A model of the relationship between FE data and traditional BTT data is presented in [421–425]. On the other hand, lumped parameter models are less detailed, yet they can be used to compute results quickly, they are independent of the actual geometry of the bladed disk, and they can be created within a short time [426]. Lumped parameter models have several times been used in connection with traditional

BTT, such as in [297]. Considering the features of both model types and the project objective of seeking a solution to the under-sampling of traditional BTT data, it was decided in favour of the lumped parameter model in order to be unconstrained by the geometry of the bladed disk and to focus on developing BLASMA.

In the absence of any phenomena that alter the natural frequencies of a bladed disk, linear vibration thereof is widely described by the time-dependent equation of motion according to:

$$M\ddot{\boldsymbol{x}}(t) + C\dot{\boldsymbol{x}}(t) + K\boldsymbol{x}(t) = \boldsymbol{f}(t) \tag{4.2}$$

where M is the mass matrix, C is the damping matrix, K is the stiffness matrix, $\boldsymbol{f}(t)$ is the external excitation force vector, $\boldsymbol{x}(t)$ is the displacement vector, $\dot{\boldsymbol{x}}(t)$ is the vibration velocity vector, $\ddot{\boldsymbol{x}}(t)$ is the vibration acceleration vector [49]. The last three are the solution and at least one of them needs to be known to compute the corresponding frequency spectrum and to form an opinion about dominant response frequencies. An example of a lumped parameter model is pictured in Figure 4.2 where the blades are modelled as a three-degree-of-freedom system. Each degree of freedom of a blade contributes one resonance to the system resonances. The number of degrees of freedom of the total system is determined by the number of point masses and orthogonal directions in space in which they are allowed to move. The modular structure of the model permits adding further degrees of freedom to make it more complex. For investigating the vibration responses of blade tips as it is done with BTT, it would theoretically be sufficient to model only a single-degree-of-freedom system. Yet, it was decided to model an entire bladed disk to allow the study of coupling between its elements.

A blade is mounted on a disk sector that is elastically connected to adjacent disk sectors by springs and dampers. There is only one rigid body mode of motion which is the rotation about the longitudinal axis, i.e., the rotation axis of the shaft. The disk possesses furthermore an interface to a rotating member to enable the rotation of the bladed disk about its centre of mass axis.

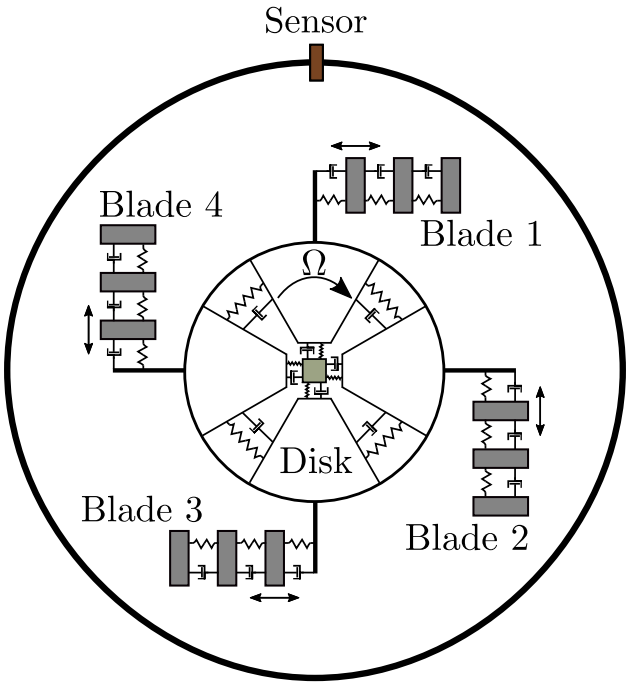


Figure 4.2: Bladed disk model

The magnitude of the coupling between each part of the bladed disk can be adjusted by setting the stiffness and damping terms appropriately. The higher the stiffness of a spring is, the more rigid the attached bodies become, and the larger the damping, the faster vibration energy is dissipated. Simply increasing damping until the vibration amplitude becomes negligibly small may work for lumped parameter models in simulations, but this would be inapplicable to real turbomachines with a wide range of operating speeds and high modal density. Finding the correct damping model, such as under-platform dampers and shrouds, for the most critical speeds is therefore challenging and a subject of further research [427]. A multi-harmonic response of the blades can be observed when applying a cyclic load with multiple frequencies. At steady state, a linear system exactly exhibits these frequencies in the response spectrum.

There are two solutions of Equation (4.2), namely the homogeneous and inhomogeneous solution. Both can be obtained using numerical solvers

provided by several programming languages. The homogeneous solution contains resonance frequencies and mode shapes of the system. Engine manufacturers specify nominal modal properties in the design process to prevent the engine from being excited at resonance under standard steady-state operating conditions. Inevitable mistuning nevertheless causes real modal properties to not match those defined. In order to avoid damage and satisfy safety regulations, manufacturers are interested in determining the real modal properties and the extent of mistuning. Helpful techniques for determining modal properties experimentally when the engine is turned off are described in [57]. When the engine is running, operational modal analysis is conducted by performing rotational speed sweeps to force the engine to briefly pass through a resonance whilst the response is measured [199, 326, 428, 429]. The inhomogenous solution of Equation (4.2) is the response of the system to external excitation. Any blade vibration measurement and data processing technique that is applied to a running engine is used with the intention of determining the trajectory of the blades for certain operating conditions. After being excited, the bladed disk may at some point change the initial transient response to a quasi-steady-state response depending on damping and the type of the force applied. In this scenerio, the system vibrates at the frequencies of excitation [57].

4.2.2 Blade trajectory

It is reasonable to assume that the total angular blade position $\varphi_{\mathrm{B}}(t)$ along the ϕ-axis is a sum of rotation and vibration terms and can be written as:

$$\varphi_{\mathrm{B}}(t) = \varphi_{\mathrm{B}}^{0} + \varphi_{\mathrm{B}}^{\mathrm{r}}(t) + \varphi_{\mathrm{B}}^{\mathrm{v}}(t) = \varphi_{\mathrm{B}}^{0} + 2\pi \int_{t_0}^{t} \Omega(\tilde{t}) d\tilde{t} + \varphi_{\mathrm{B}}^{\mathrm{v}}(t) \tag{4.3}$$

where φ_{B}^{0} is the angular starting position of a blade, $\varphi_{\mathrm{B}}^{\mathrm{r}}(t)$ is the rigid angular position of a blade, t_0 is the measurement starting time, $\Omega(t)$ is the rotational frequency in hertz, $\varphi_{\mathrm{B}}^{\mathrm{v}}(t)$ is the function of blade vibration, which is in or against the direction of rotation.

Supposing that there is no torsion, the blade vibration function $\varphi_{\mathrm{B}}^{\mathrm{v}}(t)$ in Equation (4.3) can be approximated to:

$$\varphi_{\mathrm{B}}^{\mathrm{v}}(t) = \varphi_{\mathrm{B}}^{\mathrm{F}}(t) = \frac{x_{\mathrm{B}}^{\mathrm{F}}(t)}{R_{\mathrm{B}}^{0}} \tag{4.4}$$

where $x_{\mathrm{B}}^{\mathrm{F}}(t)$ corresponds to $x_{\mathrm{B}}(t)$ from Equation (4.1) and R_{B}^{0} is the initial blade tip radius measured from the shaft centre. As the circumference at the height of the blade tip is relatively large compared with the tip deflection (i.e., $\frac{X_k}{R_{\mathrm{B}}^{0}}$ is small), the curvature of the circular orbit can be neglected in Equation (4.4) and henceforth. In the general case of multi-directional vibration, the blade vibration function in Equation (4.3) can be estimated using:

$$\varphi_{\mathrm{B}}^{\mathrm{v}}(t) = \sin(\alpha)\varphi_{\mathrm{B}}^{\mathrm{E}}(t) + \cos(\alpha)\varphi_{\mathrm{B}}^{\mathrm{F}}(t) + \frac{L_{\mathrm{S,P}}^{0}}{R_{\mathrm{B}}^{0}}(\sin(\alpha + \varphi_{\mathrm{B}}^{\mathrm{T}}(t)) - \sin(\alpha)) \tag{4.5}$$

and a Fourier series for each vibration term. The constant $L_{\mathrm{S,P}}^{0}$ is the distance between the longitudinal axis of the blade and the measurement location P at the blade tip along the chord line at the beginning of the measurement when there is no torsion (compare with L_{S1} and L_{S2} in Figure 4.1). The total blade deflection trajectory $\mathbf{\Gamma}_{\mathrm{B}}(t)$ for determining the instantaneous measurement location on the blade tip can be expressed in cylindrical coordinates $(r, \phi, a)^{\mathrm{T}}$ as:

$$\mathbf{\Gamma}_{\mathrm{B}}(t) = \begin{pmatrix} R_{\mathrm{B}}^{0} + r_{\mathrm{B}}(t) \\ \varphi_{\mathrm{B}}(t) \\ A_{\mathrm{B,P}}^{0} + a_{\mathrm{B}}(t) + a_{\mathrm{B}}^{\mathrm{E,F,T}} \end{pmatrix} \tag{4.6}$$

$$\begin{aligned} \text{with } a_{\mathrm{B}}^{\mathrm{E,F,T}} = {} & R_{\mathrm{B}}^{0}(\cos(\alpha)\varphi_{\mathrm{B}}^{\mathrm{E}}(t) - \sin(\alpha)\varphi_{\mathrm{B}}^{\mathrm{F}}(t)) \\ & + L_{\mathrm{S,P}}^{0}(\cos(\alpha + \varphi_{\mathrm{B}}^{\mathrm{T}}(t)) - \cos(\alpha)) \end{aligned} \tag{4.7}$$

where $A_{\mathrm{B,P}}^{0}$ is the initial axial position of the measurement location at the blade tip. When applying the assumptions of Section 4.1, Equation (4.6)

changes to:

$$\mathbf{\Gamma}_{\mathrm{B}}(t) = \begin{pmatrix} R_{\mathrm{B}}^{0} + r_{\mathrm{B}}(t) \\ \varphi_{\mathrm{B}}^{0} + 2\pi \int_{t_0}^{t} \Omega(\tilde{t}) d\tilde{t} + \varphi_{\mathrm{B}}^{\mathrm{F}}(t) + \varphi_{\mathrm{B}}^{\mathrm{T}}(t) \\ A_{\mathrm{B,P}}^{0} + a_{\mathrm{B}}(t) + R_{\mathrm{B}}^{0} \varphi_{\mathrm{B}}^{\mathrm{E}}(t) \end{pmatrix} \tag{4.8}$$

by taking the small-angle approximation into account and inserting Equations (4.3) and (4.5).

4.2.3 Blade width

The blades are treated as concentrated vibrating masses with a certain tip width w_{B} along the ϕ-axis in order to simulate the passages of blades along a sensor. The justification for this approach is substantiated by two real-world facts:

1. the tip of a blade is in many instances thin compared with the outer circumference of the bladed disk
2. sensors are mounted at fixed axial positions on the casing and can only receive the response of a small portion of the blade tip, usually at the leading edge, midchord, or trailing edge.

Moreover, giving the blades a certain adjustable width permits analysing the influence of blade tip dimensions on waveforms. Analogously to FE simulations, the blade can be considered meshed, thereby dividing the blade into smaller elements that are detected by the sensor. There is no requirement on the type of meshing applied. At each interface between neighbouring elements, there is a node (●) (see Figure 4.3). All nodes share the same dynamic characteristic, i.e., they vibrate at the same frequency without having a relative motion to each other. The sensor detects when a node is within the sensor medium, and thus, every node contributes to the final

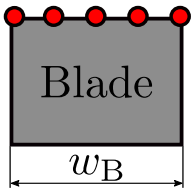


Figure 4.3: Meshing of a blade

shape of the waveform. The nodes are those points on the blade tip that are eventually sampled to generate the output signal of the sensor.

The blade width w_{B} is measured in rad and can be approximated using:

$$w_{\mathrm{B}} = \frac{b}{R_{\mathrm{B}}^{0}} \tag{4.9}$$

where b is the metric width of the blade tip.

4.3 Sensor model

The key component of the simulator is the sensor, and hence, it was necessary that some of the features of a real sensor were imparted to the modelled version. The former detects the presence of rotating and vibrating blades in various ways depending on their sensing mechanism. This, for example, may be via a continuous and coherent beam of light or an electric field. The disturbance of such sensor media is primarily caused by passing blades and linked to alterations in the sensor output. For this work, the sensor medium is a sensor field in accordance with the assumptions of Section 4.1. Real waveforms that appear in the sensor output are predominantly a product of (cf. [265, 430, 431]):

- the data acquisition hardware and software (especially coupling, digital resolution (bit-depth), **noise**, range, **sampling frequency**)

- the geometric and physical features of the bladed disk, e.g., **angular blade spacing**, **blade width**, damage state, **stagger angles of the rotor blades**, state of magnetisation
- the operating conditions, e.g., **rotational frequency**, stagger angles of the stator vanes (cf. [432]), **tip clearance**, **vibration**
- the sensor medium and sensor type, including accuracy, **extent of the sensor medium** (field of view), precision, resolution (smallest detectable change in the measured quantity), sensitivity, and **waveform function**
- the sensor position on the casing (**angular and axial dimensions**).

The independent variables that are written in **bold letters** are part of the model and have to be defined prior to the simulation.

4.3.1 Waveform equation

The type of a waveform depends on the sensor electronics. The faster a sensor is capable of responding to a change in the input, the faster the corresponding signal alters. Unlike the step impulse-like waveforms of optical sensors, bell-curve-like waveforms, which are typical of capacitive and eddy-current sensors, can comfortably be modelled with exponential functions. Using existing mathematical models that can be well fitted to sensor waveforms reduces the mismatch between the real and modelled sensor waveforms and thus minimises the error observed in the analysis of blade vibration. When one sticks to the initial assumptions of Section 4.1, the universal sensor waveform equation, which describes the sensor output over time t, is:

$$u(t) = U \frac{c_{\mathrm{B}}^{0}}{c_{\mathrm{B}}(t)} \exp(-\lambda(\varphi_{\mathrm{B}}(t) - \varphi_{\mathrm{S}}[n_{\mathrm{R}}(t)])^2) + \Delta(t) \tag{4.10}$$

where U is the nominal amplitude of a waveform in $u(t)$ that can be dimensionless, λ is the speed calibration parameter, $\varphi_{\mathrm{S}}[n_{\mathrm{R}}(t)]$ is the angular

position of the sensor that produces this waveform in revolution $n_{\mathrm{R}}(t)$, and $\Delta(t)$ comprises a signal offset $\Delta_{\mathrm{O}}(t)$ and possible noise $\Delta_{\mathrm{N}}(t)$. The final amplitude of a waveform is a function of the clearance between the blade and the casing $c_{\mathrm{B}}(t)$ in relation to the initial clearance c_{B}^{0} at engine standstill. Their quotient changes with radial vibration $r_{\mathrm{B}}(t)$ and centrifugal loading in conformity with:

$$\frac{c_{\mathrm{B}}^{0}}{c_{\mathrm{B}}(t)} = \frac{c_{\mathrm{B}}^{0}}{c_{\mathrm{B}}^{0} - (r_{\mathrm{B}}(t) + \Delta L_{\mathrm{CF}}(t))} \tag{4.11}$$

where $\Delta L_{\mathrm{CF}}(t)$ is the elongation of the blade due to the latter. It should be emphasised that the above equation does not explain blade tip rubbing against the casing; therefore, the denominator is always greater than zero. When the tip of the blade is farther away from the casing, its interaction with the sensor is weaker so the amplitude decreases. It may sometimes be helpful to normalise waveforms for data processing purposes, especially when clearance is of no concern. The recorded waveforms computed as per Equation (4.10) can be grouped sensor-wise and blade-wise, so that a data set is available with which each blade-sensor combination can be analysed separately for a given engine condition.

The speed calibration parameter λ is a positive real number that influences the slopes of the waveform edges: the greater λ is, the thinner is the waveform in time. The value of λ is usually controlled by, amongst others, the rotational speed, the extent and gradient of the sensor field, and any lag brought about by the electronics during measurements. Consequently, it is not unlikely that different sensors vary in λ for the same rotational speed.

The total angular blade position $\varphi_{\mathrm{B}}(t)$ contains the vibration terms that point in or against the direction of rotation, which are here flap-wise deflection $\varphi_{\mathrm{B}}^{\mathrm{F}}(t)$ and torsional deflection $\varphi_{\mathrm{B}}^{\mathrm{T}}(t)$. The angular orientation of the blade with respect to the angular sensor position determines the time of waveform occurrence with the waveform crest being reached when the blade is right beneath the sensor.

When a second sensor S2 is shifted axially along the chord line to the other blade edge in close angular proximity to the first sensor S1 (see Figure 4.1), the influence of sampled trajectory sections of the axial deflection $\boldsymbol{a}_{\mathrm{B},i}$ and edge-wise deflection $\boldsymbol{\varphi}^{\mathrm{E}}_{\mathrm{B},i}$ on the i-th set of two concurring sampled waveforms associated with S1 and S2 can be established as per:

$$\boldsymbol{u}_{\mathrm{S1},i} \oslash \boldsymbol{u}_{\mathrm{S2},i} - \left(1 + \frac{\boldsymbol{a}_{\mathrm{B},i} + R^{0}_{\mathrm{B}}\boldsymbol{\varphi}^{\mathrm{E}}_{\mathrm{B},i}}{W^{\mathrm{C}}_{\mathrm{B}}}\right) \simeq \mathbf{0} \tag{4.12}$$

with the chord length of an undeformed blade $W^{\mathrm{C}}_{\mathrm{B}}$ and the symbol $\oslash$ denoting the (element-wise) Hadamard division of waveform vector $\boldsymbol{u}_{\mathrm{S1},i}$ by waveform vector $\boldsymbol{u}_{\mathrm{S2},i}$. The angular distance $\Delta\varphi^{0}_{\mathrm{S}}$ between S1 and S2 can be approximated by exploiting the following geometrical relationship:

$$\Delta\varphi^{0}_{\mathrm{S}} = \frac{W^{\mathrm{C}}_{\mathrm{B}}}{R^{0}_{\mathrm{B}}} \sin\alpha. \tag{4.13}$$

The idea is to take advantage of two waveform $(\boldsymbol{u}_{\mathrm{S1},i}, \boldsymbol{u}_{\mathrm{S2},i})$ being differently affected by axial and edge-wise vibrations in the direction of the shaft along the axial coordinate. The distortions of the two sensor fields are not uniform and, accordingly, any two waveforms, which are created by the sensors S1 and S2 during one blade passage, have distinct properties. This procedure requires that both waveforms occur under the same circumstances and any vibration form is cancelled out or negligible except for $a_{\mathrm{B}}(t)$ and $\varphi^{\mathrm{E}}_{\mathrm{B}}(t)$. The basic premise is that only these vibration types are responsible for the dissimilarity between the two waveforms. When the waveforms are polluted by strong noise and liable to measurement uncertainty, utilisation of the former equation with deterministic methods becomes taxing. Instead, one may resort to stochastic methods, such as those based on the Monte Carlo principle, including ensuing parameter verification.

Ideally, a single pair of waveforms can already be sufficient to determine multi-directional blade vibration completely, but this depends crucially on the sensor sampling frequency, the field of view of the sensor, and the operating conditions, especially the rotational frequency and, hence, the blade travelling

time along the sensor. It should be mentioned that vibration terms in Equations (4.10) and (4.12) can be excluded when they are deemed irrelevant to the investigation to be conducted.

4.3.2 Sensor position

Sensors are commonly distributed around the circumference of the casing with their location being described by a two-component vector $(\phi, a)^{\mathrm{T}}$ on the surface of the casing. In three dimensional models, an axial position of the sensor would need to be specified, for instance, at the leading edge, midchord, or trailing edge. As the focus in the present work is on a two dimensional model, the axial sensor location is neglected, and therefore, the sensor position only consists of the angular coordinate.

Each sensor is assigned a particular angular position defined with respect to a zero-degree reference datum. The initial angular position of the sensor φ_{S}^{0} attains values in the interval of $[0, 2\pi)$ rad. Notwithstanding this definition, the angular position of a blade in or against the direction of rotation determined as per Equation (4.3) is continuously growing with time t, and therefore, the angular sensor position $\varphi_{\mathrm{S}}[n_{\mathrm{R}}(t)]$ must be a step function for the mere purpose of correctly assigning the blade-sensor passage to the corresponding revolution $n_{\mathrm{R}}(t)$:

$$\varphi_{\mathrm{S}}[n_{\mathrm{R}}(t)] = \varphi_{\mathrm{S}}^{0} + 2\pi n_{\mathrm{R}}(t) = \varphi_{\mathrm{S}}^{0} + 2\pi \left\lfloor \int_{t_0}^{t} \Omega(\tilde{t}) d\tilde{t} \right\rfloor . \tag{4.14}$$

The actual or apparent angular sensor position and the initial angular sensor position φ_{S}^{0} are assumed to be the same in this work; thus, influential factors, such as casing and/or sensor vibration and uncertainties from sensor positioning errors and static blade deflections, are neglected. Further information on these subjects as regards traditional BTT is provided in [433].

4.3.3 Sampling waveforms

In order to process the sensor output with a computer, the analog signal has first to be discretised through sampling. The sampling frequency of a data acquisition system f_S states how often the sensor signal is read, setting the temporal resolution for waveforms. The information density can timewise be increased by choosing a larger sampling frequency. The temporal resolution is to be distinguished from the resolution of the samples (for instance, voltage data), which essentially depends on the bit depth and signal range of the data acquisition hardware and the actual resolution of the sensor with a limited bandwidth in the analog world.

In the literature, sampling frequencies of at least several hundred kHz are recommended for experimental measurements with traditional BTT [102, 248, 254, 278, 289]. The literature values were taken into consideration as benchmarks for parameterising the sensor. Ultimately, the value of the sampling frequency should be selected on the basis of the sensor type, blade geometry, and operating conditions (such as the rotational frequency and the blade dynamics) to be anticipated. Obviously, the thinner a blade ($\sim w_\mathrm{B}$) is and the faster it moves past a sensor, the higher the sampling frequency of the sensor has to be to capture the blade passage in greater detail. For the same reason, a sensor with a smaller extent of its medium ($\sim w_\mathrm{S}$) requires a higher sampling frequency. These relations are summarised in:

$$f_\mathrm{S} \propto \frac{\Omega(t)}{w_\mathrm{S}(t) w_\mathrm{B}}, \tag{4.15}$$

which can be used to calculate a lower bound of the sampling frequency. Relation (4.15) is meant to provide an idea of the magnitude of the sampling frequency that has to be chosen for the simulation or experiment. It also qualitatively indicates how the sampling frequency should be adjusted in case one of the variables on the right side of the relation alters. When selecting the sampling frequency, a trade-off has to be made between computational efficiency and the desired accuracy. The higher the sampling frequency, the

more data points are to be saved and dealt with. An estimation of the number of samples $n_\mathrm{S}(t)$ of a waveform is given by:

$$n_\mathrm{S} = \left\lfloor \frac{f_\mathrm{S}}{\Omega(t)} \cdot \frac{w_\mathrm{S}(t)}{2\pi} \right\rfloor . \tag{4.16}$$

The theoretical minimum of the number of waveform samples is zero in the limiting case when the rotational speed becomes infinitely large. The same would analogously apply to traditional BTT. For any realistic ratio of sampling frequency to rotational speed though, the number of waveform samples is positive.

4.3.4 Angular instantaneous and apparent width of the sensor field

The number of waveforms necessary to characterise blade vibration is governed by their timewise width: the wider they are, the more pertinent information they hold. Based on typical experimental waveforms and trigger algorithms for traditional TOA calculations presented in [111,148,173,176,360,417,434–437], an estimator of the angular instantaneous and apparent width of the sensor field $w_\mathrm{S}(t)$ is proposed:

$$w_\mathrm{S}(t) = 2\pi \int_{t_\mathrm{e}}^{t_\mathrm{d}} \Omega(\tilde{t}) d\tilde{t} \approx 2\pi\Omega(t_\mathrm{e})\Delta t_\mathrm{BT} = 2\pi\Omega(t_\mathrm{e}) \left[t_\mathrm{d} - t_\mathrm{e}\right] \tag{4.17}$$

where t_e is the time of blade entry into the sensor field and t_d is the time of blade departure from the sensor field. These times are measured at the beginning (rising edge) and at the end (falling edge) of a waveform, respectively, and the difference Δt_BT is the blade travelling time along the sensor. The last parameter stands for the theoretical snapshot length of the blade vibration trajectory that is retrievable from waveforms using BLASMA.

The term ‘snapshot’ is used to describe the part of the vibration trajectory that caused the modulation of a particular waveform and is – so to speak –

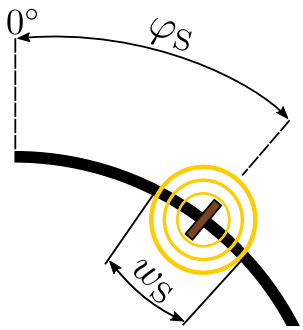


Figure 4.4: Width of the sensor field at the location of the sensor

hidden therein and needs to be extracted. It can be conceived as a view of the blade deflection trajectory in the moment when the corresponding blade passes the sensor. The larger such a snapshot and the greater the variation amongst waveforms of a certain blade-sensor combination, the easier it is to determine the correct vibration parameters. If synchronous vibration is to be investigated where, in theory, the blade arrives at the sensor always with the same deflection characteristics, the aforementioned variation can be enriched by rising the number of sensor and selecting different sensor positions, which may also apply to cases of more complex blade vibration. When placing sensors in close proximity to each other, snapshots of the blade vibration trajectory can be combined to increase the view of the deflection signal. Another available option is low-pass filtering of the waveform with a stop-band frequency above the vibration frequencies of interest to attenuate noise. This should nonetheless be done with caution since filtering introduces errors that require attention.

The instantaneous and apparent width of the sensor field is a function of the blade tip geometry, especially the width, and the real physical and measurable width of the sensor field, which ought to be considered at engine standstill when a blade were to be modal-tested right beneath a sensor. When one of the last two parameters increases or decreases, the instantaneous and apparent width of the sensor field follows correspondingly. Modelling the sensor waveform function therefore incorporates at the same time the

modelling of the blade tip width. From a practical standpoint, the angular extent of the sensor field w_S can be considered a quantity that determines the boundaries of the sensor field beyond which a blade cannot be detected (see Figure 4.4). In other words, the sensor field is only disturbed when a blade is within it through which the signal strength changes; no claim is made that w_S confirms field theory. Bear in mind that the angular extent of the sensor field should not be confused with the actual geometric dimensions of the sensor. It is essential to know when a blade can be considered present in the sensor field in order to identify only those parts of the sensor signal that are meaningful for vibration analysis. Details about the sensor field function may be asked from the manufacturer of the sensor. It became apparent from traditional BTT experiments that the exact times of a blade entering and leaving the sensor field are difficult to determine. To be able to reliably establish the occurrence of both events on a case-by-case basis, an adjustable cut-off parameter, which defines the signal strength below which sensor data is ignored and at which the blade is thought to be either arriving or leaving, was added to the set of model variables.

4.3.5 Number of complete vibration cycles in a trajectory snapshot

The number of complete vibration cycles n_C of the fundamental harmonic ω in a snapshot can be computed pursuant to:

$$n_C = \left\lfloor \frac{\omega}{2\pi} \Delta t_{BT} \right\rfloor . \tag{4.18}$$

It becomes evident that higher harmonics lead to a larger number of complete cycles in the snapshot. This number does not represent the number of cycles of the overall vibration signal, which would be a common multiple of the response frequencies in the case of dealing with integer frequencies only. Furthermore, it is also worth highlighting that the number of waveform samples implicitly coincides with the number of samples of the blade trajectory in the snapshot.

One can then infer that BLASMA would have the same performance as traditional BTT in the case of the number of waveform samples attaining the value of one.

Chapter 5

BLASMA-SCP

BLASMA-SCP (Signal Characteristics Processing) is a technique for computing and using waveform quantities to determine blade vibration parameters. Before that can happen, sensor waveforms need to be recorded under the operating conditions of interest, either in an experiment or simulation. A waveform is generated when a blade passes a sensor once per revolution, thereby modulating the waveform through vibration. Compared with traditional BTT, significantly more information about vibration can be obtained by processing full waveforms and identifying this modulation. Each signal can contain multiple waveforms, which can be characterised by various quantities. Some of these quantities are presented in the following list and illustrated in Figure 5.1:

- geometrical properties, e.g., area moment of inertia, curvature, skewness, width
- quantities from calculus, e.g., (local) maxima and minima, monotonicity, roots, **slopes** as the local values of the numerical waveform derivative $\frac{du(t)}{dt}$, waveform **integral** $\int u(t)dt$
- statistical parameters, e.g., average (μ_u), cross-correlation ($u \star u$), standard deviation (σ_u)
- signal features, e.g., amplitude $u(t_\mathrm{C})$ often used for clearance measurements, frequency spectrum, noise, phase, time of waveform occurrence or TOA (t_BTT), time of the waveform amplitude (t_C), time of blade entry into the sensor field (t_e), time of blade departure from the sensor field (t_d)

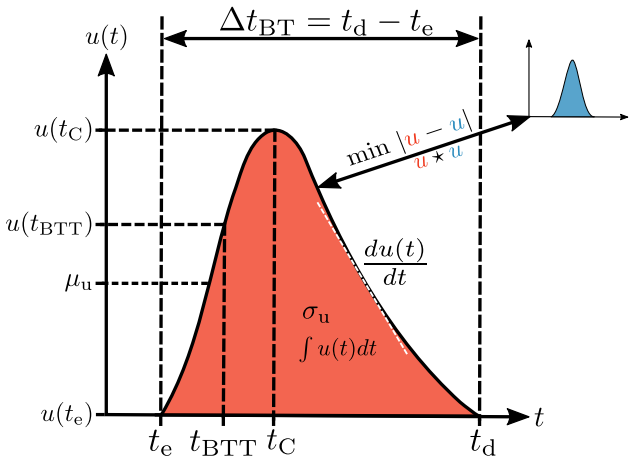


Figure 5.1: Some waveforms characteristics

- mathematical transforms, such as FFT, Hilbert transform, wavelet transform
- optimisation with problems, such as $\min |u - u|$
- resemblance to other waveforms in order to calculate reference waveforms for a particular operating condition. Reference waveforms can serve pattern matching, e.g., in artificial neural network procedures for identifying certain vibration conditions, which are typically prevalent in the engine.

For the following numerical study, a rather unconventional approach to determining vibration is presented on the basis of the slopes and the integral of a waveform, highlighted in **bold type** in the list above. These two waveform properties allow making statements on the position of the blade in its vibration cycle and can further be used to compute estimates of the amplitudes and frequency of the vibration velocity and vibration deflection.

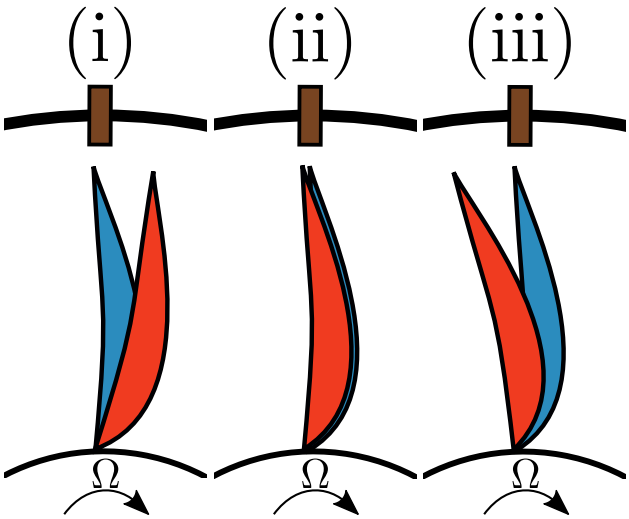


Figure 5.2: Case studies for assessing BLASMA-SCP where a vibrating blade (red (■)) is compared with a fictitiously rigid reference blade (blue (■)) in different situations

To identify the changes in waveforms through vibration, three different cases were investigated with respect to these types of blade passages beneath a sensor:

(i) a vibrating blade arrives early at the sensor and is momentarily at its positive amplitude of vibration deflection (zero vibration velocity) during the passage

(ii) a vibrating blade instantaneously has zero vibration deflection as it reaches its positive amplitude of vibration velocity

(iii) a vibrating blade arrives late at the sensor and is momentarily at its negative amplitude of vibration deflection (zero vibration velocity) during the passage.

The cases are illustrated in Figure 5.2 in which a vibrating blade is depicted in red (■) and a fictitiously rigid reference blade in blue (■).

5.1 Model parameterisation

The model parameters of the sensor and bladed disk are listed in Tables 5.1 and 5.2, respectively. The bladed disk was a modified version of the one presented in Figure 4.2 and rotated in a plane where the blades were allowed to vibrate at steady state, which was approximately reached after a third of a simulation time of 0.3 s. To simulate the three different blade passages within a small time window, a balanced and tuned rotor was considered with four equally spaced blades of which each was supposed to behave like a single-degree-of-freedom system. The disk possessed a larger stiffness coefficient than the blades to emphasise the implications of pure blade vibration for waveforms, attenuating the coupling between the blades and the disk.

The fact of the blade vibrating at steady state facilitated the interpretation of the computed waveforms because uncertainties emerging from transition states could be neglected. By applying excitation forces to the blades directly and by taking the model assumptions into account, flap-wise vibration became the only form of oscillation present in the blade trajectory, simulating a blade that resonated in its first bending mode. For this purpose, a single-harmonic force of 1 kN at a frequency of 175 Hz was selected. Having such a relatively low blade frequency to observe is more demanding because the degree of

Parameter	Value	Unit
Number of sensors	1	-
Angular sensor position (φ_{S}^{0})	0	rad
Nominal signal amplitude (U)	1	-
Speed calibration parameter (λ)	2.5e2	$\frac{1}{\mathrm{rad}^2}$
Signal offset without white Gaussian noise (Δ_{O})	0	-
Signal-to-noise ratio for white Gaussian noise	30	dB
Sampling frequency (f_{S})	1.5e5	Hz
Clearance ratio $\left(\frac{c_{\mathrm{B}}^{0}}{c_{\mathrm{B}}(t)}\right)$	1	-

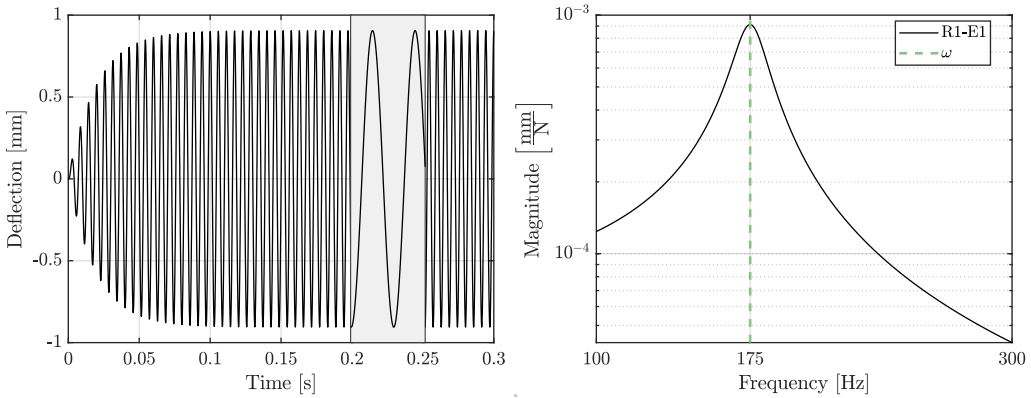
Table 5.1: Parameters for the sensor model

Parameter	Value	Unit
Blade tip radius (R_{B}^{0})	0.1	m
Number of blades	4	-
Angular blade spacing	$\frac{\pi}{2}$	rad
Blade mass	10	kg
Disk sector mass	1e3	kg
Blade stiffness coefficient	1.2e7	$\frac{\mathrm{N}}{\mathrm{m}}$
Disk stiffness coefficient	1e8	$\frac{\mathrm{N}}{\mathrm{m}}$
Ground stiffness coefficient	1e10	$\frac{\mathrm{N}}{\mathrm{m}}$
Blade damping coefficient	1e3	$\frac{\mathrm{kg}}{\mathrm{s}}$
Disk damping coefficient	1e8	$\frac{\mathrm{kg}}{\mathrm{s}}$
Ground damping coefficient	1e8	$\frac{\mathrm{kg}}{\mathrm{s}}$
Resonance frequency of interest	175	Hz
Rotational speed (Ω)	2e3	RPM
Excitation amplitude	1e3	N
Excitation frequency	175	Hz
Excitation phase angle	0	rad

Table 5.2: Parameters for the bladed disk model

waveform modulation is smaller. The response and point of operation in the FRF are shown in Figures 5.3(a) and 5.3(b), respectively. It has to be mentioned that the response plot possesses a zoomed-in view in grey ( ) in order to offer more detail about the deflection trajectory. The time axis shown belongs to the overall signal section and not the close-up. The magnitude of the response agrees with experimental measurements reported, e.g., in [203], where the length of the real blade is comparable with the blade tip radius used here. Single-harmonic vibration in real engines is a fair assumption when, for instance, the bladed disk undergoes resonance in a natural vibration mode that is frequency-wise well separated from any other mode.

It was decided to choose a sensor whose waveforms resemble those of a capacitive sensor. The justification for this decision was based on three facts. Firstly, capacitive sensors have already earned a good reputation for their capability to monitor vibration and clearance online, and plenty of pertinent



(a) Deflection trajectory of the vibrating blades at resonance – with a zoomed-in view in grey ( )

(b) FRF – Magnitude

Figure 5.3: Vibration characteristics

work has been published. Secondly, the waveforms of a capacitive sensor can be well approximated by standard mathematical expressions. This is crucial in respect of their post-processing. Thirdly, there are usually no more than two zero-crossings, if any, in real waveforms, provided that the sensor is configured appropriately. The less complicated a waveform is, the less effort has to be put into interpreting a complete blade passage and its modulation by vibration.

The number of sensors employed was limited to one for two reasons. The first was to determine the maximum accuracy that can be achieved with BLASMA-SCP under this circumstance, and the second was to provide a methodology of vibration monitoring for situations where the number of sensors is severely constrained. Since the exact waveform function of a real capacitive sensor was unavailable, a waveform presented in the work of Zielinski and Ziller [175] was replicated to define the sensor function of Equation (4.10). This was done using a non-linear least-squares fitting algorithm with which the mean sensor waveform parameters (U, λ, and Δ_O) of a 95 % confidence interval were determined; the result of the fitting is depicted in Figure 5.4. The three mentioned waveform parameters, together with the angular sensor position,

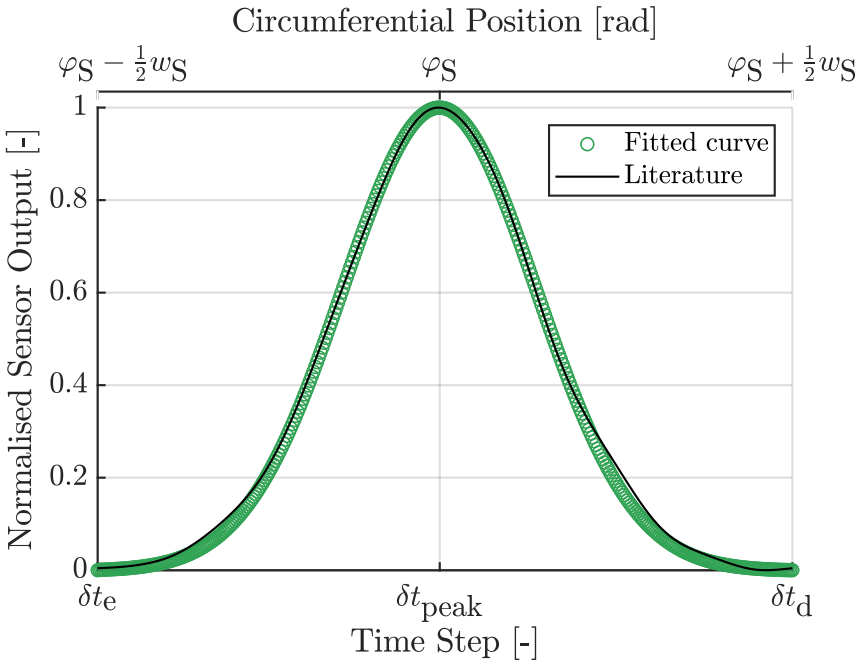


Figure 5.4: Replication of a capacitive sensor waveform reported in the literature

the signal-to-noise ratio for producing white Gaussian noise in the sensor output, the sensor sampling frequency, and the clearance ratio, which was constant in this work, are listed in Table 5.1.

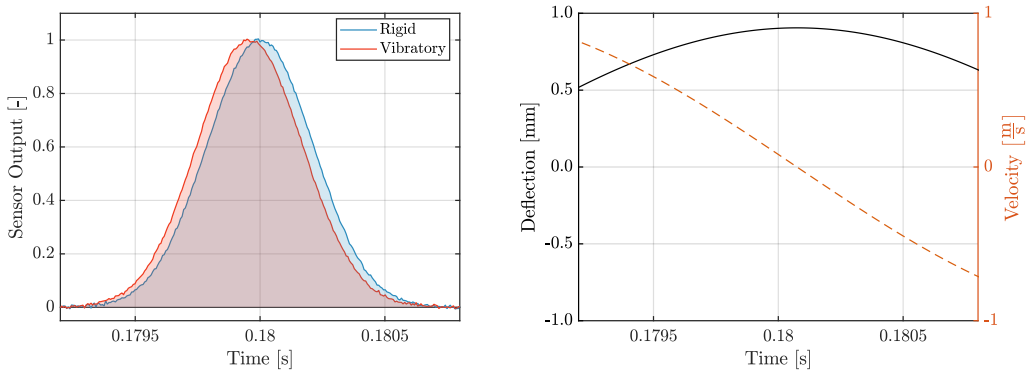
To be independent of physical units, every waveform generated by the sensor model was normalised. Noise was subsequently added in order to allow the simulation results to better match experimental measurements. The speed calibration parameter λ was adjusted to the simulation conditions by considering blade travelling times along the sensor that can be observed in comparable experiments. By doing so, the effect of narrowing or widening of the waveform with increasing or decreasing speed was taken into account as well as the implications of the blade tip width and angular extent of the sensor field attaining realistic values. The angular width of the sensor field w_S was assumed to be approximately 12°, which quantified the corresponding interval of $\left[\varphi_S - \frac{1}{2}w_S, \varphi_S + \frac{1}{2}w_S\right]$ wherein the sensor was capable of detecting

the presence of blades. Given that the time for one revolution of the bladed disk was 0.03 s at a rotational speed of 2e3 RPM, the blade travelling time along the sensor was then of the order of 1 ms. The results obtained on the basis of these assumptions agree with observations found elsewhere [249].

5.2 Simulation results

One way of identifying the modulation of a waveform is to compare this waveform with a corresponding reference waveform. The former is ascribed to the passage of a vibrating blade along the sensor and the latter to one of a fictitiously rigid blade. Such a comparison can be made immediately after the two blade types completely pass the same sensor in the same revolution. Reference waveforms can not only be taken from simulations as it is the case here but also from experiments. An example of a reference waveform from experimental data is the average of waveforms that is calculated after several consecutive revolutions under constant operating conditions. Furthermore, it is also possible to determine experimental reference waveforms from measurements when the bladed disk rotates at non-critical speeds where any vibration is negligible. A scaling of the speed calibration parameter should not be forgotten.

When choosing a reasonably high sensor sampling frequency f_S of 150 kHz, waveforms like those in Figures 5.5(a)–5.7(a) for cases (i)-(iii) can be calculated. In each figure, a waveform of a vibrating blade, depicted in red (—), is juxtaposed with one of a rigid reference blade, depicted in blue (—). Next to each of these figures, there is a plot of the corresponding blade trajectory of vibration deflection and velocity that caused the modulation of each of the corresponding red waveforms on the left side (see Figures 5.5(b)–5.7(b)). The deflection signal drawn as a solid black line (—) lags the velocity signal in dashed brown (- - -). As regards case (i), it can be seen that a positive deflection leads to an earlier arrival of the vibrating blade at the sensor, indicated by the red waveform shifted against the blue waveform towards earlier times. The



(a) Sensor waveforms

(b) Trajectory of vibration deflection and velocity during the passage

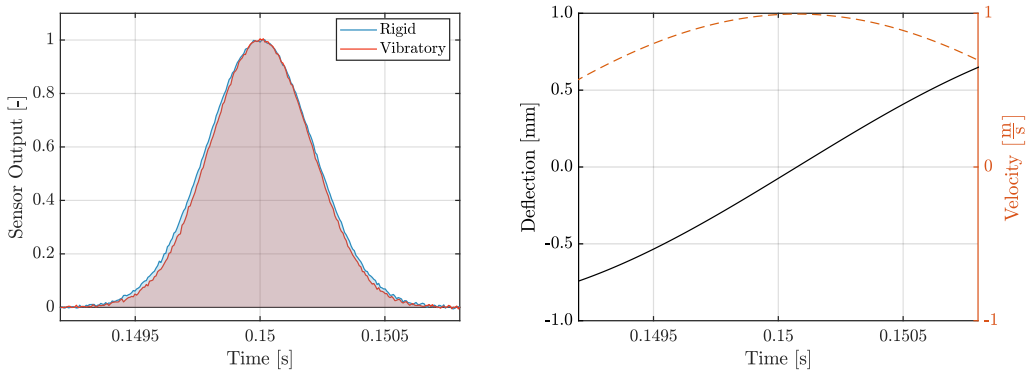
Figure 5.5: Case (i)

opposite is true when the vibrating blade arrives later (case (iii)). Clearly, the shift declines to almost zero for simultaneous arrivals of the vibrating blade and rigid blade (case (ii)). The waveforms were recorded over three consecutive revolutions, which permits first statements on the presence of vibration. The results of all four blades were comparable, wherefore it was deemed sufficient to present those belonging to blade 1. Unless otherwise stated, further signal processing is conducted on data from that blade. Apart from the phase shifts of waveforms, more information on the modulation can be obtained by computing waveform quantities.

5.3 Post-processing of the data

5.3.1 Integral of the waveform

The plots of the sensor output show the visual effects of vibration on waveforms, whose integrals and slopes were used to quantify their modulation and to compute vibration parameters. The integral values, which are the areas under the waveforms of the rigid blade $\int u^{\mathrm{r}} dt$ (blue coloured area (■)) and vibrating blade $\int u^{\mathrm{v}} dt$ (red coloured area (■)) in Figures 5.5(a)–5.7(a), can be



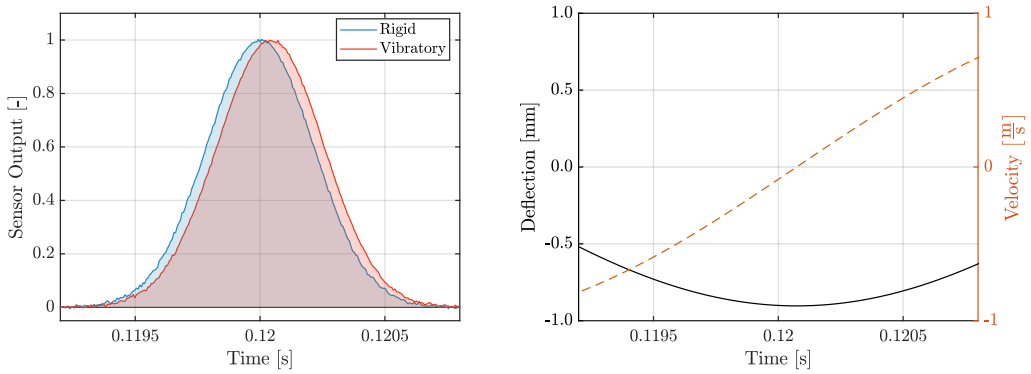
(a) Sensor waveforms

(b) Trajectory of vibration deflection and velocity during the passage

Figure 5.6: Case (ii)

found in Table 5.3. The unit of the integral values is the second (s) because the normalised sensor signal is dimensionless. The integral values of the waveforms of the rigid reference blade are the same in all three cases. Any additional velocity of the blade due to vibration during the passage beneath the sensor leads to smaller or larger values of the integral.

Regarding case (i), the vibration velocity has a zero-crossing which leads to a total velocity of the vibrating blade that is close to the rotational speed during the sensor passage (see Figure 5.5(b)). It also becomes evident that the blade changes the sign of the vibration velocity from plus to minus. The part of the waveform, which is associated with the blade having a total velocity above the rotational speed, is smaller than that part, which is associated with the blade having a total velocity below the rotational speed. The total velocity is here the superposition of rotational velocity and vibrational velocity (cf. Equation (4.3)). The respective half-side integrals clearly highlight the impact of the sign of the vibration velocity: $\int_{t_e}^{t_C} u^v dt$=38.74 s and (-$\int_{t_C}^{t_d} u^v dt$)=40.26 s. The consequence is a smaller total integral value of the waveform of the vibrating blade $\int u^v_{\text{case(iii)}} dt$ compared with that of the rigid reference blade $\int u^r_{\text{case(iii)}} dt$, which is represented by a relative change of -0.61 %. The times of the amplitudes to occur of both waveform types can be contrasted to ascertain the position of the blade in its deflection cycle. Waveform data



(a) Sensor waveforms

(b) Trajectory of vibration deflection and velocity during the passage

Figure 5.7: Case (iii)

in Figure 5.5(a) shows that the vibrating blade arrives earlier, which can be interpreted as the vibrating blade having to lead the rigid blade. When following the previously defined coordinate system, the vibrating blade can be located in the positive half of the deflection cycle. Recording waveforms over multiple revolutions let one observe a scattering of the integral values. Identifying the extreme values yields estimates that can be used for computing the deflection amplitude. Nonetheless, these values should be interpreted with care. It is not guaranteed that the actual amplitude can be found amongst the samples because the form of vibration unavoidably affects the position in the oscillation cycle at which the blade is capable of arriving at the sensor.

As for case (ii), the vibrating blade is instantaneously at its maximum total velocity and, hence, maximum vibration velocity that it can possibly attain during the passage beneath the sensor (see Figure 5.6(b)). Therefore, the blade needs less time to pass the sensor. The waveform of the vibrating blade is drastically less phase-shifted yet stronger distorted by the larger vibration velocity. This leads to a waveform of the vibrating blade in Figure 5.6(a) that is narrower than that of case (i). Consequently, the integral of the waveform of the vibrating blade is smaller, exactly 4.55 %, than that of the rigid reference blade, which confirms vibration in the direction of rotation. Both waveforms are almost aligned and on top of each other, which indicates

	Case(i)	Case (ii)	Case (iii)	Unit
$\int u^{\mathrm{r}} dt$	79.48	79.48	79.48	s
$\int u^{\mathrm{v}} dt$	79.00	75.87	79.59	s
$\frac{\int u^{\mathrm{v}} dt - \int u^{\mathrm{r}} dt}{\int u^{\mathrm{r}} dt}$	-0.61 %	-4.55 %	0.14 %	-

Table 5.3: Numerical integrals of the waveforms

a zero deflection in the vibration cycle. When the vibration velocity assumes its positive amplitude value, the vibrating blade is in the process of moving from a lagging to a leading position ahead of the rigid blade. When the vibration velocity is at its negative amplitude value, the opposite happens. A combination of the integral and phase shift allows once more the detection of blade vibration and the pinpointing of the current state in the vibration cycle.

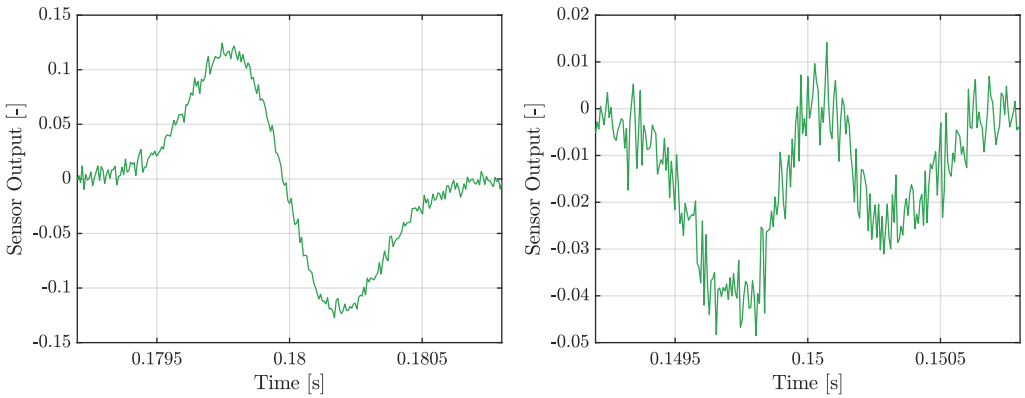
Case (iii) is the reverse of case (i), the vibration velocity has again a zero-crossing so that the vibrating blade passes the sensor roughly at rotational speed (see Figure 5.7(b)). This time though, the vibration deflection attains the negative amplitude value. Only a small difference between the integral values $\int u^{\mathrm{v}}_{\mathrm{case(iii)}} dt$ and $\int u^{\mathrm{r}}_{\mathrm{case(iii)}} dt$ can be observed (0.14 %), stating the absence of heavy waveform modulation through vibration. If merely integral values are adduced to explain blade oscillations, two possible conclusions might be drawn with respect to cases (i) and (iii): first, either the blade does almost not vibrate or, second, the blade is at its positive or negative deflection amplitude in the vibration cycle. To clarify the situation, the phase shift between the waveform of the rigid and the vibrating blade has to be taken into account. No phase shift indicates no vibration deflection, whereas a positive or negative phase shift is a sign of a vibration deflection in or against the direction of rotation. In case (iii), the waveform of the vibrating blade is shifted towards later times, caused by the negative deflection. In other words, the vibrating blade lags the rigid blade.

Another method for showing the presence of vibration is determining the function of the difference between the waveform of the vibrating blade and waveform of the rigid blade. As it can be seen in Figures 5.8(a)–5.8(c), the phase shift between the red waveform and blue waveform affects the magnitude and orientation of the noise-distorted function of the waveform difference depicted in green (—). The stronger the phase shift, the larger is the maximum difference. The waveform difference is a direct sign of waveform modulation through vibration because it exhibits the phenomenon of points of the waveform of the vibrating blade being non-linearly displaced from the corresponding ones that belong to the rigid blade. This behaviour helps to distinguish between various vibration states.

If one were to compute vibration amplitudes utilising traditional BTT with only a single red and blue waveform each, data of cases (i) and (iii) should be used for two reasons: first, there is little vibration velocity present during the passage event and, second, the vibrating blade is at the extreme of its deflection curve. The accuracy suffers when the vibration velocity is large because the vibration deflection changes rapidly in a short amount of time (cf. case (ii)). The BTT deflection amplitude X_{BTT} of the blade under consideration would then be approximated using:

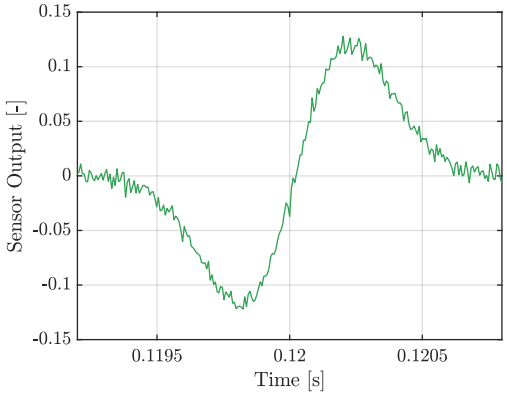
$$X_{\mathrm{BTT}} = 2\pi R_{\mathrm{B}}^{0} \Omega \, |\Delta t_{\mathrm{BTT}}| \tag{5.1}$$

where Δt_{BTT} is the timewise phase shift between the red waveform and blue waveform, which is computed from time values that are read at signal values of 0.4 at the rising edges. The timewise phase shifts attain roughly 0.04 ms in cases (i) and (iii), which yield amplitudes of about 0.838 mm each according to Equation (5.1). When taking the actual steady-state amplitude of 0.905 mm into account, the error amounts to about -7.4 %, which is above the desired industry standard of ±5 %. The amplitude estimate would be the best possible outcome of a traditional BTT investigation under the present conditions. The vibration frequency cannot be determined with a single sensor because of insufficient sampling at approximately 33 Hz only, which is too small to sample a 175-Hz vibration signal. Repeating the above approach for



(a) Case (i)

(b) Case (ii)



(c) Case (iii)

Figure 5.8: Differences between the waveforms from the passages of a vibrating blade and a rigid blade for each case

case (ii) results in an amplitude of 0.337 mm, which tallies with an absolute error of 62.76 %. This error is larger than the previous one since the blade did not assume the deflection amplitude during the sensor passage, and thus, this information is missing in the corresponding waveform data and cannot be retrieved from a single pair of red and blue waveforms.

5.3.2 Slopes of the waveform

Another distinctive attribute to determine vibration parameters are the waveform slopes of the signal rise (SR) and signal fall (SF) that are associated with the rigid blade $\frac{du^{\mathrm{r}}}{dt}|_{\mathrm{SR,SF}}$ and vibrating blade $\frac{du^{\mathrm{v}}}{dt}|_{\mathrm{SR,SF}}$. The slopes of the waveforms were calculated on the basis of a linear function in the interval in which the sensor signal strength was between 20 % and 80 % of its normalised maximum value. The rationale behind choosing this interval was to exploit the weak local non-linearity of the actual waveforms, which allowed linearisation to a degree of satisfactory accuracy. A list of the slope values concerning cases (i)-(iii) can be found in Table 5.4.

As for the waveforms of the rigid blade, the absolute slopes of the rising edges and the falling edges are the same in every case ((i)-(iii)) as expected. When it comes to the waveforms of the vibrating blade, the absolute slopes of the signal rise and signal fall differ in each case. The vibration velocity changes during the passage of a blade beneath the sensor, and therefore, the strength of the waveform modulation varies correspondingly, leading to waveform skewness or asymmetry. The variation in this modulation during the blade passage is, however, small which is why it cannot be spotted in Figures 5.5(a)–5.7(a). When viewing the data in Table 5.4, it appears that the discrepancy between the slope of the rising edge and the slope of the falling edge of a red waveform is smaller when the vibration velocity changes less in value throughout the blade passage, which is observed when the vibration velocity is in the vicinity of its maximum (case (ii)). Compared with the absolute slopes of the blue waveform of the same case, the absolute slopes of the red waveform are larger. Hence, the larger the velocity of the vibrating blade, the steeper the waveform. The sign change in the vibration velocity from plus to minus in case (i) causes the slope of the rising edge of the red waveform to be larger than the corresponding slope of the blue waveform, whilst this reverses for the falling edge. The opposite is correct in respect of case (iii). The results from the investigation into the waveform slopes are consistent with those of the waveform integrals. The steeper a signal edge is, the smaller

	Case (i)	Case (ii)	Case (iii)	Unit
$\frac{du^{\mathrm{r}}}{dt}\|_{\mathrm{SR}}$	2496	2496	2496	$\frac{1}{\mathrm{s}}$
$\frac{du^{\mathrm{r}}}{dt}\|_{\mathrm{SF}}$	-2496	-2496	-2496	$\frac{1}{\mathrm{s}}$
$\frac{du^{\mathrm{v}}}{dt}\|_{\mathrm{SR}}$	2544	2607	2458	$\frac{1}{\mathrm{s}}$
$\frac{du^{\mathrm{v}}}{dt}\|_{\mathrm{SF}}$	-2477	-2612	-2526	$\frac{1}{\mathrm{s}}$
$\frac{\frac{du^{\mathrm{v}}}{dt}-\frac{du^{\mathrm{r}}}{dt}}{\frac{du^{\mathrm{r}}}{dt}}\|_{\mathrm{SR}}$	1.90 %	4.43 %	-1.51 %	-
$\frac{\frac{du^{\mathrm{v}}}{dt}-\frac{du^{\mathrm{r}}}{dt}}{\frac{du^{\mathrm{r}}}{dt}}\|_{\mathrm{SF}}$	-0.77 %	4.63 %	1.19 %	-

Table 5.4: Numerical slopes of the waveform edges

the final waveform appears, provided that the rotational speed, the width of the blade tip, and the angular extent of the sensor field are kept constant. The slope and the integral are therefore beneficial indicators and quantifiers of the relative motion of the vibrating blade.

The slopes of the waveforms from Table 5.4 were further processed to compute the vibration velocities of a blade. For this purpose, the constant rotational speed of the blade $v_{\mathrm{B}}^{\mathrm{r}}$ was first determined according to:

$$v_{\mathrm{B}}^{\mathrm{r}} = 2\pi R_{\mathrm{B}}^{0}\Omega = 20.944\frac{\mathrm{m}}{\mathrm{s}} = \mathrm{const.} \tag{5.2}$$

Next, the instantaneous total velocity of the vibrating blade $v_{\mathrm{B}}(t)$ was estimated at times $\bar{t}_{\mathrm{SR}}$ and $\bar{t}_{\mathrm{SF}}$ using the respective slopes of the waveform edges that were associated with the vibrating blade and rigid blade as per:

$$v_{\mathrm{B}}(t)\Big|_{t=\{\bar{t}_{\mathrm{SR}},\bar{t}_{\mathrm{SF}}\}} = \frac{\frac{\mathrm{d}u^{\mathrm{v}}}{\mathrm{d}t}|_{\mathrm{SR,SF}}}{\frac{\mathrm{d}u^{\mathrm{r}}}{\mathrm{d}t}|_{\mathrm{SR,SF}}} v_{\mathrm{B}}^{\mathrm{r}}. \tag{5.3}$$

The quantities $\bar{t}_{\mathrm{SR}}$ and $\bar{t}_{\mathrm{SF}}$ are the average times in the interval in which the slopes of the rising and falling waveform edges were determined.

	Case (i)	Case (ii)	Case (iii)	Unit
$v_{\mathrm{B}}(\bar{t}_{\mathrm{SR}})$	21.341	21.872	20.627	$\frac{\mathrm{m}}{\mathrm{s}}$
$v_{\mathrm{B}}^{\mathrm{v}}(\bar{t}_{\mathrm{SR}})$	0.397	0.928	-0.317	$\frac{\mathrm{m}}{\mathrm{s}}$
$v_{\mathrm{B,s}}^{\mathrm{v}}(\bar{t}_{\mathrm{SR}})$	0.401	0.933	-0.317	$\frac{\mathrm{m}}{\mathrm{s}}$
$v_{\mathrm{B}}(\bar{t}_{\mathrm{SF}})$	20.783	21.914	21.192	$\frac{\mathrm{m}}{\mathrm{s}}$
$v_{\mathrm{B}}^{\mathrm{v}}(\bar{t}_{\mathrm{SF}})$	-0.161	0.970	0.249	$\frac{\mathrm{m}}{\mathrm{s}}$
$v_{\mathrm{B,s}}^{\mathrm{v}}(\bar{t}_{\mathrm{SF}})$	-0.159	0.976	0.249	$\frac{\mathrm{m}}{\mathrm{s}}$

Table 5.5: Estimated velocities of a blade at the time of the rise and fall of a waveform

The estimated total velocity is only valid at these times because the vibration velocity generally changes with time and the slopes of the waveforms are localised in time. In the given domain, the instantaneous vibration velocity of the blade $v_{\mathrm{B}}^{\mathrm{v}}(t)$ could be estimated using:

$$v_{\mathrm{B}}^{\mathrm{v}}(t)\Big|_{t=\{\bar{t}_{\mathrm{SR}},\bar{t}_{\mathrm{SF}}\}} = v_{\mathrm{B}}(t)\Big|_{t=\{\bar{t}_{\mathrm{SR}},\bar{t}_{\mathrm{SF}}\}} - v_{\mathrm{B}}^{\mathrm{r}}. \tag{5.4}$$

The total velocities and the vibration velocities of the blade, which were determined utilising Equation (5.4), are listed in Table 5.5. From comparing the vibration velocities $v_{\mathrm{B}}^{\mathrm{v}}(t)$ evaluated at $\{\bar{t}_{\mathrm{SR}}, \bar{t}_{\mathrm{SF}}\}$ with the matching averaged solutions $v_{\mathrm{B,s}}^{\mathrm{v}}$ of cases (i)-(iii), an acceptable agreement between the former and the latter is concluded. The errors in the vibration velocity with a maximum of 0.96 % are shown for each case in Figure 5.9. It was found that the time domain of linearisation should not be extended beyond the domain presented to prevent the errors from rising. On the other hand, reducing the size of the domain does not significantly contribute to accuracy. The errors were ultimately attributed to the linearisation of the slope, the inevitable fact of the waveform data being discrete, and general numerical noise. In the light of the small errors obtained, using more advanced techniques, such as a Taylor approximation, was deemed superfluous. Linearisation is a fast and computationally inexpensive method from a practical point of view for estimating the waveform slope for vibration analysis.

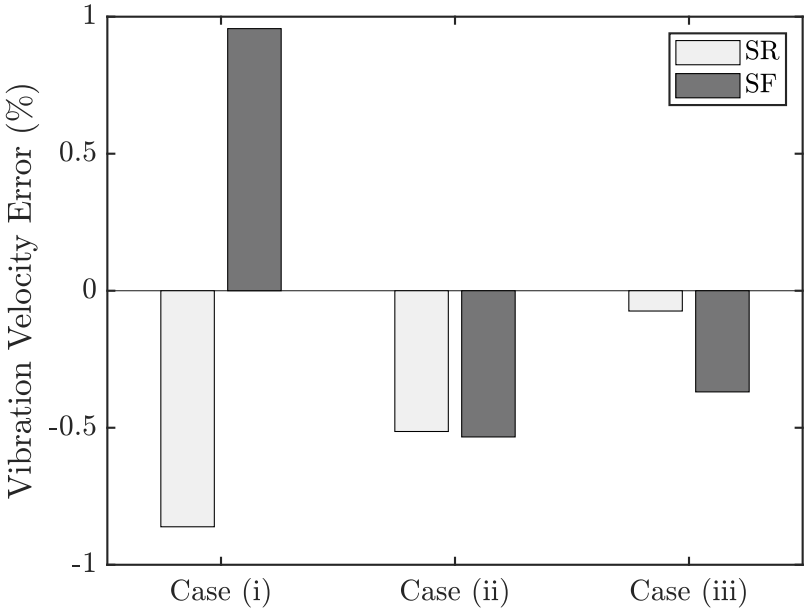


Figure 5.9: Errors in vibration velocities computed using the slopes of the waveforms at the signal rise (SR) and signal fall (SF) from the passages of a vibrating blade in each of the three case studies

The estimated vibration velocities based on the waveform slopes were used to find the frequency of single-harmonic blade vibration ω in conformity with:

$$\overline{v}^{\mathrm{v}}_{\mathrm{B,case(iii)}} = \overline{v}^{\mathrm{v}}_{\mathrm{B,case(ii)}} \cos\left(\omega\left(\overline{t}_{\mathrm{case(iii)}} - \overline{t}_{\mathrm{case(ii)}}\right)\right) \tag{5.5}$$

where $\overline{v}^{\mathrm{v}}_{\mathrm{B,case(ii)}}$ is the average vibration velocity of case (ii) and $\overline{v}^{\mathrm{v}}_{\mathrm{B,case(iii)}}$ is that of case (iii), which, together with the average times of waveform occurrences, are displayed in Table 5.6. The average values were based on the velocities at the signal rise and signal fall. The reason for referring to cases (ii) and (iii) was that the respective vibration velocities were measured at important points of the trajectory, namely a turning point and a zero-crossing. These features are advantageous for determining the vibration frequency because their spacing in time can easily be related to the vibration period. Case (iii) was preferred to case (i) because the absolute average vibration velocity was smaller in the

	Case (i)	Case (ii)	Case (iii)	Unit
$\overline{v}_{\mathrm{B}}^{\mathrm{v}}$	0.118	0.949	-0.034	$\frac{\mathrm{m}}{\mathrm{s}}$
$\bar{t}$	0.180	0.150	0.120	s

Table 5.6: Average vibration velocities of a blade and average times of waveform occurrences

former and, thus, better approximated the minimum vibration velocity of 0 $\frac{\mathrm{m}}{\mathrm{s}}$. This helped to decrease the error in the vibration frequency. It is to be remembered that the vibration velocity in case (ii) was the largest value observed, whereas the vibration velocity in case (iii) was the smallest. This constellation of values proved suitable for computing the vibration frequency. Rearranging Equation (5.5) yielded the inverse of the cosine, which has the following two solutions:

$$\omega \left(\bar{t}_{\mathrm{case(iii)}} - \bar{t}_{\mathrm{case(ii)}}\right) = \arccos\left(\frac{\overline{v}_{\mathrm{B}}^{\mathrm{v}}\left(\bar{t}_{\mathrm{case(iii)}}\right)}{\overline{v}_{\mathrm{B}}^{\mathrm{v}}\left(\bar{t}_{\mathrm{case(ii)}}\right)}\right) + 2\pi k \tag{5.6}$$

$$\omega \left(\bar{t}_{\mathrm{case(iii)}} - \bar{t}_{\mathrm{case(ii)}}\right) = 2\pi - \arccos\left(\frac{\overline{v}_{\mathrm{B}}^{\mathrm{v}}\left(\bar{t}_{\mathrm{case(iii)}}\right)}{\overline{v}_{\mathrm{B}}^{\mathrm{v}}\left(\bar{t}_{\mathrm{case(ii)}}\right)}\right) + 2\pi k. \tag{5.7}$$

The arcus cosine value of the quotient of the vibration velocity of case (iii) divided by that of case (ii) was calculated to be 1.607 rad ($\approx \frac{\pi}{2}$ rad) with the information from Table 5.6. Evaluating the arcus cosine took place in the interval of $[0, \pi]$ rad in which the cosine is bijective. It has to be borne in mind that the velocity values were not measured in the same vibration cycle; hence, there was a time difference of approximately 30 ms or one revolution in between. This difference was conserved in the average times of waveform occurrences. The following equations:

$$\omega \left(\bar{t}_{\mathrm{case(iii)}} - \bar{t}_{\mathrm{case(ii)}}\right) = 1.607 + 2\pi k \tag{5.8}$$

$$\omega \left(\bar{t}_{\mathrm{case(iii)}} - \bar{t}_{\mathrm{case(ii)}}\right) = 2\pi - 1.607 + 2\pi k \tag{5.9}$$

state that the vibration velocity values are separated by k vibration cycles with k being an integer. The above equations were transformed into:

$$\omega = \frac{1.607 + 2\pi k}{\left(\bar{t}_{\text{case(iii)}} - \bar{t}_{\text{case(ii)}}\right)} \tag{5.10}$$

$$\omega = \frac{2\pi - 1.607 + 2\pi k}{\left(\bar{t}_{\text{case(iii)}} - \bar{t}_{\text{case(ii)}}\right)} \tag{5.11}$$

with the intention of computing the vibration frequency. The parameter k can generally be reckoned on the basis of experience, FE models, and previous measurements. The presence of a particular vibration frequency can be confirmed or excluded by inserting this frequency into either Equation (5.10) or (5.11). The criterion for making this decision is k being an integer or at least very close to one. The choice between the equations is left to the discretion of the vibration specialist, but it is recommended that the selection is made dependent on the sign of the time difference to avoid any misinterpretations arising from the sign of the vibration frequency. If the average time of waveform occurrence associated with the minimum average vibration velocity (here case (iii)) is larger than that associated with the maximum average vibration velocity (case (ii)), Equation (5.10) is to be selected, otherwise Equation (5.11), which is true for the present study. After several k-values had been tested, it was found that a k of -6 resulted in a vibration frequency of 175.19 Hz, which was rounded down to the actual value (175 Hz). The error of 0.1 % was negligible. A relatively straightforward approach to validating the frequency is by computing the product of the vibration period and the modulus of the k-value, which is 34.29 ms and close to the revolution period of 30 ms. The latter value is the absolute difference between the average time of waveform occurrence in case (ii) and that in case (iii). The excess of 4.29 ms can be ascribed to the superposition of the following three effects:

1. vibration was asynchronous with the rotational speed $\left(\frac{\omega}{\Omega} \notin \mathbb{Z}\right)$, and thus, the red waveform samples of both cases were indeed not exactly 30 ms apart

2. the vibration velocity in case (iii) is actually measured in the other bijective interval of the cosine ([π,2π] rad) (cf. Figure 5.7(b))

3. unavoidable round-off errors.

As regards the second point, the error in time is of the order of $\frac{1}{2\omega}$ (2.86 ms) when choosing the wrong bijective interval and, thus, was deemed peripheral to this investigation because of the small error in frequency. When the above procedure would be repeated with Equation (5.10), a positive k of 5 would be found to produce a negative vibration frequency of -175.19 Hz, which is also correct despite the minus sign.

The last step was to integrate the time-dependent version of Equation (5.5) in order to obtain the function of vibration displacement:

$$x_{\mathrm{B}}(t) = \frac{\overline{v}^{\mathrm{v}}_{\mathrm{B,case(ii)}}}{\omega} \sin \omega t \tag{5.12}$$

where the phase shift was assumed to be zero. This assumption agrees well with the conditions of real blade vibration where the blade usually starts to vibrate from its equilibrium position at which the origin of the coordinate system is located (zero position). After the vibration frequency had been converted into $\frac{\mathrm{rad}}{\mathrm{s}}$, a deflection amplitude of 0.864 mm was obtained. This represented an error of -4.53 % with respect to the actual deflection amplitude of 0.905 mm. In direct comparison with the best BTT result, an error reduction of 38.78 % was achieved.

5.4 Conclusion

BLASMA-SCP is a method for determining vibration parameters on the basis of waveform features. For this purpose, the waveform integral and slopes of the waveform edges were computed with respect to different passages of the blade along the sensor. A detailed discussion highlighted the effect of

vibration on these quantities, which was apparent even in the presence of noise in the sensor output. In summary, the faster a blade moves past the sensor, the smaller is the integral and the larger are the slopes of the waveform edges. The sensor data was further processed to obtain the amplitudes and frequency of the vibration velocity and vibration deflection. An analysis of the error was conducted, which included a comparison with the performance of traditional BTT under its ideal working conditions. It came to light that BLASMA-SCP provides a superior accuracy of more than 38 % despite requiring less sensor data. In the event of multi-harmonic blade vibration, it becomes difficult to determine the corresponding parameters utilising BLASMA-SCP. Changes in waveform features would need to be separated in terms of their causes. It is, however, rather problematic to infer the presence and nature of multiple vibration components from scalar waveform features. Therefore, other methods that can deal with multi-harmonic vibration are proposed next.

Chapter 6

BLASMA-IWE

BLASMA-IWE (Inverse Waveform Equation) is particular useful for finding high-frequency components in the response to multi-harmonic excitation. This is achieved by rearranging Equation (4.10) to the extent that the vibration term of interest is isolated on either side of the equation. With the focus being on flap-wise vibration, the inverse waveform equation takes the following form:

$$x_{\mathrm{B}}^{\mathrm{F}}(t) = R_{\mathrm{B}}^{0}\left(\varphi_{\mathrm{S}}[n_{\mathrm{R}}(t)] - \varphi_{\mathrm{B}}^{0} - \varphi_{\mathrm{B}}^{\mathrm{r}}(t) \pm \sqrt{-\frac{\ln(\frac{u(t)-\Delta(t)}{U c_{\mathrm{B}}^{0}} c_{\mathrm{B}}(t))}{\lambda}}\right). \tag{6.1}$$

The plus-minus sign requires a case analysis: the minus sign is to be chosen for the left half of the waveform up until the maximum point, whereas the plus sign is to be chosen for the other half. It is recommended that the time axis and the maximum point are used to split the waveform into two halves. The snapshot of the vibration trajectory $x_{\mathrm{B}}^{\mathrm{F}}(t)$ possesses the timewise length of the processed waveform part with the maximum length being $t \in [t_{\mathrm{e}}, t_{\mathrm{d}}]$ when no cut-off is applied. There are various methods available to compute the vibration parameters using Equation (6.1); the most famous ones are the Fourier transform and non-linear least-squares fitting techniques. The choice of method eventually depends on the number of vibration cycles, which $x_{\mathrm{B}}^{\mathrm{F}}(t)$ contains, and prior knowledge of the kind of blade vibration to be expected. If at least one complete vibration cycle exists in the snapshot, it is advised that a sequence of copies thereof is transformed into the frequency domain with the intention of increasing the frequency resolution. Already less than ten copies can keep the errors below 5 %. In case of only having a section of

a vibration cycle in $x_{\mathrm{B}}^{\mathrm{F}}(t)$, the Fourier transform becomes unsuited for finding the vibration parameters. Least-squares methods, by contrast, can still work in this scenario, yet they require the predefinition of a vibration model that can be fitted to $x_{\mathrm{B}}^{\mathrm{F}}(t)$.

6.1 Model parameterisation

Despite the utility of the capacitive sensor from the last chapter, a different type of field sensor was employed in this study to put BLASMA to the test with a new set of sensor data. For this reason, a noiseless waveform from an authentic model of an active eddy current sensor developed with commercial FE software was taken from the work of Jamia and Friswell [249] by reading waveform points from paper in order to determine the relevant sensor parameters of Equation (4.10). This waveform had been produced by simulating the passage of a non-vibrating (i.e., rigid) blade at a rotational speed of 2e3 RPM along a single sensor. To make use of this waveform within the scope of the present work, a Gaussian function was fitted to it (see Figure 6.1(a)), thereby obtaining the waveform amplitude U and the speed calibration parameter λ. The sensor output was normalised, and the speed calibration parameter was later adjusted in such a manner that the blade

Parameter	Value	Unit
Number of sensors	1	-
Angular sensor position (φ_{S}^{0})	0	rad
Nominal signal amplitude (U)	1	-
Speed calibration parameter (λ)	5.2e3	$\frac{1}{\mathrm{rad}^2}$
Signal offset without white Gaussian noise (Δ_{O})	0	-
Signal-to-noise ratio for white Gaussian noise	15	dB
Sampling frequency (f_{S})	2e6	Hz
Clearance ratio $\left(\frac{c_{\mathrm{B}}^{0}}{c_{\mathrm{B}}(t)}\right)$	1	-

Table 6.1: Parameters for the sensor model

Parameter	Value	Unit
Blade tip radius (R_{B}^{0})	0.1	m
Number of blades	4	-
Angular blade spacing	$\frac{\pi}{2}$	rad
Total blade mass	1	kg
Disk sector mass	1e3	kg
Blade stiffness coefficient set	{1.2e6,1.2e7}	$\frac{\mathrm{N}}{\mathrm{m}}$
Disk stiffness coefficient	1e8	$\frac{\mathrm{N}}{\mathrm{m}}$
Ground stiffness coefficient	1e10	$\frac{\mathrm{N}}{\mathrm{m}}$
Blade damping coefficient	20	$\frac{\mathrm{kg}}{\mathrm{s}}$
Disk damping coefficient	1e8	$\frac{\mathrm{kg}}{\mathrm{s}}$
Ground damping coefficient	1e8	$\frac{\mathrm{kg}}{\mathrm{s}}$
Resonance frequencies of interest	{7.8e3,12.4e3}	Hz
Rotational speed (Ω)	2e3	RPM
Excitation amplitude 1	3.6	N
Excitation frequency 1	7.8e3	Hz
Excitation phase angle 1	0	rad
Excitation amplitude 2	30.4	N
Excitation frequency 2	12.4e3	Hz
Excitation phase angle 2	0	rad

Table 6.2: Parameters for the bladed disk model

travelling time along the sensor was reduced by a factor of approximately 60 from the originally reported 12 ms to 0.2 ms. The latter value was a consequence of the following:

1. The objective was to evaluate the potential of BLASMA-IWE when the snapshot contained less than one vibration cycle, i.e., the snapshot was shorter than 5 ms, which was the least common period multiple of the 7.8-kHz and 12.4-kHz harmonic components investigated.

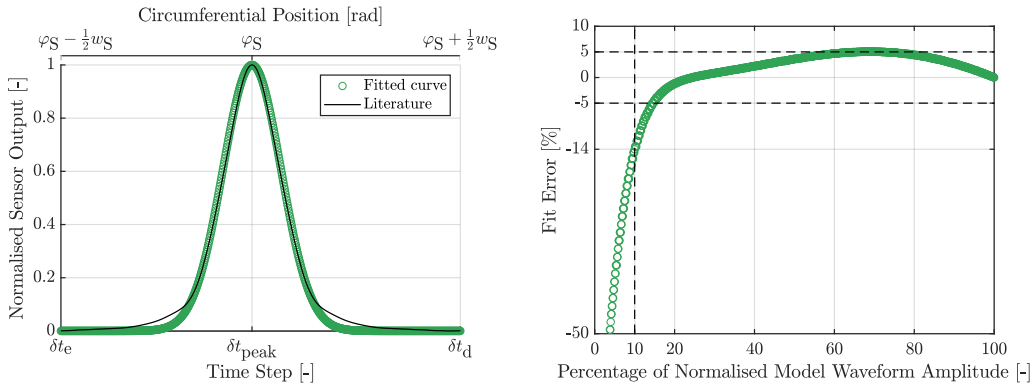
2. By considering only those parts of the waveform which were greater than or equal to 10 % of its normalised amplitude, uninformative sections of the sensor signal were excluded and random signal fluctuations, which

might falsely have suggested the presence of a blade in the sensor field, became less concerning. The cut-off value was chosen on the basis of experience; modification might have been required in the event of smaller signal-to-noise ratios.

The goodness of fit is displayed in Figure 6.1(b) where the fit error is plotted against the percentage of normalised waveform amplitude of the sensor model. The error becomes smaller, the larger the cumulative change in the sensor output is or, in other words, the closer the blade is to the sensor. At the cut-off signal strength below which sensor data is ignored, the fit error amounts to 14.4 % before finally reaching an error band of ±5 % in which it remains. Notwithstanding the imperfect fit, the sensor parameters obtained were sufficient to model realistic sensor behaviour. The large inaccuracies, which mainly occurred at lower signal levels, were associated with parts of the waveform that were not examined.

Besides the already discussed sensor parameters listed in Table 6.1, there were further ones that demanded attention. The number of sensors was kept constant to learn whether a single sensor was capable of producing enough data that allowed the application of BLASMA-IWE. The clearance between the blades and the sensor was assumed to be unaffected by rotation and vibration; thus, it remained unchanged for the duration of the simulation. A sampling frequency of 2 MHz ensured that no important detail was missed in the vibration and sensor data. The signal-to-noise ratio was reduced from the 30 dB of the BLASMA-SCP study to 15 dB with the aim of investigating the possibility of determining vibration parameters from shorter ($\sim$1 ms $\rightarrow$ $\sim$0.2 ms) and noisier snapshots.

The previously introduced rotor with four blades was spun at a rotational speed of 2e3 RPM that was adopted from [249]. In order to simulate a multi-harmonic blade response, the blade of each disk sector was modelled in accordance with Figure 4.2 as a two-degree-of-freedom oscillator, whose total mass was equally distributed. The element next to the disk sector featured a greater stiffness coefficient than the element situated farther out, whereas



(a) Replication of an eddy current sensor waveform reported in the literature

(b) Fit error

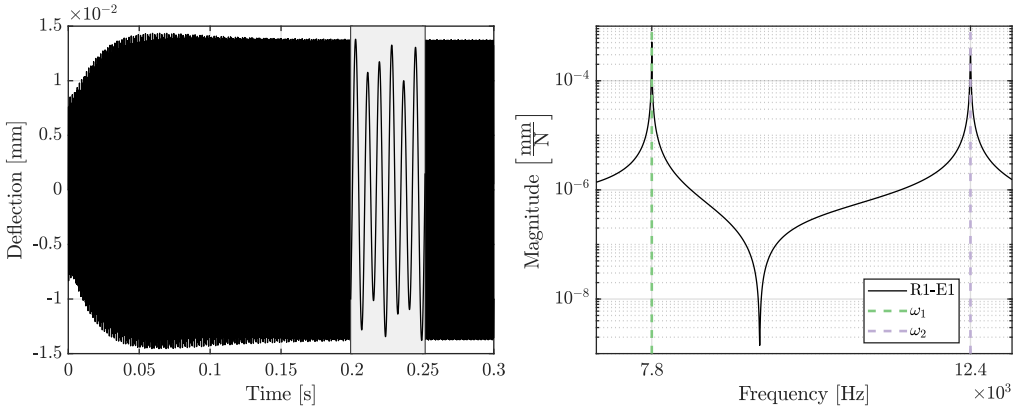
Figure 6.1: Analysis of the waveform fit

their damping function lacked any such gradient. The vibration modes to which attention is paid are shown in the FRF plot in Figure 6.2(b). The excitation parameters were chosen in such a way that a typical response of high-frequency and low-amplitude ($\mathcal{O}(\mu\text{m})$) vibration could be observed (see Figure 6.2(a)). Such oscillations can easily fall below the smallest incremental change that can be detected by the sensor (cf. sensor resolution), which needs to be taken into account for any experimental set-up. There have been reports on eddy current sensors that permit meaningful measurements in the range of several micrometers [251, 438].

In order for the bladed disk model to attain the desired resonance frequencies, a manipulation of the stiffness matrix K was required. This was done by determining the undamped eigenvector matrix Ψ_{und} and eigenvalue matrix Λ_{und} of the original system according to:

$$\Psi_{\text{und}}\Lambda_{\text{und}} = M^{-1}K\Psi_{\text{und}} \tag{6.2}$$

using the mass matrix M. Next, the eigenvalue matrix was changed to accommodate the target eigenvalues, which are the squares of the undamped natural frequencies. The undamped natural frequencies were in the ϵ-neighbourhoods of the damped natural frequencies and resonance frequencies with ϵ being



(a) Deflection trajectory of the vibrating blades at resonance – with a zoomed-in view in grey ( )

(b) FRF – Magnitude

Figure 6.2: Vibration characteristics

0.5 % thereof, thereby justifying the negligence of damping. The eigenvectors of the original system had to stay the same to keep the physical meaning of the motion valid. The new stiffness matrix $\widetilde{K}$ was then computed as follows:

$$\widetilde{K} = M\Psi_{\text{und}}\widetilde{\Lambda}_{\text{und}}\Psi_{\text{und}}^{-1} \tag{6.3}$$

where $\widetilde{\Lambda}_{\text{und}}$ contained the new eigenvalues. The other structural properties of the bladed disk remained constant and are, together with the parameters that described the system dynamics, set down in Table 6.2 for the sake of completeness.

6.2 Simulation results

The waveforms that were a result of the passages of blade 1 along the only sensor during a simulation time of 0.3 s are plotted in Figure 6.3. Next to the graph of the sensor output, there is a close-up of a waveform to display its distortion by noise; however, unequivocal evidence of the presence of vibration is missing. In contrast to the BLASMA-SCP study, no reference

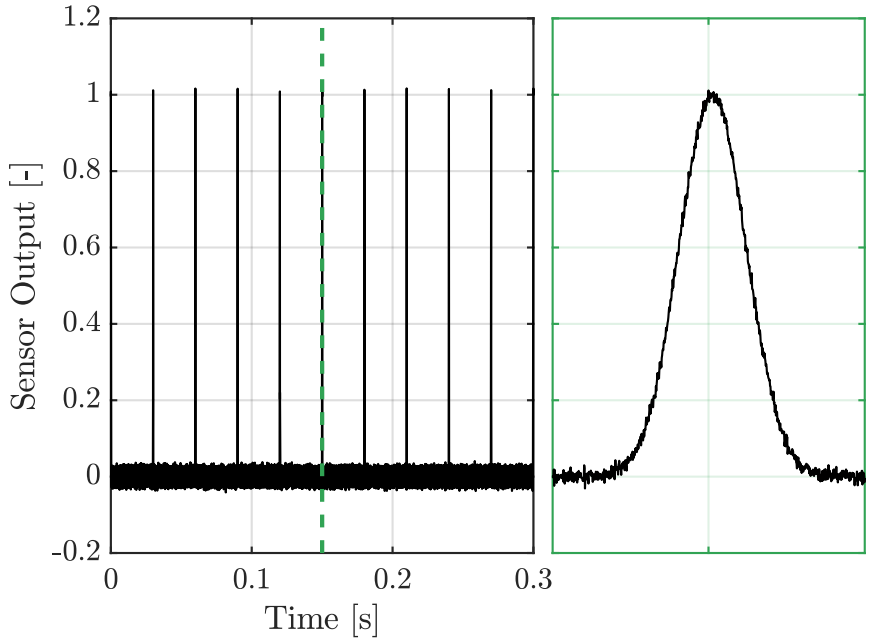
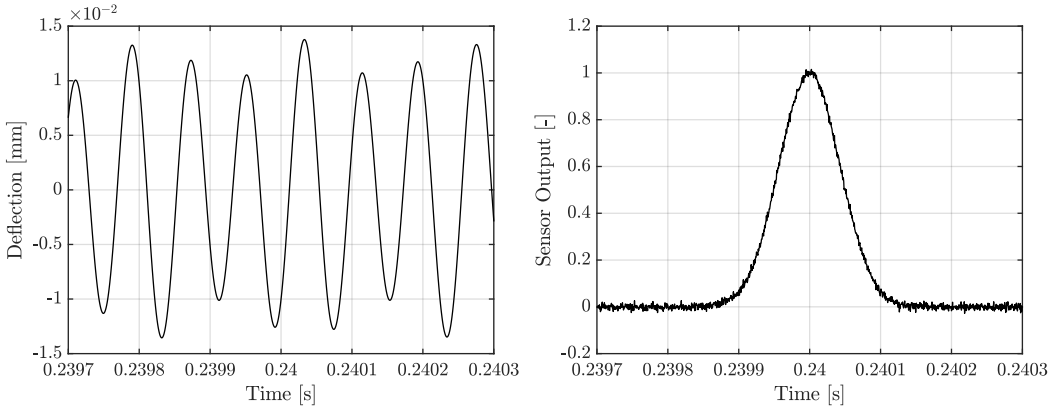


Figure 6.3: Sensor output with waveforms from passages of blade 1 on the left and a zoomed-in view of a waveform on the right

waveforms were computed in order to investigate the possibility of determining vibration parameters directly on the basis of measured waveforms, which would be beneficial to experimental studies in which meaningful reference waveforms are more difficult to obtain. It was previously discussed in detail how reference waveforms may help in visualising the effects of vibration and in reducing the amount of requisite sensor data for finding the vibration parameters by providing information that enables the vibration specialist to learn more about the blade passage beneath the sensor. Despite these advantages, reference waveforms may not always be computable, for instance, because of limited storage capacity on an aircraft. Furthermore, even small errors in the estimated positions of fictitious reference blades can lead to a wrong conclusion on the state of vibration. It is, therefore, appropriate to demand that BLASMA should still be functional in the absence of reference waveforms.



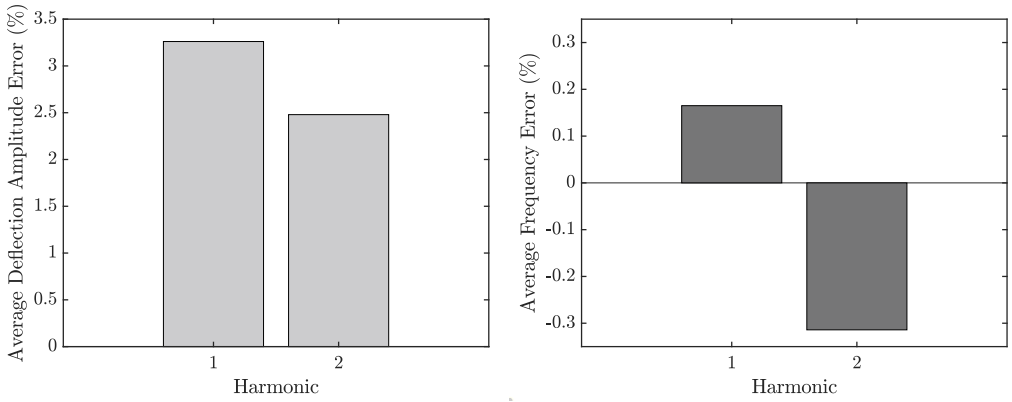
(a) Blade deflection (b) Waveform

Figure 6.4: Blade deflection (a) causes the modulation of waveform (b)

Since all blades vibrated equally, it was adequate to focus attention on blade 1. A section of its multi-harmonic vibration response in the steady-state domain is juxtaposed with the corresponding sensor output in Figure 6.4. It becomes obvious that only the response in the interval of 0.24±1e-4 s contributed to the modulation of the waveform. Although this modulation is not apparent at first glance, it can be expressed in terms of vibration parameters using BLASMA-IWE. It was discovered that a Trust-Region least-squares algorithm was fruitful in determining the vibration parameters under the given simulation conditions [439, 440]. Further particulars of the method are provided in [441, 442]. The model for the vibration response $x_{\mathrm{B}}^{\mathrm{F}}(t)$ in Equation (6.1) assumed the following form for blade 1:

$$x_{\mathrm{B1}}^{\mathrm{F}}(t) = \Delta x_{\mathrm{offset}}^{1} + X_1^1 \sin(\omega_1^1 t + \theta_1^1) + X_2^1 \sin(\omega_2^1 t + \theta_2^1) \tag{6.4}$$

which agrees with the general form of Equation (4.1). By applying the above least-squares method, errors in the average steady-state deflection amplitudes and vibration frequencies were below 3.5 % (see Figure 6.5). The averages were based on different vibration parameters each computed from one of five consecutive waveforms at steady state, which was considered to prevail from 0.15 s onwards, cf. Figure 6.2(a). The benefit of averaging commonly is that fluctuations in vibration parameters are smoothed out; these fluctuations



(a) Vibration deflection amplitudes (b) Vibration frequencies

Figure 6.5: Errors in vibration properties

depend not only on noise but also on the snapshot of the blade vibration trajectory and, thus, implicitly on the time of blade entry into the sensor field t_e and the time of blade departure from the sensor field t_d. The more of a period of a harmonic is contained within a waveform, the smaller the corresponding errors become. Interestingly, the errors in the frequencies are smaller by one order of magnitude than those in the amplitudes. In the light of the amplitudes being significantly less in value than the frequencies (i.e., $\{\omega\} \gg \{X\}$), this was deemed to be mainly caused by the fact that the sensitivity of percentage errors to changes in the associated parameter values is greater when the parameter values are small. It is also reasonable to point out that the absolute percentage errors are not uniformly distributed amongst the harmonics and parameter types, or in other words, the error in amplitude of harmonic 1 is larger than that of harmonic 2, whereas the opposite can be said in respect of the frequencies. The actual values (AV) of the vibration parameters listed in Table 6.3 were the reference for computing the percentage errors.

The least-squares method, which was applied to Equation (6.1) using the vibration model of Equation (6.4), sought the parameters that best fitted the waveform data. To achieve this, it used different parameter combinations to compute trial solutions and evaluated them on the basis of fit errors of which

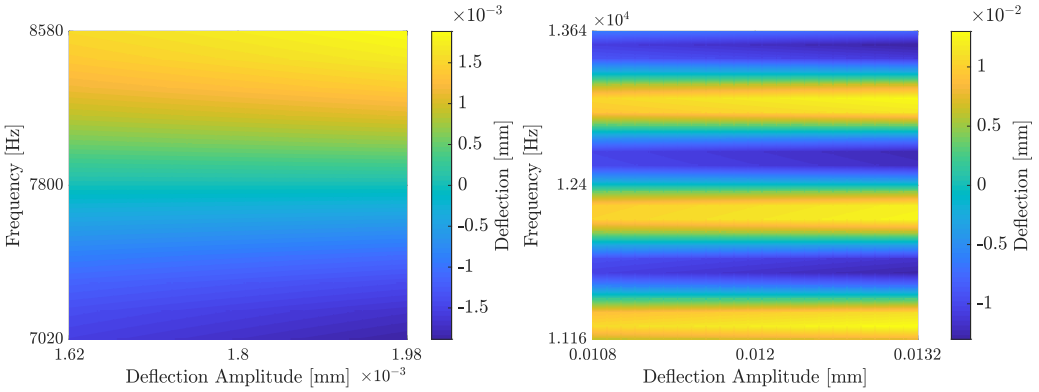
Variable	AV	Unit	$\epsilon_{\%}$	ϵ
Offset $\Delta x^1_{\text{offset}}$	0	mm	0 %	0
Amplitude (X^1_1)	1.8e-3	mm	30 %	5.4e-4
Frequency (ω^1_1)	7.8e3	Hz	50 %	3.9e3
Phase (θ^1_1)	n/a	rad	n/a	n/a
Amplitude (X^1_2)	1.2e-2	mm	30 %	3.6e-3
Frequency (ω^1_2)	12.4e3	Hz	50 %	6.2e3
Phase (θ^1_2)	n/a	rad	n/a	n/a

Table 6.3: Parameters for the least-squares fitting

the final solution offered the smallest one (refer to Figure 6.5). Theoretically, there is an infinite number of these parameter combinations, but only a few may actually be physically meaningful and compatible with the vibration model. It can therefore be helpful to have a notion of the order of magnitude of the expected solution terms to ensure the supposed vibration model is suitable for the parameter space.

Finding the vibration parameters was in the present case a multi-dimensional problem with seven unknowns at any time of the simulation in the steady-state domain. To exploit only a minimum of computer resources, historical measurement and simulation data can be taken into account for reducing the complexity of the parameter space. This was done by restricting the least-squares method to a predefined subset of the parameter space whilst identifying the solution. For each vibration parameter, this limitation was specified by an ϵ-neighbourhood with ϵ being the product of the percentage $\epsilon_{\%}$ multiplied by the corresponding actual parameter value (see Table 6.3). The latter quantity was the centre point of such a neighbourhood and, hence, determined its location and the values that were available to the least-squares method.

Even though the actual parameter values were known as a consequence of conducting a controlled simulation, the challenge of procuring them again correctly through least-squares fitting was nonetheless demanding for two reasons. First, the stated ϵ-neighbourhoods were still relatively large consider-



(a) First harmonic (b) Second harmonic

Figure 6.6: Fractions of the vibration hypersurface

ing that adjacent discrete values were permitted to differ by as little as 1e-8, which gave rise to manifold parameter combinations. Second, noise existed in the waveform data obscuring important information about the blade passage beneath the sensor.

The options of drawing the hypersurface (i.e., the function of vibration) were limited because more than three basis vectors spanned the parameter space in which it was embedded. To learn of the intricacies of such a parameter space, fractions thereof are shown in Figure 6.6 where the first and second harmonics are regarded separately for constant phases of 0 rad at a simulation time of 0.24 s. The axes of frequencies and deflection amplitudes are each limited to intervals of $[0.9, 1.1]$ that are multiplied by the corresponding actual parameter values from Table 6.3 and have a cardinality of less than 30 to reduce the raggedness of the surface for the sake of clarity. Blue patches (■) represent negative deflection, whilst positive deflection is typified by yellow areas (■) of the plot. Expectedly, deflection changes less strongly when the frequency is kept constant and the deflection amplitude is allowed to attain new values, whereas, when a particular deflection amplitude is retained and one sweeps along the frequency axis, deflection varies substantially. Different combinations of frequencies and deflection amplitudes often lead to unique total deflections. There is, however, the possibility of distinct parameter combinations resulting in similar total deflections that satisfactorily

approximate the solution. The responsibility then rests with the vibration expert to eliminate those candidates that are irrelevant to the vibration problem.

The actual phases of both harmonics were deemed unknowns for four reasons:

1. The transient might have had negligible influence on the total amplitudes as from 0.15 s, yet its imperceptible presence unavoidably caused an overlap with the pure steady-state response, which made it difficult to correctly split the total phases of both harmonics into their components without further pertinent information.

2. Generally, phases are only meaningful when a point of reference to which they refer is stated. The arbitrary nature of this point forbids speaking of a unique set of phases, especially when the system under investigation has many coupled degrees of freedom.

3. Although there are theoretical frameworks for analytically and numerically computing phases of multi-degree-of-freedom systems (e.g., in [104]), the respective equations are of little help with regard to more complicated, real vibration problems because several of their coefficients are in many instances unknown, such as the exact initial conditions and damping ratios.

4. The estimated phase values can considerably be spoilt by even the slightest unpreventable numerical noise.

Phases are therefore often neglected in real measurements unless resonance frequencies are too closely spaced and mode shapes cannot be classified without recourse to inter-blade phase differences. To circumvent the described difficulties in directly computing the phases, it was decided to evaluate the phases qualitatively by benchmarking signal sections, which are shown in Figure 6.7. The signal with the parameters obtained by BLASMA-IWE (dash-dotted green (-·-·-)) is juxtaposed with the actual solution (solid black (—))

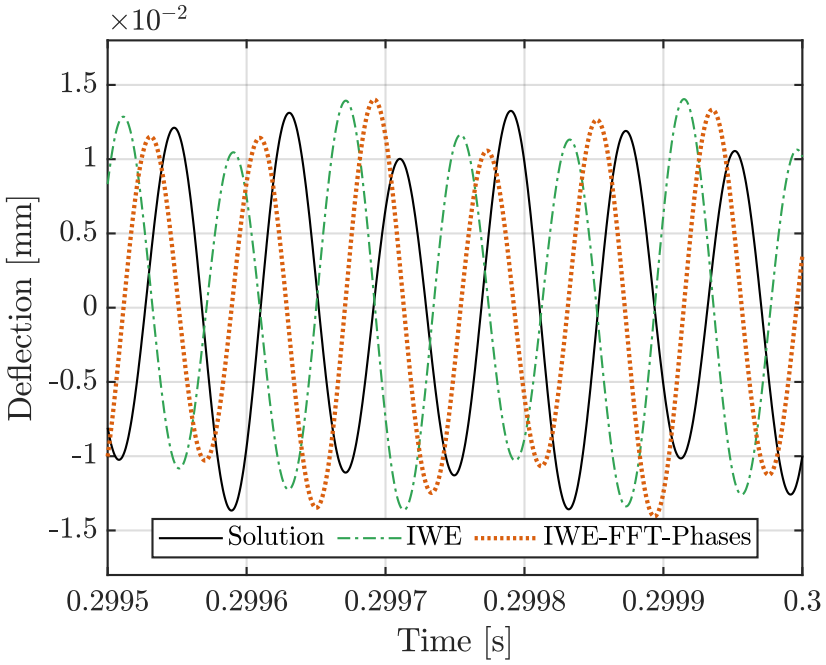


Figure 6.7: Comparison of the actual vibration deflection signal with the signal computed using the vibration parameters found by applying BLASMA-IWE and with the signal computed using the BLASMA-IWE amplitudes, BLASMA-IWE frequencies, and FFT phases (IWE-FFT-Phases)

and another signal that was calculated using the BLASMA-IWE amplitudes and frequencies but with phases from an FFT of the steady-state vibration signal (dashed orange (---)). The BLASMA-IWE phases were averaged on the basis of distinct phase values over the same number of revolutions as the errors in amplitudes and frequencies, whereas the FFT phases rested upon the entire steady-state signal. Unsurprisingly, the first and the last satisfactorily approximate the solution in amplitudes and frequencies; however, their phases do not match the ones of the solution. It seems that the BLASMA-IWE phases better tally with those of the IWE-FFT-Phases signal. Moreover, the phases provided by both methods were found to be fairly sensitive to the initial position in the cycle of the signal part to be processed. Definitive judgements about the phases should consequently be formed with care.

6.3 Conclusion

BLASMA-IWE is a method for obtaining snapshots of the vibration trajectory hidden in waveforms by utilising the inverse waveform equation without having to rely on reference waveforms. Least-squares methods proved to be suitable for ascertaining the vibration parameters on the basis of these snapshots. To demonstrate the capabilities of BLASMA-IWE, a bladed disk vibrating synchronously with the rotor speed at two high frequencies was simulated. The aim was to have the blades vibrating with low amplitudes in order to perceive whether such small vibration can be extracted from noisy waveforms that are replicas of the ones from an FE eddy current sensor model. The errors in amplitudes and frequencies were below the acceptable industry standard of ± 5 %. In the course of a qualitative comparison between parts of different vibration signals, it was underscored that it can be tricky to gauge phases when transient and steady-state vibration responses concur, which is rather the norm than an exception in real engines. One discovery of this study was that the phase errors belonging to BLASMA-IWE and an FFT were similar with respect to the solution.

There are some caveats that concern the application of BLASMA-IWE and unlock potential for future improvement. The most obvious is that the method depends on the availability of the inverse waveform equation, which may either not be computable or be concealed by the sensor manufacturer. It may be possible in the latter case to determine the sensor model through accurate measurements and modelling. At the beginning of this chapter, it was explained that the width of a waveform and, hence, the snapshot length were significantly reduced to find out if vibration parameters can still be specified under such conditions. When smaller frequencies with greater vibration periods occur, this creates a problem because the snapshot contains less useful vibration data. It is indubitably clear that a certain amount thereof is necessary to quantify the vibration parameters, otherwise the vibration parameters would converge to their BTT equivalents. Estimates can be made more accurate by processing waveforms from consecutive revolutions

collectively. Unfortunately, BLASMA-IWE can only deal with waveforms one after another, and thus, a set of amplitudes, frequencies, and phases is always linked to a single waveform. To tackle these issues, a different approach is presented in the following chapter.

Chapter 7

BLASMA-OPT

BLASMA-OPT (Optimisation) employs a gradient-based, heuristic scatter search solver algorithm for mixed-integer non-linear programming problems [443–445] in order to find the total signal offset Δx_{offset} and the parameters of harmonic k, which are amplitude X_k, frequency ω_k, and phase θ_k. The global optimisation problem for finding flap-wise vibration parameters is defined as follows:

$$\min_{\Delta x_{\text{offset}}, X_k, \omega_k, \theta_k} \sum_{i=1}^{N_{\text{W}}} \left\| \boldsymbol{u}_{\text{m},i} - \boldsymbol{u}_i \right\|_2 \tag{7.1}$$

where N_{W} is the number of processed waveforms chosen at the discretion of the vibration expert, $\boldsymbol{u}_{\text{m},i}$ is the vector containing the points of the i-th measured waveform, and $\boldsymbol{u}_i$ is the vector containing the points of the i-th modelled waveform as per Equation (4.10). Optimisation is performed for each waveform individually if N_{W} equals one. Alternatively, waveforms of multiple revolutions and/or sensors define the optimisation problem, which can improve accuracy. The objective function is non-linear, smooth and clearly multi-dimensional with four parameters in the simplest case of single-harmonic vibration. From a purely mathematical perspective, one can imagine the objective function to be a hypersurface with numerous local extrema. One of these extrema is the global minimum or optimum, whose coordinates are the sought parameters of blade vibration that caused waveform modulation. The significance of the optimum is generally not to be assessed without taking all defined constraints into consideration; together they determine the feasibility of the solution because different constraints may lead to a totally different optimum. Within the scope of this work, the optimum parameters are always interpreted as the parameters that best describe the vibration problem.

The computation time can be reduced by imposing constraints on the optimisation variables to support the optimiser in finding the global minimum and to limit the interval of attainable values to the range of interest. Such constraints would force a variable to lie within a section of the parameter space. If available, reference data from FE models or previously acquired measurement data can help to define constraints and wisely choose starting points for the optimisation. For instance, the standard TOA data, which can still be computed from already recorded waveforms, may be used for hazarding an educated guess at the blade deflection amplitude of which the time difference is an indirect indicator. A set of starting points specifies the initial value of each optimisation variable from where the optimiser begins its search for the global minimum. It may even be useful to make the optimiser run from multiple sets of starting points in order to reach more areas of the parameter space. Nevertheless, the final solution has always to be checked for its appropriateness to the present operating conditions.

On the condition that useful and complete waveforms have been recorded and the optimisation routine has correctly been parameterised, the optimiser or solver is supposed to return the global optimum after exploring the parameter space. When vibration parameters are computed for all blades, the phases belonging to blade harmonic k can be used to calculate the matching nodal diameter pattern of the bladed disk. The frequency of a harmonic can also indicate the nodal diameter mode, provided that the frequencies of nodal diameter modes of a particular mode family are sufficiently separated.

It was found that gradient-based solvers are suitable for finding the global optimum if the waveform function is differentiable; however, the choice of solver depends ultimately on the constraints of the optimisation problem. Another important point is the choice of the proper tolerance for the optimality criterion, the step size, and the constraints. The tolerance is the minimum finite difference between two adjacent real numbers below which two such numbers are considered equal. Hence, the tolerance defines one of

the stopping criteria for the optimiser. It cannot be chosen too small as the solver would otherwise fail to find the optimum. Conversely, choosing a large tolerance may culminate in having unacceptable inaccuracies.

7.1 Model parameterisation

To evaluate the capabilities of BLASMA-OPT for investigating the vibration of each blade separately, a modified version of an intermediate-pressure compressor with the following four vibration scenarios was simulated:

(i) **asynchronous** *single*-harmonic excitation at the 285 Hz resonance (ω_1) with an amplitude of 39 N at a rotational speed of 6e3 RPM, including a comparison with traditional BTT

(ii) **synchronous** *single*-harmonic excitation at the 285 Hz resonance (ω_1) with an amplitude of 39 N at a rotational speed of 5.7e3 RPM, including an error assessment of method

(iii) **asynchronous** *multi*-harmonic excitation at the 285 Hz and 960 Hz resonances (ω_1 and ω_3) with amplitudes of 39 N and 19 N, respectively, at a rotational speed of 6e3 RPM, including a phase analysis

(iv) **synchronous** *multi*-harmonic excitation at the 285 Hz and 855 Hz resonances (ω_1 and ω_2) with amplitudes of 39 N and 34 N, respectively, at a rotational speed of 5.7e3 RPM.

Table 7.1 contains the parameters for the bladed disk model, which consisted of four tuned blades equally distributed around the disk. A blade was modelled as a three-degree-of-freedom system attached to a single-degree-of-freedom disk sector, cf. Figure 4.2. The vibratory motion of a bladed disk sector occurred in the plane of rotation. The total mass of a sector blade was evenly split between its three mass elements. The damping distribution was

Parameter	Value	Unit
Blade tip radius (R_{B}^{0})	1	m
Number of blades	4	-
Angular blade spacing	$\frac{\pi}{2}$	rad
Total blade mass	1	kg
Disk sector mass	1e3	kg
Blade stiffness coefficient set	{1.2e6,1.2e7,1.2e8}	$\frac{\mathrm{N}}{\mathrm{m}}$
Disk stiffness coefficient	1e8	$\frac{\mathrm{N}}{\mathrm{m}}$
Ground stiffness coefficient	1e10	$\frac{\mathrm{N}}{\mathrm{m}}$
Blade damping coefficient	20	$\frac{\mathrm{kg}}{\mathrm{s}}$
Disk damping coefficient	1e8	$\frac{\mathrm{kg}}{\mathrm{s}}$
Ground damping coefficient	1e8	$\frac{\mathrm{kg}}{\mathrm{s}}$
Resonance frequencies of interest	{285,855,960}	Hz
Rotational speed (Ω) set	{5.7e3,6e3}	RPM
Excitation amplitude 1	39	N
Excitation frequency 1	285	Hz
Excitation phase angle set 1	{0,π,2π,3π}	rad
Excitation amplitude 2	34	N
Excitation frequency 2	855	Hz
Excitation phase angle 2	0	rad
Excitation amplitude 3	19	N
Excitation frequency 3	960	Hz
Excitation phase angle 3	0	rad

Table 7.1: Parameters for the bladed disk model

assumed to be constant across a blade, whereas blade compliance increased with distance to the disk sector. The resonance frequencies of the bladed disk were modified by following the procedure of Section 6.1 to accommodate the aforesaid agenda.

The three relevant resonances of the bladed disk are shown with the FRF in Figure 7.1, which was computed with the point of excitation being on the blade mass element that was farthest away from the disk sector and was considered the tip of the blade. The response was measured at the same location on the corresponding blade. The presence of cyclic symmetry allowed the FRF to be the same for every bladed disk sector.

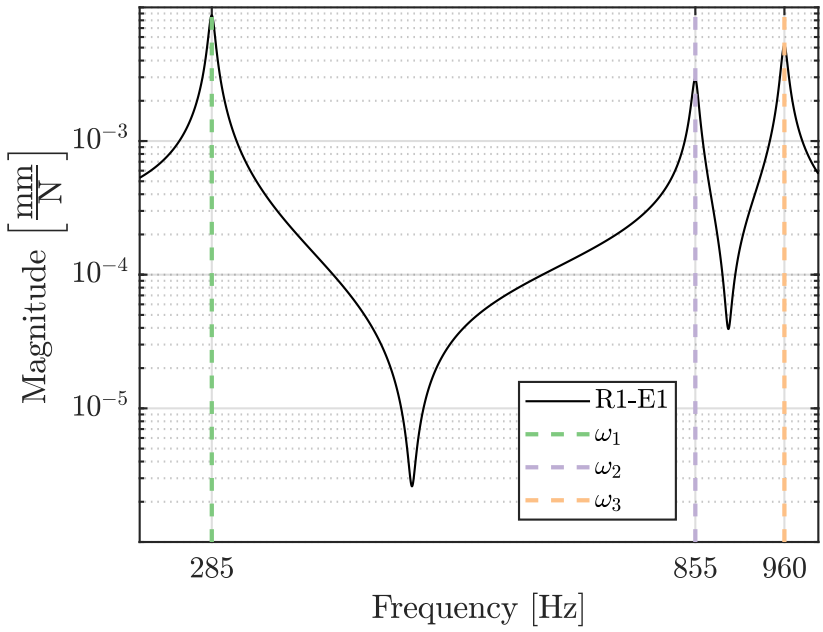


Figure 7.1: FRF – Magnitude

The force phase angles were 0 rad and excitation was applied to all blades uniformly in all scenarios, except for the error study in scenario (ii) where response phase angles from excitation with a 2-nodal-diameter travelling-wave pattern were analysed. The phase angle set in Table 7.1 shows the possible values that were used. At a rotational speed of 6e3 RPM, vibration at each of the three resonance frequencies (285 Hz, 855 Hz, 960 Hz) was asynchronous with engine-order numbers of 2.85, 8.55, and 9.6, respectively. On the other hand, the first two frequencies (285 Hz, 855 Hz) were assigned the integer engine-order numbers of 3 and 9, respectively, when the rotational speed was at 5.7e3 RPM, making vibration synchronous. Under real engine conditions, naturally occurring fluctuations in the rotational speed would hamper the observation of perfectly synchronous vibration, which leads to a superposition of asynchronous and synchronous effects.

The sampling frequency for acquiring traditional TOA data, which is ordinarily transformed into vibration parameters, would be just 100 Hz per blade and

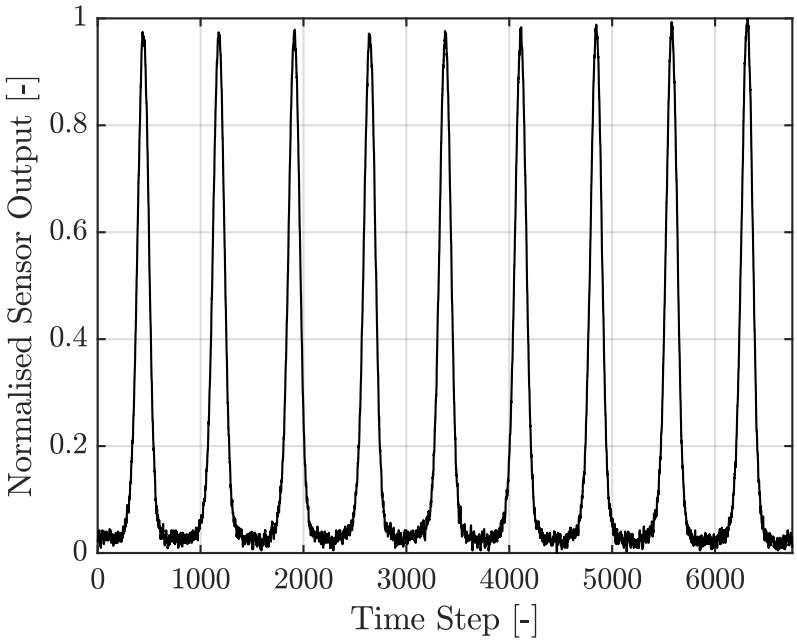


Figure 7.2: Experimental waveforms from a BTT and clearance measurement system applied to Rolls-Royce Rig750 at TU Darmstadt in Germany

sensor at 6e3 RPM. If then any of the vibration frequencies were not below 50 Hz, the measured vibration signal would not be alias-free according to the Nyquist-Shannon theorem and peaks in the spectrum might not easily be resolved. This would become worse if the sampling were additionally conducted non-uniformly. Under real engine conditions, experience shows that the sampling frequency should definitely be greater than twice the largest vibration frequency. In the absence of any reference data, at least six sensors would be required so as to reconstruct a single-harmonic blade vibration signal at 285 Hz in the ideal world, and twenty sensors in the corresponding case of 960 Hz.

In contrast to traditional BTT applications, only a single sensor was employed with BLASMA-OPT to determine asynchronous and synchronous resonance vibrations. The model of this sensor was created from experimentally measured waveforms that served to parameterise Equation (4.10). A few of them

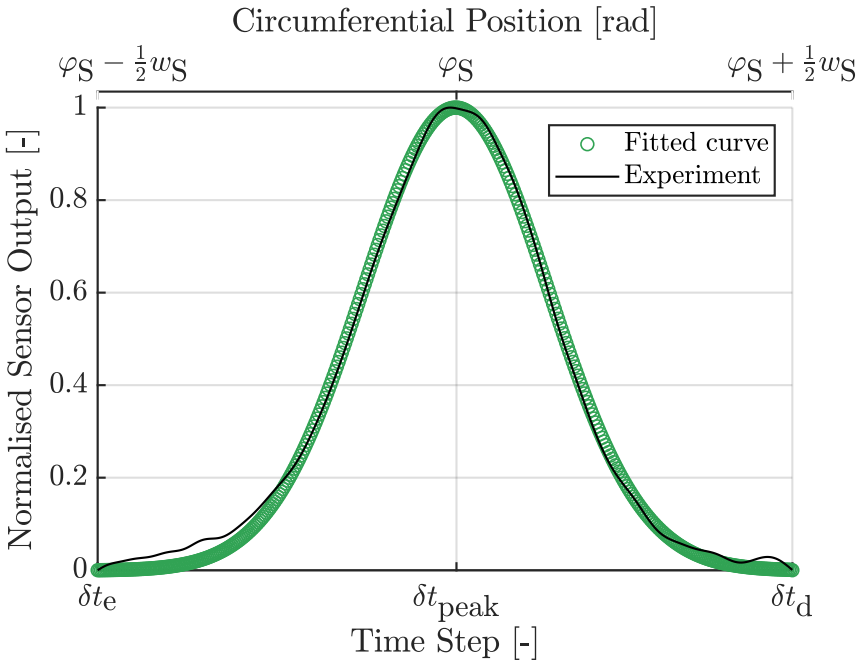


Figure 7.3: Replication of an experimentally measured waveform

were normalised using the largest measured waveform amplitude and were selected for display in Figure 7.2. These waveforms were generated at a non-critical rotational speed of 19220 RPM by a real capacitive sensor during an engine test that was conducted on Rolls-Royce Rig750 (transonic compressor) at TU Darmstadt in Germany, whose specifications and performance have already been published, such as in [69, 102].

To improve the estimation of the waveform parameters, unwanted noise from the experiments in the output of the capacitive sensor was weakened by digital low-pass filtering with 60 dB stop-band attenuation and a cut-off frequency of 1 kHz. Depicted in Figure 7.3, a single waveform was isolated from the sensor output and normalised to one. A non-linear least-squares fitting technique was then applied to this waveform to determine the waveform parameters U, λ, and Δ_O. Because the speed-sensitive calibration parameter λ was obtained from a waveform that was produced under conditions different to the present ones, λ required an adjustment for every rotational speed of interest; any

other impact on λ was neglected. The appropriate waveform model connected with Equation (4.10) at time step δt assumed the following form:

$$u(\delta t) = U \exp\left(-\lambda_{\mathrm{e}}\left(2\pi\Omega\frac{\delta t - \delta t_{\mathrm{C}}}{f_{\mathrm{S}}}\right)^2\right) + \Delta_{\mathrm{O}} \tag{7.2}$$

where f_{S} is the sampling frequency and δt_{C} is the time step at which the waveform reaches its maximum. The vibration terms in this equation were omitted since the real blades had not been at resonance during the recording of the foregoing waveform; thus, any waveform modulation due to blade vibration had been trifling. The mean model parameters (U, $\lambda(\Omega$=5.7e3 RPM), $\lambda(\Omega$=6e3 RPM), and Δ_{O}) of a 95 % confidence interval are listed in Table 7.2, complemented by the angular sensor position, the signal-to-noise ratio for producing white Gaussian noise in the virtual sensor output, the sensor sampling frequency, and the clearance ratio. The speed calibration parameter $\lambda(\Omega)$ that is relevant to the current studies was reckoned at:

$$\lambda(\Omega) = \lambda_{\mathrm{e}}(2\pi\Omega)^2 \tag{7.3}$$

with λ_{e} being the experimental speed calibration parameter.

The angular position of a sensor lies somewhere in the interval of $[0, 2\pi)$ rad and implicitly determines which part of the blade trajectory is detectable in the moment of the blade passing the sensor. BTT requires choosing the sensor position wisely by reflecting upon the vibration frequencies to be expected, which is especially recommended in the case of synchronous vibration where the blade arrives at the sensor always with the same deflection. At worst, the deflection signal has a zero-crossing at this point, which would give the false impression that there is no or very small vibration. BLASMA-OPT, by contrast, was designed with the aim of it being a universal method without the necessity to turn much thought to the sensor position prior to the measurements. The sensor position of 0 rad was hence chosen arbitrarily; any other position would have worked as well.

Parameter	Value	Unit
Number of sensors	1	-
Angular sensor position (φ_{S}^{0})	0	rad
Nominal signal amplitude (U)	1	-
Average speed calibration parameter ($\lambda(\Omega$=5.7e3 RPM))	3.8e3	$\frac{1}{\mathrm{rad}^2}$
Average speed calibration parameter ($\lambda(\Omega$=6e3 RPM))	4.0e3	$\frac{1}{\mathrm{rad}^2}$
Signal offset without white Gaussian noise (Δ_{O})	0	-
Signal-to-noise ratio for white Gaussian noise	30	dB
Sampling frequency (f_{S})	5e6	Hz
Clearance ratio $\left(\frac{c_{\mathrm{B}}^{0}}{c_{\mathrm{B}}(t)}\right)$	1	-

Table 7.2: Parameters for the sensor model

White Gaussian noise was added to the modelled sensor function of Equation (7.2) to simulate the noise contained in the real output of the capacitive sensor. The signal-to-noise ratio is a critical parameter that affects the performance of optimisation. With blade vibration occasionally at a fraction of a millimetre and with a very short blade travelling time along the sensor, noise hampers distinguishing between waveform distortions made by noise and by vibration. To avoid unrealistic solutions, it may be helpful to set boundaries for the variables on which the optimisation is performed.

The sensor sampling frequency for simulating waveforms attained 5 MHz, which was exactly the same sampling frequency that had been used for the experimental data acquisition. This relatively high sampling frequency enabled the computation of waveforms at the stated rotational speeds with great accuracy and detail. Each waveform sample corresponds to a point on the blade trajectory. Clearly, the denser the waveform points, the more information about the blade vibration trajectory can be inferred. This becomes particularly significant in the case of multi-harmonic vibration where superposed oscillation components are to be resolved.

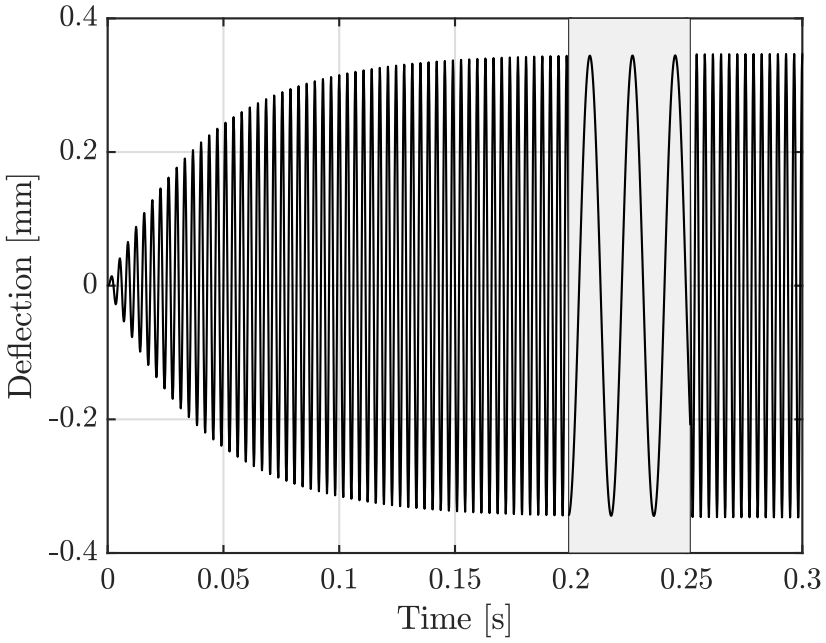


Figure 7.4: Deflection trajectory of the vibrating blades at resonance in the case of **asynchronous** and **synchronous** single-harmonic excitation – with a zoomed-in view in grey ( )

7.2 Simulation results

The first two studies to be conducted were concerned with the validation of BLASMA-OPT when the blades were excited in a single-harmonic fashion. This was followed by two similar studies in which the blades showed multi-harmonic vibration. The simulation time was chosen to be 0.3 s for the given configuration in all scenarios in order to enable the system to stabilise after being excited at resonance. The idea was to use BLASMA-OPT to identify the resonance properties of the blades, where the maximum vibration deflection amplitude and vibration frequency were of utmost importance. Having these two parameters would allow the computation of stresses and remaining blade life estimates during operation.

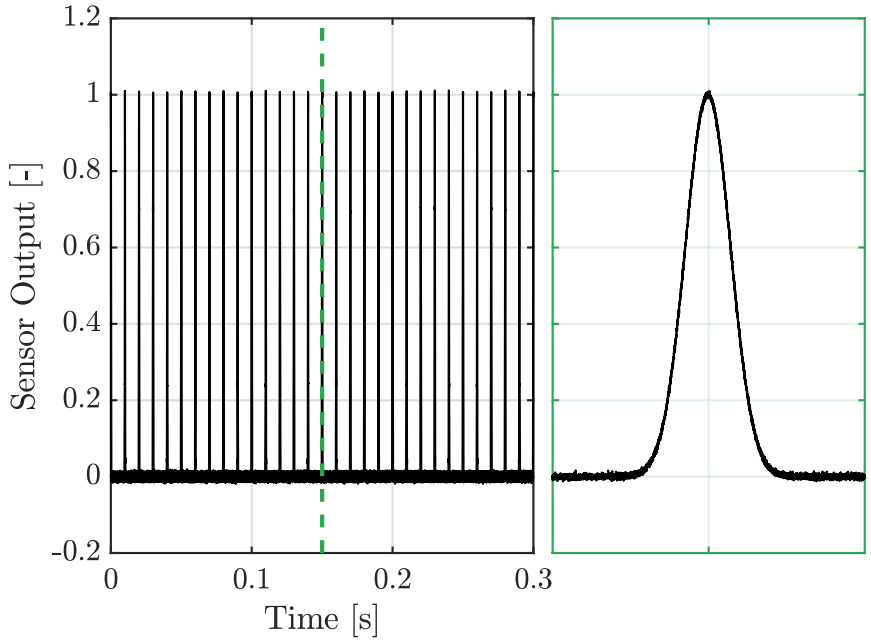
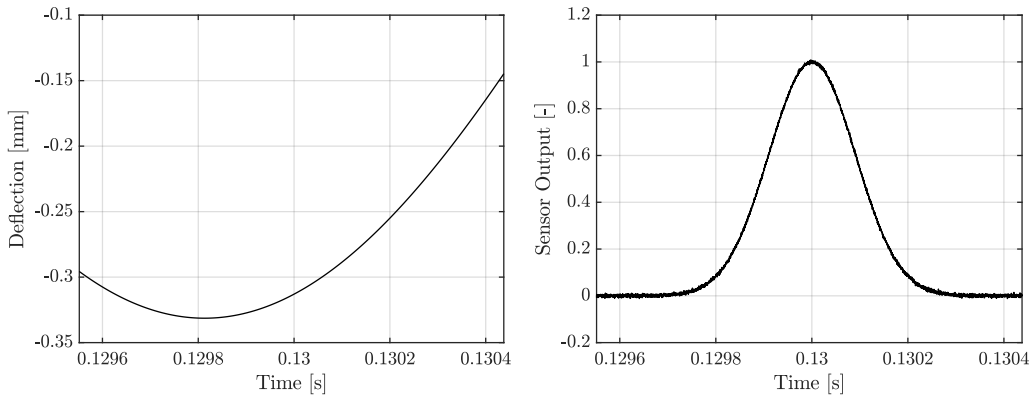


Figure 7.5: Sensor output with waveforms from passages of blade 1 on the left and a zoomed-in view of a waveform on the right

7.2.1 Asynchronous single-harmonic excitation of the blades

All blades were uniformly excited by a single-harmonic force at resonance. The resulting response, depicted in Figure 7.4, was thus the same for every blade. At resonance, the vibration deflection and vibration velocity experienced a sharp increase in amplitude over a very short time. Damping caused the system to stabilise and reach steady state. Whilst undergoing resonance vibration, the bladed disk rotated, and the blades continued to pass the sensor in successive revolutions. The waveforms that were recorded from the passages of blade 1 are presented in Figure 7.5, where the previously normalised but now noise-distorted sensor output is plotted against time. The sensor output does not reveal any sign of blade vibration.



(a) Blade deflection

(b) Waveform

Figure 7.6: Blade deflection (a) causes the modulation of waveform (b)

7.2.1.1 Determination of the processable part of a waveform

During the passage along the sensor, the blade continued to move in its vibration cycle. Figure 7.6(a) shows a snapshot of the vibration signal of the blade. It is the part of the vibration cycle which caused hidden modulation of the waveform created by the passage event (see Figure 7.6(b)). With traditional BTT, only a single data point is used per waveform, whereas with BLASMA-OPT, the whole waveform is taken into account. Every point of the waveform corresponds to a point of the total blade trajectory. To distinguish the usable part of the waveform from background noise and to ensure only true blade passage events are considered, a threshold was set to detect when the waveform reached a certain level of signal strength, which clearly depends on the signal-to-noise ratio. To meet these two requirements in the given scenario, a threshold of 10 % of the (anticipated) maximum signal strength of a waveform was chosen.

The waveform part above 10 % of signal strength was then further processed to compute the vibration properties. Filters may be applied to reduce the magnitude of noise, but it has to be borne in mind that every filter inevitably introduces additional distortions. This not necessarily helps the optimiser

in finding the vibration parameters. For this reason, no filters were applied at this stage so that the optimiser worked on measured noisy waveforms directly. When dealing with large data sets, this can tangibly reduce the amount of CPU time spent processing waveforms. Considering the frequency spectrum of impulse-like functions, one may also ponder using filter banks to sweep along the frequency axis in narrow pass-bands in order to detect the frequency of vibration. Although this seems to be a relatively straightforward approach, the frequency of vibration cannot be found in this way. Blade vibration modulates waveforms, which does not lead to a superposition of respective frequency spectra that could be filtered out otherwise.

7.2.1.2 Alternatives in the event of poor results

The length of a snapshot of the blade vibration trajectory clearly influences the accuracy of the results. When more usable data points are available, it becomes more likely that the optimiser finds the solution to the vibration problem, especially with present noise. In theory, the optimiser needs only a single waveform to find the correct vibration parameters, but it may need more waveforms when very short snapshots are present, such as when large ratios of rotational speed to vibration frequency occur. Noise-polluted data often demands using multiple waveforms, too, because noise corrupts the sensor output data, making it difficult for the optimiser to find the current state of vibration with just a single waveform. A convergence study was conducted to identify the minimum number of waveforms to reach an error bound of 2 % around a vibration parameter. The minimum number of waveforms is a valuable piece of information, which helps to select only the necessary number of waveforms. This again saves computation time and makes vibration data more quickly available during operation.

The vibration parameters of interest are the maximum amplitude at steady state, the resonance frequency, and phase. If the vibration parameters found by the optimiser with only a single waveform are considered invalid or inaccurate, there are generally two options to proceed:

- One option would be to continue with a single waveform by changing any of the defined constraints and making the first results the starting points for a new search in the same waveform data. This is only helpful when the value of the objective function computed using the parameters from the first search is still larger than the value of the objective function based on the actual vibration parameters. Obviously, the actual parameter values are usually not available, but reference vibration data can be used to compute a reference value of the objective function, which approximates the true objective function value. The correctness of the results needs to be validated against reference data from measurements or FE models. This is to prove if a further optimisation iteration with a single waveform can lead to an improvement in accuracy at all or if further waveforms are to be considered.

- The second option and the one chosen for this study is to directly increase the number of waveforms submitted to the optimiser. To have a consistent set of waveforms where there is no unexpected jump in the vibration trajectory from snapshot to snapshot, waveforms from consecutive revolutions of the same blade are processed. In any case, snapshots of the vibration trajectory cannot simply be juxtaposed to create a full picture of the vibration trajectory. The reason is that time passes between consecutive snapshots, i.e., blade-sensor passages during which the blade progresses in its vibration cycle.

7.2.1.3 Parameterisation of the optimiser

The lower boundaries (LB), upper boundaries (UB), and starting points (SP), which were chosen for the optimisation, can be found in Table 7.3. Besides boundary constraints, no extra constraints were imposed on the variables to keep the optimisation as global as possible. The actual values (AV) of each optimisation variable, which were obtained with an FFT of the deflection signal, are listed, too. With regard to the phase of the deflection signal, the

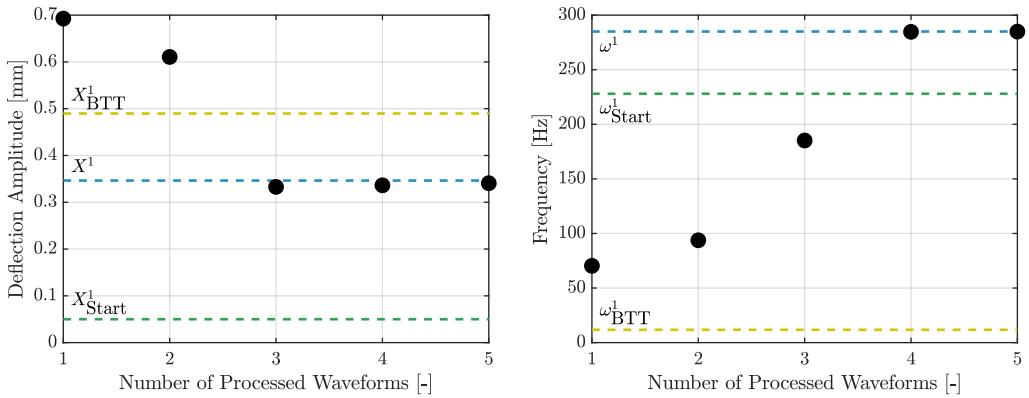
Variable	AV	LB	UB	SP	Unit
Amplitude (X^1)	3.4e-1	5e-2	10	5e-2	mm
Frequency (ω^1)	285	70	2e3	228	Hz
Phase (θ^1)	-$\frac{\pi}{2}$	-π	π	0	rad

Table 7.3: Parameters for the optimisation problem in the case of **asynchronous** and **synchronous** single-harmonic vibration

force signal had in the present case a phase of 0 rad, which meant that the deflection signal had to have a phase of -$\frac{\pi}{2}$ rad at resonance at steady state. The phase was included in the optimisation as a variable to find the exact amplitude and frequency, and to have the possibility to compute inter-blade phase shifts, which are useful for modal analysis to determine mode shapes and nodal diameters.

The boundaries of the vibration parameters should be physically meaningful and compatible with the operating conditions, the performance of the measurement equipment, and the range of interest. The lower boundary of the amplitude was chosen on the basis of the resolution of a physical sensor at the given rotational speed, whereas the upper limit was the maximum value in the safety range above which serious blade damage would be imminent in practice. The frequency limits needed to accommodate the resonance frequencies of interest, and the phase was allowed to assume values in an interval width of 2π rad.

The choice of a starting point for a variable can affect the outcome of the optimisation. The closer a starting point is to the corresponding minimum value of a vibration parameter, the less iteration steps are needed by the optimiser. To highlight that the method works and the results converge towards the actual values in an optimisation with starting points far away from the optimum and without necessarily taking reference data into account, the optimiser was set to start at the lowest amplitude boundary where the frequency of vibration was 80 % of the resonance frequency of interest (ω_1) without the sine wave being statically shifted in time.



(a) Vibration deflection amplitude X^1 (b) Vibration frequency ω^1

Figure 7.7: Results from the convergence study in the case of **asynchronous** single-harmonic vibration

7.2.1.4 Convergence study

The outcome of the convergence study with the focus on amplitude X^1 and frequency ω^1 of blade 1 is depicted in Figures 7.7(a) and 7.7(b). The amplitude and frequency found by the optimiser are plotted against the number of processed waveforms. The starting points and actual values are highlighted in green (---) and blue (---) dashed lines, respectively. The vibration parameters, depicted in black dots (●), were first determined by the optimiser using a single waveform. It appears that the snapshot of the vibration trajectory from one noisy waveform is insufficient to compute the amplitude and frequency with acceptable accuracy. The results converge towards their actual values when more waveforms from consecutive revolutions are taken into account. The amplitude lies in an error band of 2 % around the actual value when only three waveforms are processed. The frequency needs a further waveform to satisfy the error threshold. Similar trends were observed for the other blades.

The phases for all four blades scatter around -$\frac{\pi}{2}$ rad, which results from the excitation at resonance. The maximum error in the phase amounts to 2.8 %. Having almost equal phase angles reconfirms the presence of standing-wave

excitation. The phase values returned by the optimiser can directly be used to compute inter-blade phase differences. To do so, one of the blades has to be set as a reference, whilst the phases of the other blades are subtracted from this value. The same procedure can be used to compute nodal diameters resulting from travelling-wave excitation, where the blades have different phase angles. Because the optimiser works with snapshots of the vibration trajectory only, the phase results may depend on the position of the blade in its vibration cycle when it entered the sensor field. This is particularly true when the optimiser is provided with sparse data.

7.2.1.5 Comparison with traditional BTT

The results gained by applying BLASMA-OPT were benchmarked against traditional BTT data depicted in dark-yellow dashed lines (---) in Figures 7.7(a) and 7.7(b). The TOA $t^{\mathrm{v},1}_{\mathrm{BTT},i}$ of blade 1 was recorded from 0.12 s to 0.3 s in each revolution i in the steady-state domain using just one sensor to fulfil the predefined conditions of this investigation. Triggering was done on the rising edge at 40 % of the waveform amplitude. At the same time, a non-vibrating but rotating reference blade 1 served to compute reference TOA data $t^{\mathrm{r},1}_{\mathrm{BTT},i}$. The two TOA sets that were each composed of data from eighteen revolutions were transformed into time differences. Subsequently, the estimated discrete BTT deflection points $x^{\mathrm{F}}_{\mathrm{B1}}(t^{\mathrm{v},1}_{\mathrm{BTT},i})$ of blade 1 were determined with the well-known formula as per:

$$x^{\mathrm{F}}_{\mathrm{B1}}(t^{\mathrm{v},1}_{\mathrm{BTT},i}) = 2\pi R^{0}_{\mathrm{B}}\Omega \left(t^{\mathrm{v},1}_{\mathrm{BTT},i} - t^{\mathrm{r},1}_{\mathrm{BTT},i}\right). \tag{7.4}$$

There is no other means of estimating the vibration deflection from TOA data. The major drawback of this approach can directly be understood from Figure 7.6(a): The deformable blade additionally moves with an **unknown** vibration velocity that inherently **changes** between the times $t^{\mathrm{v},1}_{\mathrm{BTT},i}$ and $t^{\mathrm{r},1}_{\mathrm{BTT},i}$. Therefore, nothing but the average blade velocity at steady state ($2\pi R^{0}_{\mathrm{B}}\Omega$) can be included in Equation (7.4).

Variable	V	AV	Unit	Error
Amplitude (X^1_{BTT})	4.9e-1	3.4e-1	mm	44 %
Frequency (ω^1_{BTT})	11.8	285	Hz	-96 %
Phase (θ^1_{BTT})	-0.5	$-\frac{\pi}{2}$	rad	-68 %

Table 7.4: Vibration parameters computed on the basis of the traditional TOA

Once the deflection points were computed, a single-harmonic sine wave was fitted to the deflection data using a non-linear least-squares algorithm. An amplitude of 4.9e-1 mm, a frequency of 11.8 Hz, and a phase of -0.5 rad were determined on the basis of TOA data, which are written down in Table 7.4 where the values found (V) are contrasted with the actual values (AV). The BTT errors clearly lie outside the acceptable error range of ±5 %. Apart from the under-sampling issue, noise in the sensor output affected the determination of the TOA and introduced new errors.

Many BTT methods have been proposed in the literature in order to estimate, handle, and reconstruct sparse TOA data in the presence of non-negligible uncertainty, which are summarised in Section 2.2.3.1. Despite all these methods, it is the author's conviction that under-sampled TOA data can only be processed into meaningful vibration data either by adding further measured data to it or by making assumptions about the prevailing circumstances at the time of the measurements. The former course of action is generally fairly restricted in the case of BTT because of three things: first, there are in practice no alternatives to BTT for real online blade vibration monitoring; second, the number of BTT sensors is limited; third, the sensor position cannot be varied during operation. The other solution lacks universality and has the character of being merely suitable for laboratory exercises. It should consequently be emphasised that the under-sampling problem with traditional BTT cannot be alleviated without concessions.

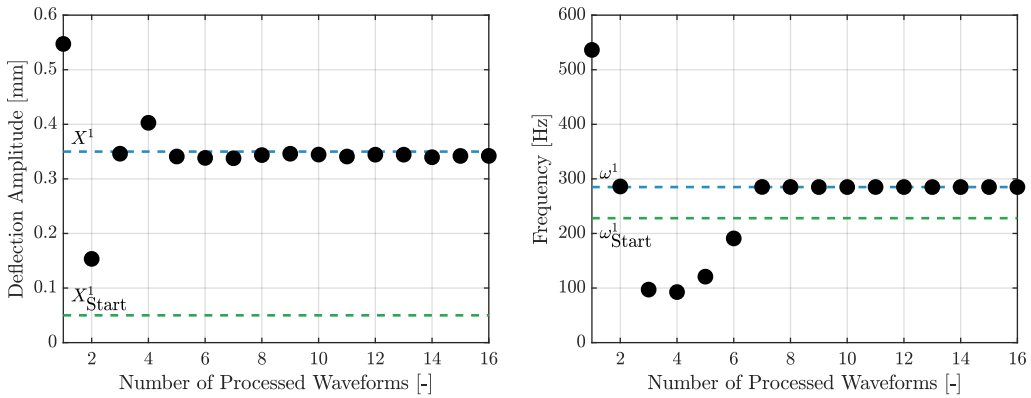
7.2.1.6 Summary

The waveform data for determining vibration parameters using BLASMA-OPT was obtained in less than 40 ms (four revolutions) and was then ready to be analysed. Traditional BTT was not capable of determining accurate results, not even when the algorithm was provided with data from eighteen revolutions. It is also worth highlighting that BTT would require TOA data from at least three revolutions with a single sensor for solving the single-harmonic vibration problem with the three unknowns (amplitude, frequency, and phase). On the other hand, BLASMA-OPT achieved sufficient accuracy in amplitude within that time already. Because BTT proved not to be reliable in the case of asynchronous single-harmonic vibration, it would certainly not deliver desired results in the more difficult case of synchronous single-harmonic vibration, let alone multi-harmonic vibration. For this reason, BTT was not considered in the following investigations.

7.2.2 Synchronous single-harmonic excitation of the blades

This section is concerned with the potential of BLASMA-OPT for synchronous vibration analysis. The rotation speed was adjusted to 5.7e3 RPM to make previous asynchronous vibration synchronous. The parameters for the optimisation from Table 7.3 were reused. The convergence of vibration deflection amplitude X^1 and frequency ω^1 of blade 1 over the number of processed waveform points is shown in Figures 7.8(a) and 7.8(b), respectively.

The difficulty of dealing with synchronous vibration is that consecutive waveform snapshots are equally modulated by blade vibration. This does not apply to the modulation by noise which is not constant. The larger the variation between waveform snapshots, the faster the optimum can be found. The reduction in variation caused the optimiser to require two further revolutions for the amplitude and three further revolutions for the frequency in



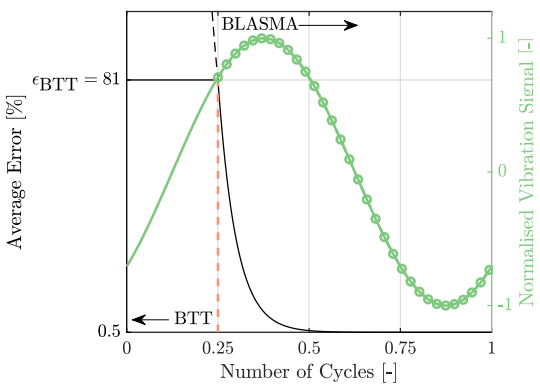
(a) Vibration deflection amplitude X^1 (b) Vibration frequency ω^1

Figure 7.8: Results from the convergence study in the case of **synchronous** single-harmonic vibration

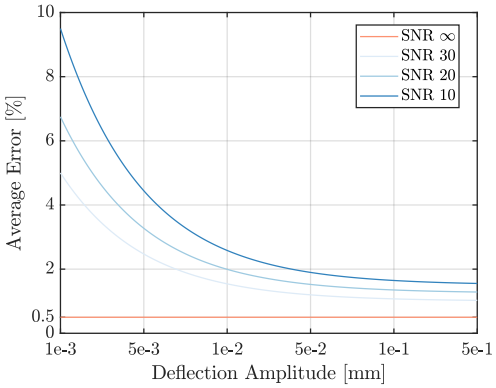
contrast to the results in the case of asynchronous single-harmonic vibration. It also becomes noticeable that there is a scattering of data points prior to reaching the desired error bound of 2 %. Data points are depicted from the first sixteen revolutions in the steady-state domain in order to highlight the stability of the optimum. This is an important characteristic of the optimum, especially in the case of large initial fluctuations.

7.2.2.1 Sensitivity analysis of BLASMA-OPT

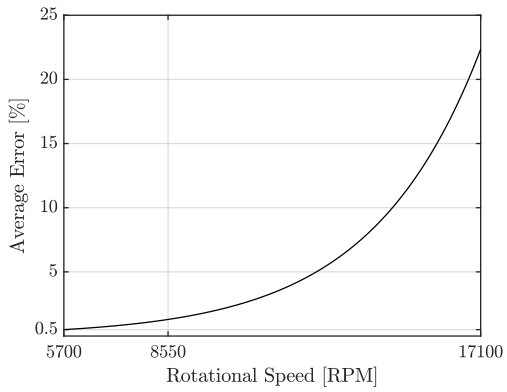
The error susceptibility of BLASMA-OPT was studied on synchronous single-harmonic vibration at 285 Hz. The lack of variation amongst waveform snapshots can impose further limitation on the extractability of vibration parameters. The number of vibration cycles, which are hidden in the waveform snapshot, influence the average error of optimisation (see Figure 7.9(a)). Moreover, the error in the results is sensitive to the vibration amplitude and the rotational speed, which is depicted in Figures 7.9(b)–7.9(c). The relevant engine orders for this investigation are highlighted in the Campbell diagram in Figure 7.9(d).



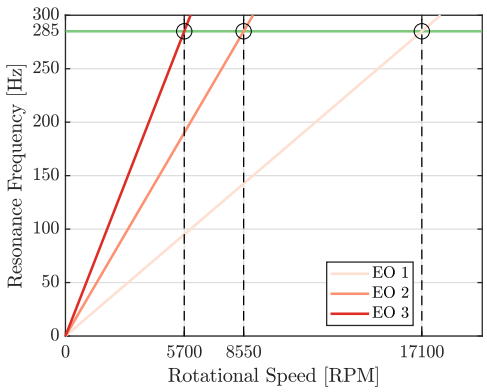
(a) Dependence on the position in the vibration cycle



(b) Amplitude sensitivity



(c) Speed sensitivity



(d) Campbell diagram

Figure 7.9: Results from the sensitivity study in the case of **synchronous** single-harmonic vibration

Number of vibration cycles n_C:

Whilst the blade is passing the sensor, it is moving in its vibration cycle. There are blade-sensor passages that are more suitable than others for optimisation. In order to find the most favourable blade-sensor passage, the average error of optimisation was examined on the basis of fitting a curve to error values from 200 simulations for different blade passages with an average fit error of 4.1 %. The result is depicted as a function of the number of vibration cycles in a waveform snapshot, which is plotted in Figure 7.9(a). Furthermore, one

cycle of the normalised vibration signal is drawn on top of the error curve (see solid green line (—)), which is supposed to show the worst-case scenario of providing an insufficient amount of data to the optimiser. This happens when the vibration cycle in the waveform snapshot has the following properties:

- the cycle is not complete (i.e., $n_C < 1$) and
- does not contain a turning point, hence, only a zero-crossing.

The intersection of the error curve and the vibration signal is found at $n_C \approx 0.25$. Below this point, the amount of data with which the objective function is fed is too little to produce meaningful results, where the average error with the given BLASMA-OPT model significantly increases (see dashed black line (---)). In such a situation, one might either change the objective function or switch to traditional BTT. The absolute average error of the latter amounts to 81 % across all vibration parameters in the present case of synchronous single-harmonic vibration. For numbers of vibration cycles above 0.25, the error quickly converges to the optimum error value at the level of numerical noise in the given scenario, which is 0.5 % and attained after taking waveform data of 100 revolutions into account. If the blade were to arrive at the sensor with a position in the vibration cycle that is close to a turning point (see green circles (○)), much less data would be required so as to significantly reduce the error. It can be inferred that the curvature of the vibration trajectory plays an important role to determine the vibration parameters correctly. To estimate the number of cycles hidden in a waveform snapshot for a particular vibration problem, Equation (4.18) can be used. It should be remembered that the focus in this research is on the assessment of BLASMA-OPT with data from a single sensor. The error value significantly improves when data from more sensors is included in the analysis. Similar achievements are observed when naturally-occurring fluctuations of the rotational speed lead to blade arrivals at sensors with different cycle positions. For all investigations but the error analysis, the optimiser had always sufficient data to find the correct vibration parameters.

Amplitude sensitivity:

The smaller the vibration deflection amplitude, the more difficult it is for optimiser to distinguish between waveform modulation by noise and by vibration. This relation is shown in Figure 7.9(b) where the result of a curve fit that is based on average error values of optimisation is plotted against the vibration deflection amplitude for different signal-to-noise ratios (SNR) (average fit error 3.5 %). The average error values were each computed from 200 simulations on the basis of 100 waveforms for different vibration deflection amplitudes in the interval of $[1\ \mu\text{m}, 5\ \text{mm}]$. In the limiting case of no noise (SNR$\rightarrow \infty$), the average error is purely due to numerical inaccuracies of the computer system and is independent of the vibration deflection amplitude. For all finite signal-to-noise ratios however, the average error is dependent on the vibration deflection amplitude and increases when the latter shrinks.

The lower amplitude limit of 1 μm is for most practical application sufficient. Most often the real sensor resolution does not enable the detection of vibration below a few micrometres. In operation, it is difficult to reliably measure with such high resolution because several counterproductive effects are brought to bear, such as general measurement uncertainty, changes in the sensor position, multi-dimensional vibrations of the entire rotor system.

Rotational speed sensitivity:

The rotational speed is another variable that is closely connected to the average error, whose curve fit function is depicted in Figure 7.9(c) (average fit error 2.9 %). Each average error value was computed from 200 simulations and waveform data of 100 revolutions. The speed sensitivity was investigated on three different engine-order (EO) scenarios that are shown in the Campbell diagram (see Figure 7.9(d)). A rotational speed of 5.7e3 RPM led to third engine-order vibration at 285 Hz, analogously 8.55e3 RPM led to second order and 17.1e3 RPM to first order vibration. The error curve extends into the speed domain that is linked to asynchronous vibration in order to enhance the curve fit. It was found that there is a relatively smooth transition between

the different speed domains within the limits of the fit error stated. This suggests that the error value is little affected by the type of vibration when a significant amount of data is provided to the optimiser.

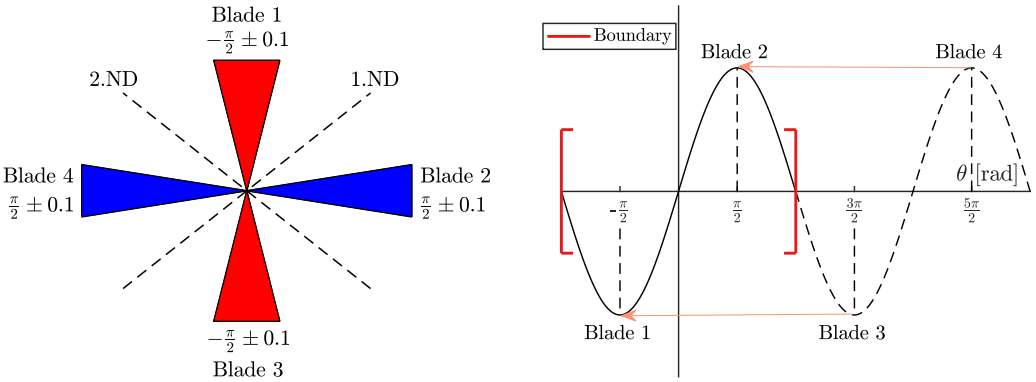
When keeping the sensor properties constant, the average error quickly rises as the rotational speed is ramped up. At a speed of approximately 12.6e3 RPM, the error crosses the 5 % mark. Values above this mark are frequently deemed inappropriate and would require changes in the simulator settings and/or experimental set-up. When the rotational speed increases, the amount of time, which a blade spends in the sensor field, drops. Hence, less vibration data, particularly data of turning points in the vibration cycle, is contained in the waveform snapshot.

Travelling-wave excitation:

Thus far, only standing-wave excitation was investigated where the forces were equal in each dimension (amplitude, frequency, phase). In order to determine the capabilities of BLASMA-OPT as regards travelling-wave excitation, 2-nodal-diameter travelling-wave excitation was applied to the blades in a single-harmonic fashion. The limiting case of two nodal diameters (ND) was chosen because it is the most complex case, which can occur with the present bladed disk, and therefore most challenging to analyse with a single sensor.

The forces were phase-shifted by a multiple of π rad, which was half of the circumferential or inter-blade phase spacing of the blades. The blades experienced the same magnitude of excitation yet not concurrently. The phase shift of π rad between neighbouring blades led to two opposite blades being at the maximum positive deflection whilst the other two were at the corresponding negative one. In an inertial frame of reference, one would observe the response of the blades to such excitation as a moving wave along the circumference of the rotor, hence, a rotating distribution of different blade deflections.

Similarly to the previous sensitivity investigations, waveform data from 200 simulations and 100 revolutions was taken to determine the phase shifts and



(a) Inter-blade phase angles and nodal diameters

(b) Determination of inter-blade phase angles

Figure 7.10: Identification of a travelling wave of **synchronous** single-harmonic blade vibration

average error values of the blades, which are shown in Figure 7.10(a). At resonance, the phase shifts of the blades were reduced by -$\frac{\pi}{2}$ rad or, more precisely: the phase shift of blade 1 became -$\frac{\pi}{2}$ rad, the phase shift of blade 2 became $\frac{\pi}{2}$ rad, and so forth. However, the boundaries of the phase shift variable for the optimisation problem were $\{-\pi, \pi\}$ rad in order to have a unique solution. As a consequence, the actual phase shifts were projected into the interval defined by the boundaries of the optimisation problem (see Figure 7.10(b)). The actual inter-blade phase shifts could nevertheless be computed from the differences between phase shifts of neighbouring blades, which were found by the optimiser. If there is a sign change in the phase shifts between two neighbouring blades, then this hints at a zero-crossing in the circumferential deflection signal between the two blades and, thus, at a nodal diameter, provided that the opposite blades on the bladed disk behave likewise.

7.2.2.2 Summary

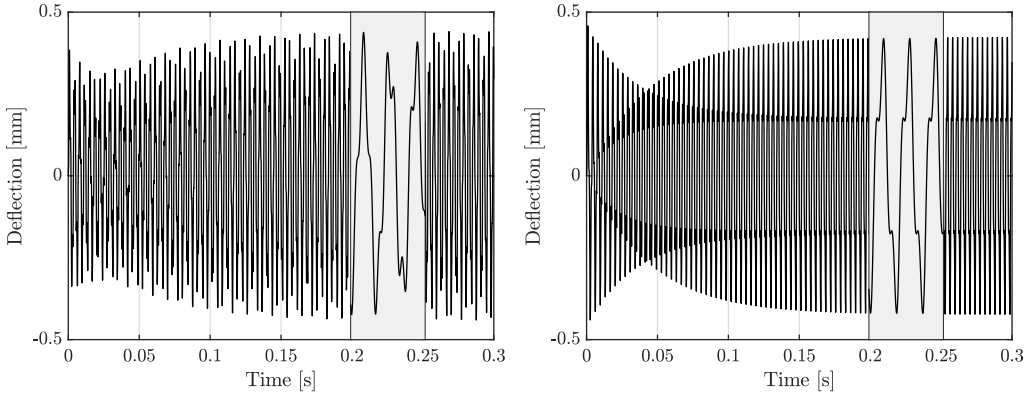
It was shown that BLASMA-OPT can deal with synchronous single-harmonic blade vibration where the maximum errors are ±2 % of the actual vibration

parameters within seven revolutions. Moreover, a sensitivity study was conducted as regards the dependence on the position in the vibration cycle, the vibration amplitude, and the rotational speed. The smaller the portion of the vibration cycle is inside the waveform snapshot and the less data around a turning point of the vibration cycle is captured, the more inaccurate are the results. When the vibration amplitude becomes smaller, it is harder for the optimiser to find the correct vibration parameters at a constant signal-to-noise ratio. Additionally, results suffer when the rotational speed is increased without compensating for the resulting smaller width of the waveform snapshot. It was further demonstrated that travelling-wave vibration can be identified with BLASMA-OPT, concluding the investigation of single-harmonic blade vibration.

7.2.3 Asynchronous multi-harmonic excitation of the blades

The blades were asynchronously excited with a standing-wave pattern by a multi-harmonic force at the first and third resonances depicted in Figure 7.1. Because the vibration results and process of determining thereof were also similar for all blades in the multi-harmonic case study, it was deemed sufficient to only regard blade 1.

The first force harmonic at 285 Hz (first resonance ω_1^1) was taken from the previous single-harmonic case study. The second force harmonic at 960 Hz (third resonance ω_3^1) was added to evaluate the capability of BLASMA-OPT to determine the variables of a multi-harmonic vibration problem from noisy waveforms. The response to this excitation can be seen in Figure 7.11(a). The other test parameters remained the same and are listed in Tables 7.1 and 7.2.



(a) Asynchronous vibration (b) Synchronous vibration

Figure 7.11: Deflection trajectory of the vibrating blades at resonance in the case of multi-harmonic excitation – with a zoomed-in view in grey ( )

7.2.3.1 Parameterisation of the optimiser

When the vibration signal contains multiple harmonics, the objective function becomes more uneven; hence, there are more local minima and maxima. The search for the global minimum becomes more troublesome especially because sensor noise leads to a distortion of the objective function, thereby requiring more data to find the optimum vibration parameters. If there is not enough data or computing power available, one can segment the parameter space to create subspaces and carefully select starting points with the help of reference data.

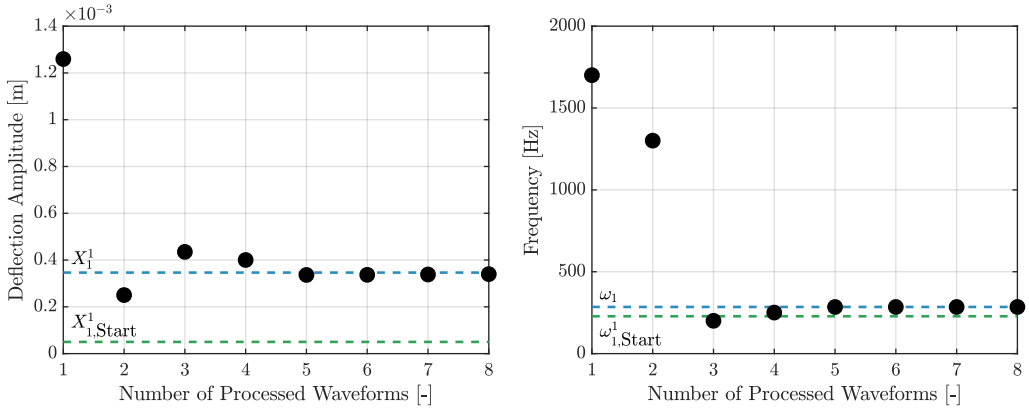
For the multi-harmonic case study, it was again decided to conduct a convergence analysis of the optimum. This was done to learn if and to what extent there was fluctuation in the results in the event of more complex vibration over several revolutions once the amplitudes and frequencies each reach a desired error bound of 2 %. The amplitudes and phases had the same starting points as those from the previous case. The starting points of the two frequencies were each set at 80 % of the actual frequencies. This is reasonable from a practical standpoint because one would define the optimisation parameters on the basis of the resonance frequencies of an FE model in place

Variable	AV	LB	UB	SP	Unit
Amplitude (X_1^1)	3.4e-1	5e-2	10	5e-2	mm
Frequency (ω_1^1)	285	70	2e3	228	Hz
Phase (θ_1^1)	n/a	-π	π	0	rad
Amplitude (X_3^1)	9.3e-2	5e-2	10	5e-2	mm
Frequency (ω_3^1)	960	70	2e3	768	Hz
Phase (θ_3^1)	n/a	-π	π	0	rad

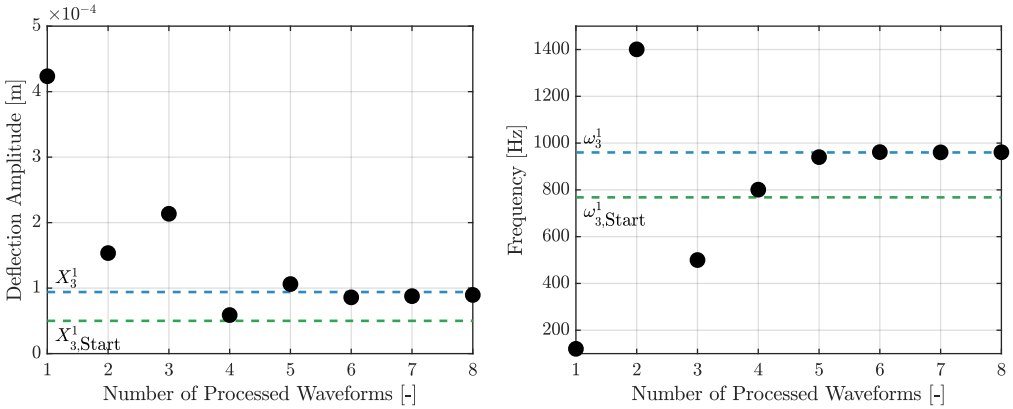
Table 7.5: Parameters for the optimisation problem in the case of **asynchronous** multi-harmonic vibration

of deflection amplitudes. The problem with deflection amplitudes is their dependence on force amplitudes, which are usually unknown during operation. Two important aspects are to be stressed. First, even if some or all starting points were to coincide with the optimum parameters, the optimiser would always perform a search in the defined (sub)space because the optimiser does not and cannot know *a priori* that the starting points are at the same time the optimum parameters. Second, the optimum is a multi-dimensional vector consisting of six elements in the present case, and if a single vector element does not match the corresponding optimum value, the resulting change in the objective function value can be significant and the whole parameter vector becomes non-optimal. The choice of a starting point may aid the optimiser in finding the correct parameters, but it does not guarantee that the optimiser find them for sure. If the actual optimum sought were not within the defined boundaries for the optimisation, the optimiser would return values that are the best solution for this scenario. A vibration specialist has then to decide whether the solution is realistic or not.

As the rotational speed of 6e3 RPM and the sensor properties remained constant, the length of a trajectory snapshot hidden in a waveform was unchanged. The difficulty was that the optimiser had to indirectly use these snapshots to determine now six vibration properties, three for each harmonic. The parameters (actual values (AV), lower and upper boundaries (LB and UB), and starting points (SP)) for the optimisation are detailed in Table 7.5.



(a) Vibration deflection amplitude X_1^1 (b) Vibration frequency ω_1^1



(c) Vibration deflection amplitude X_3^1 (d) Vibration frequency ω_3^1

Figure 7.12: Results from the convergence study in the case of **asynchronous** multi-harmonic vibration

The actual phase values are not stated in Table 7.5 because small remnants of the transient response and noise make it difficult to precisely determine them in the multi-harmonic case. Any small variation in the phase combination can lead to a signal that appears to be very different to the one that is actually expected.

7.2.3.2 Convergence study

The results of the convergence study for the amplitude and frequency of each harmonic are presented in Figures 7.12(a)–7.12(d). Figure 7.12(a) shows the amplitude X_1^1 of the first harmonic of blade 1 over the first eight revolutions at steady state. Compared with the asynchronous single-harmonic case in Figure 7.7(a), the amplitude has a larger error when only a single waveform is processed, which arises from the superposition of two harmonics. The short snapshot of the vibration trajectory hidden in a single noisy waveform is simply not enough information to detect the optimum. However, the error bound of 2 % is quickly reached within four further revolutions. It can be clearly seen that there are no large oscillations in the convergence of X_1^1 towards its actual value. The same can be said about the amplitude of the second harmonic X_3^1 (third resonance), shown in Figure 7.12(c), with the exception that another two revolutions are needed to meet the error target. More data was necessary in this case because the amplitude of the second harmonic was smaller than that of the first one. The optimiser was required to find two different amplitudes to best match the total amplitude, which was responsible for the waveform modulation.

The convergence of the frequencies ω_1^1 and ω_3^1 can be observed over the number of processed waveforms in Figures 7.12(b) and 7.12(d), respectively. In converging towards their actual values within an error bound of 2 %, the frequencies do not significantly oscillate with decaying overall magnitude apart from some initial overshooting. This is clearly an indicator of the goodness and stability of the optimisation results over different numbers of processed waveforms. The frequency ω_1^1 only needs five revolutions to reach the desired accuracy, whereas the frequency ω_3^1 was found to require six revolutions to constantly satisfy the error threshold.

To evaluate the phases computed using BLASMA-OPT, the following signals are shown in Figure 7.13:

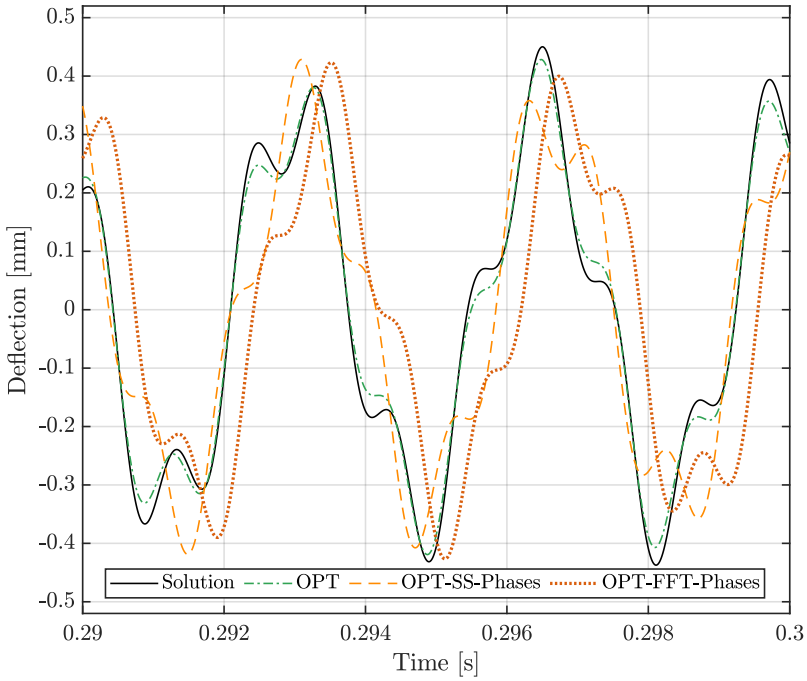


Figure 7.13: Comparison of the actual vibration deflection signal with the signal computed using the vibration parameters from optimisation (OPT), with the signal computed using the optimum amplitudes, optimum frequencies and FRF steady-state phases (OPT-SS-Phases), and with the signal computed using the optimum amplitudes, optimum frequencies and FFT phases (OPT-FFT-Phases)

1. the actual signal (solid black (—)), which is usually *a priori* unknown and solely used here as a benchmark

2. a signal (dash-dotted green (-·-·-) (OPT)) computed using the parameters provided by the optimiser (BLASMA-OPT phases: -1.4 rad for the 285 Hz component and 3.1 rad for the 960 Hz component)

3. a signal (dashed orange (- - -) (OPT-SS-Phases)) computed using the optimum amplitudes, optimum frequencies, and the FRF steady-state phases ($-\frac{\pi}{2}$ rad for the 285 Hz component (first resonance) and $-\frac{\pi}{2}$ rad for the 960 Hz component (third resonance after two anti-resonances))

4. a signal (dotted brown (·····) (OPT-FFT-Phases)) computed using the optimum amplitudes, optimum frequencies, and phases from an FFT of the actual signal at steady state (-2.1 rad for the 285 Hz component and 1.9 rad for the 960 Hz component).

To keep the data consistent for comparison, only simulation data from 0.12 s onwards was considered to compute the aforementioned signals. This time interval was chosen as there is no apparent effect of transient vibration on the amplitudes and frequencies of the signal; hence, the system was considered to be at steady state.

It should be mentioned that the OPT signal, which approximates the actual signal best, was computed with BLASMA-OPT parameters where the corresponding optimum amplitude and frequency values had reached an error bound of 2 %. The errors in the BLASMA-OPT phases resulted from the fact that the optimiser had only limited information available from each noisy waveform to determine the vibration parameters. Each snapshot of the blade trajectory was unique and the ratio of the vibration frequencies was not simply an integer multiple, hampering the computation of accurate phases because there were no repetitive waveforms available that were modulated by full vibration cycles.

The OPT-SS-Phases signal with the FRF phases bears little similarity to the actual signal and the OPT signal. This is a consequence of different damping properties that determine the transient decay rates, which can again lead to an ever constant additional phase shift between the two harmonic signal constituents. The transient responses may have at some point a negligible influence on the amplitudes and frequencies, but they can still cause a distortion of the phases. The transient responses were included, though, in order to simulate real engine vibration, where transient and steady-state vibration at different frequencies can be present simultaneously.

Inadequate results were also obtained with the phases from an FFT (see OPT-FFT-Phases signal). An explanation for this is that an FFT is easily affected by numerical noise and the choice of the initial point in time from which the

signal is transformed. Numerical noise is a consequence of processing discrete data, and its effects on the phase follows directly from the definition of the phase as the quotient of the imaginary part divided by the real part of the signal data. Even the smallest spectral leakage causes oscillations of wrapped phase angles across the entire frequency axis. Moreover, FFTs of only slightly timewise shifted signal sections contain different phase values, which merely emphasises the true nature of an FFT as being an average spectrum property of a signal of finite length. Ultimately, even if less accurate phase values are considered for the computation of nodal diameters, inter-blade phase differences remain almost unaffected by phase errors. This is because the errors in the phases would approximately be the same for every blade when the same sensor and the same number of revolutions are taken into account. A cancellation of the errors would immediately occur during the process of calculating the inter-blade phase differences.

7.2.3.3 Summary

Equally to the single-harmonic case, only 40 ms of waveform data were necessary to determine the vibration parameters with the desired accuracy. It is important to estimate the amount of data required when designing the hardware and software architecture of an online vibration monitoring system, especially, in order to quantify the amount of storage needed. The final results of the amplitudes and frequencies are similar with respect to the speed of convergence. Phases from optimisation better match the actual phases compared with the phases from the traditional approaches based on FRF and FFT. Reference data for defining boundaries and starting points can aid the optimiser in seeking the optimum and serves to evaluate results. If there were no reference data available, one could perform multiple rounds of optimisation with changing boundaries to identify the presence of vibration. Optimisation is usually performed in multiple steps with an adjustable number of solvers. It is recommended that a high number of solvers converge towards the optimum to ascertain its validity.

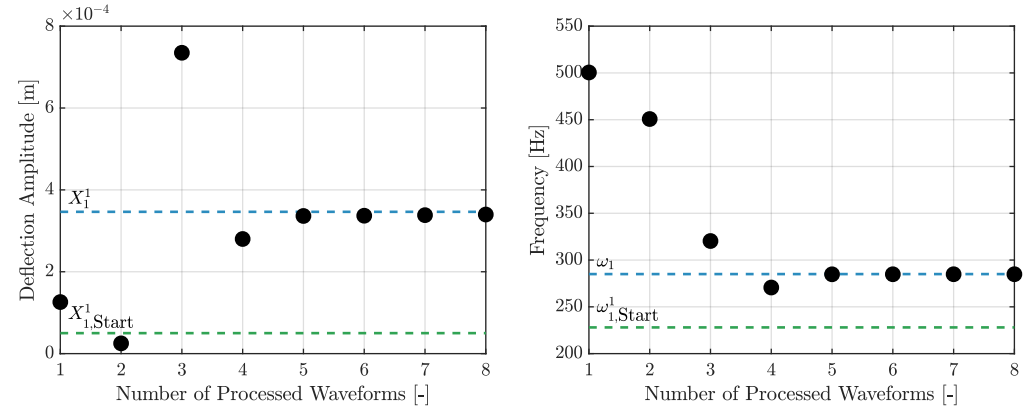
Variable	AV	LB	UB	SP	Unit
Amplitude (X_1^1)	3.4e-1	5e-2	10	5e-2	mm
Frequency (ω_1^1)	285	70	2e3	228	Hz
Phase (θ_1^1)	n/a	-π	π	0	rad
Amplitude (X_2^1)	9.3e-2	5e-2	10	5e-2	mm
Frequency (ω_2^1)	855	70	2e3	684	Hz
Phase (θ_2^1)	n/a	-π	π	0	rad

Table 7.6: Parameters for the optimisation problem in the case of **synchronous** multi-harmonic vibration

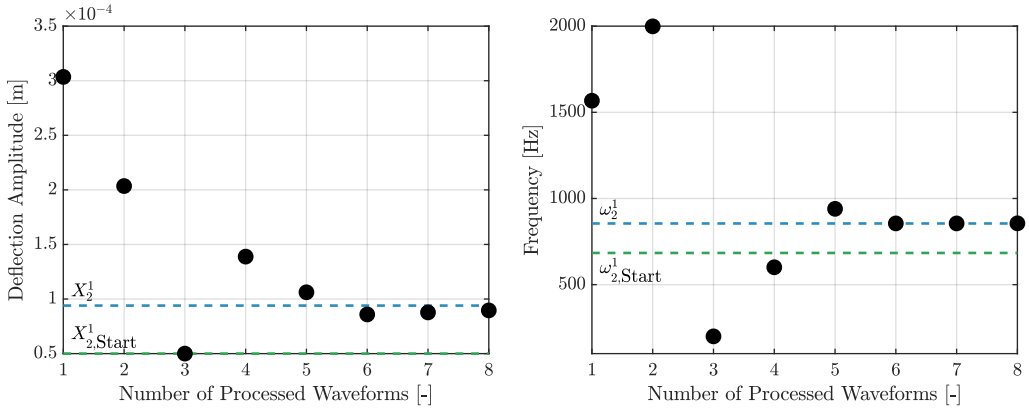
7.2.4 Synchronous multi-harmonic excitation of the blades

Synchronous multi-harmonic excitation was generated at a rotational speed of 5.7e3 RPM where the first resonance at 285 Hz (engine order 3) and second resonance at 855 Hz (engine order 9) were targeted. The optimisation was parameterised similarly to the asynchronous multi-harmonic vibration study with the corresponding parameters of blade 1 listed in Table 7.6. The same parameters were also used for the other three blades. The starting point of the frequency of the second harmonic (ω_2^1) was again 80 % of the actual frequency value.

The results of the convergence study are plotted in Figures 7.14(a)–7.14(d). The speed of convergence and the errors in all six vibration parameters are akin to the ones found in the asynchronous multi-harmonic study. When comparing the outcome of the multi-harmonic vibration studies with that of the single-harmonic studies, it appears that the scattering of frequency values observed in the multi-harmonic vibration studies tends to be larger yet not affecting the convergence towards the actual values. It was found that this arose purely from additional signal complexity since the test conditions remained unchanged.



(a) Vibration deflection amplitude X_1^1 (b) Vibration frequency ω_1^1



(c) Vibration deflection amplitude X_2^1 (d) Vibration frequency ω_2^1

Figure 7.14: Results from the convergence study in the case of **synchronous** multi-harmonic vibration

7.3 Conclusion

BLASMA-OPT is a method for seeking the optimum parameters that best describe the vibration problem. To evaluate the capabilities of the method, four different case studies of asynchronous and synchronous single-harmonic and multi-harmonic blade vibration were conducted. Real capacitive waveforms that had been generated during an experiment on a transonic compressor were replicated to develop a sensor model for the simulation. The results of the amplitudes and frequencies were shown as a function of the number of pro-

cessed waveforms generated by one sensor. Despite being susceptible to noise, optimum phases allowed the computation of inter-blade phase differences for determining nodal diameters, provided that errors were homogeneously distributed.

It was discovered that a single waveform did not contain enough information under the prevailing simulation conditions in order for the optimiser to determine the parameters with acceptable accuracy; yet, it was possible to reduce errors by submitting several waveforms at once to the optimisation routine, drawing a parallel with the implication of the mathematical law of large numbers. Less than eight waveforms were required in the present studies so as to reach an accuracy of 98 % and better, even with noise in the sensor output. The accuracy of the method was further affected by the position of the blade in its vibration cycle, the magnitude of the deflection amplitude, and the rotational speed.

Increasing the number of collectively processed waveforms offers new possibilities for analysing synchronous vibration that notoriously creates no additional variance in modulation amongst successive waveforms. One important outcome of this investigation was that the probability of obtaining suboptimal solutions could be lowered by simply making the optimiser search more but similar waveforms. The advantage was twofold: the effect of sensor noise on the optimisation was better averaged out over multiple waveforms, and the optimiser was more likely to reject unfavourable search paths early in its run.

Traditional BTT was arguably outperformed by BLASMA-OPT. There may be dissenting voices claiming that there be a lack of foundation for such a juxtaposition in the light of a constraint on the number of sensors. The author of this work is absolutely aware of the fact that BTT requires more than one sensor so as to avert under-sampling and yield satisfactory results; notwithstanding, it is equally believed that the amount of sensor data with which both methods are tested must be the same for a fair comparison.

Out of the three introduced BLASMA methods, BLASMA-OPT arose as the method with the greatest capability to determine vibration parameters: firstly, it does not demand the existence of the inverse waveform equation and reference waveforms; secondly, it enables the simultaneous processing of multiple waveforms to improve accuracy; thirdly, it permits examining multi-harmonic vibration responses. BLASMA-OPT was therefore selected as the analysis tool for the forthcoming experimental investigation.

Chapter 8

Experimental validation of sensor waveform analysis

A rig in the research facilities of Rolls-Royce at Imperial College London is suggested, which allowed BLASMA to be put to the test. The mechanics of this apparatus including its components are scrutinised first, paying attention to the blisk and the instruments for establishing the nature of vibration. The capabilities and limitations of the rig that impacted on the extent of the measurement campaign are thoroughly discussed. Presented thereafter are the results of an investigation into the state of blisk mistuning, which consisted of two parts, namely modal testing and the determination of the distortion of the blisk geometry due to the manufacturing process. Subsequently, the calibration curves are revisited, which permitted the exploration of the relationship between the signals of a single capacitive sensor for generating waveforms from blade passages, strain gauges for reference measurements, and piezoelectric patches for exciting the blades. An LDV was utilised for producing data that functioned as a common standard in the calibration process. Whilst real sensor waveforms had served in the previous study only to model the sensor, they were here also useful for ascertaining vibration parameters. Two different studies acting as a proof of concept were undertaken: in the first, the blades were excited by a single-harmonic force that caused the blisk to respond at two adjacent resonance frequencies, and in the second, the blades were subjected to multi-harmonic excitation at two well-spaced resonance frequencies. Findings indicate that BLASMA can be a valuable addition to traditional measurement approaches.

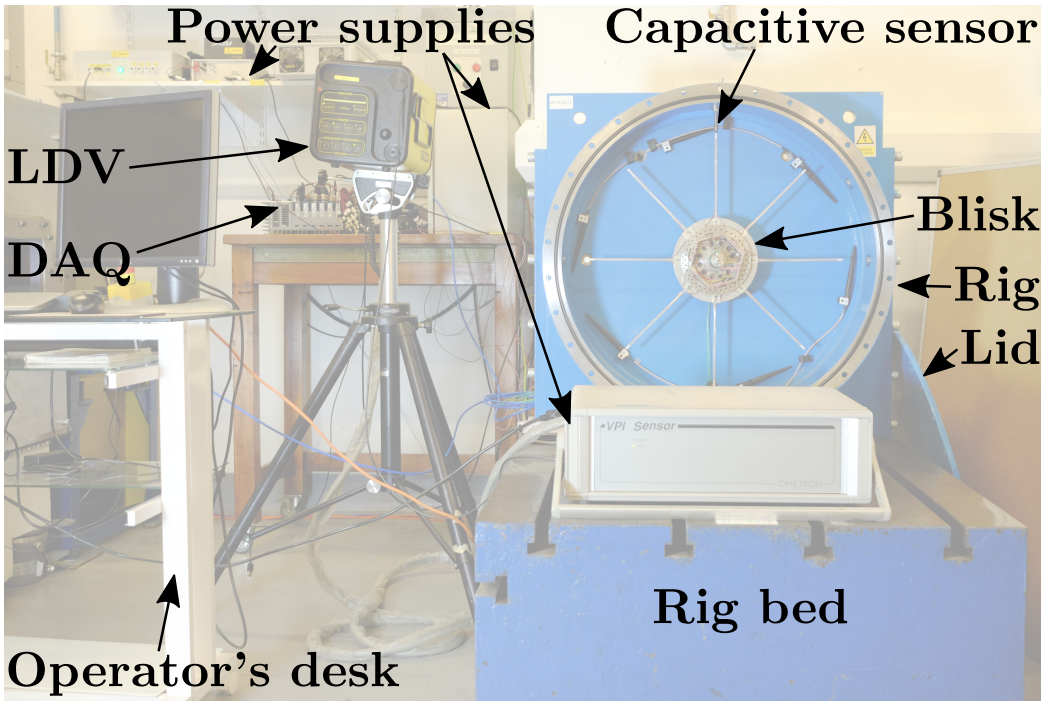


Figure 8.1: View of the test rig

8.1 Test rig

The test rig was cost-efficiently assembled from pre-existing and newly acquired hardware that are depicted in Figures 8.1–8.4. Its original purpose had been to examine the influence of Coriolis forces or gyroscopic effects on the modal properties of a bladed disk [446]. In the present work, the focus was on investigating blade vibration with BLASMA for which the blisk, the excitation equipment, and the measurement instruments were the most important components of the rig.

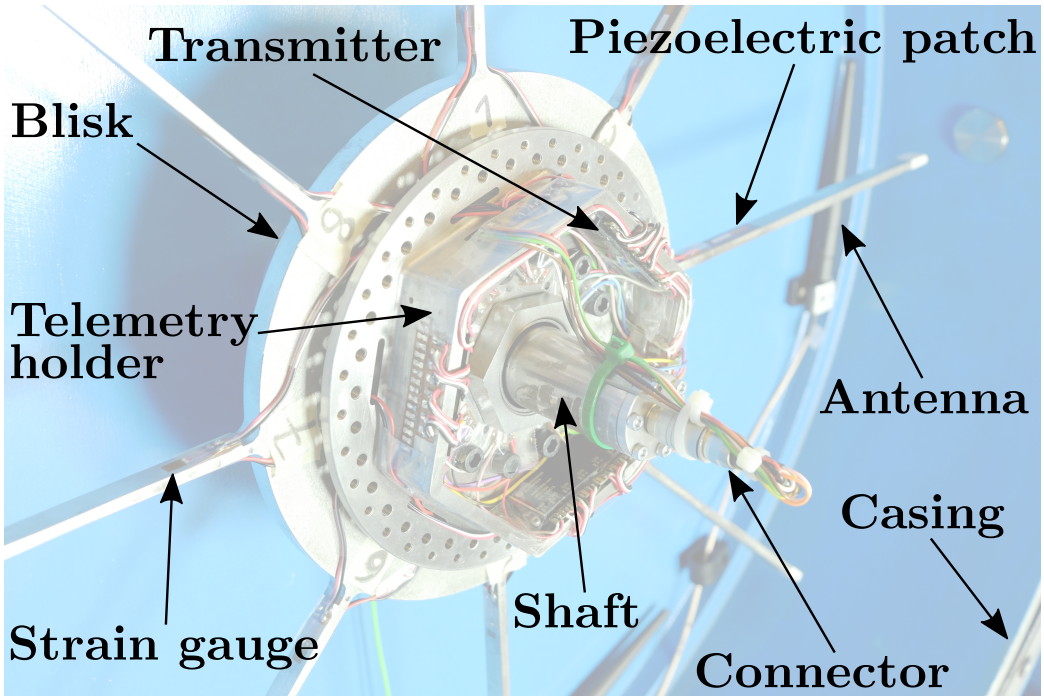


Figure 8.2: Equipment at the front of the test rig

8.1.1 Blisk

The reason for choosing a blisk instead of a disk with removable blades was to avoid any further joints that might have produced a change in the vibration behaviour, for instance, by bringing about non-linearities that would have required further research and distracted attention away from the intended course of action. The aim was also to have as little coupling between the blades as possible, so that they were able to vibrate almost independently from each other. This allowed focussing primarily on the validation of the method.

The blisk is housed in a casing that rests on a sturdy bed and can be tightly closed by a lid for creating vacuum conditions. Because of the initial uncertainty as to whether BLASMA were of any benefit to real test cases, it was opted for a low-budget design of the blisk to quickly identify the merit of

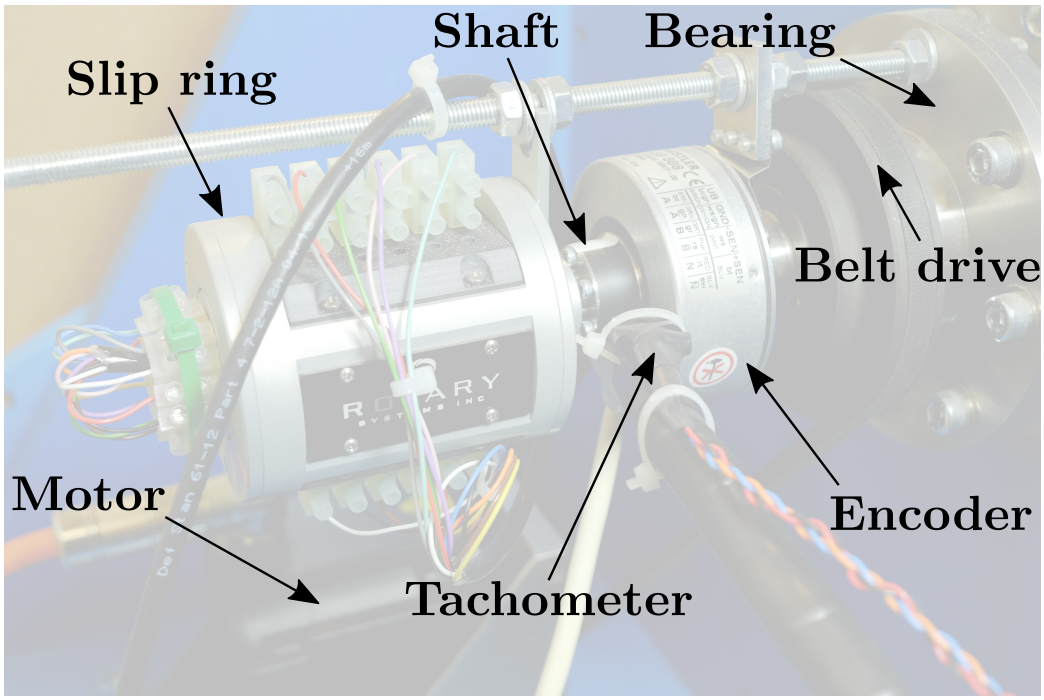


Figure 8.3: Equipment at the rear of the test rig

the approach. As it was presented in Chapter 4, the blade geometry affects the application of BLASMA, which is why it was deemed reasonable to set forth the reasons for choosing a particular blisk geometry. Made of SAE 304 stainless steel, the blisk was created as one piece by laser cutting, which is a manufacturing process that can at best achieve tolerances as little as ± 0.1 mm in the lower price segment. For testing purposes, it was decided to have eight blades equally distributed around the disk with an angle of 45° in between. Any other number of blades would have worked, too, as long as the blisk was balanced. When the number of blades is to be increased, two technical aspects have to be considered apart from financial ones:

1. waveforms will occur more densely meaning that more data is to be stored and the sensor has less time to return to the signal offset between two consecutive blade passing events

2. the increase causes a greater mass moment of inertia that affects the choice of motor, which is to spin the blisk.

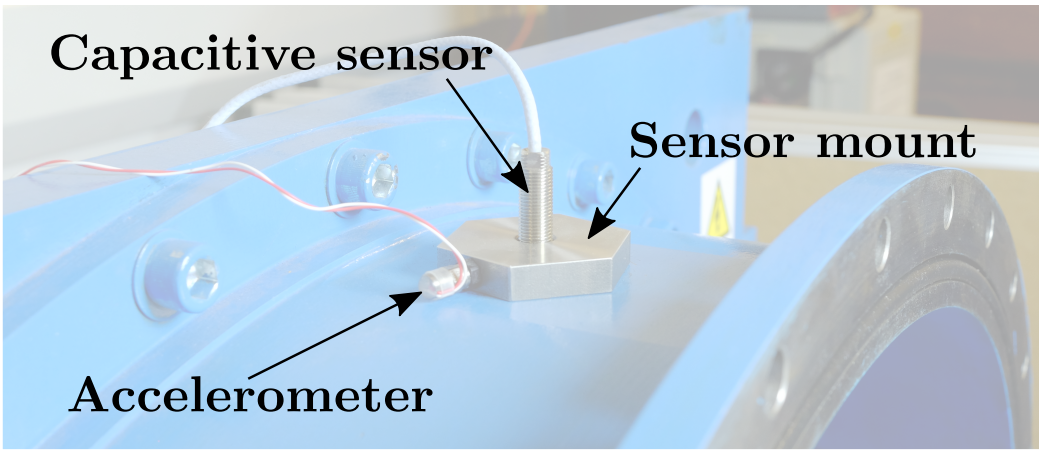


Figure 8.4: Equipment at the top of the test rig

The mass moment of inertia of the blisk $\mathcal{I}_{\mathrm{BD}}$ with respect to the longitudinal axis of the shaft was estimated using:

$$\mathcal{I}_{\mathrm{BD}} = \mathcal{I}_{\mathrm{D}} + 8\mathcal{I}_{\mathrm{B}} - \mathcal{I}_{\mathrm{BO}} \quad \text{with} \tag{8.1}$$

$$\mathcal{I}_{\mathrm{D}} = \frac{\pi}{2}\rho_{\mathrm{S304}} D_{\mathrm{BD}} R_{\mathrm{D}}^4 \tag{8.2}$$

$$\mathcal{I}_{\mathrm{B}} = \rho_{\mathrm{S304}} L_{\mathrm{B}} W_{\mathrm{B}} D_{\mathrm{BD}} \left(\frac{(L_{\mathrm{B}} + W_{\mathrm{B}})^2}{12} + C_{\mathrm{B}}^2 \right) \tag{8.3}$$

$$\mathcal{I}_{\mathrm{BO}} = \pi \rho_{\mathrm{S304}} D_{\mathrm{BD}} \sum_{i=1}^{13} R_{\mathrm{BO},i}^2 \left(\frac{R_{\mathrm{BO},i}^2}{2} + C_{\mathrm{BO},i}^2 \right) \tag{8.4}$$

where $\mathcal{I}_{\mathrm{D}}$ is the mass moment of inertia of the disk, $\mathcal{I}_{\mathrm{B}}$ is the mass moment of inertia of a blade, $\mathcal{I}_{\mathrm{BO}}$ is the mass moment of inertia of the twelve small bores (for fixing the blisk to the telemetry holder) and one large bore (for mounting the blisk onto the shaft), ρ_{S304} is the density of the blisk material, D_{BD} is the depth of the blisk, R_{D} is the radius of the disk, L_{B} is the length of a blade, W_{B} is the width of a blade, C_{B} is the distance between the blade-owned centroid and the axis of rotation, $R_{\mathrm{BO},i}$ is the radius of bore i, and $C_{\mathrm{BO},i}$ is the distance between the bore-owned centroid and the axis of rotation. These properties are listed in Table 8.1.

Property	Value	Unit
Blade centroid to rotation axis (C_{B})	200	mm
Blade cross-sectional area ($\mathcal{A}_{\mathrm{B}}$)	40	mm^2
Blade mass (m_{B})	6.4e-2	kg
Blade length (L_{B})	200	mm
Blade width (W_{B})	4	mm
Blisk depth (D_{BD})	10	mm
Density (ρ_{S304})	8e3	$\frac{\mathrm{kg}}{\mathrm{m}^3}$
Disk radius (R_{D})	100	mm
Large bore centroid to rotation axis ($C_{\mathrm{BO,l}}$)	0	mm
Large bore radius ($R_{\mathrm{BO,l}}$)	33.5	mm
Mass moment of inertia of the blades ($8\mathcal{I}_{\mathrm{B}}$)	2.22e-2	$\mathrm{kg\,m}^2$
Mass moment of inertia of the blisk ($\mathcal{I}_{\mathrm{BD}}$)	3.46e-2	$\mathrm{kg\,m}^2$
Mass moment of inertia of the bores ($\mathcal{I}_{\mathrm{BO}}$)	2.1e-4	$\mathrm{kg\,m}^2$
Mass moment of inertia of the disk ($\mathcal{I}_{\mathrm{D}}$)	1.26e-2	$\mathrm{kg\,m}^2$
Small bore centroid to rotation axis ($C_{\mathrm{BO,s}}$)	39.5	mm
Small bore radius ($R_{\mathrm{BO,s}}$)	3.3	mm
Young's modulus (E_{S304})	2e11	Pa

Table 8.1: Material and geometrical properties of the blisk

The mass moment of inertia of the blisk that attains 3.46e-2 $\mathrm{kg\,m}^2$ caused an additional time delay Δt for any change in the rotational speed $\Delta\Omega$ at the nominal torque τ as per:

$$\Delta t = \frac{\mathcal{I}_{\mathrm{BD}}}{\tau}\Delta\Omega. \tag{8.5}$$

The acquired alternating-current synchronous servo motor offers under normal operating conditions (no stalling) a constant torque of up to 3.5 Nm. This produced a Δt of roughly 10 ms per Hz, which was deemed acceptable for the system. This value was to be kept in mind since any speed fluctuations, which were tried to be compensated by the PID (proportional–integral–derivative) controller in the closed-loop feedback chain of the servo drive, had a significant effect on the features of waveforms.

The geometry of the blisk was constrained by five factors:

1. Considering that the casing geometry was fixed, the blisk needed to have a diameter of 400 mm or thereabouts to make the blades pass the capacitive sensor in close proximity. This was necessary for the sensor to produce waveforms. However, the blades had to be prevented from striking the sensor.

2. The mass moment of inertia of the blisk was supposed to be reasonably small ($\mathcal{O}$(1e-2 kg m^2)) so that the motor would be capable of accelerating the blisk swiftly.

3. The fact of the blisk being machinable: The manufacturer was consulted as regards the feasible minimum blade width for laser cutting. The recommended and chosen value in the present case was 4 mm.

4. The blisk had to have a certain minimum depth to accommodate the piezoelectric patches and strain gauges. Additionally, the value ensured that the blisk was securely fastened to the telemetry holder.

5. Stagger angles were avoided to simplify the machining process of the blisk and to comply with budget requirements. Consequently, all sections of the blade along its longitudinal axis were thought to arrive at the sensor simultaneously.

8.1.2 Actuators and sensors

8.1.2.1 Capacitive sensor for evaluating BLASMA

A capacitive sensor with an 8 mm head was mounted on the casing at 0° to the vertical. The sensor was kept in place by a sensor mount with an M10x1 tapped hole in its centre, which was designed to permit adjustments of the radial position of the sensor. An ordinary capacitive sensor was selected to

demonstrate that expensive BTT hardware would not necessarily be needed to make BLASMA work. The combination of a relatively small sensor head and the above mentioned blade geometry enabled one to observe relatively short blade travelling times along the sensor ($\mathcal{O}$(1 ms)) at low rotational speeds ($\mathcal{O}$(1e2 RPM)). Attached to the sensor mount is an accelerometer that produced vibration data that helped to establish whether alarming sensor vibration due to casing vibration in the direction of flap-wise blade vibration occurred. This was a precaution against unintentional disregard of non-negligible changes in the sensor position that might have affected key attributes of sensor waveforms.

8.1.2.2 Encoder and tachometer for speed measurements

The average rotational speed of the shaft was measured using data generated by an incremental 2048-line encoder and a self-built tachometer whose most essential component is a photoresistor. Both sensors are each powered by a 5 VDC signal that is provided by a self-built system that consists of an off-the-shelf computer power supply connected to a printed circuit board that accommodates the necessary electrical components and is protected by an enclosure. The encoder creates a digital signal that allows determining the position of the shaft with respect to a reference point from which the speed is derived, whereas the tachometer produces speed-indicating signal pulses every time a certain position on the shaft that is marked with reflective tape passes the photoresistor.

8.1.2.3 Piezoelectric patches for exciting blades

Each blade was equipped at its root with a piezoelectric patch, which was the location recommended by the manufacturer. This patch is a composite actuator that consists of a sheet of piezo-ceramic fibers that is glued at its bottom and top surfaces to a thin polymer film holding electrodes. When an

alternating voltage is applied to the actuator, it will bend and excite the blade accordingly. The electrical energy is provided by a pre-existing power supply that is composed of eight amplifiers, each for one of the piezoelectric patches. The supply of power to the piezoelectric patches was the bottleneck for the excitation of the blades and lastly for the entire measurement campaign since it determined the blade responses that could be observed. Whilst the actuators can endure operating voltages in the range from -500 V to 1500 V, the amplifiers are only capable of generating voltages between -100 V and 250 V within the frequency range of interest. The amplifiers were connected with the slip ring from which wires run through the hollow shaft to the telemetry holder and finally to the actuators. Moreover, every amplifier possesses an output monitor by which the excitation could be watched.

Without later calibration, it would have been impossible to state the correlation between voltage amplitudes of the excitation signal and amplitudes of blade displacement. Unfortunately, the supplier of the piezoelectric patches was not able to offer reliable information on the relationship between the voltage signal and forces in N, which could have helped in relating excitation and response. Neither could he give advice on the estimation of possible displacement levels in the design phase of the test rig.

8.1.2.4 Strain gauges and LDV for reference measurements

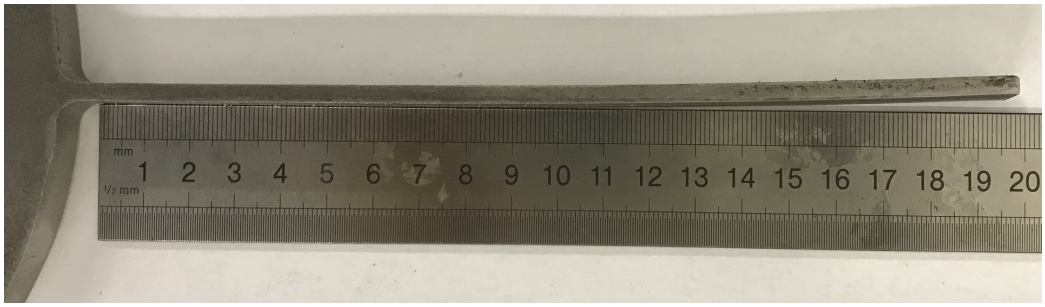
Merely employed for creating reference vibration data, a strain gauge is made of a tiny specially shaped conductor inside a supporting insulating polymer. It was attached to every blade root opposite the piezoelectric patch where the greatest strain occurred according to an FE analysis. When the blade deforms at the location of the strain gauge, the conductors acts correspondingly. This causes a change in the electrical resistance of the strain gauge as a function of the length and cross-sectional area of the conductor, which can be measured using a Wheatstone bridge and be related to strain by the so-called gauge factor. Similarly to the piezoelectric patches, the power supply for the strain gauges was connected to the telemetry holder by means of the slip ring. Each

strain gauge was then linked to any of three transmitters that were attached to the telemetry holder and supplied by 5 VDC. Every transmitter has four channels that contain a Wheatstone bridge each, which was resistor-wise fitted to the type of strain gauge used (350 Ω). Instead of sending the change in electrical resistance incurred by the strain gauge back to the slip ring and then to the data acquisition system ('DAQ'), the transmitter emits a less noise-affected radio signal that is equivalent to the change in electrical resistance. The signal is captured by the antennas of a receiver and transformed into a voltage signal for further processing.

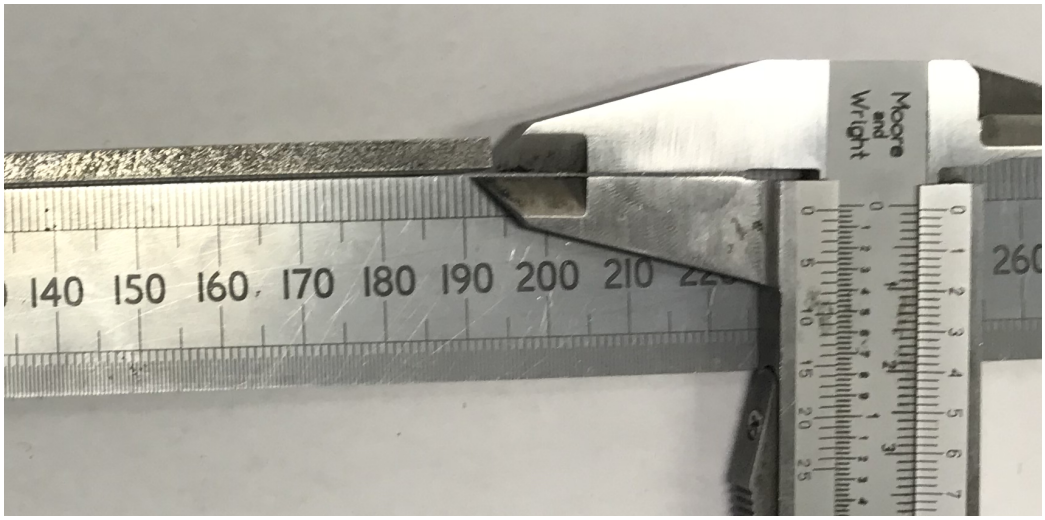
An LDV was utilized for producing reference data under stationary conditions, which helped to calibrate the capacitive sensor, piezoelectric patches, and strain gauges. The LDV was placed on a tripod and arranged in such a way that its laser beam was directed to the tip of a blade at the 0° position. To reach the blade, the laser beam travelled through one of five openings in the casing, which is at 45° to the vertical and is usually supposed to contain either a plug or a sensor mount. Reflective tape was applied to each blade tip to attenuate speckle interference at the point of incidence. LDVs commonly measure the velocity of an object that moves perpendicularly to the laser beam. Due to geometrical constraints, there was an unavoidable angle of inclination exactly when the blade was beneath the capacitive sensor. This angle was brought to a minimum of about 3.8° by carefully adjusting the height of the tripod and the tilt of the LDV. Strictly speaking, this meant that any measured velocity was to be divided by a potentially negligible factor of $\cos(3.8°)$ or 0.998 in order to calculate the actual tangential vibratory velocity of the blade tip.

8.1.3 Mistuning analysis

Upon receipt of the blisk from the manufacturer, it was found that all blades were flap-wise bent as a result of the machining process (see Figure 8.5(a)). It was communicated that this unwanted warping had been a result of the cooling



(a) Warped blade



(b) Corrected blade

Figure 8.5: Cold bending of a blade

process, which could often apply to thin-walled structures like blades and, therefore, re-machining would not provide a solution unless manufacturing becomes more advanced and, thus, expensive. Considering the geometrical constraints of the test rig, a fundamental redesign of the blisk would have been of no help but to cause a delay. To make the best of the situation, it was decided to carefully manually cold-bend the blades held in a vice. The outcome of this process is qualitatively shown in Figure 8.5(b). Prior to reshaping the blades, the maximum measured deviation $\Delta d_{\text{B-B}}^{\max}$ of the linear distance between two facing blade edges at the tip from the theoretical value was approximated at 5 mm. The theoretical linear distance $d_{\text{B-B}}$ was

estimated as specified by:

$$d_{\text{B-B}} = 2\left((L_{\text{B}} + R_{\text{D}})\sin\left(\frac{45^\circ}{2}\right) - \frac{W_{\text{B}}}{2}\right) = 225.6 \text{ mm}. \tag{8.6}$$

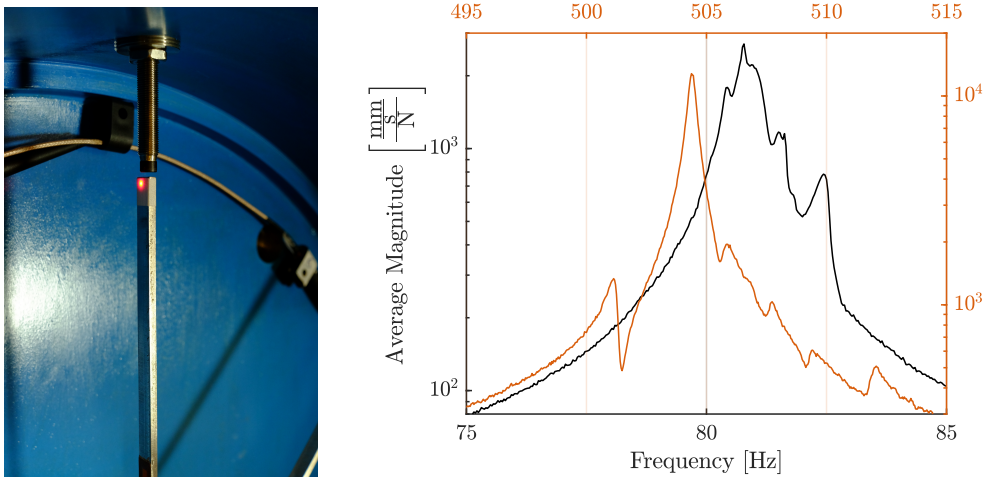
If the blade distortion had not been corrected, it would have meant that the passing times of all blades would have varied to an unacceptable degree. The delay or advance of waveforms $|\Delta t_{\text{W}}|$ would have roughly been:

$$|\Delta t_{\text{W}}| = \frac{\Delta d_{\text{B-B}}^{\max}}{(L_{\text{B}} + R_{\text{D}})\Omega}, \tag{8.7}$$

which could have had the order of magnitude of -3 for a few hundred RPM.

In order to check whether this manual post-processing of the blades caused changes in the resonance frequencies, modal analysis was conducted by hammer testing the blisk. This also served to determine the state of mistuning of the blisk, which could have generally been affected by not only the manufacturing process but also the attachment of piezoelectric patches and strain gauges to the structure. Attention was paid to the first two flap-wise bending modes that would be investigated in the later experimental studies.

The test set-up for modal testing is exhibited in Figure 8.6(a). The blisk with the piezoelectric patches and strain gauges was mounted on the shaft and fixed to the telemetry holder as if the actual experiments on the rotating system were to be carried out. A roving hammer test was conducted with the point of excitation being above the strain gauge of each blade at the height of the piezoelectric patch. First results proved that the system behaved linearly and time-invariantly, thereby justifying the suitability of hammer testing for modal analysis. To mitigate the negative impact on the quality of the vibration data by the potential back-hitting of the structure against the hammer and its force transducer, it is good practice to excite the structure at a location of lower response, which is typically closer to the blade root, and not at a location of expectedly higher response (e.g., the blade tip). The response was measured by an LDV with its measurement point at the tip



(a) Hardware configuration (b) FRF - Average Magnitude

Figure 8.6: Modal analysis of the blisk

of blade 1 at the side of the piezoelectric patch. Earlier testing with an accelerometer stuck to the tip of the blade had demonstrated its previously anticipated tangible effect on the modal properties of the structure, which had caused some significant changes in the natural frequencies ($\mathcal{O}(10$ Hz$)$); this course of action had therefore quickly been abandoned.

According to an FE model of the blisk alone, the first and second flap-wise bending mode families consisted of eight modes each; every blade caused one system mode to appear. The choice of blisk geometry led to a situation where the resonance frequencies of the first mode family fell into the interval of $[80.07, 80.1]$ Hz and those of the second one into $[500.32, 500.86]$ Hz. As intended, these small ranges together with the mode shapes proved that:

1. the blades behaved almost like cantilevers
2. there was little coupling between the blades.

Two sections of the experimental mobility FRF are drawn in Figure 8.6(b); the one in black (—) belongs to the first mode family and the other one in brown (—) to the second mode family. To ease graph-reading, the average

magnitude of all eight modes of each family was computed, which was admissible given their closeness to each other. Since the instrumented blisk was now part of the assembly, the modes of the blisk were merged with those of the other components to build the modes of the entire rig. Despite this fact, the resonance frequencies of the first two flap-wise bending mode families of the blisk in the assembly were relatively near to the blisk-alone resonance frequencies of the FE model ($\mathcal{O}(1\text{ Hz})$). The consequences for the present case were:

1. strain gauges and piezoelectric patches had only a minor effect on the modal properties, which was supported by [52, 447]
2. other components of the assembly did not significantly shift the blisk-alone resonance frequencies.

It was deemed important to consider the resonance frequencies of the assembly instead of merely those of the blisk in view of the fact that the assembly would be the system under observation for the validation of BLASMA.

The frequencies of the two mode families were spread over a slightly wider range with two large magnitude peaks standing out at 80.78 Hz and 504.38 Hz, which are denoted by ω_1^{p} and ω_2^{p}, respectively. These frequencies would later be relevant to determining the excitation frequencies for the studies on BLASMA because they promised discernible blade responses with the available excitation hardware. In contrast to other segments of the FRF, they provoked a greater response of the blades for the same magnitude of excitation. Taking into account that the maximum excitation magnitude provided by the piezoelectric patches was limited, it was essential to know at which frequencies the response was capable of becoming large. It had to be ensured that the response of the blades would be observable and not be:

1. smaller than the resolution of the strain gauges and capacitive sensor
2. indistinguishable from noise.

Some of the modes of the two families were either so close to each other or so highly damped that they could not be properly resolved. It is also worth mentioning that there were no other modes near the two mode families in a radius of 100 Hz and that the modes of consideration had the largest average peaks in the interval of $(0, 1e3]$ Hz.

8.1.4 Calibration

The actuation and measurement equipment at the root of each blade and the capacitive sensor worked with voltage signals that had to be related to flap-wise vibration. They were calibrated against reference data that was created by an LDV with the same arrangement of hardware as the one for modal testing (cf. Figure 8.6(a)). This was necessary because it was at the beginning not obvious how the excitation signal translated into blade tip displacement. Similarly, the latter was to be associated with the voltage signal measured at the Wheatstone bridge and with the one produced by the capacitive sensor.

Calibration was conducted for every blade and, since it was quite repetitive, it is representatively explained using blade 1. At the beginning, blade 1 was positioned beneath the capacitive sensor and its piezoelectric patch was powered by an electromotive force. The excitation frequency was the frequency of the greatest response peak of the first bending mode family in the FRF (80.78 Hz), whilst the excitation amplitude was maximised at 175 V in the available voltage range of [-100,250] V by offsetting the signal by 75 V. The occurring observable response of blade 1 was measured by the capacitive sensor, strain gauge, and LDV and recorded using a LabView tool. The strain gauge signal was found to be considerably noisy as a result of the signal transport through the slip ring and by radio. To make this data more meaningful, a digital filter with a bandpass of [65,95] Hz was applied, which helped to attenuate interference at the mains frequency (50 Hz) and multiples thereof. Because the available LDV was only of use at engine standstill for

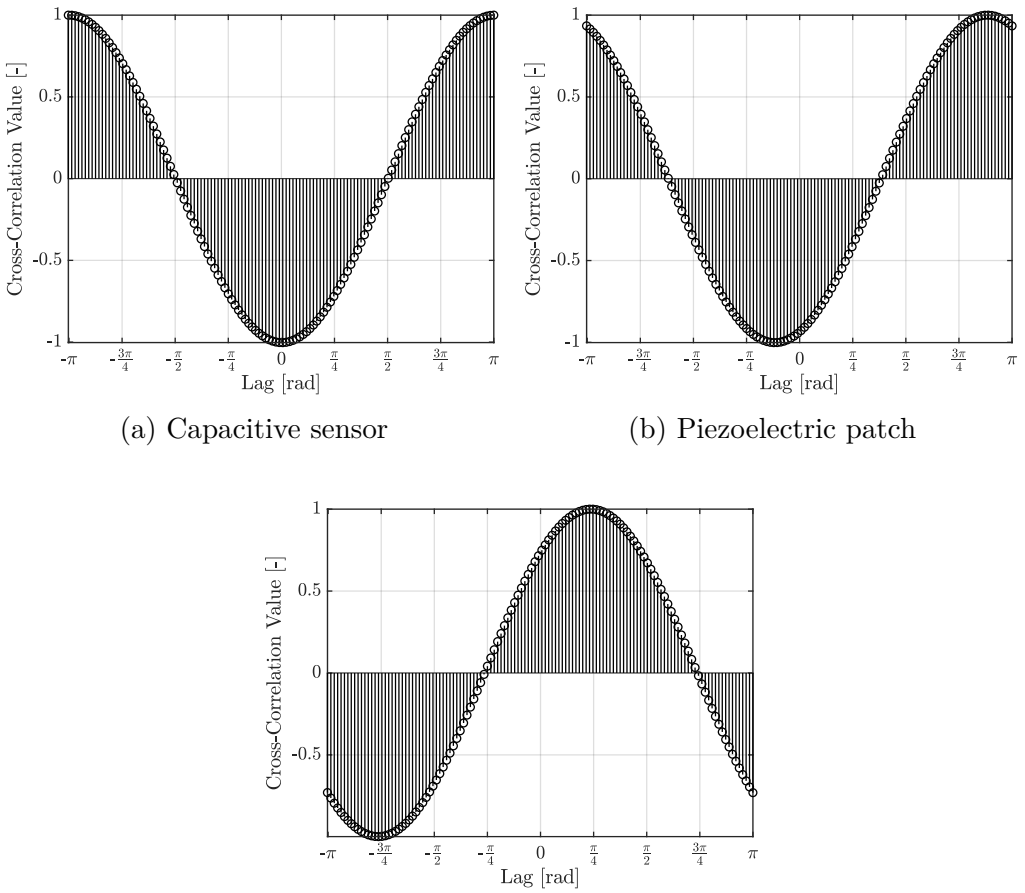
measuring flap-wise blade displacement under the given circumstances, the blisk did not rotate during the measurements. The underlying assumption was that the relationship between the signals of the four instruments would not significantly vary in the speed regime of later experiments. There was no other equipment, such as that based on photogrammetry and point-tracking, that could have accurately measured flap-wise displacement of the order of a few millimetres and less during rotation, taking the casing and blisk geometry into account.

8.1.4.1 Phase lag

Part of the calibration was the study of the correlation between the integrated velocity signal of the LDV and any of the three other signals as a function of the phase lag of the former, which is shown in Figures 8.7(a)–8.7(c). All signals were normalised using their respective amplitudes. The LDV integrated velocity signal was shifted in time against one of the other signals at discrete intervals of the phase lag and the corresponding correlation was computed. When the correlation attained one, the shifted LDV integrated velocity signal was regarded to be in phase with the other signal. The phase lag at which this occurred was the value by which the actual LDV integrated velocity signal lagged the other signal. Were this to happen at a lag of 0 rad, the two actual measured signals would have been in phase during the measurements. In the present case, the LDV integrated velocity lagged:

- the response-measuring capacitive sensor by π rad
- the piezoelectric patch (actuator) by $\frac{7\pi}{8}$ rad
- the response-measuring strain gauge by $\frac{\pi}{4}$ rad.

With respect to the piezoelectric patch, it is worth pointing out that merely the monitoring signal of the amplifier was available. There were no means to obtain the actual signal sent to the actuator.



(a) Capacitive sensor

(b) Piezoelectric patch

(c) Strain gauge

Figure 8.7: Lag with respect to the LDV integrated velocity signal

Some lag was due to unavoidable delay caused by the electronics during the transmission and processing of signals, whereas the rest was owed to the mechanics of the system ($\Delta\theta_{\mathrm{M}}$). On the latter point, one can conceive of the following relationship between the response and excitation signals: The blade velocity measured by the LDV was positive when the blade approached the LDV because the laser beam was reflected with a higher frequency than when the blade receded from the LDV (Doppler shift). The LDV integrated velocity signal was therefore at its positive maximum when the blade was closest to the LDV. In this position, the blade was farthest away from the capacitive sensor, whose signal was expected to have a zero-crossing ($\Delta\theta_{\mathrm{M,CS\text{-}LDV}} = \frac{\pi}{2}$ rad). At

the same time at the side of the blade that faced the LDV, the piezoelectric patch was maximally contracted and was thus supposed to produce the negative signal amplitude ($\Delta\theta_{\text{M,PEP-LDV}} = \pi$ rad). The fact that the blade displacement naturally lagged the force signal at resonance by $\frac{\pi}{2}$ rad was already accommodated in $\Delta\theta_{\text{M,PEP-LDV}}$. Contrarily, the strain gauge was maximally stretched, which entailed the positive voltage amplitude to be generated ($\Delta\theta_{\text{M,SG-LDV}} = 0$ rad). When all influence factors were taken into account, it was fairly difficult to make sound judgements upon the definite values of the phases, which was the reason why they would not be further scrutinised.

8.1.4.2 Parameter curves

Finally, the calibration curves for the operating conditions prevailing at the maximum FRF peaks of the first two bending mode families were computed in dependence of the LDV integrated velocity or flap-wise displacement. The methodology of obtaining the curves was the same for both mode families, and thus, it was deemed sufficient to dedicate the below explanation to the first mode family with its curves being drawn in Figure 8.8.

The underlying assumption was that the signals exhibited the intended phase shifts denoted by $\Delta\theta_{\text{M}}$. When the phase shift is either 0 rad or π rad, the calibration curve is predictably linear. A circular curve is found in the case of a phase shift of $\frac{\pi}{2}$ rad, which has to be read clockwise. For instance, when the LDV integrated velocity changes from 0 mm to its negative amplitude, the voltage signal of the capacitive sensor transitions from its negative amplitude to 0 V. The anticlockwise direction would demand -$\frac{\pi}{2}$ rad, which is also a legitimate interpretation of the phase difference between the two signals. However, it was not possible to tell from the cross-correlation data whether the LDV integrated velocity signal led or lagged the signal of the capacitive sensor, which culminated in the arbitrary decision in favour of the latter.

The relationship between the measurement and excitation instruments was established by combining experimental results and theory. It was considered

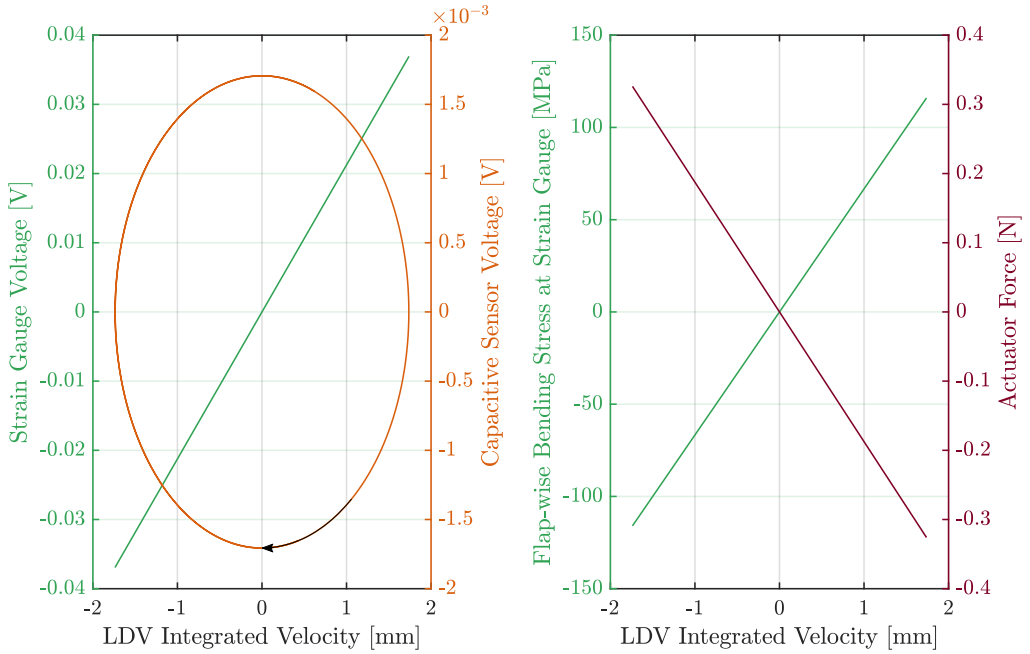


Figure 8.8: Calibration curves belonging to the first bending mode family

important to quantify the piezoelectric force that brought about a certain tip deflection in order to be able to fully grasp the dynamics of the blisk. The tip response could be linked to the signal of the piezoelectric patch in two ways. The first took the amplitude of the LDV integrated velocity X_{LDV} and the magnitude of the mobility FRF $\left|H_{\mathrm{M}}\left(\omega_1^{\mathrm{p}}\right)\right|$ from the mistuning analysis at the peak frequency of the first mode family ω_1^{p} in order to associate them with the force amplitude F_{PEP} of the piezoelectric patch in N as per:

$$F_{\mathrm{PEP}} = \frac{X_{\mathrm{LDV}}\omega_1^{\mathrm{p}}}{\left|H_{\mathrm{M}}\left(\omega_1^{\mathrm{p}}\right)\right|}, \tag{8.8}$$

which yields 3.26e-1 N. This force was modelled to be physically equivalent to the real excitation that was generated by the piezoelectric patches. The frequency ω_1^{p} in Equation (8.8) converts the mobility FRF into the receptance FRF. The spatial variables are illustrated in Figure 8.9. It is to be recalled that the hammer for modal testing struck the structure on the side of the

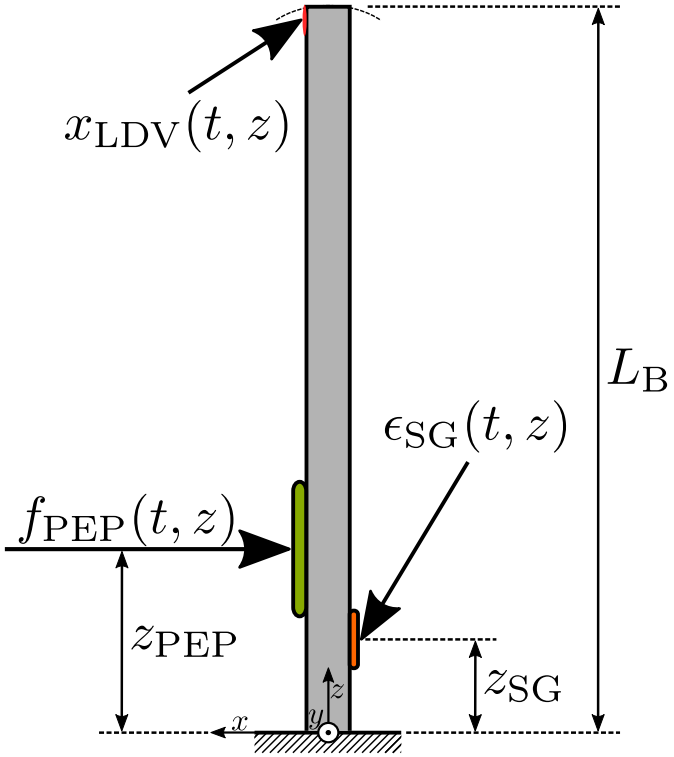


Figure 8.9: Model of a beam with clamped-free boundary conditions

piezoelectric patch above the strain gauge at a z of z_{PEP} $\left(\frac{L_{\mathrm{B}}}{4}\right)$, whilst the LDV measured the response at the tip of the blade on the same side of the actuator. The fact that excitation and response measurement occurred on opposite surfaces did not influence the force magnitude.

The alternative to this approach resorted to the dynamic model of a damped Euler-Bernoulli beam and required the modelling of a cantilever. This was feasible because the slender and homogeneous blade showed only small displacements that were assumed not to destroy the orthogonality of all possible cross-sections of the blade along its longitudinal axis and the neutral axis. Moreover, a cantilever with the same geometrical and material properties as the blade was found to have its first undamped natural frequency at 80.76 Hz ($\omega^{\mathrm{C}}_{\mathrm{und},1}$) and damped natural frequency at 80.63 Hz ($\omega^{\mathrm{C}}_{\mathrm{d},1}$), which are in the immediate proximity of the damped natural frequency of the greatest magni-

tude peak of the first bending mode family of the blade ω_1^{p} (80.78 Hz). The frequency $\omega_{\mathrm{und},1}^{\mathrm{C}}$ was determined during the solving of the equation of motion for the undamped cantilever:

$$\omega_{\mathrm{und},1,(1,2)}^{\mathrm{C}} = \pm 3.516 \sqrt{\frac{E_{\mathrm{S304}} \mathcal{I}_{\mathrm{A,y}}}{\rho_{\mathrm{S304}} \mathcal{A}_{\mathrm{B}} L_{\mathrm{B}}^4}} \tag{8.9}$$

from which $\omega_{\mathrm{d},1}^{\mathrm{C}}$ was inferred as per:

$$\omega_{\mathrm{d},1,(1,2)}^{\mathrm{C}} = \omega_{\mathrm{und},1,(1,2)}^{\mathrm{C}} \sqrt{1 - \xi_{\mathrm{S304}} \left(\omega_{\mathrm{d},1,(1,2)}^{\mathrm{C}}\right)^2} \tag{8.10}$$

where $\xi_{\mathrm{S304}} \left(\omega_{\mathrm{d},1,(1,2)}^{\mathrm{C}}\right)$ is the damping ratio at frequencies $\omega_{\mathrm{d},1,(1,2)}^{\mathrm{C}}$. In the following derivation of the relationship between the amplitude of the piezoelectric patch and the blade tip displacement, only positive frequencies were considered, which were simply denoted by $\omega_{\mathrm{und},1}^{\mathrm{C}}$ and $\omega_{\mathrm{d},1}^{\mathrm{C}}$.

After examining the moments and forces exerted on an infinitesimal element of the blade, one arrived at the following equation of motion for the damped cantilever (cf. [448–450]):

$$\rho_{\mathrm{S304}} \mathcal{A}_{\mathrm{B}} \frac{\partial^2 x(t,z)}{\partial t^2} + c_{\mathrm{B}} \left(\omega_{\mathrm{d},1}^{\mathrm{C}}\right) \frac{\partial x(t,z)}{\partial t} + E_{\mathrm{S304}} \mathcal{I}_{\mathrm{A,y}} \frac{\partial^4 x(t,z)}{\partial z^4} = \sum q \tag{8.11}$$

with the damping coefficient $c_{\mathrm{B}} \left(\omega_{\mathrm{d},1}^{\mathrm{C}}\right)$ essentially describing material damping as a function of the damping ratio ξ_{S304} at frequency $\omega_{\mathrm{d},1}^{\mathrm{C}}$:

$$c_{\mathrm{B}} \left(\omega_{\mathrm{d},1}^{\mathrm{C}}\right) = 2 \rho_{\mathrm{S304}} \mathcal{A}_{\mathrm{B}} \omega_{\mathrm{d},1}^{\mathrm{C}} \xi_{\mathrm{S304}} \left(\omega_{\mathrm{d},1}^{\mathrm{C}}\right) \tag{8.12}$$

and the distributed load $q_{\mathrm{PEP}}(t,z)$ due to the external force $f_{\mathrm{PEP}}(t,z)$ with amplitude F_{PEP} exerted on the blade by the piezoelectric patch:

$$\begin{aligned} \sum q = -q_{\mathrm{PEP}}(t,z) &= -\frac{\partial f_{\mathrm{PEP}}(t,z)}{\partial z} \\ &= -\frac{3 F_{\mathrm{PEP}}}{L_{\mathrm{B}}} \left(\frac{z}{L_{\mathrm{B}}} - 1\right)^2 \sin\left(\omega_{\mathrm{d},1}^{\mathrm{C}} t\right) \end{aligned} \tag{8.13}$$

and the area moment of inertia $\mathcal{I}_{\mathrm{A,y}}$ about the y-axis:

$$\mathcal{I}_{\mathrm{A,y}} = \frac{D_{\mathrm{BD}} W_{\mathrm{B}}^3}{12} \tag{8.14}$$

where $x(t,z)$ is the flap-wise displacement of the beam at time t and at distance z to the clamp (disk), $\mathcal{A}_{\mathrm{B}}$ is the cross-sectional area along the longitudinal axis of the blade, and E_{S304} is Young's modulus. The spatial integral of the distributed load $q_{\mathrm{PEP}}(t,z)$ equals $f_{\mathrm{PEP}}(t,z)$ with the point of attack at a z of $\frac{L_{\mathrm{B}}}{4}$ (z_{PEP}), which is the z-coordinate of the centroid of $q_{\mathrm{PEP}}(t,z)$.

The damping ratio ξ_{S304} at frequency $\omega_{\mathrm{d},1}^{\mathrm{C}}$ was approximated to be 3.09e-3 by applying the half power method:

$$\xi_{\mathrm{S304}}\left(\omega_{\mathrm{d},1}^{\mathrm{C}}\right) \approx \frac{\omega_{\mathrm{b},1}^{\mathrm{p}} - \omega_{\mathrm{a},1}^{\mathrm{p}}}{2\omega_1^{\mathrm{p}}} \tag{8.15}$$

where the frequencies in the nominator were measured at $2^{-0.5}\left|H_{\mathrm{M}}\left(\omega_1^{\mathrm{p}}\right)\right|$ on the right side $\left(\omega_{\mathrm{b},1}^{\mathrm{p}}\right)$ and on the left side $\left(\omega_{\mathrm{a},1}^{\mathrm{p}}\right)$ of the greatest peak of first bending mode family of the blade in the FRF. The damping ratio of 304 stainless steel at ω_1^{p} agrees with similar observations in [451].

The flap-wise displacement $x(t,z)$ was expected to have the shape of the first bending mode of the beam, which was established by modal analysis. To obtain the mode shapes, the homogeneous version of Equation (8.11) was defined according to:

$$\rho_{\mathrm{S304}}\mathcal{A}_{\mathrm{B}}\frac{\ddot{\mathfrak{t}}(t)}{\mathfrak{t}(t)} + c_{\mathrm{B}}(\omega_1^{\mathrm{p}})\frac{\dot{\mathfrak{t}}(t)}{\mathfrak{t}(t)} + E_{\mathrm{S304}}\mathcal{I}_{\mathrm{A,y}}\frac{\mathfrak{x}''''(z)}{\mathfrak{x}(z)} = 0 \tag{8.16}$$

The method of the separation of variables ($x(t,z) = \mathfrak{t}(t)\mathfrak{t}(t)$) was already applied with the temporal solution being denoted by $\mathfrak{t}(t)$ and the spatial solution by $\mathfrak{x}(z)$. The temporal derivatives are written in Newton's notation, whereas the spatial derivative in Lagrange's notation. The temporal solution

was customarily assumed to take the form of:

$$\mathfrak{t}(t) = \mathfrak{T} \exp(\nu t) \tag{8.17}$$

with the supposed complex eigenvalues $\nu_{1,2}$:

$$\nu_{1,2} = \left(-\xi_{\mathrm{S304}} \left(\omega_{\mathrm{d},1}^{\mathrm{C}} \right) \pm \sqrt{\xi_{\mathrm{S304}} \left(\omega_{\mathrm{d},1}^{\mathrm{C}} \right)^2 - 1} \right) \omega_{\mathrm{und},1}^{\mathrm{C}} \tag{8.18}$$

where $\mathfrak{T}$ is the complex amplitude. Equation (8.17) was inserted in Equation (8.16) to acquire:

$$\mathfrak{x}''''(z) - \underbrace{(-1) \cdot \left(\frac{\rho_{\mathrm{S304}} \mathcal{A}_{\mathrm{B}} \nu^2}{E_{\mathrm{S304}} \mathcal{I}_{\mathrm{A,y}}} + \frac{c_{\mathrm{B}} \left(\omega_{\mathrm{d},1}^{\mathrm{C}} \right) \nu}{E_{\mathrm{S304}} \mathcal{I}_{\mathrm{A,y}}} \right)}_{=\kappa^4} \mathfrak{x}(z) = 0 \tag{8.19}$$

whose complex solution (mode shapes) for the cantilever in the first bending mode was:

$$\mathfrak{x}(z) = \cosh(\kappa z) - \cos(\kappa z) - \zeta(\sinh(\kappa z) - \sin(\kappa z)) \tag{8.20}$$

with:

$$\zeta = \frac{\cosh(\kappa z) + \cos(\kappa z)}{\sinh(\kappa z) + \sin(\kappa z)}. \tag{8.21}$$

The mode shape with the positive sign was afterwards normalised using $\mathfrak{x}(z = L_{\mathrm{B}})$, then the magnitude was computed before the mode shape was scaled by X_{LDV} in order to build the real-valued steady-state solution $x_{\mathrm{ss}}(t, z)$ of Equation (8.11) at resonance:

$$x_{\mathrm{ss}}(t, z) = X_{\mathrm{LDV}} \left| \frac{\mathfrak{x}(z)}{\mathfrak{x}(z = L_{\mathrm{B}})} \right| \sin\left(\omega_{\mathrm{d},1}^{\mathrm{C}} t - \Delta\theta_{\mathrm{M,PEP\text{-}LDV}} \right) \tag{8.22}$$

which was inserted in Equation (8.11) that was afterwards integrated with respect to z and evaluated at a t of $\frac{\pi}{2\omega_{\mathrm{d},1}^{\mathrm{C}}}$ $(t^\star)$ so as to link the LDV integrated

velocity X_{LDV} with the force amplitude F_{PEP}:

$$F_{\mathrm{PEP}} = -\frac{1}{\sin\left(\omega_{\mathrm{d},1}^{\mathrm{C}} t^{\star}\right)}\left(\rho_{\mathrm{S304}}\mathcal{A}_{\mathrm{B}}\int_{0}^{L_{\mathrm{B}}}\left.\frac{\partial^2 x_{\mathrm{ss}}(t,z)}{\partial t^2}\right|_{t=t^{\star}} dz + c_{\mathrm{B}}\left(\omega_{\mathrm{d},1}^{\mathrm{C}}\right)\int_{0}^{L_{\mathrm{B}}}\left.\frac{\partial x_{\mathrm{ss}}(t,z)}{\partial t}\right|_{t=t^{\star}} dz + E_{\mathrm{S304}}\mathcal{I}_{\mathrm{A,y}}\int_{0}^{L_{\mathrm{B}}}\left.\frac{\partial^4 x_{\mathrm{ss}}(t,z)}{\partial z^4}\right|_{t=t^{\star}} dz\right). \tag{8.23}$$

which helped both to calculate the force in N and to associate this force with the voltage signal of the piezoelectric patch. It is also worth pointing out that any time t could have been picked for Equation (8.23) except those at which the denominator attains zero. When evaluating this equation with a computer, it is recommended that the sine function in the denominator is as distant from its roots as possible in order to improve numerical stability. Any integer multiple of $t^{\star}$ ensures that the force and displacement are at their respective amplitudes, which is valid for linear time-invariant systems like the present one.

Interestingly, the force amplitude F_{PEP} attained 1.43e-1 N, which is 43.87 % (=r_{F}) of the solution obtained with the receptance FRF using Equation (8.8) (3.26e-1 N). It is believed that this discrepancy was essentially caused by ignoring the rest of the blisk in the cantilever model. One can imagine that the excitation produced by a single piezoelectric patch does not only produce the vibration of the blade to which it is attached but also produce vibration that is transmitted to other parts of the blisk. Hence, a greater force is needed in the case of the real blisk to achieve the same tip displacement X_{LDV} as the cantilever model. Additionally, there could have been further unknown and disregarded damping mechanism such as structural damping in the joints between the blisk and other engine components and aerodynamic damping brought about by atmospheric gases, which is usually fairly small for a stationary system compared with mechanical damping. It was therefore decided to compute the calibration curves on the basis of the receptance

FRF. Despite the difficulties in properly modelling the blades, the cantilever beam approach was not developed in vain since it could be adjusted to the real scenario by duly taking the correction factor r_{F} into account. A voltage amplitude of 175 V was capable of generating a force amplitude of 3.26e-1 N $\left(k_{\mathrm{F}} = 1.86\text{e-}3\ \frac{\mathrm{N}}{\mathrm{V}}\right)$ and an absolute amplitude of tip displacement of 1.74 mm as regards the first bending mode family. The force-to-voltage ratio also pertains to the second bending mode family with the difference that a force of 3.26e-1 N causes a smaller tip deflection (1.32 mm) because $\frac{\left|H_{\mathrm{M}}\left(\omega_2^{\mathrm{p}}\right)\right|}{\omega_2^{\mathrm{p}}}$ $\left(4.04\ \frac{\mathrm{mm}}{\mathrm{N}}\right)$ is smaller than $\frac{\left|H_{\mathrm{M}}\left(\omega_1^{\mathrm{p}}\right)\right|}{\omega_1^{\mathrm{p}}}$ $\left(5.33\ \frac{\mathrm{mm}}{\mathrm{N}}\right)$.

The bending stress σ_{SG} and strain ϵ_{SG} in the contact area between the blade and strain gauge at a z of z_{SG} $\left(\frac{L_{\mathrm{B}}}{8}\right)$ was determined pursuant to:

$$\begin{aligned}\sigma_{\mathrm{SG}}(t = t^{\star}, z = z_{\mathrm{SG}}) &= E_{\mathrm{S304}}\epsilon_{\mathrm{SG}}(t = t^{\star}, z = z_{\mathrm{SG}}) \\ &= -\frac{M_{\mathrm{y}}(t = t^{\star}, z = z_{\mathrm{SG}})}{\mathcal{I}_{\mathrm{A,y}}} x_{\mathrm{SG}}\end{aligned} \tag{8.24}$$

with the internal bending moment about the y-axis from the dynamic force and moment equilibria that ignore higher-order differentials:

$$M_{\mathrm{y}}(t, z) = -\frac{1}{r_{\mathrm{F}}} \int_0^z \int_0^{\bar{z}} \left(\rho_{\mathrm{S304}} \mathcal{A}_{\mathrm{B}} \frac{\partial^2 x_{\mathrm{ss}}(t, \tilde{z})}{\partial t^2} + q_{\mathrm{PEP}}(t, \tilde{z})\right) d\tilde{z} d\bar{z} \tag{8.25}$$

where x_{SG} is the location of the strain gauge on the x-axis $\left(\text{-}\frac{W_{\mathrm{B}}}{2}\right)$. The minus sign before M_{y} in Equation (8.24) accounts for the fact that a positive bending moment causes tension at negative x-values in the given coordinate system. The bending moment and thus the bending stress was manipulated by the correction factor r_{F} in order to adjust the cantilever model to the real blade. Eventually, the amplitude of the bending moment was computed to be 3.09 Nm and that of the bending stress was estimated at 115.95 MPa, which is well below the average yield strength of 304 stainless steel (258 MPa reported in [452]) and the fatigue strength of around 180 MPa at 1e8 vibration cycles (cf. [453]), so that vibration occurred in the linear-elastic domain of the material below the endurance limit. The calibration curves that were

based on these quantities enabled one to identify, with respect to the actual flap-wise displacement, the force $f_{\mathrm{PEP}}(t, z)$ induced by the electric patch and the flap-wise bending stress experienced by strain gauge. Furthermore, the actual flap-wise displacement was related to the voltage signal of the capacitive sensor and, thus, implicitly to the blade tip displacement that was measured by the capacitive sensor. This broadened the understanding of the interdependence of the response and excitation signals.

8.2 Experimental results

BLASMA-OPT was applied to experimentally measured data that was recorded during the following two test cases:

(i) **synchronous** *single*-harmonic excitation at 80 Hz (ω_1) with an amplitude of 3.26e-1 N at a rotational speed of 3e2 RPM

(ii) **asynchronous** and **synchronous** *multi*-harmonic excitation at 80 Hz and 504 Hz (ω_1 and ω_2) with amplitudes of 2.33e-2 N and 3.03e-1 N, respectively, at a rotational speed of 3e2 RPM

with any other (global) parameters being kept constant. In order to drive the relatively sturdy blades, the amplifiers of the piezoelectric patches provided the maximum excitation in V that either drove one single mode or was split between two modes. The voltages were converted into forces in N with the help of the force-to-voltage ratio (k_{F}). This was possible because calibration was performed under similar excitation conditions. The frequencies of the two mode families that caused the greatest average responses in the FRF were rounded to integer values in such a way that not only asynchronous but also synchronous blade responses were evoked. This created losses in the average specific resonance amplification of 1.93e3 $\frac{\mathrm{mm/s}}{\mathrm{N}}$ for the first mode family and 7.12e3 $\frac{\mathrm{mm/s}}{\mathrm{N}}$ for the second mode family. The discrepancy between

the loss factors was compensated by exciting the second flap-wise bending mode with a larger force amplitude. Despite the attenuated actuation, the remaining resonance amplification was discovered to be high enough to observe discernible blade responses that have relevance in practice.

After the blades were excited, the blisk was spun from zero to 3e2 RPM (nominal) and given 30 s to reach steady state, which was an empirically found time value that allowed transients to decay. The rotational speed was measured as the average of the rotational speed obtained with the tachometer and the one derived from the position signal of the encoder with the intention of softening the impact of fluctuations in the encoder and tachometer signals that caused the measured rotational speed to scatter around the nominal value. For three reasons, it was decided not to increase the nominal rotational speed beyond 3e2 RPM:

1. it was necessary to ensure that the blade travelling time along the available sensor or the snapshot length was sufficiently large to contain enough data of low-frequency vibration at 80 Hz so that only few revolutions were needed to capture enough data for obtaining the vibration parameters ($\mathcal{O}(1\ \mu\text{s})$), which reduced the amount of data to be recorded.

2. to acquire rotational speed information as accurately as possible, it was considered vital to have encoder and tachometer data concurrently at hand to check two sets of speed data against each other. The encoder signal was less affected by noise than the tachometer signal, whereas the latter did not require to be derived from the position signal as a result of which other errors were introduced. The encoder provided, however, the position data that can be considered the trajectory of a fictitiously rigid blade. The encoder produced in total when both channels were combined 4,096 impulses per revolution, which were 20,480 impulses per second. The maximum sampling rate of the available data acquisition hardware to sample all recorded channels synchronously and coherently was 51.2 kHz samples per second, which had a Nyquist frequency of 25.6 kHz. It was learnt that increasing the speed caused

hardly predictable discontinuities in the encoder signal, making it not usable for the study.

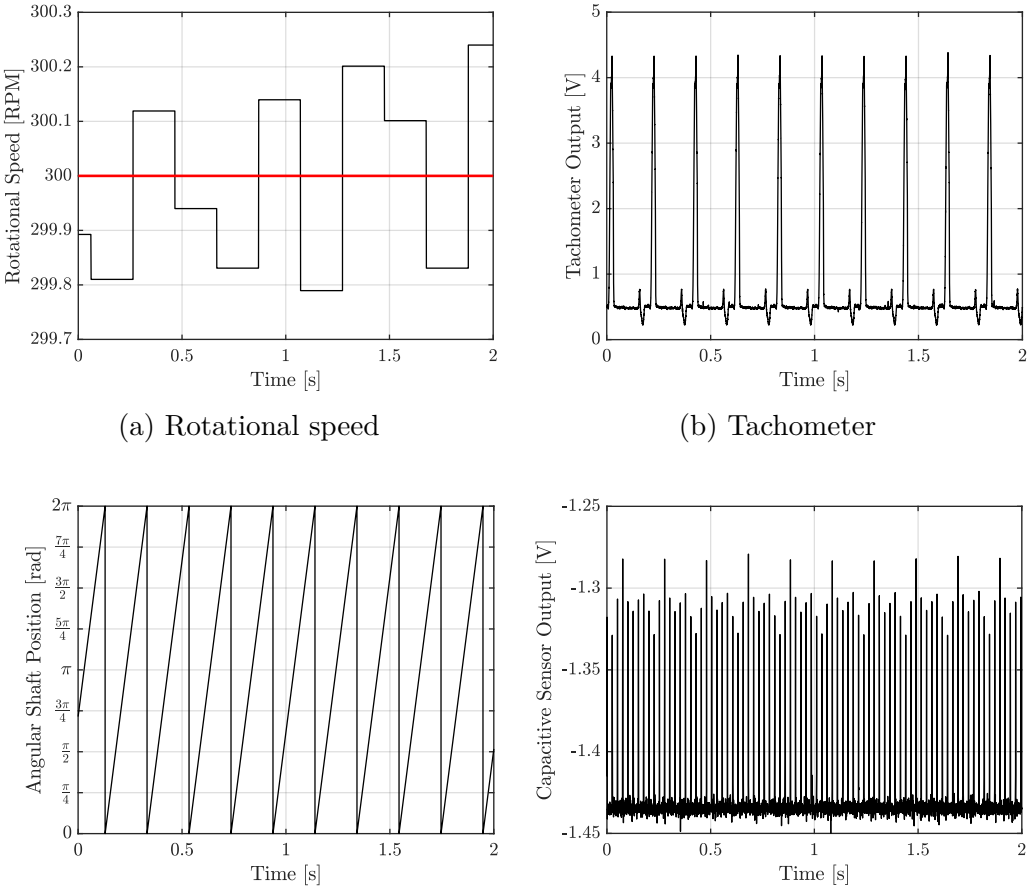
3. there was no significant influence of centrifugal loading on the resonance frequencies with respect to vibration in the plane of rotation, which becomes apparent through the following rough approximation provided by [454]:

$$\omega_{\mathrm{r}} = \sqrt{\omega_{\mathrm{s}}^2 + \left(1.173 + 1.558\frac{R_{\mathrm{D}}}{L_{\mathrm{B}}}\right)\Omega^2} \approx \omega_{\mathrm{s}} \tag{8.26}$$

where ω_{r} is the peak frequency of either mode family in the rotating frame of reference at an Ω of 3e2 RPM and ω_{s} in the inertial frame of reference.

The courses of the global parameters, namely rotational speed, the shaft position, and tachometer signal, that were relevant for both experimental studies are presented as a function of time during the first two seconds of data recording in Figures 8.10(a)–8.10(c). The shaft position based on the encoder signal was wrapped to the interval of $[0,2\pi]$ rad. The encoder was adjusted in such a way that it marked a new revolution when blade 1 was right beneath the capacitive sensor. The tachometer output reached a peak when blade 3 was below the sensor. This shift in impulse production had a smoothing effect on the average of the rotational speed. It has to be borne in mind though that the fluctuations in the rotational speed were inevitably perpetual, which can be seen in Equation (8.5). Any deviation from the nominal rotational speed was counteracted by the PID motor controller. Especially because of the relatively large inertia of the blisk, this required a certain amount of time to take effect during which the actual speed was changing again, thereby making it impossible to seriously rid oneself of this nuisance.

The output of the capacitive sensor is depicted from afar in Figure 8.10(d) to show the variability in the waveform amplitudes, which, apart from noise, was mainly due to the following circumstances:



(a) Rotational speed

(b) Tachometer

(c) Shaft position

(d) Capacitive sensor

Figure 8.10: Measurements of global parameters

1. the blades were differently long
2. fluctuations in the rotational speed

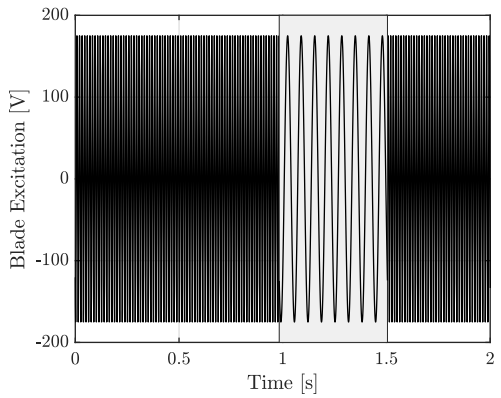
which both affected the clearance between the blades and the sensor. The plot does not invite to see any impacts of vibration on the waveforms, yet it allows distinguishing between consecutive waveforms and assigning single waveforms to blades more easily (e.g., by peak picking) for subsequent processing. The accelerometer, which was attached to the sensor mount, continuously produced data with which the position of the sensor could be monitored. Fortunately, the casing was rigid enough to avoid any significant change in the sensor

position. Any sensor acceleration was not distinguishable from the noise in the output of the accelerometer.

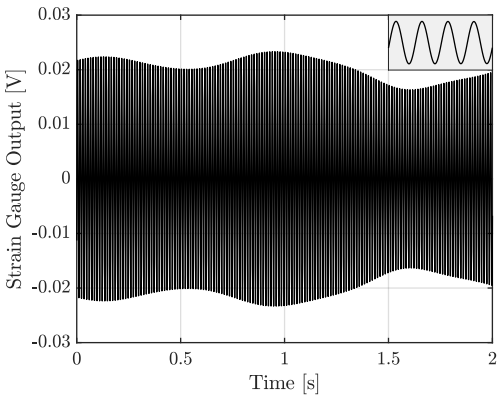
The data analysis shared some similarity with the one of the numerical investigation of BLASMA-OPT in Chapter 7 but differed in that experimentally measured waveforms were directly inserted in the optimisation routine and not only used to build the sensor model. For the experimental investigation, each waveform was linked to its own sensor model to take the fact into account that experimental waveforms varied amongst themselves. The amplitude boundaries for the optimisation problem where adopted from the previous studies; however, the frequency boundaries were reduced to intervals of [0.5,1.5] of the resonance frequencies to expedite convergence of the vibration parameters. The lower frequency boundary was determined by the smallest excitation frequency, whilst the upper boundary was based on the largest one. When running an engine, it is generally helpful to have an idea about potential blade responses in order to be able to decipher the measurement data. The starting points of the optimisation for the amplitudes were at the lower amplitude boundary and those for the frequencies at 80 % of the expected resonance frequencies. Phases were not investigated because of the reasons mentioned in Section 8.1.4.1 and the difficulty of separating the densely spaced modes of any of the two mode families alluded to in Section 8.1.3. It also made little sense to include traditional BTT analysis considering that the sampling frequency of TOA data would have had the same magnitude as the rotational speed (5 Hz).

8.2.1 Synchronous single-harmonic excitation of the blades

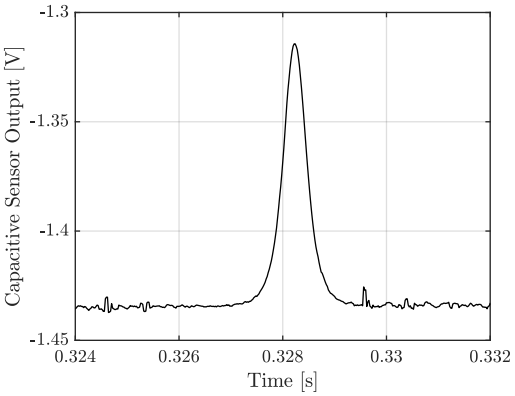
Each blade was excited by a single-harmonic force at 80 Hz, which gave rise to vibration at engine-order number 16 at the nominal rotational speed. When being completely accurate, there was no perfect synchronous vibration due to the unavoidable variations in the rotational speed, which was a necessary



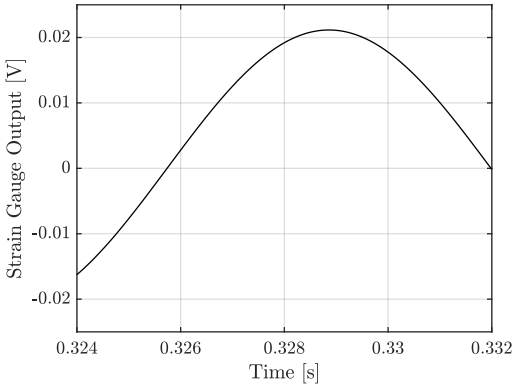
(a) Piezoelectric patch signal – with a zoomed-in view in grey ( )



(b) Strain gauge signal – with a zoomed-in view in grey ( )



(c) Waveform



(d) Section of the strain gauge signal corresponding to the waveform in (c)

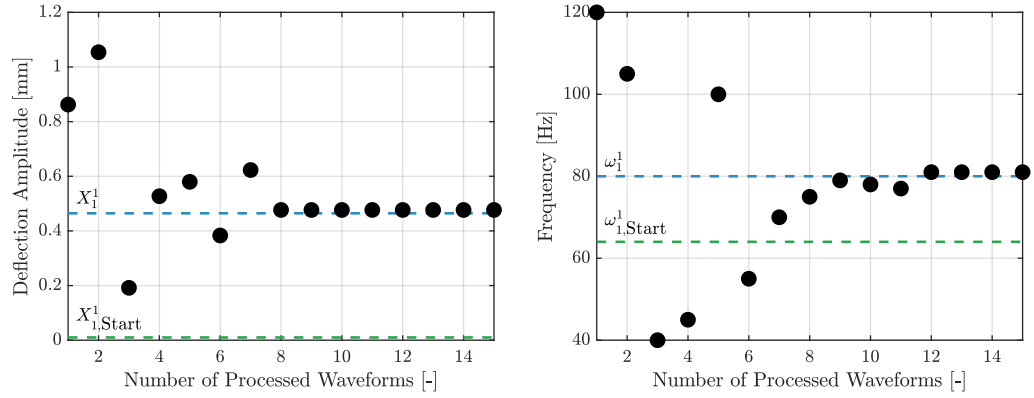
Figure 8.11: Excitation and response signals from the synchronous single-harmonic excitation study

evil in conducting experiments. With the largest deviation from the nominal rotational speed being smaller than 0.3 RPM, the divergence from synchronous vibration was quantified in terms of engine-order numbers at not greater than |±2e-2|, which was deemed negligible.

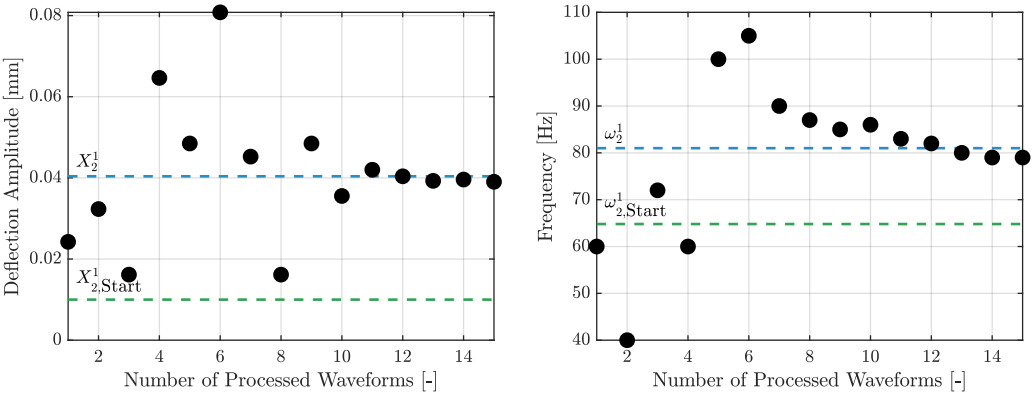
Since the results of all blades were of comparable quality, the ones belonging to blade 1 were selected for discussion. The excitation and response signals are displayed in Figures 8.11(a)–8.11(d) over the course of two seconds. The

excitation signal of the piezoelectric patch was taken from the monitoring channel of the respective amplifier and manipulated in such a way that it typified the expected true excitation signal sent to the blade for inducing vibration. Apparently, this excitation signal must have been slightly and unintentionally altered during the transmission from the stationary amplifier to the rotating blisk, which did not occur at engine halt and only became apparent when eyeing the strain gauge readings because of the inaccessibility to real actuation data. Several attempts at substantially mitigating this problem by investigating and exchanging electrical components along the transmission failed to bear fruits. As a consequence, one had to deal with the fact that multi-harmonic vibration in form of beat vibration existed, which is exhibited in Figure 8.11(b). To highlight beating, the strain gauge signal was bandpass-filtered in the same way as described in Section 8.1.4. The author is convinced that the closeness of the resonance frequencies of the first bending mode family contributed to the occurrence of this phenomenon. After analysing the strain gauge measurements, it stood to reason that vibration at 80 Hz was dominant accompanied by another signal component at 81 Hz with its amplitude being an order of magnitude smaller. The latter oscillatory constituent seemed unwilling to decay even after offering the system additional time to stabilise itself.

A waveform produced by the capacitive sensor is presented in Figure 8.11(c) that is juxtaposed with the strain gauge signal at the time (see Figure 8.11(d)). Waveforms like this one were modulated by blade vibration whose parameters were to be determined using BLASMA-OPT. The vibration parameters (black dots (●)), namely two deflection amplitudes and frequencies, are shown as a function of the number of processed waveforms in Figures 8.12(a)–8.12(d). The optimiser started its search from the values denoted by green dashed lines (---). All vibration parameters have in common that they quite heavily and almost arbitrarily scatter for small sets of waveform data. After a certain number of waveforms was submitted to the optimisation routine, the errors in the vibration parameters entered the interval of ±5 % with regard to the actual values, which are depicted as blue dashed lines (---) in the graph.



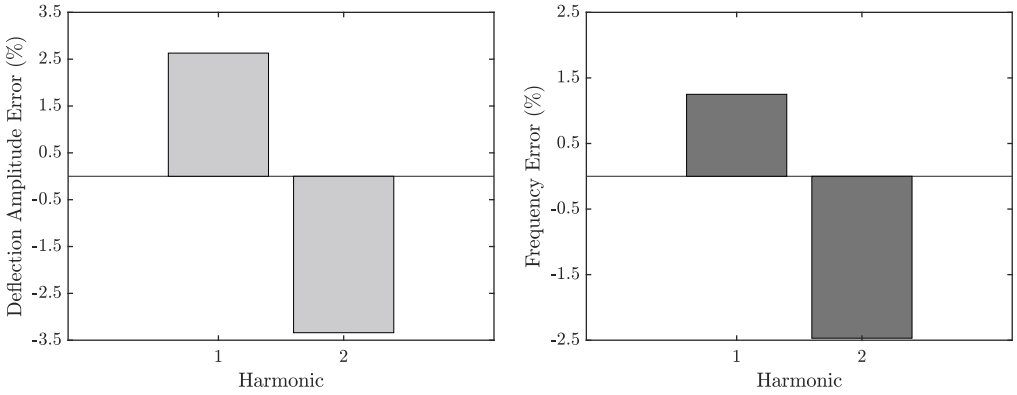
(a) Vibration deflection amplitude X_1^1 (b) Vibration frequency ω_1^1



(c) Vibration deflection amplitude X_2^1 (d) Vibration frequency ω_2^1

Figure 8.12: Results from the study of single-harmonic excitation

The actual values only serve as a benchmark against which the final BLASMA-OPT amplitudes and frequencies are compared. The amplitude of the 80-Hz harmonic (4.65e-1 mm) was ascertained with the help of the calibration data. In contrast, the amplitude of the unexpected 81-Hz harmonic (4.04e-2 mm) was established by multiplying the amplitude of the 80-Hz harmonic and the voltage ratio of the two harmonics from an FFT of the strain gauge signal. It comes to light that the amplitude and frequency of the first harmonic required the least amount of waveform data to converge, which is not unexpected given that this harmonic is dominant in the signal. The errors after processing fifteen waveforms are disclosed in Figures 8.13(a)–8.13(b) with the largest absolute error in amplitude being smaller than 3.5 % and that in frequency



(a) Vibration deflection amplitudes (b) Vibration frequencies

Figure 8.13: Errors in vibration properties in the case of single-harmonic excitation

than 2.5 %. It is also obvious that the errors in the vibration parameters for the dominant harmonic were the least. It would have been interesting to see the development of the errors without the presence of the unavoidable 81-Hz harmonic.

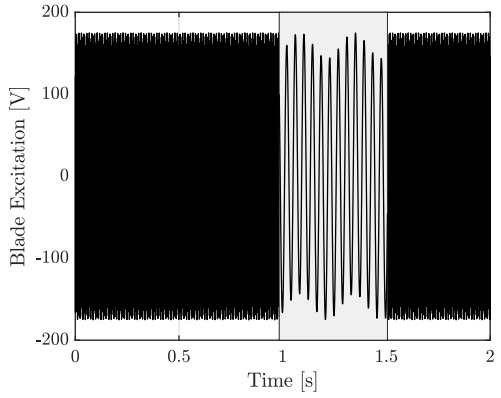
Despite being in the desired interval of accuracy, the errors could have potentially been improved when the optimiser would have been provided with even more waveforms; yet, there was a trade-off to be made between accuracy and processing time. Considering that there were 21 channels (8 strain gauges, 8 piezoelectric patches, 1 actuation monitoring channel, 1 capacitive sensor, 1 accelerometer, 1 tachometer, and 1 encoder), the number of data samples produced per second was greater than 1e6 and the required storage capacity per second was approximately 125 $\frac{\text{MB}}{\text{s}}$ for such a relatively simple test rig, let alone real engines. Being a limited quantity in online vibration monitoring, the time needed to process this data generally grows exponentially. It was therefore crucial that the methodology only depended on average computer performance and storage capacity.

8.2.2 Asynchronous and synchronous multi-harmonic excitation of the blades

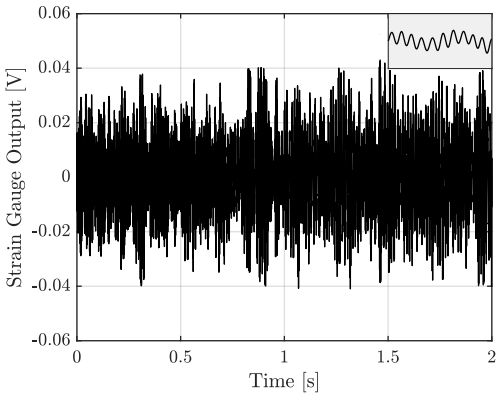
The blades were now intentionally excited in a multi-harmonic fashion at 80 Hz and 504 Hz, which was supposed to create synchronous and asynchronous vibration at the nominal rotational speed with engine order numbers of 16 and 100.8, respectively. The variation in the former was kept at the same level as in the previous study and that in the latter was calculated to be less than |±1e-1|, which made the second harmonic truly asynchronous at all times. The excitation and response signals are revealed in Figures 8.14(a)–8.14(d). Most of the pertinent explanation from the above section applies here too. A noteworthy difference is that the strain gauge signal was again filtered but with the bandpass on this occasion being between 65 Hz and 520 Hz. Therefore, more unwanted noise exists in the signal, which makes it more challenging to interpret the measurements. An analysis of the frequency spectrum of the strain gauge signal nevertheless confirmed that the desired frequency components were prominent.

In the previous study it became evident that excitation at 80 Hz caused an adjacent mode to become active under rotation. Since this time the 80-Hz excitation harmonic was assigned a smaller force amplitude, the 81-Hz harmonic became indistinguishable from background noise and thus of peripheral concern. The second excitation harmonic at 504 Hz gave also rise to adjacent modes, but thanks to the steep shape of the main resonance peak of the second bending mode family (cf. Figure 8.6(b)), the magnitudes of accompanying modes were too little to be worth of consideration regardless of exciting the second bending mode exclusively or in conjunction with the first one within the available voltage range of the actuators.

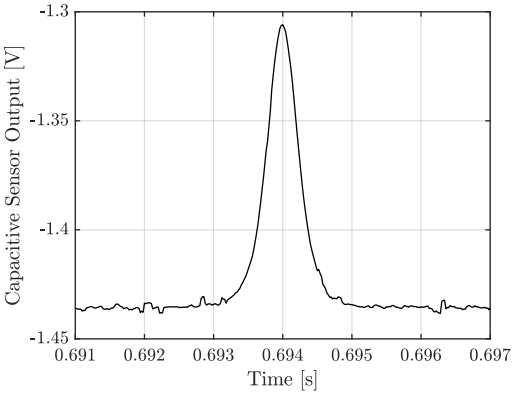
The results of all four vibration parameters are exhibited in Figures 8.15(a)–8.15(d). The style of the graphs and the amount of processed waveform was kept, and the amplitudes of both harmonics were determined to be 3.61e-02 mm for the 80-Hz and 5.43e-01 mm for the 504-Hz signal compo-



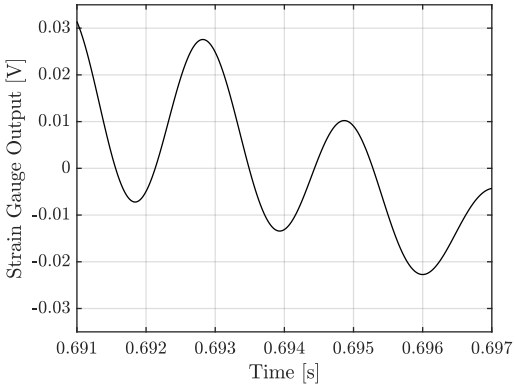
(a) Piezoelectric patch signal – with a zoomed-in view in grey ( )



(b) Strain gauge signal – with a zoomed-in view in grey ( )



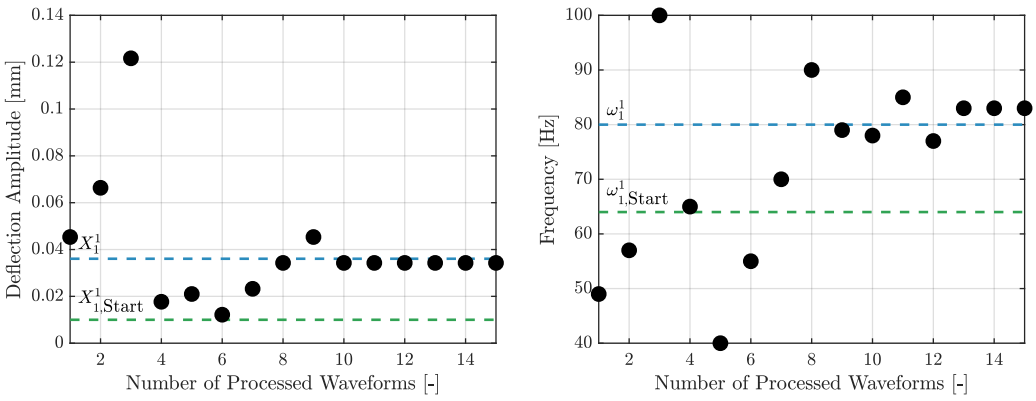
(c) Waveform



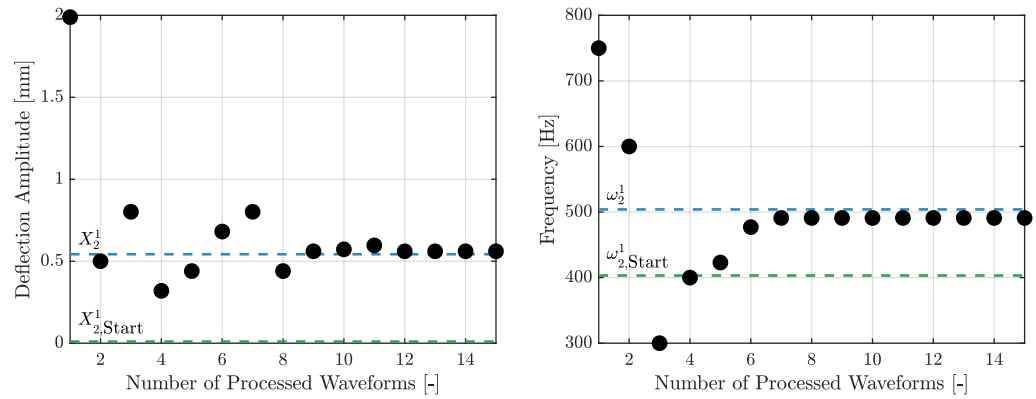
(d) Section of the strain gauge signal corresponding to the waveform in (c)

Figure 8.14: Excitation and response signals from the asynchronous and synchronous multi-harmonic excitation study

nents on the basis of calibration data. The amplitude and frequency of the higher harmonic stay after nine waveforms within the desired error bounds, followed by the amplitude of the 80-Hz harmonic that needs another waveform. Contrarily, the frequency of the latter mode requires thirteen waveforms of the capacitive sensor to celebrate the same accomplishment. In addition to its dependence on the dominance of one or more harmonics over others, the speed of convergence is clearly linked to the amount of harmonic-specific vibration data that can be extracted from a waveform. Balanced against the



(a) Vibration deflection amplitude X_1^1 (b) Vibration frequency ω_1^1

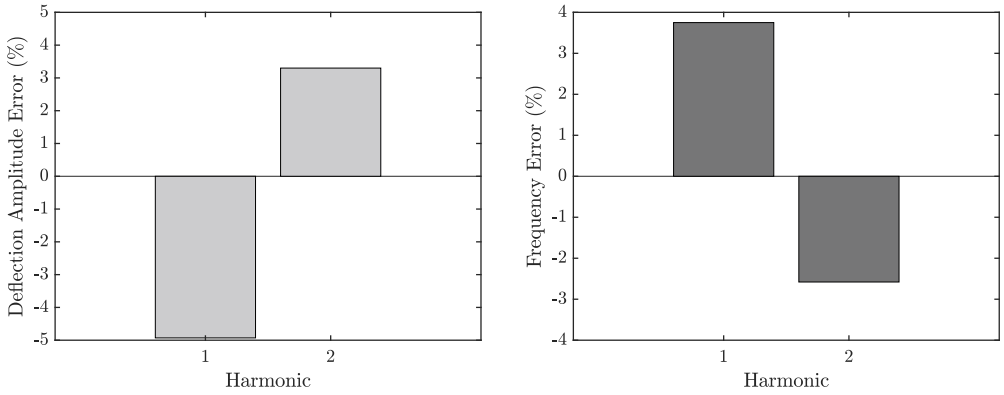


(c) Vibration deflection amplitude X_2^1 (d) Vibration frequency ω_2^1

Figure 8.15: Results from the study of multi-harmonic excitation

case of a 80-Hz harmonic, more insightful information about the vibration cycle of the 504-Hz is contained in a waveform.

The errors based on the analysis of fifteen waveforms are detailed in Figures 8.16(a)–8.16(b). It seems that there is some correlation between the speed of convergence and the error magnitude. The errors of the amplitude and frequency of the first harmonic are -4.93 % and 3.75 %, respectively, whereas the corresponding ones of the second harmonic attain 3.3 % and -2.58 %. Hence, the absolute error in each parameter dimension of the latter harmonic is more than one percentage point smaller.



(a) Vibration deflection amplitudes (b) Vibration frequencies

Figure 8.16: Errors in vibration properties in the case of multi-harmonic excitation

8.3 Conclusion

A test rig was introduced that produced valuable data for the assessment of BLASMA. The components and limitations of the rig were discussed with respect to their implications for the scope of the measurement campaign. On this account, the state of mistuning of the blisk was determined, which was succeeded by the calibration of the entire system so as to relate excitation and response signals and to be able to estimate the displacement of the blade tip in the rotating reference frame. Two controlled experimental studies were conducted: the first one was meant to understand the behaviour of the blisk when there was only a single synchronous excitation frequency and the second one aimed at the same but with two excitation frequencies that caused asynchronous and synchronous responses. In the discourse on the findings of these studies, it was referred to the general uncertainty of not knowing all excitation sources when taking measurements on rotating structures. Eliminating this uncertainty for a given system is only possible when there is a working method that produces reliable information on the vibration characteristics of the blisk. Being the method that was used to retrieve the vibration parameters from waveforms, BLASMA-OPT was capable

of establishing the vibration state that best fitted to the present conditions, which was independently confirmed by the analysis of strain gauge data. The results of the amplitudes and frequencies obtained are within the industrial error standard of ±5 %. In the last chapter of this work, recommendations are offered on how to proceed hereupon.

Chapter 9

Contributions and outlook

The objective of this work was to venture on a new route to blade vibration monitoring. A novel methodology, Blade Tip-Timing (BTT) and clearance sensor waveform analysis (BLASMA), for investigating blade vibration with traditional BTT hardware was developed. BLASMA is in stark contrast to other, elsewhere proposed BTT methods since BLASMA does not rely on under-sampled, single-point-based TOA data. Instead, complete sensor waveforms that characterise the entire passage of the blade beneath the sensor are processed to determine the vibration parameters using three different algorithms: BLASMA-SCP (Signal Characteristics Processing), BLASMA-IWE (Inverse Waveform Equation), and BLASMA-OPT (Optimisation). Simulations were conducted to evaluate these methods numerically and to weigh their strengths and weaknesses against each other. Respective case studies put emphasis on single-harmonic and multi-harmonic blade vibration. Emerging as the most promising of three, BLASMA-OPT underwent additional testing on experimentally measured data for which a test rig was built. The major contributions of this PhD project are humbly summarised as follows:

1. An exhaustive literature database was created that offers a detailed overview on every aspect of BTT and enables one to recognise fresh research paths in the field of vibration monitoring, such as the one of this work on the basis of waveform processing. This tool greatly facilitates the ability to separate one's work from that of other members of the research community in order to avoid unnecessary repetition of existing knowledge.

2. The methods treated herein can be applied alongside BTT; hence, their integration into an existing measurement infrastructure can be easily achieved without requiring large financial resources. Moreover, BLASMA has a modular structure that can accommodate additional methods to deal with any kind of waveform and vibration phenomena.

3. The solutions scrutinised only rely on the employment of a single sensor to address situations where there is a restriction on the number of sensors or where BTT is not capable of producing useful vibration data; nonetheless, they are scalable to such an extent that data from multiple sensors can be combined to further reduce errors and permit the examination of even more complex vibration that was outside the purview of this project.

The work done on waveform processing serves as a proof of concept from which the author's successors may continue their research. Below is an action plan for future activities with items being listed in descending order of importance felt by the author:

1. BLASMA methods should be enhanced for the purpose of processing experimentally measured waveforms immediately after the waveforms have been recorded during operation. It is also advised that all methods be benchmarked against each other not only with respect to their capability and accuracy but also with respect to their computational efficiency in the light of limited computer power on-board real engines.

2. The ideal field of view of the sensor should be identified on the basis of several common bladed disk geometries so that the casing integrity is ensured, waveforms of neighbouring blades do not overlap, and waveforms can contain a relatively large snapshot of the blade vibration trajectory, keeping in mind that the blade travelling time along the sensor or the snapshot width is a critical parameter. A possible scenario would be to use a single but wider and perhaps slightly bent sensor, which would be

flush-mounted on the casing circumference at a rotor stage. It would be helpful to have great flexibility in the positioning of the sensor.

3. Sensor modelling requires some attention to further increase measurement accuracy for different engine conditions. Instead of fitting a mathematical model to already measured waveforms, one should try to access the real sensor function designed by the manufacturer or even create a sensor with a customised function that can potentially be more beneficial to the analysis of blade vibration.

4. There are questions to be answered of how the capability of BLASMA is affected by measurement uncertainty, e.g., from sensor position errors due to casing vibration.

5. Experimental work with authentic BTT hardware that is specially made for vibration monitoring should be carried out so as to establish the level of improvement in comparison with the results of the present work.

6. BLASMA should be applied under cruise conditions to record and analyse genuine vibration data.

7. It is recommended that a database of waveforms for various engine conditions be created, which is expected to be of use in connection with machine learning techniques (such as pattern recognition), statistical evaluation, and Monte Carlo simulations. By doing so, one would gain a better understanding of the variance of waveforms as a function of the state of operation.

8. Learning from other prospective areas of application (such as gearboxes, turbochargers, and wind turbines) can lead to alternative ways of evolving waveform processing.

Bibliography

[1] J. S. Rao, *Turbomachine Blade Vibration*. Wiley & Sons, 1991.

[2] S. S. Manson, A. J. Mayer (Jr.), H. F. Calvert, and M. P. Hanson, "Factors Affecting Vibration of Axial-Flow Compressor Blades," *Proceedings of the Society for Experimental Stress Analysis*, vol. 7, no. 2, pp. 1–15, 1948.

[3] A. Kühhorn and J. Nipkau, "On the Influence of Strain Gauge Instrumentation on Blade Vibrations of Integral Blisk Compressor Rotors Applying a Discrete Model," *Proceedings of ASME Turbo Expo*, no. GT2009-59207, pp. 245–253, 2009.

[4] P. Russhard, "The Rise and Fall of the Rotor Blade Strain Gauge," *Proceedings of the VETOMAC X*, pp. 27–37, 2014.

[5] J. Szwedowicz, S. M. Senn, and R. S. Abhari, "Optimum Strain Gauge Application to Bladed Assemblies," *Proceedings of ASME Turbo Expo*, no. GT2002-30306, pp. 725–733, 2002.

[6] D. L. Gillaugh, A. A. Kaszynski, J. M. Brown, D. A. Johnston, and J. C. Slater, "Accurate Strain Gauge Limits Through Geometry Mistuning Modeling," *Journal of Propulsion and Power*, vol. 34, no. 6, pp. 1401–1408, 2018.

[7] V. E. H. Ellis, "Vibration Monitoring in Rotary Machines," 1986.

[8] J. F. Wolfinger, A. S. Assa, and J. M. Reschovsky, "Apparatus and Method for Measuring Vibration of a Rotating Member," 1988.

[9] J. Frischbier, G. Schulze, M. Zielinski, G. Ziller, C. Blaha, and D. K. Hennecke, "Blade Vibrations of a High Speed Compressor Blisk-Rotor - Numerical Resonance Tuning and Optical Measurements -," *Proceedings*

of the ASME International Gas Turbine and Aeroengine Congress and Exhibition, no. 96-GT-24, pp. 1–7, 1996.

[10] B. J. Halkon and S. J. Rothberg, "Vibration measurements using continuous scanning laser Doppler vibrometry: theoretical velocity sensitivity analysis with applications," *Measurement Science and Technology*, vol. 14, pp. 382–393, 2003.

[11] I. A. Sever, *Experimental Validation of Turbomachinery Blade Vibration Predictions*. PhD thesis, University of London, 2004.

[12] T. Pfister, L. Büttner, J. Czarske, H. Krain, and R. Schodl, "Turbo machine tip clearance and vibration measurements using a fibre optic laser Doppler position sensor," *Measurement Science and Technology*, vol. 17, pp. 1693–1705, 2006.

[13] F. Dreier, T. Pfister, and J. Czarske, "Monitoring of Blade Vibrations and Tip Clearance at Non-Metallic Rotors in Turbo Machines," *Proceedings of ASME Turbo Expo*, no. GT2012-69540, pp. 1–10, 2012.

[14] T. Pfister, P. Günther, F. Dreier, and J. Czarske, "Novel Dynamic Rotor and Blade Deformation and Vibration Monitoring Technique," *Proceedings of ASME Turbo Expo*, no. GT2011-45346, pp. 1–10, 2011.

[15] F. Dreier, P. Günther, T. Pfister, J. W. Czarske, and A. Fischer, "Interferometric Sensor System for Blade Vibration Measurements in Turbomachine Applications," *IEEE Transactions on Instrumentation and Measurement*, vol. 62, no. 8, pp. 2297–2302, 2013.

[16] M. Neumann, F. Dreier, P. Günther, A. Fischer, J. Czarske, F. Holzinger, and H.-P. Schiffer, "A Laser-Optical Sensor System for Simultaneous Tip Clearance and Vibration Monitoring of Compressor Rotor Blades," *Proceedings of ASME Turbo Expo*, no. GT2014-25335, pp. 1–9, 2014.

[17] M. Neumann, F. Dreier, P. Günther, U. Wilke, A. Fischer, L. Büttner, F. Holzinger, H.-P. Schiffer, and J. Czarske, "A laser-optical sensor

system for blade vibration detection of high-speed compressors," *Mechanical Systems and Signal Processing*, vol. 64-65, pp. 337–346, 2015.

[18] J. E. Hancox and R. J. Parker, "A Novel Scanning Laser-Doppler Vibrometer," *Rolls-Royce Report PVK1-28D*, 1987.

[19] J. E. Hancox, "Application of the ARL Scanning Laser Doppler Vibrometer to a Rotating Test Piece," *Rolls-Royce Report RR(OH)1088*, 1990.

[20] I. A. Sever, A. B. Stanbridge, and D. J. Ewins, "Turbomachinery Blade Vibration Measurements with Tracking LDV under Rotation," *Proceedings of SPIE*, vol. 6345, no. 63450L, pp. 1–10, 2006.

[21] D. Di Maio, *SLDV Technology for Measurement of Mistuned Bladed Disc Vibration*. PhD thesis, University of London, 2007.

[22] M. T. Endo, A. N. Montagnoli, and R. Nicolleti, "Measurement of Rotor Vibration Through Photographic Images," *Proceedings of the 22nd International Congress of Mechanical Engineering*, pp. 442–448, 2013.

[23] P. Neri and B. Peeters, "Non-Harmonic Fourier Analysis for bladed wheels damage detection," *Journal of Sound and Vibration*, vol. 356, pp. 181–194, 2015.

[24] J. Ratz, G. L. Forbes, and R. B. Randall, "Gas Turbine Blade Natural Frequency Measurement Using External Casing Vibrations," *Proceedings of the 59th International Instrumentation Symposium and MFPT Conference*, pp. 1–10, 2013.

[25] J. R. Cox, S. A. Arnold, and P. Anusonti-Inthra, "Rotor Blade Fault Detection through Statistical Analysis of Stationary Component Vibration," *Proceedings of the 52nd AIAA/SAE/ASEE Joint Propulsion Conference*, no. AIAA 2016-4642, pp. 1–21, 2016.

[26] A. P. Kurkov, "Flutter Spectral Measurements Using Stationary Pressure Transducers," *Journal of Engineering for Power*, vol. 103, no. April 1981, pp. 461–467, 1981.

[27] R. L. Matusheski, R. Colsher, and A. L. Moffa, "Turbine Blade Monitoring Using Acoustic Pressure Sensors," *Proceedings of the Steam and Combustion Turbine-Blading Conference and Workshop*, no. 5, pp. 21–48, 1992.

[28] G. L. Forbes and R. B. Randall, "Estimation of turbine blade natural frequencies from casing pressure and vibration measurements," *Mechanical Systems and Signal Processing*, vol. 36, pp. 549–561, 2013.

[29] W. L. Murray III and N. L. Key, "Detection of Rotor Forced Response Vibrations Using Stationary Pressure Transducers in a Multistage Axial Compressor," *International Journal of Rotating Machinery*, no. 198534, pp. 1–10, 2015.

[30] Q. V. Davis and W. K. Kulczyk, "Vibrations of Turbine Blades measured by Means of a Laser," *Nature*, vol. 222, no. 5192, pp. 475–476, 1969.

[31] V. Badami, "GE Perspective on Tip-Timing, Panel Session (Panel Session on State-of-the-Art and Future Developments of Tip Timing)," *Proceedings of ASME Turbo Expo*, no. GT2012-70188, 2012.

[32] C. Vining, "Introduction and History of Tip-Timing (Panel Session on State-of-the-Art and Future Developments of Tip Timing)," *Proceedings of ASME Turbo Expo*, no. GT2012-70185, 2012.

[33] M. Zielinski, "MTU Perspective on Tip-Timing (Panel Session on State-of-the-Art and Future Developments of Tip Timing)," *Proceedings of ASME Turbo Expo*, no. GT2012-70184, 2012.

[34] P. Russhard, "RR Perspective on Tip-Timing (Panel Session on State-of-the-Art and Future Developments of Tip Timing)," *Proceedings of ASME Turbo Expo*, no. GT2012-70187, 2012.

[35] M. Mittelbach, "Siemens Perspective on Tip-Timing (Panel Session on State-of-the-Art and Future Developments of Tip Timing)," *Proceedings of ASME Turbo Expo*, no. GT2012-70189, 2012.

[36] B. Klein, "Tip-Timing Measurements on Turbochargers (Panel Session on State-of-the-Art and Future Developments of Tip Timing)," *Proceedings of ASME Turbo Expo*, no. GT2012-70186, 2012.

[37] I. A. Sever, "State-of-the-Art BTT," *Rolls-Royce Report*, no. October, 2016.

[38] P. Russhard and J. D. Back, "Method for analysing vibration in rotor blades," 2014.

[39] H.-P. Dickmann, T. Secall Wimmel, J. Szwedowicz, D. Filsinger, and C. H. Roduner, "Unsteady Flow in a Turbocharger Centrifugal Compressor: Three-Dimensional Computational Fluid Dynamics Simulation and Numerical and Experimental Analysis of Impeller Blade Vibration," *Journal of Turbomachinery*, vol. 128, no. July 2006, pp. 455–465, 2006.

[40] K. Vogel, A. D. Naidu, and M. Fischer, "Comparison of the Influence Coefficient Method and Travelling Wave Mode Approach for the Calculation of Aerodynamic Damping of Centrifugal Compressors and Axial Turbines," *Proceedings of ASME Turbo Expo*, no. GT2017-64643, pp. 1–9, 2017.

[41] D. Heller, I. Sever, and C. W. Schwingshackl, "Vibration Analysis Using Blade Tip-Timing Sensor Signals," *Proceedings of the Engineering Integrity Society Conference*, pp. 1–10, 2018.

[42] D. Heller, I. Sever, and C. W. Schwingshackl, "Vibration Analysis from Simulated Tip Timing Sensor Signal Shape Modulation," *Proceedings of ASME Turbo Expo*, no. GT2018-75010, pp. 1–16, 2018.

[43] T. Nicholas and J. R. Zuiker, "On the use of the Goodman diagram for high cycle fatigue design," *International Journal of Fracture*, vol. 80, no. 2-3, pp. 219–235, 1996.

[44] D. S. Whitehead, "Aerodynamic Aspects of Blade Vibration," *Proceedings of the Institution of Mechanical Engineers*, vol. 180, no. 9, pp. 49–60, 1965.

[45] J. J. Kielb and R. S. Abhari, "Experimental Study of Aerodynamic and Structural Damping in a Full-Scale Rotating Turbine," *Journal of Engineering for Gas Turbines and Power*, vol. 125, no. January 2003, pp. 102–112, 2003.

[46] J. H. Griffin, "A Review of Friction Damping of Turbine Blade Vibration," *International Journal of Turbo and Jet Engines*, vol. 7, pp. 297–307, 1990.

[47] Universal Technology Corporation, "High Cycle Fatigue (HCF) Science and Technology Program 2001 Annual Report," *US Air Force Publications*, no. AFRL-PR-WP-TR-2002-2060, 2002.

[48] N. A. Cumpsty, *Compressor Aerodynamics*. Krieger Publishing, 5 ed., 2004.

[49] M. I. Friswell, J. E. T. Penny, S. D. Garvey, and A. W. Lees, *Dynamics of Rotating Machines*. Cambridge University Press, 2010.

[50] H. Ma, Y. Lu, Z. Wu, X. Tai, H. Li, and B. Wen, "A new dynamic model of rotor–blade systems," *Journal of Sound and Vibration*, vol. 357, pp. 168–194, 2015.

[51] V. Ruffini, C. Schwingshackl, and J. Green, "Experimental and Analytical Study of Coriolis Effects in Bladed Disk," *Proceedings of the ASME International Design Engineering Technical Conferences & Computers and Information in Engineering Conference*, no. DETC2015-46621, pp. 1–10, 2015.

[52] V. Ruffini, J. S. Green, and C. W. Schwingshackl, "The Influence of Mistuning and Coriolis Effects on the Modal Parameters of Bladed Discs: An Experimental Study," *Proceedings of ASME Turbo Expo*, no. GT2017-63437, pp. 1–12, 2017.

[53] S. C. Stapelfeldt, *Advanced methods for multi-row forced response and flutter computations*. PhD thesis, Imperial College London, 2014.

[54] R. E. Kielb, J. W. Barter, J. P. Thomas, and K. C. Hall, "Blade Excitation by Aerodynamic Instabilities – A Compressor Blade Study," *Proceedings of ASME Turbo Expo*, no. GT2003-38634, pp. 1–8, 2003.

[55] C. Hah, M. Voges, M. Mueller, and H.-P. Schiffer, "Characteristics of Tip Clearance Flow Instability in a Transonic Compressor," *Proceedings of ASME Turbo Expo*, no. GT2010-22101, pp. 1–12, 2010.

[56] J. Schreiber, *Investigation of experimental and numerical methods, and analysis of stator clocking and instabilities in a high-speed multistage compressor*. PhD thesis, École Centrale de Lyon, 2016.

[57] D. J. Ewins, *Modal Testing - Theory, Practice and Application*. Research Studies Press, 2 ed., 2000.

[58] D. Vogt, "Turbomachinery Blade Vibrations – Meeting the Challenge," *Proceedings of ISROMAC*, pp. 1–81, 2012.

[59] M. Vahdati, A. I. Sayma, J. G. Marshall, and M. Imregun, "Mechanisms and Prediction Methods for Fan Blade Stall Flutter," *Journal of Propulsion and Power*, vol. 17, no. 5, pp. 1100–1108, 2001.

[60] T. Miyakozawa, *Flutter and Forced Response of Turbomachinery with Frequency Mistuning and Aerodynamic Asymmetry*. PhD thesis, Duke University, 2008.

[61] Y. J. Chan, *Variability of Blade Vibration of Mistuned Bladed Discs*. PhD thesis, University of London, 2009.

[62] M. Nikolic, *New Insights Into the Blade Mistuning Problem*. PhD thesis, University of London, 2006.

[63] K. Ekici, R. E. Kielb, and K. C. Hall, "The effect of aerodynamic asymmetries on turbomachinery flutter," *Journal of Fluids and Structures*, vol. 36, pp. 1–17, 2013.

[64] D. S. Whitehead, "Effect of Mistuning on the Vibration of Turbo-Machine Blades Induced by Wakes," *Journal of Mechanical Engineering Science*, vol. 8, no. 1, pp. 15–21, 1966.

[65] B. Beirow, F. Figaschewsky, A. Kühhorn, and A. Bornhorn, "Modal Analyses of an Axial Turbine Blisk With Intentional Mistuning," *Journal of Engineering for Gas Turbines and Power*, vol. 140, no. January 2018, pp. 1–11, 2018.

[66] B. Beirow, F. Figaschewsky, A. Kühhorn, and A. Bornhorn, "Vibration analysis of an axial turbine blisk with optimized intentional mistuning pattern," *Journal of Sound and Vibration*, vol. 442, pp. 11–27, 2019.

[67] A. Picou, E. Capiez-Lernout, C. Soize, and M. Mbaye, "Robust dynamic analysis of detuned-mistuned rotating bladed disks with geometric nonlinearities," *Computational Mechanics*, pp. 1–20, 2019.

[68] A. Hajnayeb, M. Nikpour, S. Moradi, and G. Rossi, "A new reference tip-timing test bench and simulator for blade synchronous and asynchronous vibrations," *Measurement Science and Technology*, vol. 29, pp. 1–7, 2018.

[69] F. Holzinger, F. Wartzek, M. Nestle, H.-P. Schiffer, and S. Leichtfuß, "Self-Excited Blade Vibration Experimentally Investigated in Transonic Compressors - Acoustic Resonance," *Proceedings of ASME Turbo Expo*, no. GT2015-43618, pp. 1–16, 2015.

[70] D. H. Diamond, P. S. Heyns, and A. J. Oberholster, "A Comparison Between Three Blade Tip Timing Algorithms for Estimating Synchronous Turbomachine Blade Vibration," *Proceedings of the 9th WCEAM*, pp. 215–225, 2015.

[71] R. S. Mohan, A. Sarkar, and A. S. Sekhar, "Vibration analysis of a steam turbine blade," *Proceedings of the Inter-noise*, pp. 1–10, 2014.

[72] M. P. Boyce, *Gas Turbine Engineering Handbook*. Elsevier Science, 4 ed., 2011.

[73] M. F. Platzer and F. O. Carta, "AGARD Manual on Aeroelasticity in Axial-Flow Turbomachines Volume 1 Unsteady Turbomachinery Aerodynamics," *NATO Report*, vol. 1, no. AGARD-AG-298, 1987.

[74] M. Vahdati, F. Zhao, and P. Sureshkumar, "A Review of Computational Methods for Aeroelastic Instabilities of Multi-Stage Compressor," *Proceedings of Global Power and Propulsion Society*, no. GPPS-BJ-2019-14, pp. 1–11, 2019.

[75] E. K. Armstrong and R. E. Stevenson, "Some Practical Aspects of Compressor Blade Vibration," *Journal of the Royal Aeronautical Society*, vol. 64, no. 591, pp. 117–130, 1960.

[76] C. Hah, J. Bergner, and H.-P. Schiffer, "Tip Clearance Vortex Oscillation, Vortex Shedding and Rotating Instabilities in an Axial Transonic Compressor Rotor," *Proceedings of ASME Turbo Expo*, no. GT2008-50105, pp. 1–9, 2008.

[77] S. Tavakoli, L. Griffin, and P. Fleming, "An Overview of Compressor Instabilities: Basic Concepts and Control," *IFAC Automatic Control in Aerospace*, pp. 523–528, 2004.

[78] K. C. Hall, R. E. Kielb, and J. P. Thomas, *Unsteady Aerodynamics, Aeroacoustics and Aeroelasticity of Turbomachines*. Springer, 2006.

[79] L. Y. Zhang, L. He, and H. Stüer, "A Numerical Investigation of Rotating Instability in Steam Turbine Last Stage," *Journal of Turbomachinery*, vol. 135, no. January 2013, pp. 1–9, 2013.

[80] M. Baumgartner, F. Kameier, and J. Hourmouziadis, "Non-Engine Order Blade Vibration in a High Pressure Compressor," *Proceedings of the 12th International Symposium on Airbreathing Engines*, pp. 1–13, 1995.

[81] G. Cicatelli and C. H. Sieverding, "The Effect of Vortex Shedding on the Unsteady Pressure Distribution Around the Trailing Edge of a

Turbine Blade," *Journal of Turbomachinery*, vol. 119, no. October 1997, pp. 810–819, 1997.

[82] Y. L. Lau, R. C. K. Leung, and R. M. C. So, "Vortex-induced vibration effect on fatigue life estimate of turbine blades," *Journal of Sound and Vibration*, vol. 307, pp. 698–719, 2007.

[83] X. Zhao, Q. Zhou, S. Yang, and H. Li, "Rotating Stall Induced Non-Synchronous Blade Vibration Analysis for an Unshrouded Industrial Centrifugal Compressor," *Sensors*, vol. 19, pp. 4995–5012, 2019.

[84] I. J. Day, "Stall, Surge, and 75 Years of Research," *Journal of Turbomachinery*, vol. 138, no. January 2016, pp. 1–16, 2016.

[85] M. Jüngst, F. Holzinger, H.-P. Schiffer, and S. Leichtfuss, "Analysing Non-Synchronous Blade Vibrations in a Transonic Compressor Rotor," *Proceedings of the 11th European Conference on Turbomachinery Fluid dynamics & Thermodynamics*, pp. 1–13, 2015.

[86] B. de Jager, "Rotating stall and surge control: A survey," *Proceedings of the 34th Conference on Decision & Control*, pp. 1857–1862, 1995.

[87] E. M. Greitzer, "Surge and Rotating Stall in Axial Flow Compressors – Part I: Theoretical Compression System Model," *Journal of Engineering for Power*, vol. April 1976, pp. 190–198, 1976.

[88] E. M. Greitzer, "Surge and Rotating Stall in Axial Flow Compressors – Part II: Experimental Results and Comparison With Theory," *Journal of Engineering for Power*, vol. April 1976, pp. 199–211, 1976.

[89] W. R. Sears, "Rotating Stall in Axial Compressors," *Zeitschrift für angewandte Mathematik und Physik*, vol. 6, no. 6, pp. 429–455, 1955.

[90] P. P. Walsh and P. Fletcher, *Gas Turbine Performance*. Blackwell Science, 2 ed., 2004.

[91] A. Abdel-Rahim, F. Sisto, and S. Thangam, "Computational Study of Stall Flutter in Linear Cascades," *Journal of Turbomachinery*, vol. 115, no. January 1993, pp. 157–166, 1993.

[92] J. T. Gravdahl and O. Egeland, *Compressor Surge and Rotating Stall: Modeling and Control*. Springer Science & Business Media, 2012.

[93] Q. Sun, C. Wang, and P. Lin, "Rapid Detection of Rotating Stall in Axial Flow Compressors on Computer Cluster," *Proceedings of the 29th Chinese Control And Decision Conference*, pp. 7366–7371, 2017.

[94] Advisory Group for Aerospace Research and Development, "Multilingual Aeronautical Dictionary," 1980.

[95] A. R. Collar, "The Expanding Domain of Aeroelasticity," *The Aeronautical Journal*, vol. 50, no. 428, pp. 613–636, 1946.

[96] F. O. Carta, "Coupled Blade-Disk-Shroud Flutter Instabilities in Turbojet Engine Rotors," *Journal of Engineering for Power*, no. July 1967, pp. 419–426, 1967.

[97] M. Vahdati, G. Simpson, and M. Imregun, "Mechanisms for Wide-Chord Fan Blade Flutter," *Journal of Turbomachinery*, vol. 133, no. October 2011, pp. 1–7, 2011.

[98] Z. Fu and Y. Wang, "Mistuning and Structural Coupling Effects on Flutter of Turbomachinery Blades," *Applied Mechanics and Materials*, vol. 482, pp. 311–314, 2014.

[99] V. V. Vedeneev, M. Kolotnikov, and P. Makarov, "Experimental Validation of Numerical Blade Flutter Prediction," *Journal of Propulsion and Power*, vol. 31, no. 5, pp. 1281–1291, 2015.

[100] E. H. Dowell, *A Modern Course in Aeroelasticity*. Kluwer Academic Publishers, 5 ed., 2015.

[101] C. E. Seeley, C. Wakelam, X. Zhang, D. Hofer, and W.-M. Ren, "Investigations of Flutter and Aerodynamic Damping of a Turbine Blade:

Experimental Characterization," *Journal of Turbomachinery*, vol. 139, no. August 2017, pp. 1–7, 2017.

[102] F. Holzinger, F. Wartzek, M. Jüngst, H.-P. Schiffer, and S. Leichtfuss, "Self-Excited Blade Vibration Experimentally Investigated in Transonic Compressors: Rotating Instabilities and Flutter," *Journal of Turbomachinery*, vol. 138, no. April 2016, pp. 1–9, 2016.

[103] M. F. Platzer and F. O. Carta, "AGARD Manual on Aeroelasticity in Axial-Flow Turbomachines Volume 2 Structural Dynamics and Aeroelasticity," *NATO Report*, vol. 2, no. AGARD-AG-298, 1988.

[104] D. J. Inman, *Engineering Vibration*. Pearson, 4 ed., 2014.

[105] K. W. Jones and C. J. Cross, "Traveling Wave Excitation System for Bladed Disks," *Journal of Propulsion and Power*, vol. 19, no. 1, pp. 135–141, 2003.

[106] J. Strnad and J. Liska, "Advanced method of noncontact measurement of shrouded blade vibration in steam turbine: evaluation of bladed disc mode shape," *Computers, Automatic Control, Signal Processing and Systems Science*, pp. 39–43, 2014.

[107] D. Hemberger, D. Filsinger, and H.-J. Bauer, "Influence of Aerodynamic Mistuning and Aerodynamic Coupling on Vibration Behavior of Mistuned Small Radial Turbine Wheels," *Proceedings of ASME Turbo Expo*, no. GT2017-63069, pp. 1–8, 2017.

[108] H. Stargardter, "Optical Determination of Rotating Fan Blade Deflections," *Journal of Engineering for Power*, no. April 1977, pp. 204–209, 1977.

[109] D. Möller, M. Jüngst, F. Holzinger, C. Brandstetter, H.-P. Schiffer, and S. Leichtfuß, "Mechanism of Nonsynchronous Blade Vibration in a Transonic Compressor Rig," *Journal of Turbomachinery*, vol. 139, no. January 2017, pp. 1–10, 2017.

[110] A. V. Srinivasan, "Flutter and Resonant Vibration Characteristics of Engine Blades," *Proceedings of the ASME International Gas Turbine and Aeroengine Congress and Exhibition*, no. 97-GT-533, pp. 1–36, 1997.

[111] R. Szczepanik, R. Przysowa, and J. Spychała, "Application of Blade-Tip Sensors to Blade-Vibration Monitoring in Gas Turbines," *Thermal Power Plants*, pp. 145–176, 2012.

[112] B. D. Hockaday, "Comparing Lensed and Un-Lensed Optical Spot Probes for Blade Tip Timing Measurements," *Proceedings of ASME Turbo Expo*, no. GT2012-68499, pp. 1–9, 2012.

[113] P. Procházka and F. Vaněk, "Sensors and Methods for Blade Damage Operational Assessment in Low-Pressure Steam Turbine Stages," *Key Engineering Materials*, vol. 569-570, pp. 726–733, 2013.

[114] P. Procházka and F. Vaněk, "Operational Measurement of Stationary Characteristics and Positions of Shrouded Steam Turbine Blades," *IEEE Transactions on Instrumentation and Measurement*, vol. 65, no. 5, pp. 1079–1086, 2016.

[115] P. Procházka, "Methods and Measuring Systems for Calibration of Non-Contact Vibrodiagnostics Systems," *Proceedings of the Instrumentation and Measurement Technology Conference*, pp. 1–6, 2017.

[116] R. M. Cotgrove and M. I. Wood, "Opportunities for Advanced Sensors for Condition Monitoring of Gas Turbines," *Proceedings of the International Conference on Opportunities and Advances in International Power Generation*, pp. 119–124, 1996.

[117] K. Turner, M. Adams, and M. Dunn, "Simulation of Engine Blade Tip-Rub Induced Vibration," *Proceedings of ASME Turbo Expo*, no. GT2005-68217, pp. 1–6, 2005.

[118] A. Maslovskiy, M. Bakulin, and M. Snitko, "Microwave Blade Tip Clearance Measurements: Principles, Current Practices and Future

Opportunities," *Proceedings of ASME Turbo Expo*, no. GT2012-69201, pp. 1–5, 2012.

[119] J. Zubia, I. García, A. Berganza, J. Beloki, J. Arrue, and J. Mateo, "Improvements in the Design of an Optical Sensor for Tip-Clearance Measurements in Turbines," *Proceedings of the 16th International Conference on Transparent Optical Networks*, no. Mo.C7.5, pp. 1–4, 2014.

[120] J. Binghui and H. Lei, "An Optical Fiber Measurement System for Blade Tip Clearance of Engine," *International Journal of Aerospace Engineering*, no. 4168150, pp. 1–9, 2017.

[121] V. Sridhar and K. S. Chana, "Tip-Clearance Measurements on an Engine High Pressure Turbine Using an Eddy Current Sensor," *Proceedings of ASME Turbo Expo*, no. GT2017-63803, pp. 1–7, 2017.

[122] V. Sridhar and K. S. Chana, "Development of a Combined Eddy Current and Pressure Sensor for Gas Turbine Blade Health Monitoring," *Proceedings of ASME Turbo Expo*, no. GT2017-63807, pp. 1–8, 2017.

[123] R. Fernández, J. Amorebieta, G. Durana, J. Beloki, and J. Zubia, "Performance comparison among three optical fibre-based displacement sensors for Blade Tip Clearance measurements," *Proceedings of the IEEE 5th International Workshop on Metrology for AeroSpace*, pp. 657–662, 2018.

[124] T. N. Satish, A. Vivek, S. N. Anagha, A. N. V. Rao, G. Uma, M. Umapathy, U. Chandrasekhar, and G. Kiran, "Novel resistor-capacitor (RC) network-based capacitance signal conditioning circuit for tip clearance measurement on gas turbine engine," *Proceedings of the Institution of Mechanical Engineers, Part G: Journal of Aerospace Engineering*, pp. 1–19, 2019.

[125] J. Wu, B. Wen, Y. Zhou, Q. Zhang, S. Ding, F. Du, and S. Zhang, "Eddy Current Sensor System for Blade Tip Clearance Measurement Based on a Speed Adjustment Model," *Sensors*, vol. 19, pp. 761–777, 2019.

[126] Z. Liu, Z. Zhao, Y. Lyu, and L. Zhao, "Experimental Investigation of Inductive Sensor Characteristic for Blade Tip Clearance Measurement at High Temperature," *Sensors*, vol. 19, pp. 3694–3706, 2019.

[127] A. Pepe, M. Sepe, D. Nurzad, and R. Garbin, "Method of Monitoring Rubbing Between a Rotary Party and a Stationary Part in a Rotating Turbomachine, Monitoring Arrangement and Turbomachine," 2019.

[128] M. Aslinezhad and M. A. Hejazi, "Turbine blade tip clearance determination using microwave measurement and k-nearest neighbour classifier," *Measurement*, vol. 151, no. 107142, pp. 1–9, 2020.

[129] X. Zhang, Y. Xiong, S. Xie, and H. Liu, "Optical-fiber-based dynamic measurement system for 3D tip clearance of rotating blades," *Optics Express*, vol. 27, no. 22, pp. 32075–32095, 2019.

[130] B. Yu, H. Ke, E. Shen, and T. Zhang, "A review of blade tip clearance–measuring technologies for gas turbine engines," *Measurement and Control*, pp. 1–19, 2020.

[131] J. Wu, B. Wen, Q. Zhang, Y. Zhou, S. Ding, F. Du, S. Zhang, and Z. Wang, "A novel blade tip clearance measurement method based on event capture technique," *Mechanical Systems and Signal Processing*, vol. 139, no. 106626, pp. 1–16, 2020.

[132] J. M. Gil-García, J. Zubia, and G. Aranguren, "Architecture for Measuring Blade Tip Clearance and Time of Arrival with Multiple Sensors in Airplane Engines," *International Journal of Aerospace Engineering*, no. 3756278, pp. 1–7, 2018.

[133] C. Lawrence and E. H. Meyn, "The Use of an Optical Data Acquisition System for Bladed Disk Vibration Analysis," *NASA Lewis Research Center Report*, no. NASA-TM-86891, 1984.

[134] G. Battiato, C. M. Firrone, and T. M. Berruti, "Forced response of rotating bladed disks: Blade Tip-Timing measurements," *Mechanical Systems and Signal Processing*, vol. 85, pp. 912–926, 2017.

[135] J. Yuan, F. Scarpa, G. Allegri, B. Titurus, S. Patsias, and R. Rajasekaran, "Efficient computational techniques for mistuning analysis of bladed discs: A review," *Mechanical Systems and Signal Processing*, vol. 87, pp. 71–90, 2017.

[136] A. Nazari, A. Yousefi-Koma, S. Zohoori, and M. Safa, "Experimental Investigation of Nodal Diameters of an Integrated Bladed Disk," *Proceedings of the 16th International Conference of Iranian Aerospace Society*, no. AERO2017DC10100030009, pp. 1–5, 2017.

[137] D. S. Whitehead, "The Analysis of Blade Vibration due to Random Excitation," *Aeronautical Research Council Reports and Memoranda*, no. 3253, pp. 1–19, 1960.

[138] Y.-H. Wang, G.-W. Fu, and F. Duan, "Research for data analysis methods of blade tip-timing measuring," *Journal of Foshan University (Natural Science Edition)*, vol. 2, 2004.

[139] A. Lifson and H. R. Simmons, "Vibration Monitoring of Turbomachinery," *Proceedings of the 19th Turbomachinery Symposium*, pp. 101–118, 1990.

[140] P. Parge, B. Trevillion, and P. Carle, "Non-Intrusive Vibration Monitoring for Turbine Blade Reliability," *Proceedings of the 2nd International Machinery Monitoring and Diagnostic Conference*, pp. 435–446, 1990.

[141] S. Heath and M. Imregun, "A Survey of Blade Tip-Timing Measurement Techniques for Turbomachinery Vibration," *Journal of Engineering for Gas Turbines and Power*, vol. 120, no. October 1998, pp. 784–791, 1998.

[142] P. Beauseroy and R. Lengellé, "Nonintrusive turbomachine blade vibration measurement system," *Mechanical Systems and Signal Processing*, vol. 21, pp. 1717–1738, 2007.

[143] K. Grant, *Experimental Testing of Tip-Timing Methods used for Blade Vibration Measurement in the Aero-Engine*. PhD thesis, Cranfield University, 2004.

[144] S. J. Posta, "Low-Cost Optical Data Acquisition System for Blade Vibration Measurement," *NASA Lewis Research Center Report*, no. N88-23240, 1988.

[145] A. P. Kurkov, "Measurements of Self-excited Rotor-blade Vibrations Using Optical Displacements," *NASA Lewis Research Center Report*, no. N83-14523, 1982.

[146] R. Anderson, W. Atkinson, T. Bonsett, and J. Osani, "The Propulsion Instrumentation Working Group: Introduction and Discussion of Subteam Activities," *Proceedings of the 20th AIAA Advanced Measurement and Ground Testing Technology Conference*, pp. 1–20, 1998.

[147] H. Jones, "Shedding light on vibration," *Mechanical Engineering*, vol. 118, no. 11, pp. 94–97, 1996.

[148] K. S. Chana, V. Sridhar, and D. Singh, "The Use of Eddy Current Sensors for the Measurement of Rotor Blade Tip Timing: Development of a New Method Based on Integration," *Proceedings of ASME Turbo Expo*, no. GT2016-57368, pp. 1–8, 2016.

[149] S. Heath, *A Study of Tip-Timing Measurement Techniques for the Determination of Bladed-Disk Vibration Characteristics*. PhD thesis, University of London, 1996.

[150] A. A. Gubran and J. K. Sinha, "Comparison between Long and Short Blade Vibration Using Shaft Instantaneous Angular Speed in Rotating Machine," *Proceedings of ASME Turbo Expo*, no. GT2014-25904, pp. 1–7, 2014.

[151] A. A. Gubran and J. K. Sinha, "Shaft instantaneous angular speed for blade vibration in rotating machine," *Mechanical Systems and Signal Processing*, vol. 44, pp. 47–59, 2014.

[152] P. Procházka, F. Vaněk, J. Cibulka, and V. Bula, "Contactless Measuring Method of Blade Vibration During Turbine Speed-Up," *Engineering Mechanics*, vol. 17, no. 3/4, pp. 173–186, 2010.

[153] H. Guo, F. Duan, and J. Zhang, "Blade resonance parameter identification based on tip-timing method without the once-per revolution sensor," *Mechanical Systems and Signal Processing*, vol. 66-67, pp. 625–639, 2016.

[154] H. Guo, F. Duan, and M. Wang, "Blade synchronous vibration measurement based on tip-timing at constant rotating speed without once-per-revolution sensor," *Proceedings of SPIE*, vol. 9903, no. 990311, pp. 1–7, 2016.

[155] J. Zhang, F. Duan, and J. Jiang, "Analysis of a Signal Preprocessing Method for Blade Tip-Timing without the Once-per Revolution Sensor," *Proceedings of the 2nd International Conference on Electrical, Automation and Mechanical Engineering*, vol. 86, pp. 94–98, 2017.

[156] R. Reinhardt, D. Lancelle, O. Hagendorf, M. Schultalbers, O. Magnor, and P. Duenow, "Improved reference system for high precision blade tip timing on axial compressors," *Proceedings of SPIE*, vol. 10323, no. 103231J, pp. 1–4, 2017.

[157] S. H. Hesler and C. A. Suprock, "Improving Turbomachinery Health Monitoring Using Advanced Shaft Telemetry System," *Proceedings of ASME Turbo Expo*, no. GT2017-64899, pp. 1–7, 2017.

[158] J.-L. Zhang, F.-J. Duan, and G.-Y. Niu, "The Preprocessing Method of the Blade Tip-timing Measurement without a Once-per-revolution Sensor and Error Analysis," *Acta Metrologica Sinica*, vol. 39, no. 4, pp. 498–503, 2018.

[159] K. Lizoul, H. André, and F. Guillet, "Improvement of instantaneous angular speed estimation based on frequency demodulation method under non stationary conditions," *Proceedings of ISMA2018 and USD2018*, pp. 1971–1984, 2018.

[160] J.-w. Zhang, L.-b. Zhang, K.-Q. Ding, and L.-x. Duan, "Blade Tip-timing Technology with Multiple Reference Phases for Online Monitoring of High-speed Blades under Variable-speed Operation," *Measurement Science Review*, vol. 18, no. 6, pp. 243–250, 2018.

[161] W. Wang, S. Ren, L. Chen, and H. Shao, "Research on the key blade vibration measurement phase interpolation," *Journal of Vibration, Measurement and Diagnosis*, vol. 2, pp. 361–365, 2017.

[162] W. Wang, S. Ren, L. Chen, and H. Shao, "The Blade Vibration Measurement Research Based on the Key Phase Interpolation Method," *Journal of Vibration, Measurement and Diagnosis*, vol. 37, no. 2, pp. 361–365, 2017.

[163] K. Chen, W. Wang, X. Zhang, and Y. Zhang, "New step to improve the accuracy of blade tip timing method without once per revolution," *Mechanical Systems and Signal Processing*, vol. 134, no. 106321, pp. 1–19, 2019.

[164] D. H. Diamond, P. S. Heyns, and A. J. Oberholster, "Improved Blade Tip Timing measurements during transient conditions using a State Space Model," *Mechanical Systems and Signal Processing*, vol. 122, pp. 555–579, 2019.

[165] D. H. Diamond, P. S. Heyns, and A. J. Oberholster, "A Method and System for Monitoring Rotor Blades of a Turbomachine Using Blade Tip Timing (BTT)," 2019.

[166] C. Fan, Y. Wu, P. Russhard, and A. Wang, "An Improved Blade Tiptiming Method for Vibration Measurement of Rotating Blades During Transient Operating Conditions," *Journal of Vibration Engineering & Technologies*, pp. 1–10, 2020.

[167] P. Russhard, "Derived Once per Rev Signal generation for Blade Tip Timing Systems," *Proceedings of IET & ISA 60th International Instrumentation Symposium*, no. 1, pp. 1–5, 2014.

[168] P. Russhard, "Blade Tip Timing (BTT) Uncertainties," *AIP Conference Proceedings*, vol. 1740, no. 020003, pp. 1–13, 2016.

[169] M. Witos, M. Zieja, and J. Kozdra, "Non-Contact Structural Health Monitoring of Rotating Components Using Inductive Sensor and Time

of Arrival Signal," *Proceedings of the 21st International Workshop on Electromagnetic Nondestructive Evaluation*, pp. 1–48, 2016.

[170] B. W. Hayes, *Design, Implementation, and Analysis of a Time of Arrival Measurement System for Rotating Machinery.* PhD thesis, University of Tennessee, 2012.

[171] T. M. Pickering, *Methods for Validation of a Turbomachinery Rotor Blade Tip Timing System Methods.* PhD thesis, Virginia Polytechnic Institute and State University, 2014.

[172] V. Kharyton, G. Dimitriadis, and C. Defise, "A Discussion on the Advancement of Blade Tip Timing Data Processing," *Proceedings of ASME Turbo Expo*, no. GT2017-63138, pp. 1–11, 2017.

[173] J. Zhang, F. Duan, G. Niu, J. Jiang, and J. Li, "A Blade Tip Timing Method Based on a Microwave Sensor," *Sensors*, vol. 17, pp. 1097–1107, 2017.

[174] V. Kharyton and R. Bladh, "Using Tiptiming and Strain Gauge Data for the Estimation of Consumed Life in a Compressor Blisk Subjected to Stall-Induced Loading," *Proceedings of ASME Turbo Expo*, no. GT2014-27251, pp. 1–10, 2014.

[175] M. Zielinski and G. Ziller, "Noncontact vibration measurements on compressor rotor blades," *Measurement Science and Technology*, vol. 11, pp. 847–856, 2000.

[176] R. Przysowa and K. Kaźmierczak, "Triggering Methods in Blade Tip-Timing Systems," *Proceedings of the VETOMAC XII*, pp. 129–138, 2016.

[177] Y. Zablotskiy, A. Korostelev, and L. Sviblow, "Device for Non-Contact Analysis of Vibration Movement of Turbomachinery Blades," *Avt. Svid. No 160886*, 1964.

[178] P. F. Rozelle, D. H. Evans, and B. B. Seth, "Development and Application of a Blade Vibration Monitor," *Proceedings of the 7th ASME PWR Conference*, pp. 37–45, 1989.

[179] R. Kudelski and R. Szczepanik, "Inflight Early Detection of Cracks in Turbine Aero-Engine Compressor Blades," *Proceedings of the 12th World Conference on Non-Destructive Testing*, pp. 616–622, 1989.

[180] M. Mase, P. F. Rozelle, and T. W. Zagar, "Blade Vibration Monitoring Technology," *Proceedings of the Steam and Combustion Turbine-Blading Conference and Workshop*, no. 5, pp. 1–20, 1992.

[181] D. Goyal and B. S. Pabla, "The Vibration Monitoring Methods and Signal Processing Techniques for Structural Health Monitoring: A Review," *Archives of Computational Methods in Engineering*, vol. 23, pp. 585–594, 2016.

[182] M. Witos, M. Zieja, and J. Kozdra, "Non-Contact Structural Health Monitoring of Rotating Components Using Inductive Sensor and Time of Arrival Signal," *Studies in Applied Electromagnetics and Mechanics*, vol. 42, pp. 265–272, 2017.

[183] Z.-Q. Fang, F. Duan, Y.-Y. Sun, and X.-M. Zhao, "Research on Tip-timing Sensor for Non-contact Measurement of Blade Vibration in Rotating Turbo-machinery," *Acta Metrologica Sinica*, vol. 2, 2003.

[184] Y.-G. Zhang, F. Duan, S. Li, T. Ouyang, Z.-Q. Fang, and S.-H. Ye, "Design of Double-Shielded Capacitive Pulse Sensor with High Tip-Timing Precision," *Chinese Journal of Sensors and Actuators*, vol. 10, 2007.

[185] Y.-G. Zhang, F. Duan, T. Ouyang, and S.-H. Ye, "Emulational Analysis for Tip-Timing Precision of Double-Shielded Capacitive Pulse Sensor," *Chinese Journal of Sensors and Actuators*, vol. 1, 2008.

[186] F. Duan, M. Li, T. Ouyang, and X. Kong, "Analysis of the tip-timing precision of double-shielded capacitive pulse sensor," *Proceedings of the*

International Conference on Measuring Technology and Mechatronics Automation, pp. 81–84, 2009.

[187] T. Qing-bin, M. Hui-ping, L. Li-hua, Z. Xiao-dong, and L. Gui-bin, "Measurements of Radiation Vibrations of Turbomachine Blades Using an Optical-Fiber Displacement-Sensing System," *Journal of Russian Laser Research*, vol. 32, no. 3, pp. 216–229, 2011.

[188] W. C. Nieberding and J. L. Pollack, "Optical Detection of Blade Flutter," *NASA Lewis Research Center Report*, no. TM X-73573, 1977.

[189] M. J. Scotto and M. E. Eismeier, "High-Speed Noncontacting Instrumentation for Jet Engine Testing," *Journal of Engineering for Power*, vol. 102, no. October 1980, pp. 912–917, 1980.

[190] L. W. Langley and E. P. Sivertson, "Eddy Current Transducing System - Final Report," *US Department of Energy Report*, no. DE-FG01-89CE15426, 1991.

[191] W. F. Cullinane and R. R. Strange, "Gas turbine engine validation instrumentation: measurements, sensors, and needs," *Proceedings of SPIE*, vol. 3852, no. 0277-786X, pp. 2–13, 1999.

[192] J. Geisheimer, "Microwave Blade Tip Sensor: An Update," *Proceedings of the NASA Seal/Secondary Air System Workshop*, vol. 1, no. NASA/CP-2007-214995, pp. 147–169, 2006.

[193] P. Procházka, F. Vaněk, L. Pešek, J. Cibulka, and P. Vaněk, "Magnetoresistive sensor for position sensing of rotating machine parts," *Intellectual Property Office of the Czech Republic*, no. 20637, 2009.

[194] P. Russhard, "Blade Tip Timing – Frequently asked Questions," *Rolls-Royce Publications*, pp. 1–27, 2012.

[195] P. Russhard, "A Comparison of Multi Fibre and Single Fibre Optical Probes," *Proceedings of the 60th International Instrumentation Symposium and IET Conference*, pp. 1–5, 2014.

[196] B. D. Hockaday, "Quantifying Optical Tip-Timing Probe Error With Laboratory Apparatus," *Proceedings of ASME Turbo Expo*, no. GT2011-46677, pp. 1–8, 2011.

[197] R. Marsili, R. Tomassini, and G. Rossi, "A calibration technique for non contact measurement systems of jet engine blades vibration during operation," *Proceedings of the IEEE International Workshop on Metrology for AeroSpace*, pp. 489–495, 2017.

[198] M. Wang, F. Duan, H. Guo, and J. Zhang, "Signal Processing Method of Increasing Precision of Optical Fiber Sensor Based Tip-Timing System," *Nanotechnology and Precision Engineering*, vol. 14, no. 3, pp. 173–180, 2016.

[199] G. Battiato, C. M. Firrone, and T. M. Berruti, "A Benchmark for Tip Timing Measurement of Forced Response in Rotating Bladed Disks," *Proceedings of the 11th International Conference on Engineering Vibration*, pp. 1–13, 2015.

[200] X.-H. Kong, F. Duan, M. Li, and T. Ouyang, "Research on torsional-axial vibration measurement using fiber-optic bundle sensor," *Transducer and Microsystem Technologies*, vol. 1, 2011.

[201] I. García, J. Zubia, J. Beloki, I. Ayesta, and G. Aldabaldetreku, "Tip timing measurements for Structural Health Monitoring in a low-pressure turbine using three optical sensors," *Proceedings of the 8th European Workshop On Structural Health Monitoring*, pp. 1–9, 2016.

[202] J.-F. Brouckaert, R. Marsili, R. Tomasini, and G. Rossi, "Proposal of a new calibration technique of non contact blade vibration measuring systems," *Proceedings of the 59th International Instrumentation Symposium and 2013 MFPT Conference*, pp. 108–167, 2013.

[203] C. P. Lawson and P. C. Ivey, "Tubomachinery blade vibration amplitude measurement through tip timing with capacitance tip clearance probes," *Sensors and Actuators A: Physical*, vol. 118, pp. 14–24, 2005.

[204] K. S. Chana and D. N. Cardwell, "The Use of Eddy Current Sensor Based Blade Tip Timing for FOD Detection," *Proceedings of ASME Turbo Expo*, no. GT2008-50791, pp. 1–10, 2008.

[205] J. Fraden, *Handbook of Modern Sensors - Physics, Design, and Applications*. Springer-Verlag New York, 3 ed., 2004.

[206] B. L. Koff, "Aircraft Engine Design Using Experimental Stress Analysis Techniques," *Proceedings of the AIAA/SAE/ASME 15th Joint Propulsion Conference*, no. 79-1193, pp. 1–11, 1979.

[207] L. J. Kiraly, "Digital System for Dynamic Turbine Engine Blade Displacement Measurements," *National Aeronautics and Space Administration Report*, no. NASA-TM-81382, 1980.

[208] A. von Flotow and P. Tappard, "Overview of Blade Vibration Monitoring Capabilities," *Hood Technology Publications*, pp. 1–22, 2011.

[209] H. Roth, "Vibration Measurements on Turbomachine Rotor Blades with Optical Probes," *Proceedings of the Joint Fluids Engineering Gas Turbine Conference and Products Show*, pp. 215–224, 1980.

[210] M. Zielinski and G. Ziller, "Optical Blade Vibration Measurement at MTU," *Proceedings of the AGARD Conference*, pp. 1–31, 1998.

[211] I. García, J. Beloki, J. Zubia, G. Aldabaldetreku, M. Asunción Illarramendi, and F. Jiménez, "An optical fiber bundle sensor for tip clearance and tip timing measurements in a turbine rig," *Sensors*, vol. 13, pp. 7385–7398, 2013.

[212] I. García, J. Zubia, G. Durana, G. Aldabaldetreku, M. A. Illarramendi, and J. Villatoro, "Optical Fiber Sensors for Aircraft Structural Health Monitoring," *Sensors*, vol. 15, pp. 15494–15519, 2015.

[213] J. M. Gil-García, I. García, J. Zubia, and G. Aranguren, "Blade tip clearance and time of arrival immediate measurement method using an optic probe," *Metrology for Aerospace*, pp. 118–122, 2015.

[214] F. Duan, J. Zhang, J. Jiang, H. Guo, and D. Ye, "Method to improve the blade tip-timing accuracy of fiber bundle sensor under varying tip clearance," *Optical Engineering*, vol. 55, no. 1, pp. 1–4, 2016.

[215] H. Roth, "Schwingungsmessungen an Turbinenschaufeln mit optischen Methoden," *Brown Boveri Mitt*, pp. 1–77, 1977.

[216] J. F. Brouckaert, R. Marsili, G. Rossi, and R. Tomassini, "Development and experimental characterization of a new non contact sensor for blade tip timing," *AIP Conference Proceedings*, vol. 1457, pp. 61–68, 2012.

[217] M. M. Ross and D. Crommentuijn-Marsh, "High temperature, high precision, casing-mounted optical sensors for in-situ measurement of blade vibration in rotating turbo-machinery," *Proceedings of SPIE*, vol. 3783, no. 0277-786X, pp. 362–372, 1999.

[218] I. G. Esteban-Barcina, *Desarrollo de un sensor de fibra óptica para la medida del tip clearance y tip timing en motores aeronáuticos.* PhD thesis, University of the Basque Country, 2017.

[219] L. Andrenelli, N. Paone, and G. L. Rossi, "Large-bandwidth reflection fiber-optic sensors for turbomachinery rotor blade diagnostics," *Sensors and Actuators A: Physical*, vol. 32, pp. 539–542, 1992.

[220] D. N. Cardwell, K. S. Chana, and P. Russhard, "The Use of Eddy Current Sensors for the Measurement of Rotor Blade Tip Timing - Sensor Development and Engine Testing," *Proceedings of ASME Turbo Expo*, no. GT2008-50792, pp. 1–11, 2008.

[221] H. R. Simmons, D. L. Michalsky, K. E. Brewer, and A. J. Smalley, "Measuring Rotor and Blade Dynamics Using an Optical Blade Tip Sensor," *Proceedings of the ASME International Gas Turbine and Aeroengine Congress and Exposition*, no. 90-GT-91, pp. 1–6, 1990.

[222] J. M. Gil-García, I. García, J. Zubia, and G. Aranguren, "Measurement of blade tip clearance and time of arrival in turbines using an

optic sensor," *Proceedings of the International Conference on Applied Electronics*, pp. 1–4, 2015.

[223] M. Drumm and W. C. Haase, "High Performance Rotor Health Monitoring," *Proceedings of the Digital Avionics Systems Conference*, no. 6.E.4, pp. 1–8, 2000.

[224] V. Kharyton, *Faults Detection in Blades of an Aviation Engine in Operation*. PhD thesis, Ecole Centrale de Lyon, 2009.

[225] K. Tamura, M. Ono, S. Torii, T. Shimmyo, and A. Kondou, "Development of Reliability Verification Technology for Gas Turbine Rotor Blades Using an Actual Unit," *Mitsubishi Heavy Industries Technical Review*, vol. 52, no. 4, pp. 22–26, 2015.

[226] J. Feng, F. Duan, D. Ye, X. Jin, and J. Zheng, "An Optical Fiber Tip-Timing Sensor with High Temperature Resistant Capability and Testing Device," *Nanotechnology and Precision Engineering*, vol. 14, no. 3, pp. 167–172, 2016.

[227] D. Sabbatini, B. Peeters, T. Martens, and K. Janssens, "Data acquisition and processing for tip timing and operational modal analysis of turbomachinery blades," *AIP Conference Proceedings*, vol. 1457, pp. 52–60, 2012.

[228] Y.-H. Wang, S.-H. Ye, F. Duan, X.-H. Feng, and Y.-Z. Zheng, "Research for Tip-Timing Sensor Based on Optical Fiber Technology," *Journal of Tianjin University*, vol. 5, 2002.

[229] A. P. Kurkov and H. S. Dhadwal, "Simultaneous Optical Measurements of Axial and Tangential Steady-State Blade Deflections," *NASA Glenn Research Center Report*, no. NASA/TM–1999-209051, 1999.

[230] H. Guo, F. Duan, and Z. Cheng, "Numerical analysis of the blade tip-timing signal of a fiber bundle sensor probe," *Optical Engineering*, vol. 54, no. 3, pp. 1–6, 2015.

[231] A. Warnick, "Capacitance Probe," 1958.

[232] C. Lawson, *Capacitance Tip Timing Techniques in Gas Turbines*. PhD thesis, Cranfield University, 2003.

[233] C. Lawson and P. Ivey, "Compressor Blade Tip Timing Using Capacitance Tip Clearance Probes," *Proceedings of ASME Turbo Expo*, no. GT2003-38284, pp. 1–8, 2003.

[234] L. K. Baxter, *Capacitive Sensors - Design and Applications*. IEEE Press, 1997.

[235] A. Stevenson, "Capacitive measurement of rotor blade speed and vibration," 2006.

[236] A. Bruère, "Vibrational characterisation of blades during revolution by capacitive technique and blade passing time measurement and analysis," *Proceedings of the 5ième Colloque "Analyse Vibratoire Expérimentale"*, pp. 1–5, 2016.

[237] P. C. Ivey, K. R. Grant, and C. Lawson, "Tip Timing Techniques for Turbomachinery HCF Condition Monitoring," *Proceedings of the 16th Symposium on Measuring Techniques in Transonic and Supersonic Flow in Cascades and Turbomachines*, pp. 1–7, 2002.

[238] C. Lawson and P. Ivey, "The Use of Commercially Available Capacitance Tip-Clearance Probes for Tip-Timing of Aero-Engine Compressor Blades," *Proceedings of the 38th AIAA/ASME/SAE/ASEE Joint Propulsion Conference & Exhibit*, no. AIAA 2002-3730, pp. 1–10, 2002.

[239] C. P. Lawson and P. C. Ivey, "The Measurement of Turbomachinery Blade Vibration Through Tip Timing with Capacitance Tip Clearance Probes," *Proceedings of ASME Turbo Expo*, no. GT2004-53563, pp. 1–9, 2004.

[240] M. Zielinski and G. Ziller, "Noncontact Blade Vibration Measurement System for Aero Engine Application," *Proceedings of the 17th International Society of Air-breathing Engines Conference*, pp. 1–9, 2005.

[241] W. Y. Du, *Resistive, Capacitive, Inductive, and Magnetic Sensor Technologies*. CRC Press, 2015.

[242] A. Abdul-Aziz, M. R. Woike, N. C. Oza, B. L. Matthews, and J. D. Lekki, "Rotor health monitoring combining spin tests and data-driven anomaly detection methods," *Structural Health Monitoring*, vol. 11, no. 1, pp. 3–12, 2011.

[243] Pentair, "High Temperature Clearance and Vibration Monitoring Systems," *Publications of Pentair*, pp. 1–16, 2013.

[244] M. Jüngst, D. Franke, H.-P. Schiffer, and T. Giersch, "Aeroelastic Effects in a Transonic Compressor with Nonaxisymmetric Tip Clearance," *Proceedings of the Global Power and Propulsion Society*, no. GPPS-NA-2018-0041, pp. 1–11, 2018.

[245] S. Bornassi, M. Ghalandari, and S. F. Maghrebi, "Blade synchronous vibration measurements of a new upgraded heavy duty gas turbine MGT-70(3) by using tip-timing method," *Mechanics Research Communications*, vol. 104, no. 103484, pp. 1–6, 2020.

[246] J. H. Glenn, "Advanced Capacitive-Sensor Turbine-Blade-Monitoring System," *NASA Tech Briefs*, 2002.

[247] M. L. Adams (Jr.), *Rotating Machinery Vibration - From Analysis to Troubleshooting*. CRC Press, 2 ed., 2010.

[248] C. Mandache, T. Mcelhinney, and N. Mrad, "Aircraft Engine Blade Tip Monitoring Using Pulsed Eddy Current Technology," *Proceedings of the 4th International Symposium on NDT in Aerospace*, pp. 1–9, 2012.

[249] N. Jamia, M. I. Friswell, S. El-Borgi, and P. Rajendran, "Coupled Mechanical and Electromagnetic Modeling of Eddy Current Sensors," *Proceedings of the VII International Conference on Coupled Problems in Science and Engineering*, pp. 357–368, 2017.

[250] M. Dowell, G. Sylvester, R. Krupp, and G. Zipfel, "Progress in Turbomachinery Prognostics and Health Management via Eddy-Curent Sensing," *Proceedings of the IEEE Aerospace Conference*, vol. 6, pp. 133–143, 2000.

[251] R. Przysowa and E. Rokicki, "Inductive Sensors for Blade Tip-Timing in Gas Turbines," *Journal of KONBiN*, vol. 4, no. 36, pp. 147–164, 2015.

[252] M. Dowell and G. Sylvester, "Turbomachinery Prognostics and Health Management via Eddy Current Sensing: Current Developments," *Proceedings of the IEEE Aerospace Conference*, vol. 3, pp. 1–9, 1999.

[253] N. Jamia, M. I. Friswell, and S. El-Borgi, "The effect of sensor characteristics on blade tip timing measurements," *Proceedings of the 11th International Conference on Vibrations in Rotating Machinery*, pp. 299–307, 2016.

[254] W. Wang, H. Shao, L. Chen, and H. Song, "Investigation on the Turbine Blade Tip Clearance Monitoring Based on Eddy Current Pulse-Trigger Method," *Proceedings of ASME Turbo Expo*, no. GT2016-56931, pp. 1–10, 2016.

[255] V. Sridhar, K. S. Chana, and M. J. Pekris, "High temperature eddy current sensor system for turbine blade tip clearance measurements," *Proceedings of the 12th European Conference on Turbomachinery Fluid Dynamics and Thermodynamics*, 2017.

[256] P. Procházka, "Sensors for noncontact vibration diagnostics in rotating machinery," *AIP Conference Proceedings*, vol. 1740, no. 020002, pp. 1–8, 2016.

[257] J. S. Wilson, *Sensor Technology Handbook*. Elsevier, 2005.

[258] M. Baba, N. Minagawa, and R. Mihara, "Blade Vibration Measurement of Turbo Pump Inducer Hydrogen Condition," *Proceedings of the 56th*

International Astronautical Congress of the International Astronautical Federation, the International Academy of Astronautics, and the International Institute of Space Law, pp. 1–6, 2005.

[259] C. Teolis, A. Teolis, J. Paduano, and M. Lackner, "Analytic Representation of Eddy Current Sensor Data for Fault Diagnostics," *Proceedings of the IEEE Aerospace Conference*, pp. 3496–3506, 2005.

[260] C. Roeseler, A. von Flotow, and P. Tappert, "Monitoring Blade Passage in Turbomachinery Through the Engine Case (No Holes)," *Proceedings of the IEEE Aerospace Conference*, vol. 6, pp. 3125–3129, 2002.

[261] A. von Flotow and M. J. Drumm, "Blade-Tip Monitoring with Through-the-Case Eddy Current Sensors," *Sensors*, vol. 21, no. 6, pp. 28–35, 2004.

[262] A. von Flotow and M. Drumm, "High temperature, through the case, eddy current blade tip sensors," *Technical Papers of ISA*, vol. 451, pp. 165–172, 2004.

[263] C. Vining, S. Arnold, B. Hayes, and R. Howard, "Comparison of Eddy Current Probes to Generation 4 Line Probes," *Proceedings of the 51th International Society of Automation*, 2005.

[264] R. Boll and K. J. Overshott, "Magnetic Sensors," in *Sensors - A Comprehensive Survey*, VCH, 1989.

[265] J. G. Webster, *The Measurement, Instrumentation and Sensors Handbook*. CRC Press, 1999.

[266] P. Procházka and F. Vaněk, "Contactless Diagnostics of Blade Vibration of Low- Pressure Steam Turbine Stages," *Proceedings of ISMA2010 and USD2010*, pp. 2921–2936, 2010.

[267] F. Mevissen and M. Meo, "A Review of NDT/Structural Health Monitoring Techniques for Hot Gas Components in Gas Turbines," *Sensors*, vol. 19, pp. 711–747, 2019.

[268] E. Cardelli, A. Faba, R. Marsili, G. Rossi, and R. Tomassini, "Magnetic nondestructive testing of rotor blade tips," *Journal of Applied Physics*, vol. 117, no. 17A705, pp. 1–4, 2015.

[269] P. Procházka, "Electromagnetic Simulator of Rotating Machine Blades for Noncontact Sensor Dynamic Testing," *IEEE Transactions on Instrumentation and Measurement*, vol. 67, no. 6, pp. 1506–1508, 2018.

[270] P. Procházka and F. Vaněk, "Non-contact systems for monitoring blade vibrations of steam turbines," *Proceedings of ISMA2012 and USD2012*, pp. 3359–3371, 2012.

[271] P. Procházka and F. Vaněk, "Non-contact Measurement of Stationary Characteristics of Shrouded Steam Turbine Blades under Rotation," *Proceedings of the Instrumentation and Measurement Technology Conference*, pp. 2084–2088, 2015.

[272] R. Tomassini and G. Rossi, "Noncontact vibration measurements using magnetoresistive sensing elements," *AIP Conference Proceedings*, vol. 1740, no. 020004, pp. 1–10, 2016.

[273] P. Procházka and F. Vaněk, "Contactless Diagnostics of Turbine Blade Vibration and Damage," *Journal of Physics: Conference Series*, vol. 305, no. 012116, pp. 1–11, 2011.

[274] R. Tomassini, G. Rossi, and J.-F. Brouckaert, "On the development of a magnetoresistive sensor for blade tip timing and blade tip clearance measurement systems," *Review of Scientific Instruments*, vol. 87, no. 102505, pp. 1–6, 2016.

[275] P. Procházka and F. Vaněk, "Non-contact methods of sensing vibrations of turbine blades," *Proceedings of the 10th International Conference on Vibrations in Rotating Machinery*, pp. 221–232, 2012.

[276] R. Tomassini, G. Rossi, and J.-F. Brouckaert, "On the Development of a Magnetoresistive Sensor for Blade Tip Timing and Blade Tip Clearance

Measurement Systems," *AIP Conference Proceedings*, vol. 1600, pp. 65–73, 2014.

[277] P. Procházka and F. Vaněk, "New Methods of Noncontact Sensing of Blade Vibrations and Deflections in Turbomachinery," *IEEE Transactions on Instrumentation and Measurement*, vol. 63, no. 6, pp. 1583–1592, 2014.

[278] R. Tomassini, G. Rossi, and J.-F. Brouckaert, "Blade Tip Clearance and Blade Vibration Measurements Using a Magnetoresistive Sensor," *Proceedings of the 11th European Conference on Turbomachinery Fluid dynamics & Thermodynamics*, pp. 1–11, 2015.

[279] R. Przysowa, E. Rokicki, and R. Szczepanik, "Application of Magnetic Blade Tip Sensor to Monitor Rotor Whip and Detect Bearing Failure," *PIWG and EVI-GTI Joint Conference*, pp. 1–19, 2007.

[280] J. Geisheimer, O. Hochreutiner, T. Holst, S. Merchant, C. Hill, and R. Figoras, "Microwave sensor for tip timing applications," *Proceedings of the 59th International Instrumentation Symposium and 2013 MFPT Conference*, pp. 168–208, 2013.

[281] A. Abdul-Aziz, M. R. Woike, R. C. Anderson, and K. Aboumerhis, "Propulsion health monitoring assessed by microwave sensor performance and blade tip timing," *Proceedings of SPIE*, vol. 10973, no. 109730Q, pp. 1–10, 2019.

[282] A. Abdul-Aziz, S. Mustapha, and K. Aboumerhi, "Numerical validation using finite element to assess the performance of microwave sensor in detecting blade tip displacement," *Proceedings of SPIE*, vol. 11382, no. 1138202, pp. 1–11, 2020.

[283] M. R. Woike, J. W. Roeder, C. E. Hughes, and T. J. Bencic, "Testing of a Microwave Blade Tip Clearance Sensor at the NASA Glenn Research Center," *Proceedings of the 47th American Institute of Aeronautics and Astronautics Aerosciences Conference*, pp. 1–14, 2009.

[284] X. Xie, "Design of Slot Antenna Based Sensors for Blade Tip Clearance Measurement in Turbine Engines," *Proceedings of the IEEE 5th International Workshop on Metrology for AeroSpace*, pp. 192–196, 2019.

[285] M. R. Woike, A. Abdul-Aziz, and T. J. Bencic, "A Microwave Blade Tip Clearance Sensor for Propulsion Health Monitoring," *NASA Technical Paper*, no. NASA/TM—2010-216736, 2010.

[286] M. Violetti, Q. Xu, O. Hochreutiner, and A. K. Skrivervik, "New Microwave Sensor for On-line Blade Tip Timing in Gas and Steam Turbines," *Proceedings of APMC*, no. 4B3-16, pp. 1055–1057, 2012.

[287] M. J. Platt, "Blade Vibration Measurement System," *NASA Glenn Research Center Report*, no. 20150005319, 2014.

[288] D. Kwapisz, M. Hafner, and R. Rajamani, "Application of Microwave Sensing to Blade Health Monitoring," *Proceedings of the European Conference of the Prognostics and Health Management Society*, pp. 1–8, 2012.

[289] M. Woike, A. Abdul-Aziz, and M. Clem, "Structural Health Monitoring on Turbine Engines Using Microwave Blade Tip Clearance Sensors," *Proceedings of SPIE*, vol. 9062, no. 90620L, pp. 1–14, 2014.

[290] P. Loftus, "Analysis of Blade Tip Timing Data," *Rolls-Royce Report EIR01011*, 1987.

[291] P. E. McCarty and J. W. Thompson (Jr.), "Development of a Noninterference Technique for Measurement of Turbine Engine Compressor Blade Stress," *Arnold Engineering Development Center Report*, no. AEDC-TR-79-78, 1980.

[292] P. E. McCarty, J. W. Thompson, and R. S. Ballard, "Development of a Noninterference Compressor Blade Stress Measurement System," *Instrument Society of America*, pp. 745–757, 1980.

[293] A. K. Zimmer, *Investigation of the Impact of Turbine Blade Geometry on Near-Field Microwave Blade Tip Time of Arrival Measurements*. PhD thesis, Georgia Institute of Technology, 2008.

[294] W. B. Watkins and W. W. Robinson, "Noncontact Engine Blade Vibration Measurements and Analysis," *Proceedings of the AIAA/SAE/ASME/ASEE 21st Joint Propulsion Conference*, no. AIAA-85-1473, pp. 1–9, 1985.

[295] W. B. Watkins and R. M. Chi, "A Noninterference Blade Vibration Measurement System for Gas Turbine Engines," *Proceedings of the AIAA/SAE/ASME/ASEE 23rd Joint Propulsion Conference*, no. AIAA-87-1758, pp. 1–6, 1987.

[296] I. B. Carrington, J. R. Wright, J. E. Cooper, and G. Dimitriadis, "A comparison of blade tip timing data analysis methods," *Proceedings of the Institution of Mechanical Engineers, Part G: Journal of Aerospace Engineering*, vol. 215, pp. 301–312, 2001.

[297] G. Dimitriadis, I. B. Carrington, J. R. Wright, and J. E. Cooper, "Blade-Tip Timing Measurement of Synchronous Vibrations of Rotating Bladed Assemblies," *Mechanical Systems and Signal Processing*, vol. 16, no. 4, pp. 599–622, 2002.

[298] J. G. Garrido and G. Dimitriadis, "Multiple Frequency Analysis Methods for Blade Tip-Timing Data Analysis," *Proceedings of the 7th Biennial Conference on Engineering Systems Design and Analysis*, no. ESDA2004-58272, pp. 1–9, 2004.

[299] J. Gallego-Garrido, G. Dimitriadis, and J. R. Wright, "A Class of Methods for the Analysis of Blade Tip Timing Data from Bladed Assemblies Undergoing Simultaneous Resonances - Part I: Theoretical Development," *International Journal of Rotating Machinery*, no. 27247, pp. 1–11, 2007.

[300] J. Gallego-Garrido, G. Dimitriadis, I. B. Carrington, and J. R. Wright, "A Class of Methods for the Analysis of Blade Tip Timing Data from

Bladed Assemblies Undergoing Simultaneous Resonances - Part II: Experimental Validation," *International Journal of Rotating Machinery*, no. 73624, pp. 1–10, 2007.

[301] M. Li, F. Duan, and T. Ouyang, "Analysis of Blade Vibration Frequencies from Blade Tip Timing Data," *Proceedings of SPIE*, vol. 7544, no. 75445F, pp. 1–8, 2010.

[302] W. Wang, S. Ren, S. Huang, Q. Li, and K. Chen, "New Step to Improve the Accuracy of Blade Synchronous Vibration Parameters Identification Based On Combination of GARIV and LM Algorithm," *Proceedings of ASME Turbo Expo*, no. GT2017-63986, pp. 1–10, 2017.

[303] M. E. Mohamed, P. Bonello, and P. Russhard, "An experimentally validated modal model simulator for the assessment of different Blade Tip Timing algorithms," *Mechanical Systems and Signal Processing*, vol. 136, no. 106484, pp. 1–33, 2020.

[304] K. Shin and J. K. Hammond, *Fundamentals of Signal Processing for Sound and Vibration Engineers*. John Wiley & Sons, 2008.

[305] P. Neri, "Bladed wheels damage detection through Non-Harmonic Fourier Analysis improved algorithm," *Mechanical Systems and Signal Processing*, vol. 88, pp. 1–8, 2017.

[306] I. B. Carrington, *Development of Blade Tip Timing Data Analysis Techniques*. PhD thesis, University of Manchester, 2002.

[307] H. T. Jones, "Development of a Noninterference Technique for Measuring Turbine Engine Rotor Blade Stresses," *Proceedings of the AIAA/SAE/ASME/ASEE 21st Joint Propulsion Conference*, no. AIAA-85-1472, pp. 1–5, 1985.

[308] B. Salhi, M. Berthillier, J. Lardies, P. Voinis, and C. Bodel, "A Subspace Method for Modal Identification of Bladed Assemblies Using Blade Tip-Timing Data," *Proceedings of ASME Turbo Expo*, no. GT2007-28151, pp. 1–10, 2007.

[309] R. M. Chi and H. T. Jones, "Demonstration Testing of a Noninterference Technique for Measuring Turbine Engine Rotor Blade Stresses," *Proceedings of the AIAA/SAE/ASME/ASEE 24th Joint Propulsion Conference*, no. AIAA-88-3143, pp. 1–7, 1988.

[310] T. Ouyang, F. Duan, M. Li, and D.-C. Ye, "A method for identifying rotating blade asynchronous vibration by all-phase FFT," *Journal of Vibration Engineering*, vol. 3, 2011.

[311] H. Jones, "A Nonintrusive Rotor Blade Vibration Monitoring System," *Proceedings of the ASME International Gas Turbine and Aeroengine Congress and Exhibition*, no. 96-GT-84, pp. 1–8, 1996.

[312] R. Rzadkowski, E. Rokicki, L. Piechowski, and R. Szczepanik, "Analysis of middle bearing failure in rotor jet engine using tip-timing and tip-clearance techniques," *Mechanical Systems and Signal Processing*, vol. 76-77, pp. 213–227, 2016.

[313] P. Russhard and J. D. Back, "Method for analysing vibration in rotor blades," 2009.

[314] A. P. Kurkov, "Formulation of Blade-Flutter Spectral Analyses in Stationary Reference Frame," *NASA Lewis Research Center Report*, no. 2296, 1984.

[315] A. Muszynska, "Vibrational Diagnostics of Rotating Machinery Malfunctions," *International Journal of Rotating Machinery*, vol. 1, no. 3-4, pp. 237–266, 1995.

[316] J. D. Back and P. Russhard, "Method for analysing vibration in rotor blades," 2014.

[317] Y. Huang, G. Dimitriadis, J. Li, and R. E. Kielb, "System Eigenvalue Identification of Mistuned Bladed Disks Using Least-Squares Complex Frequency-Domain Method," *Proceedings of ASME Turbo Expo*, no. GT2017-63008, pp. 1–9, 2017.

[318] C. Stéphan, M. Berthillier, J. Lardiès, and A. Talon, "Tip-Timing Data Analysis for Mistuned Bladed Discs Assemblies," *Proceedings of ASME Turbo Expo*, no. GT2008-50825, pp. 1–9, 2008.

[319] A. Vercoutter, M. Berthillier, A. Talon, B. Burgardt, and J. Lardies, "Tip Timing Spectral Estimation Method for Aeroelastic Vibrations of Turbomachinery Blades," *Proceedings of the International Forum on Aeroelasticity and Structural Dynamics*, no. IFASD-2011-82, pp. 1–9, 2011.

[320] A. Vercoutter, M. Berthillier, A. Talon, B. Burgardt, and J. Lardies, "Estimation of turbomachinery blade vibrations from tip-timing data," *Proceedings of the 10th International Conference on Vibrations in Rotating Machinery*, pp. 233–245, 2012.

[321] A. Vercoutter, J. Lardies, M. Berthillier, A. Talon, and B. Burgardt, "Improvement of Compressor Blade Vibrations Spectral Analysis from Tip Timing Data: Aliasing Reduction," *Proceedings of ASME Turbo Expo*, no. GT2013-96016, pp. 1–8, 2013.

[322] A. Bouchain, J. Picheral, E. Lahalle, G. Chardon, A. Vercoutter, and A. Talon, "Blade vibration study by spectral analysis of tip-timing signals with OMP algorithm," *Mechanical Systems and Signal Processing*, vol. 130, pp. 108–121, 2019.

[323] A. Bouchain, J. Picheral, E. Lahalle, A. Vercoutter, B. Burgardt, and A. Talon, "New Possibilities for Analyzing Complex Asynchronous Blade Vibrations From Tip-Timing Data Using a Sparse Spectral Analysis Method," *Proceedings of ASME Turbo Expo*, no. GT2019-91573, pp. 1–9, 2019.

[324] L. Carassale, M. Marrè-Brunenghi, and S. Patrone, "Modal Identification of Dynamically Coupled Bladed Disks in Run-Up Tests," *Proceedings of ASME Turbo Expo*, no. GT2016-57251, pp. 1–11, 2017.

[325] W. W. Robinson and R. S. Washburn, "A Real Time Non-Interference Stress Measurement System (NSMS) for Determining Aero Engine Blade

Stresses," *Proceedings of the 37th Symposium of the Instrumentation Society of America*, pp. 91–103, 1991.

[326] K.-K. Joung, S.-C. Kang, K.-S. Paeng, N.-G. Park, H.-J. Choi, Y.-J. You, and A. von Flotow, "Analysis of Vibration of the Turbine Blades Using Non-Intrusive Stress Measurement System," *Proceedings of ASME Power*, no. POWER2006-88239, pp. 1–7, 2006.

[327] V. Kharyton, J.-P. Laine, F. Thouverez, and O. Kucher, "Simulation of Tip-Timing Measurements of a Cracked Bladed Disk Forced Response," *Proceedings of ASME Turbo Expo*, no. GT2010-22388, pp. 1–10, 2010.

[328] V. Kharyton, C. Gibert, L. Blanc, and F. Thouverez, "Mode family identification of a blisk by tip timing measurements," *Proceedings of the 20ème Congrès Français de Mécanique*, pp. 1–6, 2011.

[329] V. Kharyton, C. Gibert, L. Blanc, and F. Thouverez, "Elements of Dynamic Characterization of a Bladed Disk by Using the Tip-Timing Method under Vacuum Conditions," *Proceedings of ASME Turbo Expo*, no. GT2011-46435, pp. 1–9, 2011.

[330] P. Russhard, "Analysis of Rotating Stall in a Contra-Rotating System using Blade Tip Timing," *Rolls-Royce Publications*, pp. 1–33, 2012.

[331] R. Przysowa, "The Analysis of Synchronous Blade Vibration with the Use of Linear Sine Fitting," *Journal of KONBiN*, vol. 2, no. 30, pp. 5–19, 2014.

[332] R. Szczepanik, E. Rokicki, R. Rzadkowski, and L. Piechowski, "Tip-Timing and Tip-Clearance for Measuring Rotor Turbine Blade Vibrations," *Journal of Vibration Engineering & Technologies*, vol. 2, no. 5, pp. 395–406, 2014.

[333] C. Krause, T. Giersch, M. Stelldinger, B. Hanschke, and A. Kühhorn, "Asynchronous Response Analysis of Non-Contact Vibration Measurements on Compressor Rotor Blades," *Proceedings of ASME Turbo Expo*, no. GT2017-63200, pp. 1–7, 2017.

[334] D. H. Diamond and P. S. Heyns, "A Novel Method for the Design of Proximity Sensor Configuration for Rotor Blade Tip Timing," *Journal of Vibration and Acoustics*, vol. 140, no. December 2018, pp. 1–8, 2018.

[335] R. Hohenberg, "Detection and Study of Compressor-Blade Vibration," *Experimental Mechanics*, vol. 7, no. 6, pp. 19A–24A, 1967.

[336] P. Nava, N. Paone, G. L. Rossi, and E. P. Tomasini, "Design and Experimental Characterization of a Nonintrusive Measurement System of Rotating Blade Vibration," *Journal of Engineering for Gas Turbines and Power*, vol. 116, no. July 1994, pp. 657–662, 1993.

[337] A. Kurkov and J. Dicus, "Synthesis of Blade Flutter Vibratory Patterns Using Stationary Transducers," *Proceedings of ASME Turbo Expo*, no. 78-GT-160, pp. 1–9, 1978.

[338] I. Y. Zablotskiy and Y. A. Korostelev, "Measurement of Resonance Vibrations of Turbine Blades with the ELURA Device," *Energomashinostroneniye*, no. 2, pp. 36–39, 1970.

[339] S. Heath and M. Imregun, "An Improved Single-Parameter Tip-Timing Method for Turbomachinery Blade Vibration Measurements Using Optical Laser Probes," *International Journal of Mechanical Sciences*, vol. 38, no. 10, pp. 1047–1058, 1996.

[340] G. Schlagwein and U. Schaber, "Non-contact blade vibration measurement analysis using a multi-degree-of-freedom model," *Proceedings of the Institution of Mechanical Engineers, Part A: Journal of Power and Energy*, vol. 220, pp. 611–618, 2006.

[341] H. Guo, F. Duan, and M. Wang, "Engine order identification based on blade tip-timing single parameter method," *Journal of Tianjin University Science and Technology*, vol. 49, no. 9, pp. 951–955, 2016.

[342] G. Rigosi, G. Battiato, and T. M. Berruti, "Synchronous vibration parameters identification by tip timing measurements," *Mechanics Research Communications*, vol. 79, pp. 7–14, 2017.

[343] Y.-G. Zhang, F. Duan, Z.-Q. Fang, S. Li, T. Ouyang, S.-H. Ye, and X.-J. Shi, "Research on Analyzing Amplitude of Synchronous Blade Vibration Using Speed-Vector-End-Tracking Method," *Chinese Journal of Sensors and Actuators*, vol. 9, 2007.

[344] Y.-G. Zhang, F. Duan, Z.-Q. Fang, and S.-H. Ye, "Research on amplitude measurement of synchronous blade vibration using fiber-optic bundle sensor," *Journal of Optoelectronics.Laser*, vol. 1, 2008.

[345] F. Duan, T. Ouyang, M. Li, Z. Zhong, X. Shi, and Z. Fan, "Research on Detecting Technology of Rotating Blade Vibration Performance Parameters," *Proceedings of the International Conference on Measuring Technology and Mechatronics Automation*, pp. 693–696, 2009.

[346] T. Ouyang, W.-L. Guo, F. Duan, and M. Li, "New method for identifying rotating blades synchronous vibration based on tip-timing," *Journal of Vibration and Shock*, vol. 8, 2011.

[347] B. Salhi, J. Lardiès, M. Berthillier, P. Voinis, and C. Bodel, "A subspace approach for the analysis of blade tip timing data," *Proceedings of the 12th IFToMM World Congress*, pp. 1–6, 2007.

[348] B. Salhi, J. Lardiès, M. Berthillier, P. Voinis, and C. Bodel, "Modal parameter identification of mistuned bladed disks using tip timing data," *Journal of Sound and Vibration*, vol. 314, pp. 885–906, 2008.

[349] B. Salhi, J. Lardiès, and M. Berthillier, "Parameter Identification of Bladed Assemblies Using a Subspace Method," *International Journal for Simulation and Multidisciplinary Design Optimization*, vol. 2, pp. 267–272, 2008.

[350] B. Salhi, J. Lardies, and M. Berthillier, "Identification of modal parameters and aeroelastic coefficients in bladed disk assemblies," *Mechanical Systems and Signal Processing*, vol. 23, pp. 1894–1908, 2009.

[351] S. Heath, "A New Technique For Identifying Synchronous Resonances Using Tip-Timing," *Proceedings of the ASME International Gas Turbine and Aeroengine Congress and Exhibition*, no. 99-GT-402, pp. 1–8, 1999.

[352] Steve Heath, "A New Technique for Identifying Synchronous Resonances Using Tip-Timing," *Journal of Engineering for Gas Turbines and Power*, vol. 122, no. April 2000, pp. 219–225, 2000.

[353] T. Ouyang, F. Duan, M. Yan, M. Li, Z.-C. Zhong, and X.-J. Shi, "Research on identifying synchronous blade vibration using two-parameter-plot method," *Transducer and Microsystem Technologies*, vol. 3, 2010.

[354] P. Wang, D. Karg, Z. Fan, R. X. Gao, K. Kwolek, and A. Consiglio, "Non-contact identification of rotating blade vibration," *Mechanical Engineering Journal*, vol. 2, no. 3, pp. 1–12, 2015.

[355] F. M. Besem, R. E. Kielb, and N. L. Key, "Forced Response Sensitivity of a Mistuned Rotor From an Embedded Compressor Stage," *Journal of Turbomachinery*, vol. 138, no. March 2016, pp. 1–10, 2016.

[356] S. Murae, W. Sato, and A. Yamagata, "Experimental Study on Blade Vibration of Double-scroll Turbine," *Proceedings of the International Gas Turbine Congress*, no. IGTC-2019-183, pp. 1–5, 2019.

[357] I. A. Sever, "Discussions about BTT," *Rolls-Royce Meetings*, no. July, 2017.

[358] Z. Hu, J. Lin, Z.-S. Chen, Y.-M. Yang, and X.-J. Li, "A Non-Uniformly Under-Sampled Blade Tip-Timing Signal Reconstruction Method for Blade Vibration Monitoring," *Sensors*, vol. 15, pp. 2419–2437, 2015.

[359] J. Lin, Z. Hu, Z. S. Chen, Y. M. Yang, and H. L. Xu, "Sparse reconstruction of blade tip-timing signals for multi-mode blade vibration monitoring," *Mechanical Systems and Signal Processing*, vol. 81, pp. 250–258, 2016.

[360] M. Pan, Y. Yang, F. Guan, H. Hu, and H. Xu, "Sparse Representation Based Frequency Detection and Uncertainty Reduction in Blade Tip Timing Measurement for Multi-Mode Blade Vibration Monitoring," *Sensors*, vol. 17, pp. 1745–1763, 2017.

[361] Z. Chen, Y. Yang, Y. Xie, B. Guo, and Z. Hu, "Non-contact crack detection of high-speed blades based on principal component analysis and Euclidian angles using optical-fiber sensors," *Sensors and Actuators A: Physical*, vol. 201, pp. 66–72, 2013.

[362] L. Yue, H. Liu, C. Zang, D. Wang, W. Hu, and L. Wang, "The Parameter Identification Method of Blade Asynchronous Vibration under Sweep Speed Excitation," *Journal of Physics: Conference Series*, vol. 744, no. 012051, pp. 1–10, 2016.

[363] C. Zhongsheng, Y. Yongmin, G. Bin, and H. Zheng, "Blade damage prognosis based on kernel principal component analysis and grey model using subsampled tip-timing signals," *Journal of Mechanical Engineering Science*, vol. 228, no. 17, pp. 3178–3185, 2014.

[364] B.-N. Fan, "The Study of Signal Reconstruction and Denoising of Rotating Machinery," *Value Engineering*, vol. 31, 2015.

[365] M. Pan, F. Guan, H. Hu, Y. Yang, and H. Xu, "Compressed sensing based on dictionary learning for reconstructing blade tip timing signals," *Proceedings of the Prognostics and System Health Management Conference*, pp. 1–6, 2017.

[366] H. Xu, Z. Chen, Y. Yang, L. Tao, F. Guan, and H. Hu, "Damage detection in high-speed rotated blades by blade tip-timing method based on compressed sensing," *Proceedings of the Prognostics and System Health Management Conference*, pp. 1–5, 2017.

[367] C. Zhan, Z. Chen, Z. Hu, Y. Yang, and H. Hu, "Nonlinear Time Transformation-Based Vibration Signal Reconstruction for Blade Tip-Timing under Rotation Speed Fluctuations," *Proceedings of the Prognostics and System Health Management Conference*, pp. 1–5, 2017.

[368] A. Bouchain, J. Picheral, E. Lahalle, and A. Vercoutter, "Méthode parcimonieuse pour l'analyse spectrale de signaux tip-timing," *Proceedings of the 26ème Colloque GRETSI Traitement du Signal*, pp. 1–4, 2017.

[369] A. Bouchain, J. Picheral, E. Lahalle, A. Vercoutter, and A. Talon, "Sparse Method for Tip-Timing Signals Analysis with Non Stationary Engine Rotation Frequency," *Proceedings of the 26th European Signal Processing Conference*, pp. 1730–1734, 2018.

[370] Z. Chen, J. Liu, C. Zhan, J. He, and W. Wang, "Reconstructed Order Analysis-Based Vibration Monitoring under Variable Rotation Speed by Using Multiple Blade Tip-Timing Sensors," *Sensors*, vol. 18, pp. 3235–3258, 2018.

[371] F. Yang, Y. Yang, H. Hu, F. Guan, and G. Shen, "An Improved Algorithm for Accelerating the Sparse Reconstruction Speed of Blade Tip-Timing Signal," *Proceedings of the IEEE 8th Joint International Information Technology and Artificial Intelligence Conference*, pp. 1035–1038, 2019.

[372] Z. Chen, J. He, and C. Zhan, "Undersampled Blade Tip-Timing Vibration Reconstruction under Rotating Speed Fluctuation: Uniform and Nonuniform Sensor Configurations," *Shock and Vibration*, no. 8103216, pp. 1–13, 2019.

[373] H. Xu, Y. Yang, H. Hu, F. Guan, and Z. Chen, "Compressed Sensing-based Blind Reconstruction of Multi-frequency Blade Vibration from Under-sampled BTT Signals," *Journal of Mechanical Engineering*, vol. 55, no. 13, pp. 113–121, 2019.

[374] K. Chen, Y. Zhang, W. Wang, X. Zhang, and D. Hu, "Identification Method of Blade Vibration with High EO Based on Virtual Sensor Interpolation," *Journal of Mechanical Engineering*, vol. 55, no. 19, pp. 1–8, 2019.

[375] C. He, H. Li, X. Zhao, W. Wang, and S. Wu, "Analysis Method for Under-sampled Blade Tip-timing Signal Based on the Rotational Invariance Technique with Total Least Squares Principle," *Journal of Mechanical Engineering*, vol. 55, no. 19, pp. 103–111, 2019.

[376] X. Zhang, J. Tian, Z. Sun, and H. Ouyang, "Compressive sensing identification method of blade tip timing signals based on arbitrary sensor arrangement," *Journal of Aerospace Power*, vol. 35, no. 1, pp. 41–51, 2020.

[377] Z. Wang, Z. Yang, S. Wu, H. Li, S. Tian, and X. Chen, "An Improved Multiple Signal Classification for Non-uniform Sampling in Blade Tip Timing," *IEEE Transactions on Instrumentation and Measurement*, pp. 1–11, 2020.

[378] J. Roberts, "Comparison of TT measurements with strain gauges," *Von Karman Institute for Fluid Dynamics Lecture Series*, 2007.

[379] T. Maywald, B. Beirow, C. R. Heinrich, and A. Kühhorn, "Vacuum Spin Test Series of a Turbine Impeller With Focus on Mistuning and Damping By Comparing Tip Timing and Strain Gauge Results," *Proceedings of ASME Turbo Expo*, no. GT2015-42649, pp. 1–10, 2015.

[380] O. Freund, M. Montgomery, M. Mittelbach, and J. R. Seume, "Non-contact test set-up for aeroelasticity in a rotating turbomachine combining a novel acoustic excitation system with tip-timing," *Measurement Science and Technology*, vol. 25, no. 035008, pp. 1–13, 2014.

[381] W. B. Watkins and R. M. Chi, "Noninterference Blade-Vibration Measurement System for Gas Turbine Engines," *Journal of Propulsion and Power*, vol. 5, no. 6, pp. 727–730, 1989.

[382] A. Kulkarni and G. LaRue, "Vibratory Response Characterization of a Radial Turbine Wheel for Automotive Turbocharger Application," *Proceedings of ASME Turbo Expo*, no. GT2008-51355, pp. 1–9, 2008.

[383] I. B. Carrington, J. R. Wright, J. E. Cooper, and G. Dimitriadis, "A Comparison of Blade Tip-Timing Data Analysis Methods," *Proceedings of the 1st International Conference on the Integration of Dynamics, Monitoring and Control*, pp. 1–6, 1999.

[384] S. Heath and M. Imregun, "A Review of Analysis Techniques for Blade Tip-Timing Measurements," *Proceedings of the ASME International Gas Turbine and Aeroengine Congress and Exhibition*, no. 97-GT-213, pp. 1–8, 1997.

[385] R. Przysowa and P. Russhard, "Non-contact measurement of blade vibration in an axial compressor," *Preprints*, pp. 1–16, 2019.

[386] C. Heinz, M. Schatz, M. V. Casey, and H. Stüer, "Impact of Mistuning on the Vibration Behaviour of the Last Stage in a Model Three Stage Low Pressure Steam Turbine," *Proceedings of ASME Turbo Expo*, no. GT2011-45784, pp. 1–10, 2011.

[387] D. Hemberger, D. Filsinger, and H.-J. Bauer, "Investigations on Maximum Amplitude Amplification Factor of Real Mistuned Bladed Structures," *Proceedings of ASME Turbo Expo*, no. GT2012-68084, pp. 1–12, 2012.

[388] M. Mercadal, A. von Flotow, and P. Tappert, "Damage Identification by NSMS Blade Resonance Tracking in Mistuned Rotors," *Proceedings of the IEEE Aerospace Conference*, vol. 7, pp. 3263–3277, 2001.

[389] R. Rzadkowski, A. Maurin, L. Kubitz, and R. Szczepanik, "Forced Vibration of Mistuned Bladed Discs in Last Stage LP Steam Turbine," *Proceedings of ASME Turbo Expo*, no. GT2016-57427, pp. 1–8, 2016.

[390] J. Li, N. Aye-Addo, N. Kormanik III, D. Matthews, N. Key, and R. Kielb, "Mistuned Higher-Order Mode Forced Response of an Embedded Compressor Rotor, Part I: Steady and Unsteady Aerodynamics," *Proceedings of ASME Turbo Expo*, no. GT2017-64633, pp. 1–13, 2017.

[391] J. Li, N. Aye-Addo, R. Kielb, and N. Key, "Mistuned Higher-Order Mode Forced Response of an Embedded Compressor Rotor, Part II: Mistuned Forced Response Prediction," *Proceedings of ASME Turbo Expo*, no. GT2017-64647, pp. 1–13, 2017.

[392] D. Heller, I. A. Sever, and C. W. Schwingshackl, "Blade Timing," 2019.

[393] D. Heller, I. A. Sever, and C. W. Schwingshackl, "Determination of Blade Vibration by Blade Tip-Timing Sensor Waveform Analysis," *Proceedings of the 23rd Blade Mechanics Seminar*, pp. 1–25, 2018.

[394] D. Heller, I. A. Sever, and C. W. Schwingshackl, "A method for multi-harmonic vibration analysis of turbomachinery blades using Blade Tip-Timing and clearance sensor waveforms and optimization techniques," *Mechanical Systems and Signal Processing*, vol. 142, no. 106741, pp. 1–24, 2020.

[395] C. Teolis and A. Teolis, "Method of Determining the Operating Status of a Turbine Engine Utilizing an Analytic Representation of Sensor Data," 2008.

[396] E. D. Cohen, *Vibration Detection in Turbomachinery Using Non-Contacting Sensors*. PhD thesis, Massachusetts Institute of Technology, 2006.

[397] E. D. Cohen and J. D. Paduano, "System and Method for Providing Vibration Detection in Turbomachinery," 2009.

[398] N. Jamia, M. I. Friswell, and S. El-Borgi, "Robust Condition Monitoring of Gas Turbines," *Publications of Swansea University*, 2017.

[399] N. Jamia, M. I. Friswell, S. El-Borgi, and R. Fernandes, "Simulating eddy current sensor outputs for blade tip timing," *Advances in Mechanical Engineering*, vol. 10, no. 1, pp. 1–12, 2018.

[400] N. Jamia, M. I. Friswell, S. El-Borgi, and P. Rajendran, "Simulating Eddy Current Sensors in Blade Tip Timing Application: Modeling

and Experimental Validation," *Proceedings of ASME International Mechanical Engineering Congress and Exposition*, no. IMECE2018-87414, pp. 1–9, 2018.

[401] N. Jamia, M. Friswell, S. El-Borgi, and P. Rajendran, "Blade tip timing based condition monitoring of bladed disks in rotating machines," *Proceedings of ISMA2018 and USD2018*, pp. 941–955, 2018.

[402] N. Jamia, M. I. Friswell, S. El-Borgi, and P. Rajendran, "Modelling and experimental validation of active and passive eddy current sensors for blade tip timing," *Sensors and Actuators A: Physical*, vol. 285, pp. 98–110, 2019.

[403] N. Jamia, M. I. Friswell, S. El-Borgi, and P. Rajendran, "Blade Tip Timing Based Condition Monitoring of Bladed Disks in Rotating Machines (poster)," *Publications of Swansea University*, 2019.

[404] N. Jamia, *Modelling and experimental validation of eddy current sensors for blade tip timing*. PhD thesis, Swansea University, 2019.

[405] P. Rajendran, N. Jamia, S. El-Borgi, and M. I. Friswell, "Wavelet Transform-Based Damage Identification in Bladed Disks and Rotating Blades," *Shock and Vibration*, no. 3027980, pp. 1–16, 2018.

[406] N. Jamia, P. Rajendran, S. El-Borgi, and M. I. Friswell, "Mistuning identification in a bladed disk using wavelet packet transform," *Acta Mechanica*, vol. 229, pp. 1275–1295, 2018.

[407] A. Chernyavskii, A. I. Danilin, and S. I. Adamov, "Hardware/software blade pulse emulator for measuring parameters of control systems of turbomachine blade deformation condition," *Sensors and Systems*, vol. 4, pp. 14–17, 2010.

[408] A. Z. Chernyavskii, A. I. Danilin, and S. A. Danilin, "Converters of dynamic displacement parameters of the blades of turbine-driven sets based on nonlinear approximation of primary signals," *Proceedings of*

All-Russian Conference on Radioelectronics and Telecommunication, pp. 44–46, 2012.

[409] A. Z. Chernyavskiy, A. I. Danilin, and S. A. Danilin, "Parameters Transducers of the Blade's Dynamic Movements of Turbounits Based on Nonlinear Approximation of Primary Signals," *Vestnik of Samara State University*, vol. 7, no. 38, pp. 117–123, 2012.

[410] A. I. Danilin, A. Z. Chernyavskiy, and S. A. Danilin, "The Device for the Determination of Blades Oscillation Parameters Based on Nonlinear Approximation of Primary Transducers Sign," *Vestnik of Samara State University*, vol. 5, no. 36, pp. 194–202, 2012.

[411] A. I. Danilin and A. A. Gretskov, "Doppler Method for Measuring Fluctuations of Elements Rotationg Parts Power," *Vestnik of Samara State University*, vol. 3, no. 34, pp. 171–178, 2012.

[412] V. G. Domrachev, V. M. Grechishnikov, A. Z. Chernyavskii, A. I. Danilin, and S. A. Danilin, "Determination of the Oscillation Parameters of the Blades of Turbine-Driven Sets Based on Nonlinear Approximation of the Signals of Primary Converters," *Mechanical Measurements*, vol. 56, no. 11, pp. 1242–1247, 2014.

[413] A. Z. Chernyavskii and S. A. Danilin, "An algorithm for the evaluation of the noise resistance of a method used for the determination of the parameters of vibration of the blades of turboaggregates based on the nonlinear approximation of signals from primary transducers," *Scientific Publications of the Samara State Aerospace University*, vol. 18, no. 4, pp. 161–165, 2016.

[414] A. I. Danilin and A. A. Gretskov, "Analysis of Information Characteristics of a Dynamic Displacement Doppler Transducer Signal," *Vestnik of Samara State University*, vol. 15, no. 3, pp. 170–177, 2016.

[415] A. I. Danilin, A. Z. Chernyavskij, S. A. Danilin, and A. A. Gretskov, "Method for Determining the Oscillation Parameters of Turbo-Machine Blades and a Device for Putting the Same into Practice," 2017.

[416] A. Z. Chernyavskii, A. I. Danilin, S. A. Prokhorov, and S. A. Danilin, "Accuracy of Determination of the Parameters of Vibration of Turbomachine Blades with the Use of a Nonlinear Approximation of the Signals of Primary Transducers," *Measurement Techniques*, vol. 60, no. 11, pp. 1130–1136, 2018.

[417] M. Witos and M. Wachlaczenko, "Structural Health Monitoring of Compressor Blades with the use of Variable Reluctance Sensor and Impedance Method," *Proceedings of the 19th World Conference on Non-Destructive Testing*, pp. 1–8, 2016.

[418] W. C. Haase and Z. S. Haase, "High-Speed, Capacitance-Based Tip Clearance Sensing," *Proceedings of the IEEE Aerospace Conference*, pp. 1–8, 2013.

[419] T. Dadáková and Z. Kubín, "Calibration of BTT Measurement with Respect to Sensor Position over Shrouded LSB," *Acta Polytechnica CTU Proceedings*, vol. 20, pp. 29–33, 2018.

[420] M. I. Friswell and J. E. Mottershead, *Finite Element Model Updating in Structural Dynamics*. Springer Netherlands, 1995.

[421] M. Mohamed, P. Bonello, and P. Russhard, "The Determination of Steady-State Movements Using Blade Tip Timing Data," *Proceedings of ASME Turbo Expo*, no. GT2018-75488, pp. 1–10, 2018.

[422] M. Mohamed, P. Bonello, and P. Russhard, "Development of A Finite Element Model Simulator For Blade Tip Timing Data Generation," *Proceedings of the 23rd Blade Mechanics Seminar*, pp. 1–28, 2018.

[423] Z. Kubín, T. Mísek, J. Hlous, T. Dadaková, J. Kellner, and T. Bachorec, "Calibration of blade tip-timing sensor for shrouded 40" last stage blade," *Mechanical Systems and Signal Processing*, vol. 108, pp. 88–98, 2018.

[424] M. Mohamed, P. Bonello, and P. Russhard, "Determination of Simultaneous Steady-State Movements Using Blade Tip Timing Data," *Proceedings of ASME Turbo Expo*, no. GT2019-90042, pp. 1–12, 2019.

[425] M. Mohamed, P. Bonello, and P. Russhard, "A novel method for the determination of the change in blade tip timing probe sensing position due to steady movements," *Mechanical Systems and Signal Processing*, vol. 126, pp. 686–710, 2019.

[426] R. R. Craig and A. J. Kurdila, *Fundamentals of Structural Dynamics*. John Wiley & Sons, 2 ed., 2006.

[427] L. Pesaresi, L. Salles, A. Jones, J. S. Green, and C. W. Schwingshackl, "Modelling the nonlinear behaviour of an underplatform damper test rig for turbine applications," *Mechanical Systems and Signal Processing*, vol. 85, pp. 662–679, 2017.

[428] C. Heinz, M. Schatz, M. V. Casey, and H. Stüer, "Experimental and Analytical Investigations of a Low Pressure Model Turbine During Forced Response Excitation," *Proceedings of ASME Turbo Expo*, no. GT2010-22146, pp. 1–11, 2010.

[429] H. S. Dhadwal, M. Radzikowski, D. Strukov, and A. Kurkov, "Real Time Flutter Monitoring System for Turbomachinery," *Proceedings of ASME Turbo Expo*, no. GT2004-53992, pp. 1–12, 2004.

[430] J. L. Geisheimer, S. A. Billington, and D. W. Burgess, "A Microwave Blade Tip Clearance Sensor for Active Clearance Control Applications," *Proceedings of the 40th AIAA/ASME/SAE/ASEE Joint Propulsion Conference and Exhibit*, no. AIAA 2004-3720, pp. 1–8, 2004.

[431] M. Wachlaczenko and M. Witos, "Structural Health Monitoring of Compressor and Turbine Blades with the Use of Variable Reluctance Sensor and Tip Timing Method," *Proceedings of the 19th World Conference on Non-Destructive Testing*, pp. 1–8, 2016.

[432] M. T. Schobeiri, "Impact of Turbine Blade Stagger Angle Adjustment on the Efficiency and Performance of Gas Turbines During Off-Design and Dynamic Operation," *Proceedings of ASME Turbo Expo*, no. GT2018-75968, pp. 1–11, 2018.

[433] F. Figaschewsky, B. Hanschke, and A. Kühhorn, "Efficient Generation of Engine Representative Tip Timing Data Based on a Reduced Order Model for Bladed Rotors," *Journal of Engineering for Gas Turbines and Power*, vol. 141, no. January 2018, pp. 1–9, 2018.

[434] J. Gil-García, A. Solís, G. Aranguren, and J. Zubia, "An Architecture for On-Line Measurement of the Tip Clearance and Time of Arrival of a Bladed Disk of an Aircraft Engine," *Sensors*, vol. 17, pp. 2162–2176, 2017.

[435] W. Wang, H. Shao, X. Shao, and K. Song, "Investigation on the Turbine Blade Tip Clearance Measurement and Active Clearance Control Based on Eddy Current Pulse-Trigger Method," *Proceedings of ASME Turbo Expo*, no. GT2017-63980, pp. 1–11, 2017.

[436] W. Wang, H. Shao, L. Chen, and W. Qu, "Investigation on the Blade Tip Clearance Monitoring of Turbomachinery Based on the Pulse-Trigger Method," *Journal of Vibration, Measurement and Diagnosis*, vol. 37, no. 3, pp. 583–587, 2017.

[437] B. Hayes, "Design, Implementation, and Analysis of a Time of Arrival Measurement System for Rotating Machinery," *Proceedings of the 58th International Instrumentation Symposium*, pp. 1–60, 2012.

[438] Z. Zhao, Z. Liu, Y. Lv, and X. Xu, "Design and verification of high resolution eddy current sensor for blade tip clearance measurement," *Chinese Journal of Scientific Instrument*, vol. 39, no. 6, pp. 132–139, 2018.

[439] T. F. Coleman and Y. Li, "On the Convergence of Reflective Newton Methods for Large-Scale Nonlinear Minimization Subject to Bounds," *Mathematical Programming*, vol. 67, no. 2, pp. 189–224, 1994.

[440] T. F. Coleman and Y. Li, "An Interior Trust Region Approach for Nonlinear Minimization Subject to Bounds," *SIAM Journal on Optimization*, vol. 6, no. 2, pp. 418–445, 1996.

[441] Y.-x. Yuan, "A review of trust region algorithms for optimization," in *ICIAM 99: Proceedings of the Fourth International Congress on Industrial & Applied Mathematics*, pp. 271–282, Oxford University Press, 2000.

[442] Y.-x. Yuan, "Recent advances in trust region algorithms," *Mathematical Programming*, vol. 151, pp. 249–281, 2015.

[443] Z. Ugray, L. Lasdon, J. Plummer, F. Glover, J. Kelly, and R. Martí, "Scatter Search and Local NLP Solvers: A Multistart Framework for Global Optimization," *INFORMS Journal on Computing*, vol. 19, no. 3, pp. 328–340, 2007.

[444] J. Nocedal and S. J. Wright, *Numerical Optimization*. Springer, 2 ed., 2006.

[445] S. S. Rao, *Engineering Optimization: Theory and Practice*. John Wiley & Sons, 4 ed., 2009.

[446] V. Ruffini, *Coriolis effects in bladed discs*. PhD thesis, Imperial College London, 2016.

[447] V. Ruffini, T. Nauman, and C. W. Schwingshackl, "Impulse Excitation of Piezoelectric Patch Actuators for Modal Analysis," *Topics in Modal Analysis & Testing*, vol. 10, pp. 97–106, 2017.

[448] D. Weichert, *Mechanics of Materials*. RWTH Aachen University, 1999.

[449] D. J. Inman, *Vibration with Control*. John Wiley & Sons, 2006.

[450] G. A. Lesieutre and J. L. Kauffman, "'Geometric' Viscous Damping Model for Nearly Constant Beam Modal Damping," *AIAA Journal*, vol. 51, no. 7, pp. 1688–1694, 2013.

[451] M. Colakoglu and K. L. Jerina, "Damping behaviour of cyclically deformed 304 stainless steel," *Indian Journal of Engineering & Materials Sciences*, vol. 10, pp. 480–485, 2003.

[452] M. Milad, N. Zreiba, F. Elhalouani, and C. Baradai, "The effect of cold work on structure and properties of AISI 304 stainless steel," *Journal of Materials Processing Technology*, vol. 203, pp. 80–85, 2008.

[453] North American Stainless, "Long Products Stainless Steel Grade Sheet for AISI 304," *Product report*, pp. 1–8, 2020.

[454] S. Putter and H. Manor, "Natural Frequencies of Radial Rotating Beams," *Journal of Sound and Vibration*, vol. 56, no. 2, pp. 175–185, 1978.